U.S. DEPARTMENT OF ENERGY

PNNL-23393

Prepared for the
U.S. Nuclear Regulatory Commission
under a Related Services Agreement
with the U.S. Department of Energy
Contract DE-AC05-76RL01830

Phased Array Ultrasonic Sound Field Mapping in Cast Austenitic Stainless Steel

SL Crawford
MS Prowant
AD Cinson
MR Larche
AA Diaz
MT Anderson

May 2014

Pacific Northwest
NATIONAL LABORATORY

Proudly Operated by Battelle Since 1965

DISCLAIMER

PACIFIC NORTHWEST NATIONAL LABORATORY
operated by
BATTELLE
for the
UNITED STATES DEPARTMENT OF ENERGY
under Contract DE-AC05-76RL01830

Printed in the United States of America

Available to DOE and DOE contractors from the
Office of Scientific and Technical Information,
P.O. Box 62, Oak Ridge, TN 37831-0062;
ph: (865) 576-8401
fax: (865) 576-5728
email: reports@adonis.osti.gov

Available to the public from the National Technical Information Service,
U.S. Department of Commerce, 5285 Port Royal Rd., Springfield, VA 22161
ph: (800) 553-6847
fax: (703) 605-6900
email: orders@ntis.fedworld.gov
online ordering: http://www.ntis.gov/ordering.htm

This document was printed on recycled paper.
(9/2003)

PNNL-23393

Phased Array Ultrasonic Sound Field Mapping in Cast Austenitic Stainless Steel

SL Crawford
MS Prowant
AD Cinson
MR Larche
AA Diaz
MT Anderson

May 2014

Prepared for
U.S. Nuclear Regulatory Commission
under a Related Services Agreement
with the U.S. Department of Energy
Contract DE-AC05-76RL01830

Pacific Northwest National Laboratory
Richland, Washington 99352

Acronyms and Abbreviations

ASME	American Society of Mechanical Engineers
CASS	cast austenitic stainless steel
dB	decibels
DMW	dissimilar metal weld
GUI	graphical user interface
ID	inner diameter
ISI	inservice inspection
LWR	light water reactor
NDE	nondestructive examination
OD	outer diameter
PA	phased array
PNNL	Pacific Northwest National Laboratory
PWR	pressurized water reactor
SAFT	synthetic aperture focusing technique
Sk0	skew 0
Sk10	skew 10
SkT	skew T
TLR	technical letter report
TRL	transmit receive longitudinal
WSS	wrought stainless steel

Contents

Figures

Tables

1.0 Introduction

Coarse grained, cast austenitic stainless steel (CASS) materials and dissimilar metal welds (DMW) were used in the fabrication of primary coolant loop piping components, cladded components, overlay-repaired pipe joints, and Alloy 600/182/82 components in light water reactors (LWRs) in the United States. Conventional ultrasonic volumetric examinations are challenging in these materials because of a number of factors associated with the material microstructures, surface conditions and geometries encountered in the field. Ultrasonic beams are attenuated with scattering as the primary effect and redirected because of the heterogeneous and anisotropic nature of the material. Regardless, these components are subject to volumetric in-service inspection (ISI) as specified in Section XI of the American Society of Mechanical Engineers (ASME) Boiler and Pressure Vessel Code. The Pacific Northwest National Laboratory (PNNL) has been involved with nondestructive examination (NDE) of coarse-grained CASS components for over 35 years. Earlier work at PNNL employed lower ultrasonic frequencies and longer wavelengths coupled with advanced signal processing methodologies, including the synthetic aperture focusing technique (SAFT) (Hall et al. 1988; Doctor et al. 1996). Beam profiling activities were also conducted with conventional single-element probes and showed the distortion that occurs with a vertically polarized shear wave probe as compared to a longitudinal wave probe (Good and Van Fleet 1987; Good and Van Fleet 1988, 1990). The effects of probe frequency were also explored in greater depth, including the use of probes in the 250-kHz to 4-MHz range (Diaz et al. 1998; Diaz et al. 2008). More recent efforts have been directed toward the application of phased array (PA) technology (Anderson et al. 2007) to the examination of these materials and components. This study mapped the phased array-generated acoustic sound fields through three types of CASS microstructure in four specimens to quantitatively assess the beam formation effectiveness in these materials. The beams were generated with three different PA probes operating at center frequencies of 0.5, 0.8, and 1.0 MHz and represented probes designed for the evaluation of coarse-grained materials. Several different refracted and skew angles were also evaluated at each probe frequency. After the initial evaluation of each CASS specimen, a 6.4-mm (0.25-in. slice) of material was removed from the end of a specimen and the beam mapping repeated. This slice and beam mapping process was performed three times for a total of four beam mappings per specimen.

This technical letter report (TLR) provides a summary of the study that was conducted at PNNL over the past 2 years. The TLR is organized with Section 2.0 providing the objectives and scope of the work. Section 3.0 describes common CASS material types and the specific specimens evaluated. The experimental setup, data acquisition protocol, and PA probes are presented in Sections 4.0 and 5.0. Section 6.0 presents the ultrasonic data acquisition and analyses conducted. The measurements performed on the sound field images include a measure of scatter, partitioning, and beam redirection. Additionally, various experimental parameters are evaluated and correlated to the sound field measurements in this section. Lastly, a discussion and conclusions are presented in Section 7.0 with references listed in Section 8.0. Supporting documentation is provided in Appendices A through E.

2.0 Objective and Scope

The objective of this sound field mapping exercise is to relate ultrasonic inspection parameters or variables to phased array ultrasonic beam formation capabilities in CASS materials where the materials have been characterized by grain type, orientation, and size. The materials were measured for mean grain size as well as maximum grain size in cross-sectional slices from each specimen. In order to better understand the impacts of the CASS microstructures on sound field coherence and propagation, phased array ultrasonic beam formation was characterized in terms of beam scatter, partitioning, and redirection. The effects of the input ultrasonic inspection parameters such as probe center frequency and refracted and skew angles are discussed with respect to the specimen microstructure as they all relate to beam formation. Also examined was the ability to focus the sound field at the intended target. Lastly, suggested guidelines for a more effective evaluation of CASS components are presented.

3.0 Materials

Three specimens containing four microstructures representing vintage CASS material used in the nuclear industry (Diaz et al. 1998) were evaluated in this study. Additionally, a fine-grained, isotropic reference specimen fabricated from wrought stainless steel was also examined, and used as the baseline material. These specimens are described in this section.

3.1 CASS Specimens

CASS materials are found extensively in the primary piping systems in pressurized water reactors (PWRs). The microstructures of these materials are classified as columnar (dendritic), equiaxed, or a mixture of the two. Banding and layered combinations of these microstructures are also found in these materials. The specimens are first described and then the characteristics of their microstructures are discussed.

3.1.1 Description of Specimens

Specimen B-519 consisted of a pipe section with equiaxed microstructure welded to a pipe section with columnar microstructure. The material was from two different heats of ASTM A-351 Grade CF-8A centrifugally cast pipe (Diaz et al. 1998; Anderson et al. 2007). Slices cut from each end of the welded pipe specimen were polished and etched to reveal the grain structures as shown in Figure 3.1. The two sides of the specimen were denoted B-519E and B-519C for equiaxed and columnar grains, respectively. Both sides of this specimen were evaluated in the sound field mapping activity. The other two specimens are marked AAD-2 and AAD-3 and provide a total of four microstructures that were evaluated. Both AAD specimens have a multi-banded and mixed coarse grained microstructure as shown in Figure 3.2 and are from the Southwest Research Institute (Diaz et al. 1998; Ruud et al. 2009). Dimensions of the specimens are given in Table 3.1. The full pipe dimensions are given in the outer diameter (OD) and inner diameter (ID) columns, while the extent columns list the actual dimensions of the specimens. Measured velocity values are provided in the right column. Data for the wrought stainless steel (WSS) reference specimen, discussed in Section 3.2, are presented in the bottom row.

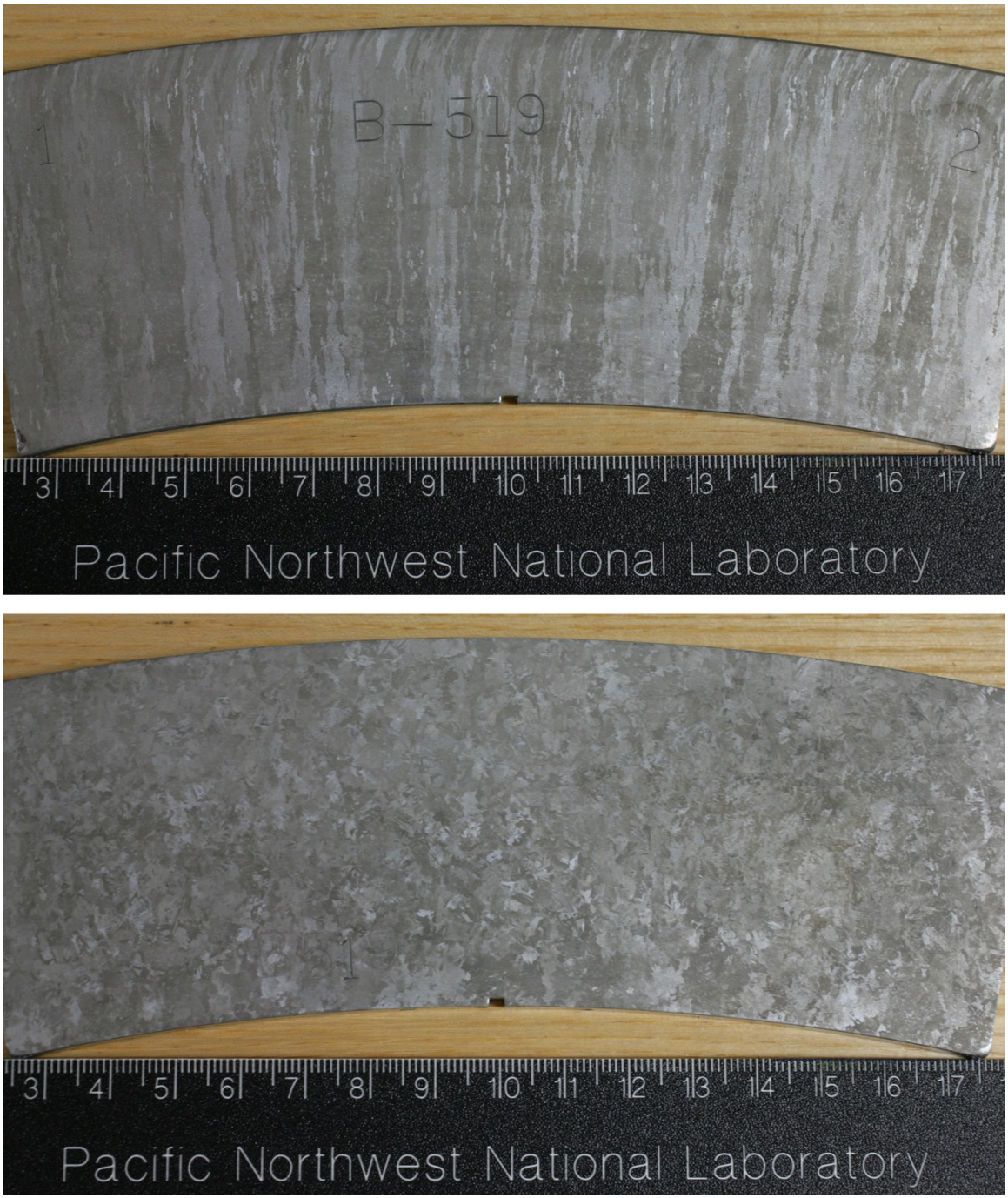

Figure 3.1. Grain Structure of Columnar B-519C (top) and Equiaxed B-519E (bottom)

Figure 3.2. Grain Structure of Banded Specimens AAD-2 (top) and AAD-3 (bottom)

Table 3.1. Measurements of Specimens Used in the Study in mm (in.)

			Extent, mm (in.)			Velocity, mm/µsec (in./µsec)
	OD, mm (in.)	ID, mm (in.)	Thickness	Circ.	Axial	
AAD-2	730.25 (28.8)	601.1 (23.7)	64.6 (2.5)	362.2 (14.3)	310.9 (12.2)	5.74 (0.226)
AAD-3	965.2 (38.0)	797.6 (31.4)	83.3 (3.3)	285.5 (11.2)	207.0 (8.1)	5.59 (0.220)
B-519E	845.8 (33.3)	729.0 (28.7)	58.4 (2.3)	174.6 (6.9)	141.7 (5.6)	5.85 (0.230)
B-519C		723.9 (28.5)	61.0 (2.4)			5.44 (0.214)
WSS	914.4 (36.0)	787.4 (31.0)	63.5 (2.5)	508.0 (20.0)	508.0 (20.0)	5.66 (0.223)

3.1.2 Grain Size Calculation

The grain sizes were measured based on a linear intercept method in the radial and circumferential directions. Using a high-resolution camera, each specimen was photographed, and the area representing ±45 mm (1.8 in.) from center in the horizontal and radial directions was loaded into MATLAB. This area approximately represented the region of beam forming and mapping. Mean and maximum grain sizes were determined from the three cut surfaces and one base material surface for each of the four specimens. In the AAD-3 specimen, bands were first highlighted in different colors to enhance and segregate the various regions. The results are displayed in Figure 3.3 on the left. Then the individual grains, as outlined on the right of Figure 3.3, were characterized by size and orientation.

An edge detection algorithm run in the MATLAB software assisted the analyst in outlining and characterizing the grains in each end face of the specimens (Figure 3.4). Because of the complexity of the grain images, not all of the grain boundaries were detected by the algorithm. At times additional manual touchup was required to emphasize grain boundaries before the software could identify and process them. Using the boundary information obtained within MATLAB, the average and maximum grain size in the circumferential and radial directions were easily extracted for each defined area.

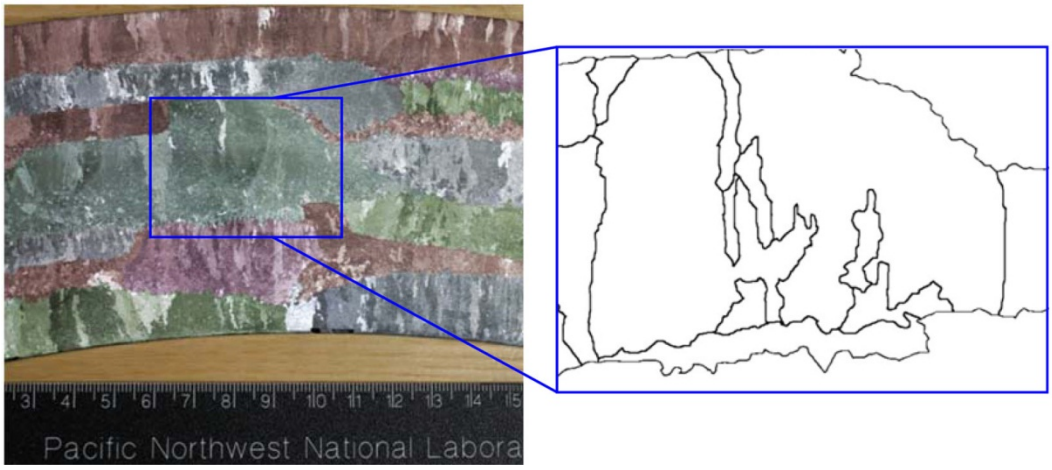

Figure 3.3. Outline of Etched Grains Found in One Band of AAD-3

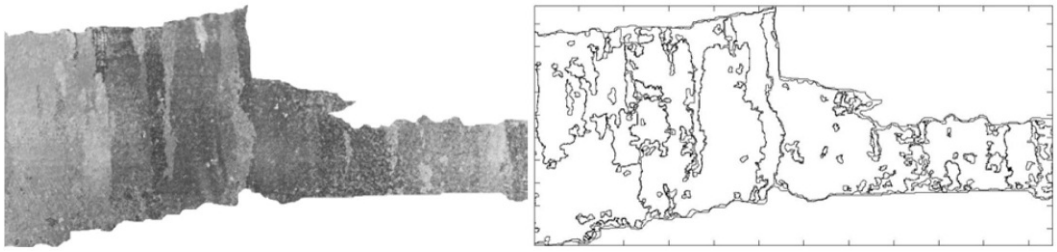

Figure 3.4. Outlined Banded Grains (right) from High-Resolution Image (left)

Mean grain size measurements are listed in Table 3.2 and the maximum grain size measurements are listed in Table 3.3. Because of the mixed banded nature of the AAD specimens, a range is given for the mean and maximum grain dimensions. Photographs of the specimen faces are displayed in Appendix A. The slice-to-slice variation in the mean data values was nominally 2 mm or less except for the AAD specimens where the variation was as high as 3 mm in the radial direction. Variations in the maximum grain diameters as measured from slice to slice were in the 0- to 8-mm range except in the AAD-2 and AAD-3 specimens where the variation was as great as 15 mm. The equiaxed specimen, B-519E, showed the most uniformity through all measured surfaces.

Elongation values (similar to the inverse of aspect ratio) are also given in Table 3.2 and compare the radial to circumferential grain values. Specimen B-519C with columnar grains has the largest elongation values, 3.0 in slice 2, and the equiaxed grains of B-519E are all 1.0, indicative of equal sides in the grains. As expected, the mixed banded AAD specimens have variable elongation with values in the 0.7 to 2.3 range. These two specimens also have elongation values less than 1, representing grains larger in the circumferential direction than the radial direction.

Table 3.2. Mean Grain Measurements and Elongation of Specimens by Slice

	Mean Grain Size (mm [in.])		
	Radial	**Circumferential**	**Elongation (r/c)**
Slice 1			
B-519E	1.6 (0.061)	1.5 (0.060)	1.0
B-519C	5.5 (0.217)	2.1 (0.082)	2.6
AAD-3	1.4–8.3 (0.055–0.327)	1.6–6.2 (0.063–0.244)	0.7–2.2
AAD-2	1.7–4.6 (0.067–0.181)	1.5–4.6 (0.059–0.181)	1.0–1.6
Slice 2			
B-519E	1.6 (0.062)	1.5 (0.060)	1.0
B-519C	7.7 (0.304)	2.6 (0.101)	3.0
AAD-3	1.3–8.8 (0.051–0.346)	1.6–5.0 (0.063–0.197)	0.8–2.1
AAD-2	4.9–5.2 (0.193–0.205)	2.7–4.7 (0.106–0.185)	1.1–1.8
Slice 3			
B-519E	1.5 (0.060)	1.5 (0.059)	1.0
B-519C	6.8 (0.268)	2.7 (0.107)	2.5
AAD-3	1.5–9.0 (0.059–0.354)	1.8–4.5 (0.071–0.177)	0.7–2.3
AAD-2	3.6–4.6 (0.142–0.181)	2.2–5.3 (0.087–0.209)	0.9–1.6
Slice 4			
B-519E	1.9 (0.075)	2.0 (0.079)	1.0
B-519C	5.3 (0.209)	2.2 (0.087)	2.4
AAD-3	1.4–5.8 (0.055–0.228)	1.8–4.3 (0.071–0.169)	0.8–1.6
AAD-2	3.0–3.8 (0.118–0.150)	2.2–4.3 (0.087–0.169)	0.9–1.4
Average			
B-519E	1.6 (0.063)	1.6 (0.063)	1.0
B-519C	6.3 (0.248)	2.4 (0.094)	2.6
AAD-3	3.8 (0.150)	2.9 (0.114)	1.2
AAD-2	3.8 (0.150)	3.3 (0.130)	1.2

Table 3.3. Maximum Grain Size Measurements of Specimens by Slice

	Maximum Grain Size (mm [in.])	
	Radial	**Circumferential**
Slice 1		
B-519E	8.0 (0.315)	14.9 (0.587)
B-519C	48.5 (1.909)	8.1 (0.319)
AAD-3	3.0–30.1 (0.118–1.185)	6.2–30.6 (0.244–1.205)
AAD-2	6.2–18.2 (0.244–0.717)	6.6–13.1 (0.260–0.516)
Slice 2		
B-519E	6.8 (0.268)	13.9 (0.547)
B-519C	55.3 (2.177)	11.7 (0.461)
AAD-3	1.7–31.2 (0.067–1.228)	4.5–19.7 (0.117–0.776)
AAD-2	8.3–23.3 (0.327–0.917)	9.4–17.2 (0.371–0.677)
Slice 3		
B-519E	5.5 (0.217)	10.8 (0.425)
B-519C	54.0 (2.126)	9.8 (0.386)
AAD-3	3.4–35.8 (0.134–1.409)	7.1–16.9 (0.280–0.665)
AAD-2	12.2–23.3 (0.480–0.917)	7.8–13.8 (0.307–0.543)
Slice 4		
B-519E	12.3 (0.484)	18.3 (0.720)
B-519C	58.8 (2.315)	9.9 (0.390)
AAD-3	4.7–36.0 (0.185–1.417)	6.3–29.8 (0.248–1.173)
AAD-2	12.4–22.8 (0.488–0.898)	8.9–29.2 (0.350–1.150)
Average		
B-519E	8.2 (0.3231)	14.5 (0.571)
B-519C	54.2 (2.134)	9.9 (0.390)
AAD-3	12.8 (0.504)	12.6 (0.496)
AAD-2	15.4 (0.606)	13.0 (0.512)

3.2 Reference Specimen

A Type 304 stainless steel rolled plate (508.0 by 508.0 by 63.5 mm or 20.0 by 20.0 by 2.5 in.) was used as a reference specimen. This wrought stainless steel (WSS) specimen has an OD of 91.4 cm (36 in.). It was designed as a calibration piece for low frequency PA probes used in the evaluation of thick-section CASS components. Part of its design included the introduction of notches and side-drilled holes. A blank section in the specimen was evaluated to assess the three PA probes' beam-forming capabilities in a relatively fine-grained, isotropic material. No quantification of the grain sizes is available, but a nominal range of 0.050 to 0.150 mm ($2.0 – 5.9 \times 10^{-3}$ in.) could be considered for a 304 stainless steel (Kestenbach and Meyers 1976), presenting at least an order of magnitude (if not two orders) smaller grains than the equiaxed specimen.

3.3 Wavelength

The specimens were examined with three phased array probes designed to have center frequencies of 0.5, 0.8, and 1.0 MHz, as discussed in Section 4.0. Velocities were measured on the specimens with a conventional single-element probe and are listed in Table 3.4. A determination of the acoustic wavelengths and how they compare to the grain sizes is useful in understanding the sound field degradation and, in particular, attenuation from scattering. Scattering occurs in an isotropic material when the grain diameter is small or comparable to the wavelength and when certain inhomogeneities have acoustic impedance values that are different than the surrounding material, such as found in CASS materials. The three scattering regimes are Rayleigh, stochastic and geometrical and are defined as (Szilard 1982):

Rayleigh	$\lambda >> D$	$A_s \propto D^3F^4$
Stochastic	$\lambda \cong D$	$A_s \propto DF^2$
Geometric	$\lambda << D$	$A_s \propto 1/D$

where λ is the wavelength, D is the average grain diameter, A_s is attenuation due to scattering, and F is the acoustic frequency. Separation of the regimes is not sharply defined and is directly influenced by large grains present in the CASS materials. Table 3.4 lists the wavelengths for the specimens in this study. The WSS specimen is fine-grained and assumed to be homogeneous; therefore, has negligible scattering. The CASS specimens, however, are nominally in the Rayleigh or stochastic range where scattering increases with frequency to the second or fourth power. Equiaxed specimen B519-E, with the largest λ/D ratio, is assumed to represent the Rayleigh regime and therefore produce the most scattering.

Table 3.4. Acoustic Wavelengths in the Specimens

Specimen	Velocity, mm/μsec (in./μsec)	Wavelength, mm (in.)		
		0.5 MHz	0.8 MHz	1.0 MHz
AAD-2	5.74 (0.226)	11.5 (0.45)	7.2 (0.28)	5.7 (0.23)
AAD-2	5.59 (0.220)	11.2 (0.44)	7.0 (0.28)	5.6 (0.22)
B-519C	5.44 (0.214)	10.9 (0.43)	6.8 (0.27)	5.4 (0.21)
B-519E	5.85 (0.230)	11.7 (0.46)	7.3 (0.29)	5.9 (0.23)
WSS	5.66 (0.223)	11.3 (0.45)	7.1 (0.28)	5.7 (0.22)

4.0 Phased-Array Probes

Three PA probes were evaluated in this beam mapping study and they are representative of probes that could be used during an inservice inspection (ISI) on coarse-grained components, depending on specimen configuration and in-field access constraints. The probes are first characterized by their center frequencies of 0.5, 0.8, and 1.0 MHz and are displayed in Figure 4.1 in their standard transmit receive longitudinal (TRL) configuration. During this study only the transmit probe was used to generate a sound field. Each transmitter contained ten elements in the primary or forward axis, and five in the secondary or lateral axis. The forward direction represented the axial direction on the specimen, while the lateral direction corresponded to the circumferential direction on the specimen. Probe size information is listed in Table 4.1.

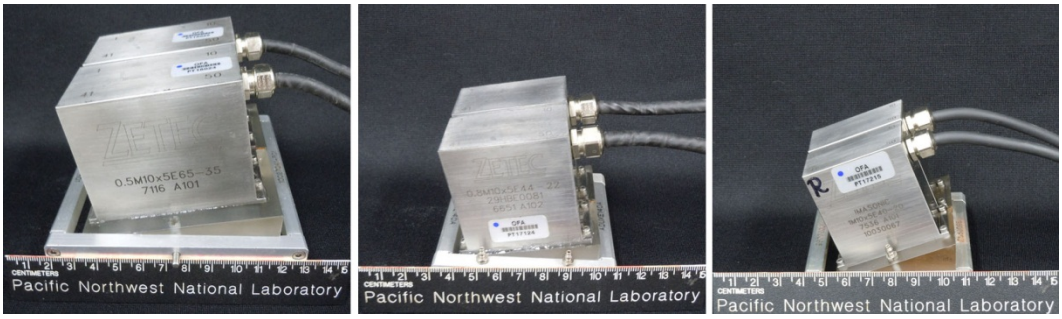

Figure 4.1. Phased Array Probes with Center Frequencies of 0.5, 0.8, and 1.0 MHz, left to right. The scale is in cm units.

Table 4.1. Probe Size Information

	Element Size, mm (in.)		Aperture, mm (in.)	
Frequency, MHz	**Primary**	**Secondary**	**Primary**	**Secondary**
0.5	5.5 (0.22)	6.0 (0.24)	64.0 (2.52)	34.0 (1.34)
0.8	3.6 (0.14)	3.6 (0.14)	43.2 (1.70)	21.2 (0.84)
1.0	3.5 (0.14)	3.5 (0.14)	39.5 (1.56)	19.5 (0.77)

5.0 Experimental Setup and Data Acquisition

Data were acquired with a ZETEC DYNARAY Lite system running UltraVision version 3.3R4 software and at refracted angles of 30 to 70 degrees in 5-degree increments with a projection style focus used with each probe. This produced a beam focused in a horizontal plane at a prescribed offset from the front of the wedge. The offset was selected to place the focal plane at the end of the specimen where the beam was then mapped. The values were adjusted as needed to keep the entire beam within the physical bounds of the specimen. Offsets that were used for the CASS specimens are listed in Table 5.1 for each specimen, refracted angle, and probe. Figure 5.1 displays the UltraVision beam modeling results for a 40-degree refracted angle with the side view on the left and the end view on the right. The beam was focused in a plane appropriately aligned with the front edge of the wedge in the example. The horizontal axis in the figure represents approximately 242 mm (9.5 in.) and the vertical axis represents 190 mm (7.5 in.).

Table 5.1. Projection Focus Offsets for the Cast Specimens, Refracted Angles, and Probe Frequencies

	0.5 MHz		0.8 MHz		1.0 MHz	
	Focus, mm (in.)	**Angles, degrees**	**Focus, mm (in.)**	**Angles, degrees**	**Focus, mm (in.)**	**Angles, degrees**
B-519E	−10 (−0.39)	35–45	−7 (−0.28)	35–40	0	35–45
	0	45–55	0	40–50	10 (0.39)	45–55
	15 (0.59)	50–65	15 (0.59)	50–65	30 (1.18)	55–70
	30 (1.18)	60–70	30 (1.18)	65–70		
B-519C	−5 (−0.20)	35–45	0	35–50	15 (0.59)	35–70
	0	45–55	15 (0.59)	50–70		
	15 (0.59)	55–70				
AAD-2	−10 (−0.39)	35–45	0	35–55	5 (0.20)	35–50
	0	45–60	15 (0.59)	55–70	20 (0.79)	50–70
	15 (0.59)	60–70				
AAD-3	5 (0.20)	35–50	15 (0.59)	35–55	20 (0.79)	35–70
	20 (0.79)	50–70	30 (1.18)	55–70		

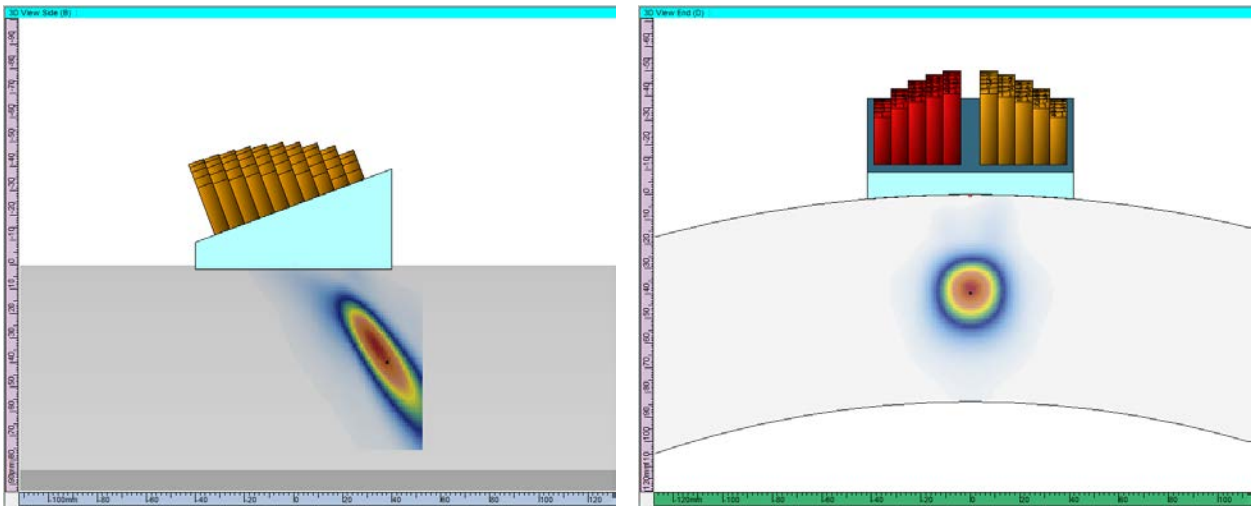

Figure 5.1. UltraVision Software Modeling Results for a 40-degree Refracted Angle with the Projection Focus Coincident with the Front Edge of the Wedge. The side view is displayed on the left and the end view on the right.

In order to register all of the acquired data images, a fiducial transmitting pinducer (point source) was placed in-line with the end face of the specimen as shown in Figure 5.2. The pinducer was placed in a small notch located at the ID of each specimen and circumferentially centered. A diagram of the setup is shown on the left with the stationary fiducial source pinducer under the specimen and the raster scanned receive pinducer to the right of the specimen. The setup as photographed is seen on the right side of Figure 5.2. Figure 5.3 further shows the end view of the specimen and fiducial pinducer on the left with a data image on the right. Both pinducers were fitted into collimator sleeves to narrow the effective area over which they either transmitted or received ultrasonic energy. These were necessary to isolate the fiducial response from the PA probe beam response.

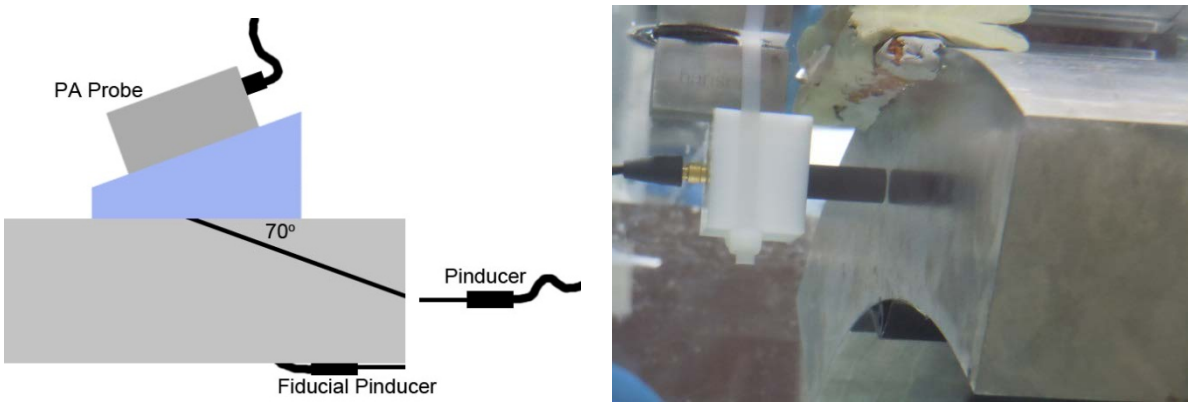

Figure 5.2. A Diagram of the Data Acquisition Setup is on the Left and a Photograph of the Actual Setup is on the Right

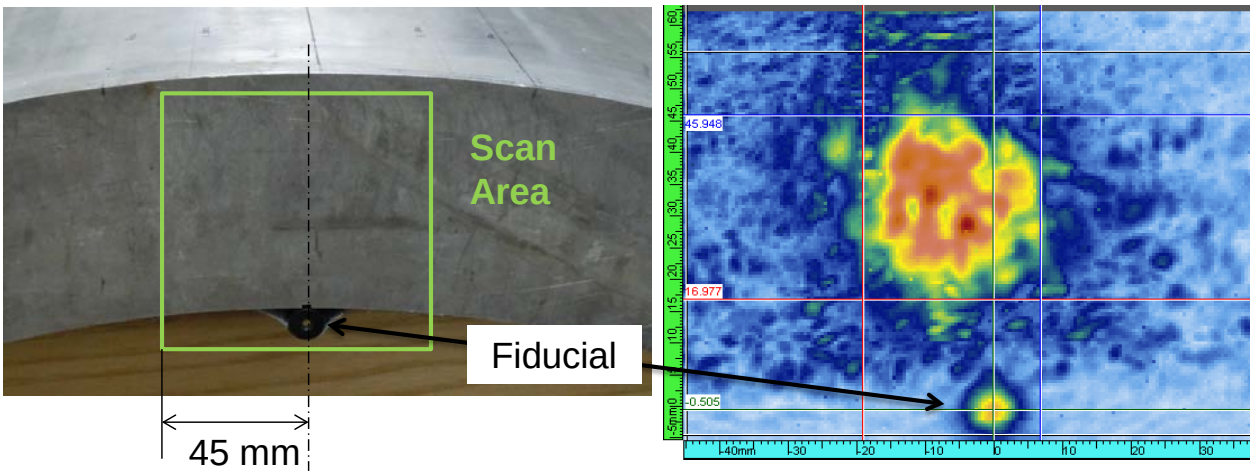

Figure 5.3. The End of a Specimen and the General Region that was Imaged is Displayed on the Left with a Data Image on the Right

Data were acquired with four different beam skew angles. Typically, components are evaluated at various skew angles to better capture off-axis features of a flaw. The angles are diagramed in Figure 5.4 for a TRL probe. By convention, the zero-degree angle focuses the beam in the center, between the transmitter and receiver. The +10-degree and −10-degree angles are projected to the right and left of center, respectively. These traditional skew angles are specified in the Ultravision software and focal laws are appropriately modified to account for the beam skew. A fourth and custom angle, specified as skew T (transmit), was defined at a projection directly in front of the transmit probe. As this is a nonstandard feature of the software, the angles for the skew T setups were hand-calculated and then the required focal laws were generated in the Ultravision software. The skew T angles for the 0.5-MHz probe equated to a −16.4 to −29 degree standard Ultravision skew for refracted angles from 70 to 35 degrees. Similarly, the skew T angles for the 0.8-MHz probe were −15.2 to −32.2 degrees and −13.4 to −25.5 degrees for the 1.0-MHz probe at refracted angles of 70 to 35 degrees. The use of this skew was employed to capture the primary axis sound field formation without any lateral component.

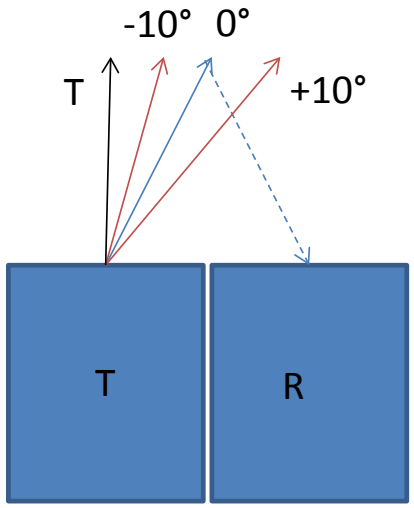

Figure 5.4. Diagram of Beam Skew Angles

After mapping the sound fields on the four specimens, a 6.4-mm (0.25-in.) thick slice was removed from the specimen end and the beam mapping was repeated. This process of mapping and slicing was performed three times with a final mapping after the third slice of material was removed. Data were collected with a constant part path for each configuration (probe, specimen and slice, angle, etc.) and with a variable part path (fixed position on the surface) as shown in Figure 5.5 on the right and left sides, respectively. Ideally, the variable part path allows for a mapping of the beam as it formed and propagated through the specimen. The constant part path enabled examination of the focused sound field variations through different material in the same specimen. PNNL also used the terms relative and absolute to describe the two acquisition scenarios. Relative data referred to data acquired with a constant part path relative to the end of the specimen. Absolute data referred to data acquired with a fixed or absolute position on the specimen throughout the slicing operations. The base specimens and slices were polished and etched to reveal measureable grain microstructures and these results are discussed in Section 3.0.

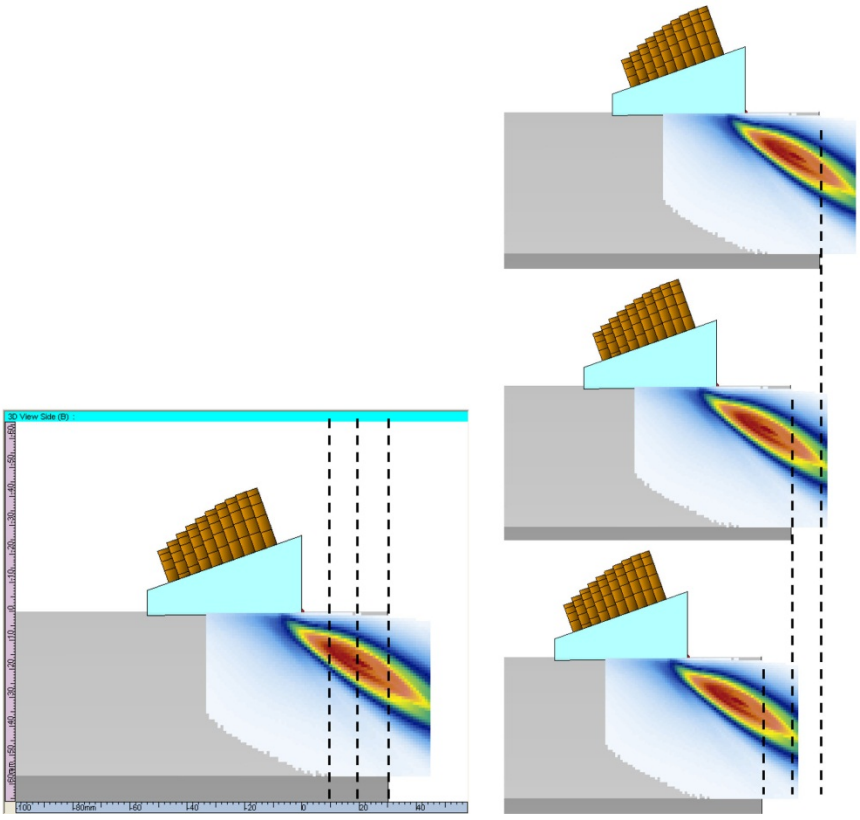

Figure 5.5. Variable Part Path (left) and a Constant Part Path (right). The dashed lines represent slices removed from the end of the specimen.

6.0 Data Analyses

The analyses presented in this section attempt to quantify the variations in the sound field data images attributed to the general degradation of sound field coherence as a function of many parameters. Section 6.1 discusses the sound field image selection process. Sections 6.2 and 6.3 discuss partitioning and scatter measurements as affected by inspection parameters. Combined plots of the partitioning and scatter values in Section 6.4 further show the influence of inspection parameters on the quality of the beam formation as explained in terms of a linear discriminant analysis. Section 6.5 presents the data based on a peak amplitude response, and lastly Section 6.6 discusses the sound field position error. These measures provide a means to evaluate sound propagation behavior and the degradation of sound field coherence. They further allow one to determine the quality of the beam formation and how effectively the beam insonified and targeted the specified point.

As an overview, the sound fields were generated in materials with four types of grain structure and the grains were characterized by average and maximum gain diameter, as listed below in the left column of Table 6.1. Additionally, data were acquired at four positions (slices) in the specimens (only one position for the WSS specimen). The ultrasonic inspection parameters included probe frequency and wavelength, refracted angle, and skew angle as listed in the center column. Note that data images were also acquired at five refracted angles not listed (30, 40, 50, 60, and 65) and with constant and variable part paths as previously discussed. The complete data set included nearly 2800 files. To manage the scope of this project and still capture inspection parameter influences on sound field formation, the inspection parameters were pared down to those listed and only the constant part path data were analyzed. Note that the −10 degree skew data were also not fully analyzed. These pared-down combinations of materials and inspection parameters represented over 600 data files. Finally, the data files were evaluated for sound field coherence as measured in terms of image partition and image scatter. The images were additionally characterized in terms of peak amplitude loss and sound field redirection as listed in the right column.

Table 6.1. Sound Field Beam Mapping Overview

Material	Inspection Parameters	Sound Field Characterization
Microstructure • Columnar • Equiaxed • Banded/Layered • WSS	Inspection Frequency (and Wavelength) • 0.5 MHz • 0.8 MHz • 1.0 MHz	Characterization • Partitioning • Scatter • Peak Amplitude Loss • Redirection
Grain Diameter • Average • Maximum	Refracted Angle • 35-degree • 45-degree • 55-degree • 70-degree	
Slice • 0 • 1 • 2 • 3	Probe Skew Angle • T • −10-degree (not analyzed) • 0-degree • +10-degree	

6.1 Data Images

The data images that were analyzed for beam partitioning, scatter, and redirection were generated by electronic gating of the acquired data files to isolate the signals of interest. Each image was cropped to the half amplitude or −6 dB levels. Results for Specimens B-519C, B-519E, AAD-2, and AAD-3 are displayed in Figures 6.1, 6.3, 6.5, and 6.7. These data images represent a 45-degree refracted angle and a 0-degree beam skew angle. The top row in each figure is 0.5-MHz data, the middle row is 0.8-MHz data, and the bottom row is 1.0-MHz data. The four columns represent the slices from the specimens, 0 through 3. In general, the cut-to-cut variation shown in a row is not as great as the variation from probe frequency, shown in a column. For example, the columnar microstructure of B-519C in Figure 6.1 shows a greater amount of partitioning with increased frequency. Similarly, the equiaxed microstructure of B-519E in Figure 6.3 shows a greater amount of scatter with increased frequency. The trends in the mixed and banded microstructures of AAD-2 and AAD-3 in Figures 6.5 and 6.7 are not as evident, but they do exhibit both partitioning and scatter to some degree. The full set of sound field images for the four specimens, four refracted angles, three beam skew angles, and four faces are presented in Appendix B.

Paired with each set of sound field images from a CASS specimen is the corresponding baseline sound field acquired from the fine-grained WSS specimen. These images are presented in Figures 6.2, 6.4, 6.6, and 6.8. The three data images, left to right, represent probe frequencies of 0.5, 0.8, and 1.0 MHz, respectively. As an example, the same focal laws to form the beam with the 0.5-MHz probe in the B-519C CASS specimen in Figure 6.1, top row, were used to form the beam in the WSS specimen as shown in Figure 6.2, left image. The nearly Gaussian beams in the WSS specimen illustrate what one might expect when propagating a sound field through a fine-grained, isotropic material. These beams lack the higher degree of scatter and partitioning that is prevalent in the CASS specimens. The WSS peak response is nominally obtained at the center of the image and is represented by the dark red color. Moving outwards, the response decreases monotonically as the color scale moves through the range of colors from red-orange to yellow to green, cyan, and blue, representing the full dynamic range of sound field amplitudes where color correlates to sound field intensity in decibels (dB). The full set of sound field images in the fine-grained WSS specimen for the four refracted angles and three beam skew angles is presented in Appendix C.

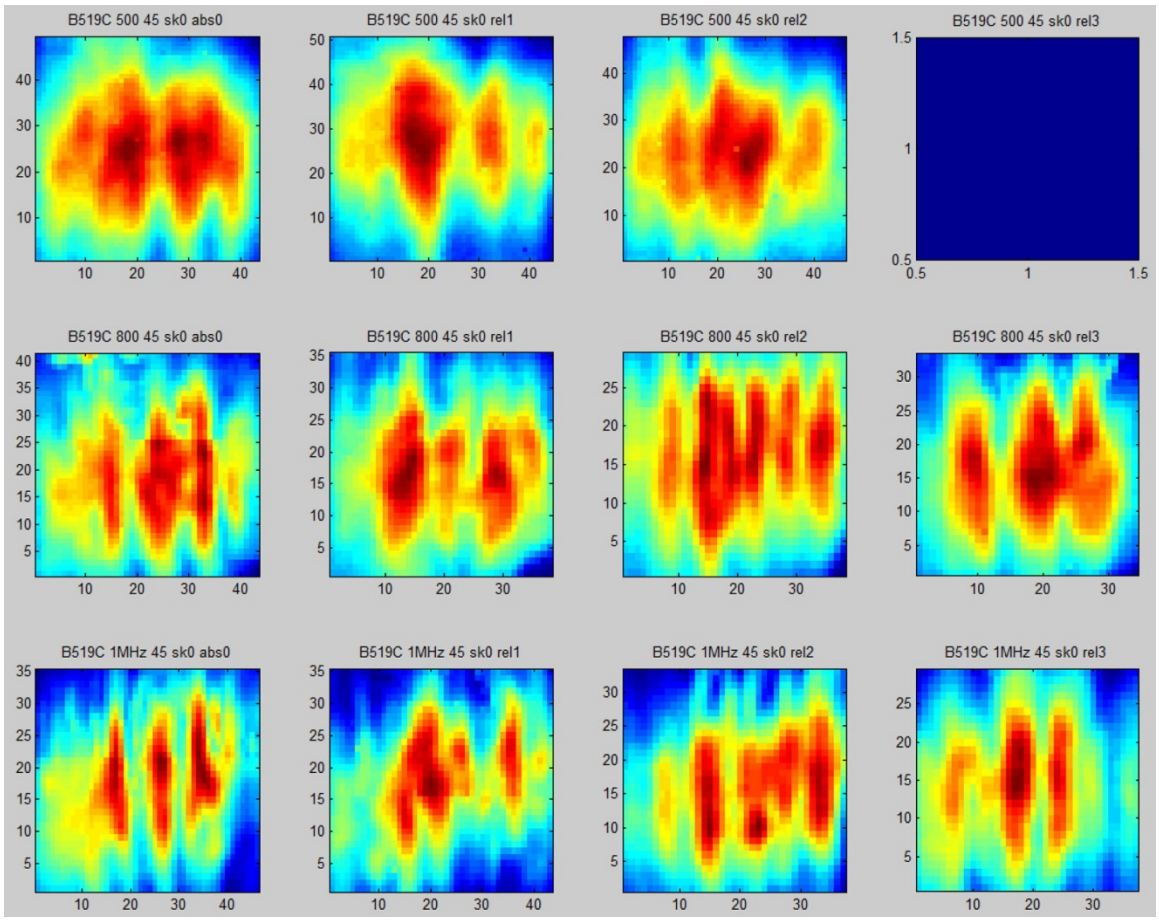

Figure 6.1. Sound Field in Specimen B-519C at a 45-degree Refracted Angle and 0-degree Beam Skew with 0.5-, 0.8-, and 1.0-MHz Probe Frequencies, Top to Bottom, and Slices 0 Through 3, Left to Right. The data file for B-519C, 0.5 MHz, rel3, upper right, was corrupted.

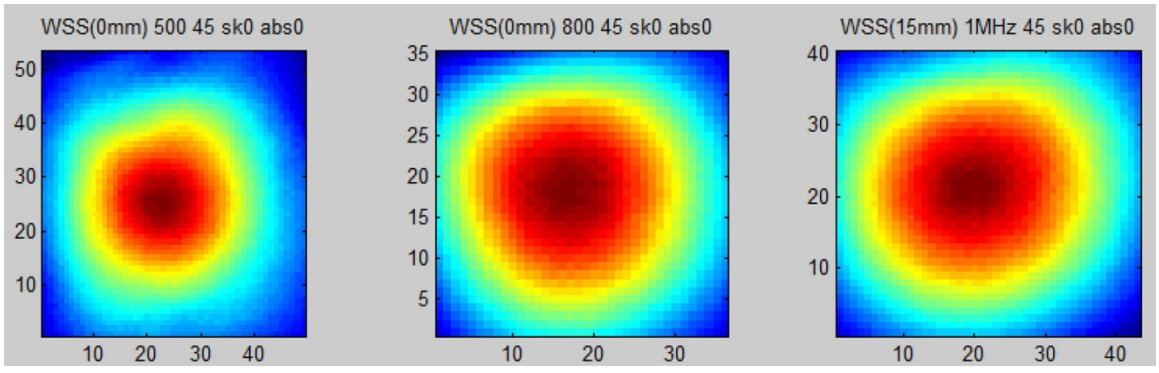

Figure 6.2. Baseline Sound Fields in WSS Specimen with Focal Laws Corresponding to Specimen B-519C, at a 45-degree Refracted Angle, 0-degree Beam Skew, and Probe Frequencies 0.5, 0.8, and 1.0 MHz, Left to Right

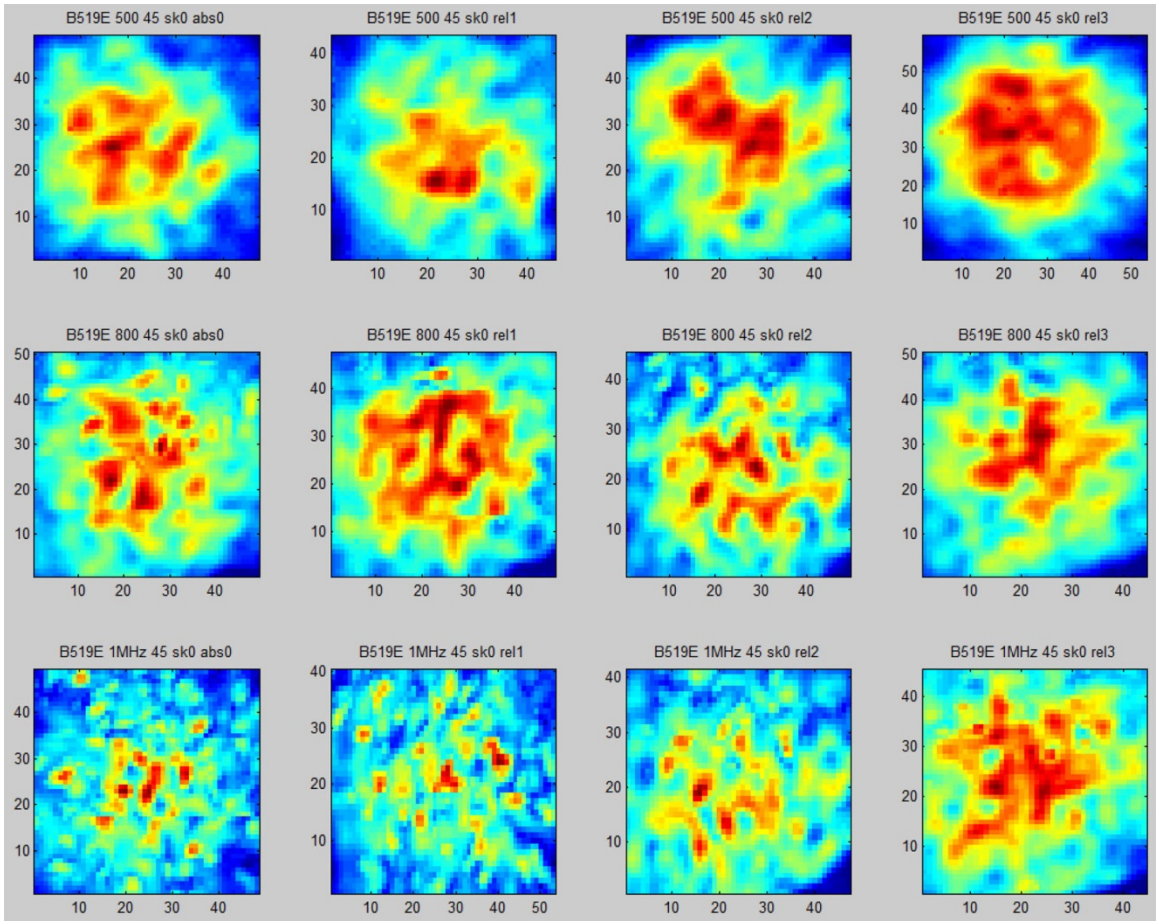

Figure 6.3. Specimen B-519E at a 45-degree Refracted Angle and 0-degree Beam Skew with 0.5-, 0.8-, and 1.0-MHz Probe Frequencies, Top to Bottom, and Slices 0 Through 3, Left to Right

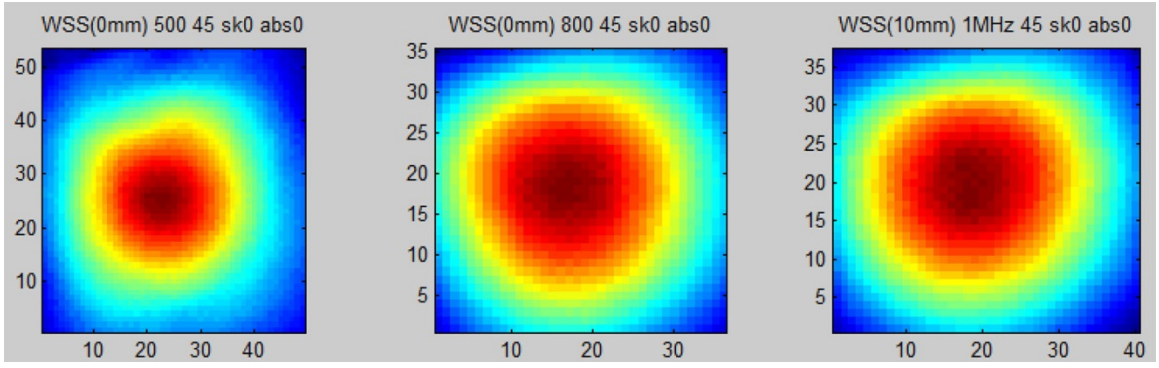

Figure 6.4. Sound Fields in WSS Specimen with Focal Laws Corresponding to Specimen B-519E, at a 45-degree Refracted Angle, 0-degree Beam Skew and Probe Frequencies 0.5, 0.8, and 1.0 MHz, Left to Right

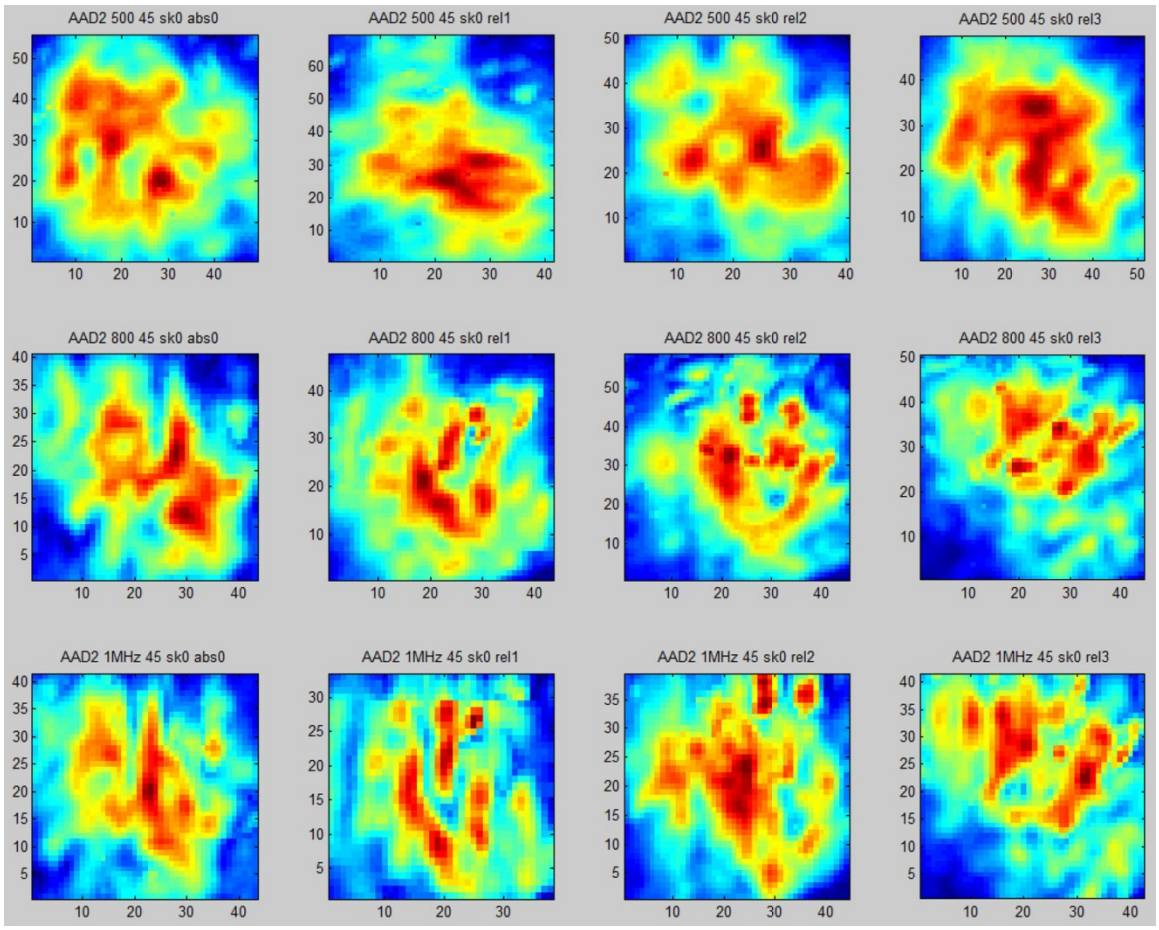

Figure 6.5. Specimen AAD-2 at a 45-degree Refracted Angle and 0-degree Beam Skew with 0.5-, 0.8-, and 1.0-MHz Probe Frequencies, Top to Bottom, and Slices 0 Through 3, Left to Right

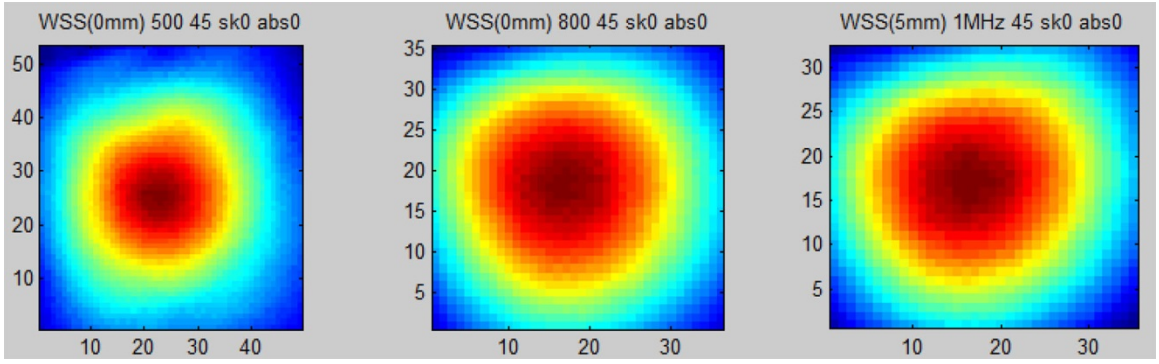

Figure 6.6. Sound Fields in WSS Specimen with Focal Laws Corresponding to Specimen AAD-2, at a 45-degree Refracted Angle, 0-degree Beam Skew and Probe Frequencies 0.5, 0.8, and 1.0 MHz, Left to Right

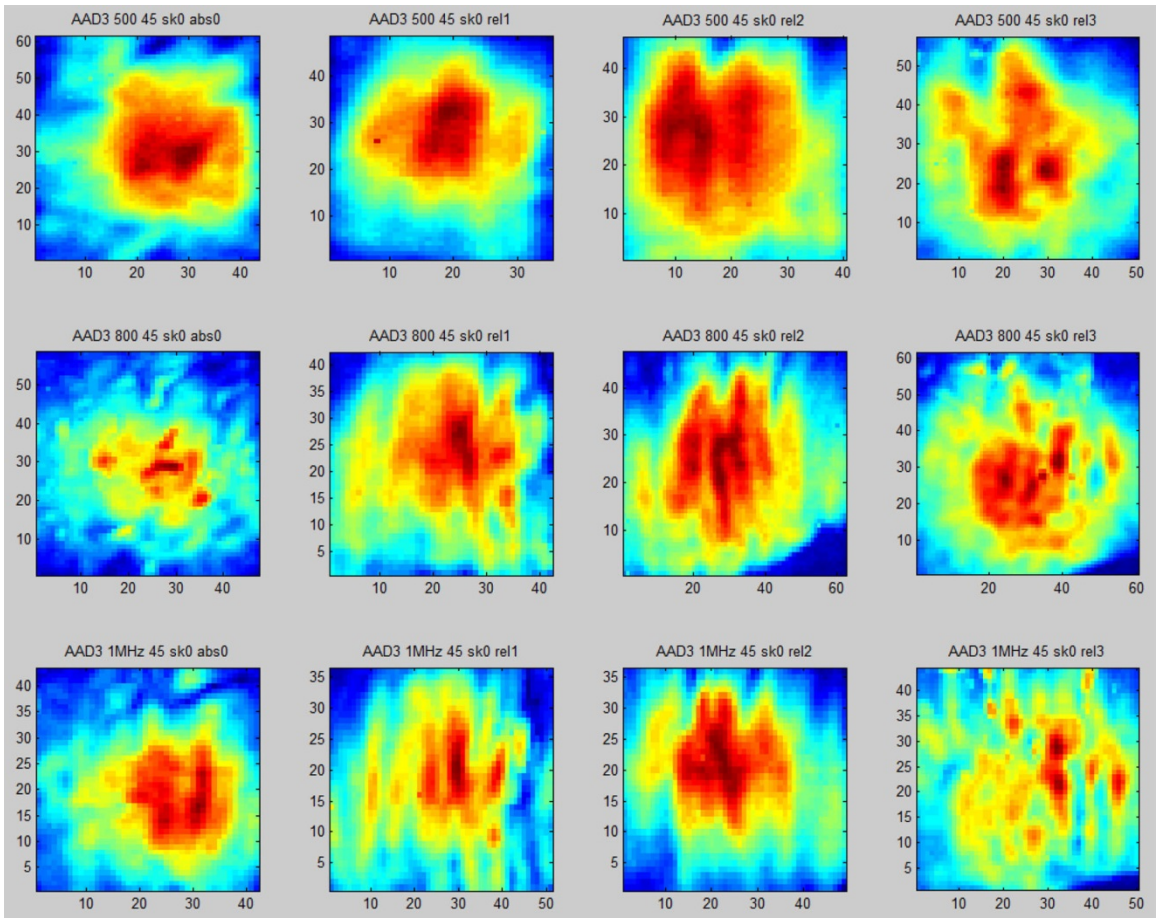

Figure 6.7. Specimen AAD-3 at a 45-degree Refracted Angle and 0-degree Beam Skew with 0.5-, 0.8-, and 1.0-MHz Probe Frequencies, Top to Bottom, and Slices 0 Through 3, Left to Right

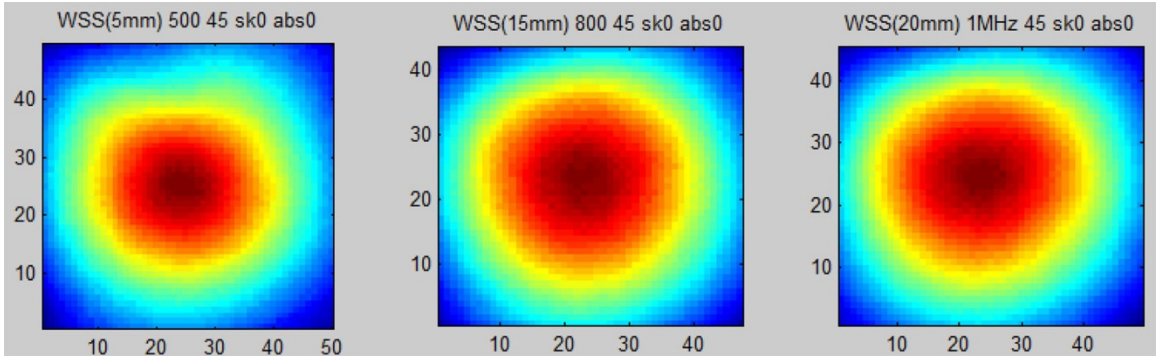

Figure 6.8. Sound Fields in WSS Specimen with Focal Laws Corresponding to Specimen AAD-3, at a 45-degree Refracted Angle, 0-degree Beam Skew and Probe Frequencies 0.5, 0.8, and 1.0 MHz, Left to Right

6.2 Beam Partitioning

A metric was developed to measure partitioning of the data images. Partitioning was defined as the ratio of threshold crossings in the horizontal direction and in the vertical direction. The inputs for this calculation, including the specimen, probe frequency, refracted angle, beam skew angle, and specimen slices, were selected in the graphical user interface (GUI) depicted in Figure 6.9.

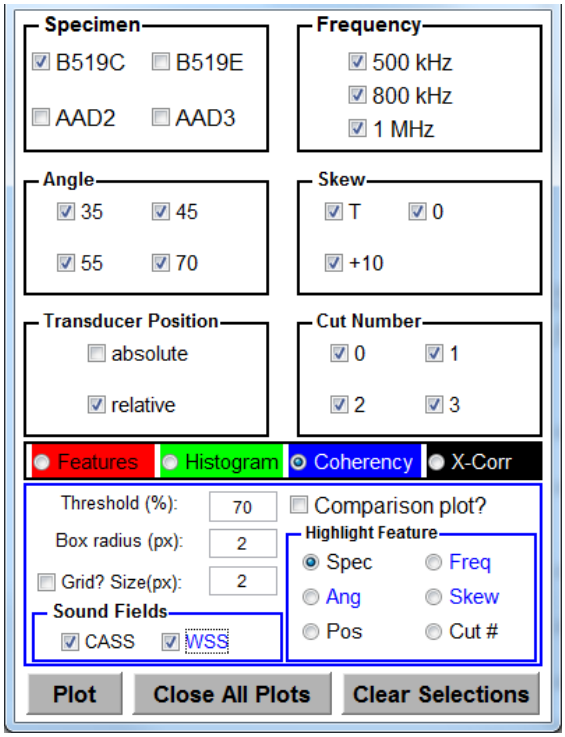

Figure 6.9. Graphical User Interface for Sound Field Image Display and Analyses

This tool used a specified threshold level (70%) and a grid spacing (2 pixels). Points along the vertical and horizontal lines determined by the pixel grid were tracked as they crossed the threshold level in a positive slope direction as demonstrated in Figure 6.10. A profile along the horizontal line in the image is displayed above the image and the profile along the vertical line in the image is shown at the right. Each profile also has a red line drawn at the 70% threshold level and the points that cross the threshold at a positive slope are circled. Instead of a zero-crossing algorithm, this is basically a threshold-level crossing with positive slopes. The threshold level and grid spacing were chosen to capture the essence of the data without being overly or insufficiently sensitive to changes. The average number of such crossings for all horizontal lines was determined as well as the average number for all vertical lines.

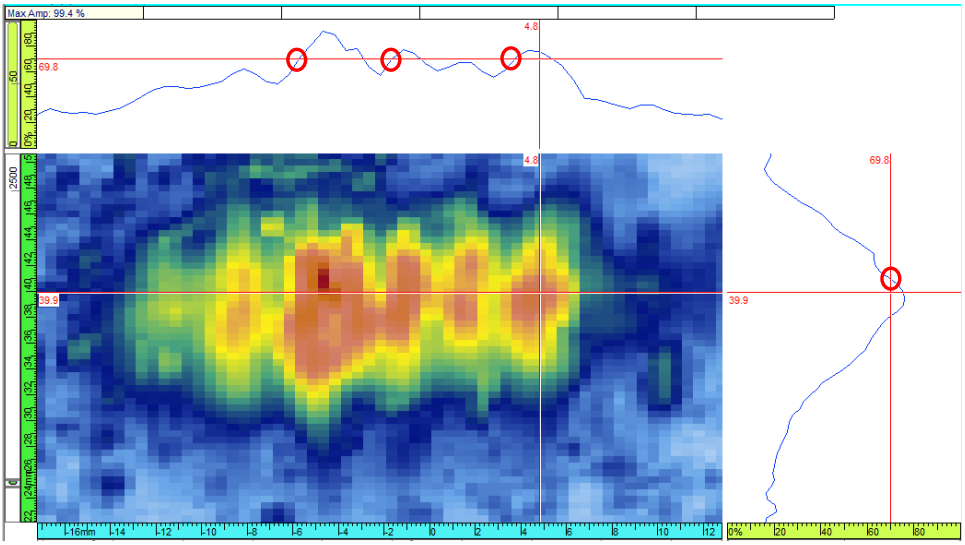

Figure 6.10. Example of Threshold Crossings for Partition Calculation

A ratio of these two values (horizontal/vertical) was computed and the results are plotted in Figure 6.11 for the skew T (SkT) data. Because the partition measure is a ratio of threshold crossings, it has no units. From left to right, the B-519C specimen data is presented followed by the B-519E, AAD-2, and AAD-3 data. For each specimen, the data are further subdivided into probe frequency (0.5, 0.8, and 1.0 MHz) and then refracted angle (35, 45, 55, and 70 degree). A CASS data point represents an average of the four faces (slices 0–3) from a specimen with plus and minus one standard deviation error bars. The WSS specimen data are also shown and represent the standard fine-grained material (no error bars because only one measurement on the WSS specimens). All WSS points were nominally measured at 1.0, indicating no partitioning. Specimen B-519C (columnar) shows the greatest partitioning with an overall average of 1.9. Partitioning tends to increase as probe frequency increases. Equiaxed specimen B-519E shows the least partitioning (average of 1.0) as well as the least variation among specimen slices as noted by the small error bars. It has several partition values less than 1 indicating wide grains; that is, larger in the circumferential direction than the radial extent. As expected, the mixed and banded specimens AAD-2 and AAD-3 present a combination of the columnar and equiaxed partition features. There does not appear to be an overall correlation between refracted angle and partitioning. For instance, one cannot say that a 35-degree refracted angle produces less partitioning than at 45 degrees.

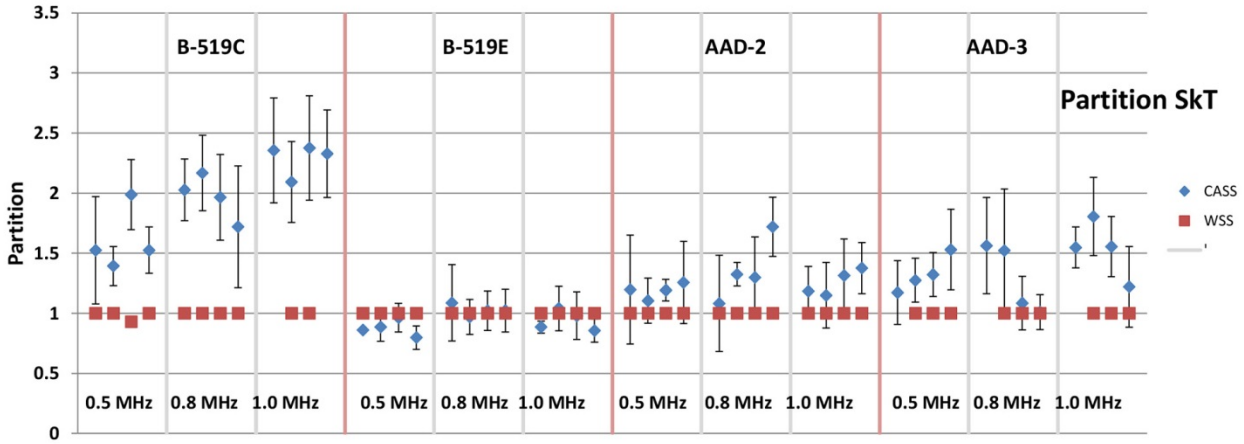

Figure 6.11. Partition Measurements for a Beam Skew of SkT on Four CASS Specimens and an Equivalent WSS Specimen with Three Probe Frequencies and Four Refracted Angles

Figures 6.12 and 6.13 display the partition results for skew 0 and 10 degrees, respectively. The general trends hold over the three skew angles in that columnar microstructure shows the most partitioning, the equiaxed the least, and the mixed banded is variable. Each specimen and skew angle tends to demonstrate an increase in partitioning with increasing frequency. There are minor variations as the skew angle is changed, but no single skew angle produces the least or greatest partitioning across all specimens.

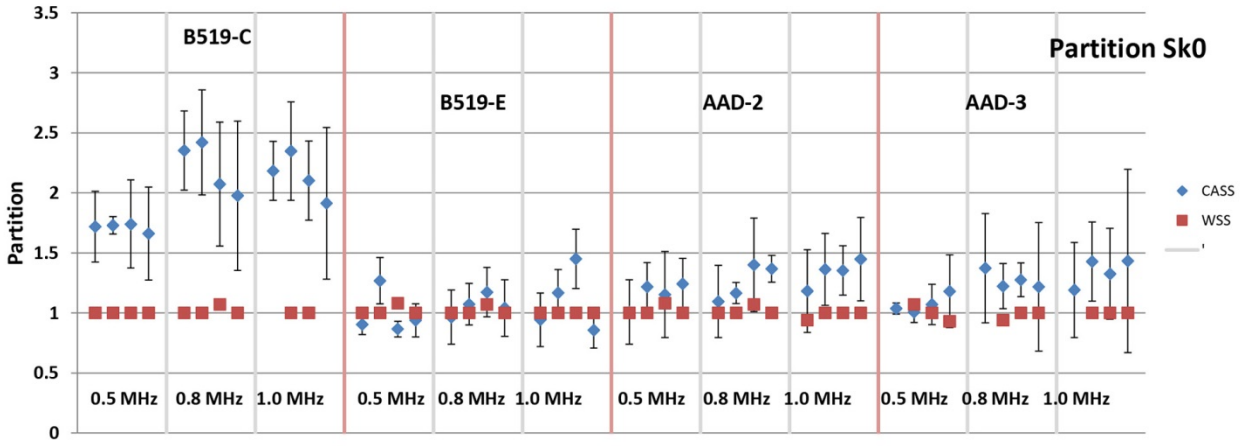

Figure 6.12. Partition Measurements for a Beam Skew of 0 degrees on Four CASS Specimens and an Equivalent WSS Specimen with Three Probe Frequencies and Four Refracted Angles

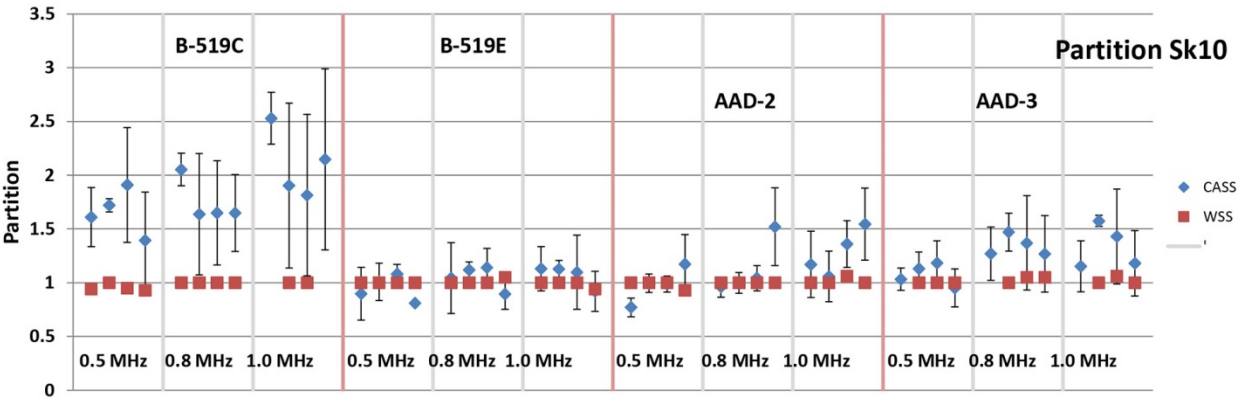

Figure 6.13. Partition Measurements for a Beam Skew of 10 degrees on Four CASS Specimens and an Equivalent WSS Specimen with Three Probe Frequencies and Four Refracted Angles

6.3 Beam Scatter

A metric to measure scatter (lack of coherence) in the images from the beam mapping exercise was developed (in MATLAB) and evaluated on the data. The input parameters were selected through the GUI previously shown in Figure 6.9. The measure of scatter considered data image points above a user-selected threshold (70%) and calculated the difference between the pixel value and surrounding pixel values of all points at a selected distance (2 pixels, 1.0 mm or 0.04 in.). These difference values for a specific pixel were averaged to give a mean difference value for that pixel and then all such calculated values were averaged to give one value for the image. For an image with low scatter, such a difference value was expected to be small, while an image with a higher amount of scatter was expected to have a large difference value. This scatter difference was also calculated on an ideal Gaussian data image for comparison. The final measure of scatter for an empirical image was determined as the difference between the calculated Gaussian and the acquired image value. Resulting negative values, shown in Figure 6.14, for the skew T, CASS data evaluated indicate more variation (scatter) than the ideal Gaussian case. This measure, like partitioning, has no units. In each figure, the specimen groups are delineated by the red vertical lines and the probe frequency for a specific specimen by gray vertical lines. The data points within a specimen and frequency group represent the four refracted angles—35, 45, 55, and 70 degrees. A CASS data point represents an average of the four faces (slices 0–3) from a specimen with plus and minus one standard deviation error bars. Also shown in the figure are the WSS fine-grained standard data (no error bars because only one measurement on the WSS specimens). These points are nominally zero indicating little or no scatter.

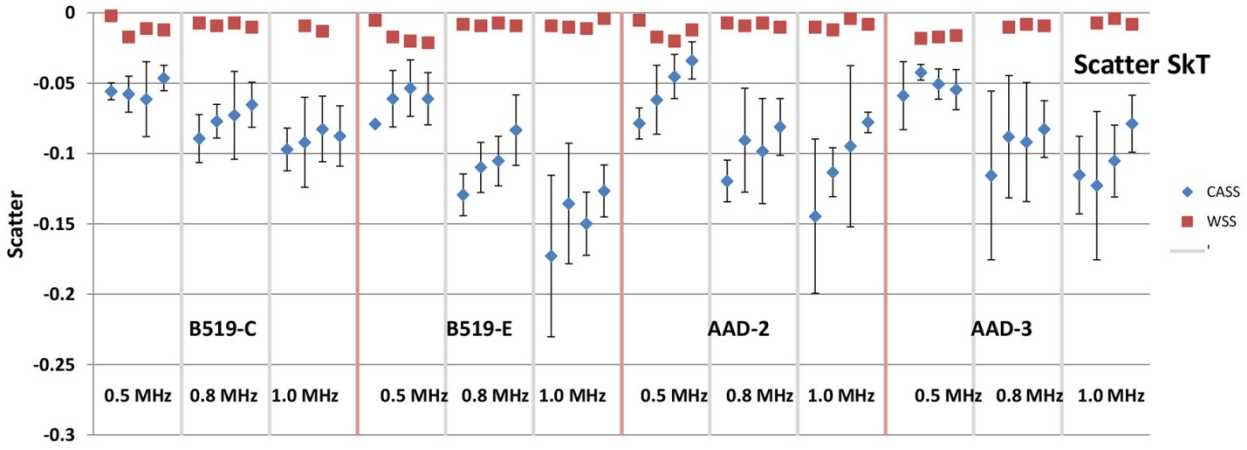

Figure 6.14. Scatter Measurements for a Beam Skew of SkT on Four CASS Specimens and an Equivalent WSS Specimen with Three Probe Frequencies and Four Refracted Angles

Scatter data for skew 0 and skew 10 are shown in Figures 6.15 and 6.16, respectively. The average scatter for the WSS skew T data is −0.010, for the skew 0 data is −0.011, and for the skew 10 data is −0.010. Specimen B-519C shows the least amount of scatter at each frequency and skew, except for specimen AAD-3 at skew 10 and 1.0 MHz, where the average AAD-3 specimen scatter is similar to the average B-519C scatter. The variation in the AAD-3 data (noted by larger error bars) is, however, greater than in the columnar material. Additional observations are: 1) the equiaxed specimen, B-519E, shows the greatest scatter; 2) across all specimens, the scatter increases with increasing frequency at the 0.5- to 0.8-MHz points; 3) scatter increases at the 0.8- to 1.0-MHz steps for specimens B-519C and B-519E; and 4) scatter increases or is the same at the 0.8- to 1.0-MHz steps for the mixed AAD specimens.

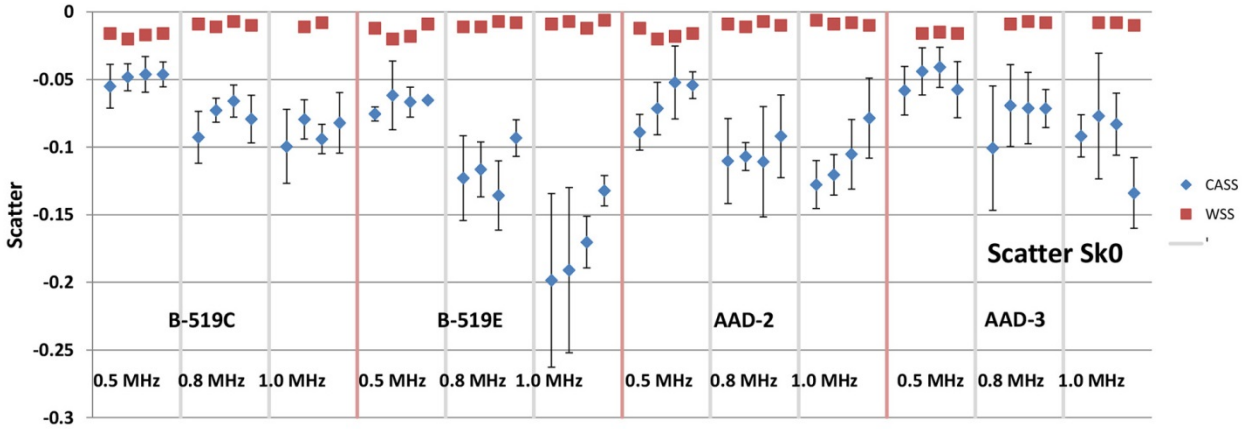

Figure 6.15. Scatter Measurements for a Beam Skew of 0 degrees on Four CASS Specimens and an Equivalent WSS Specimen with Three Probe Frequencies and Four Refracted Angles

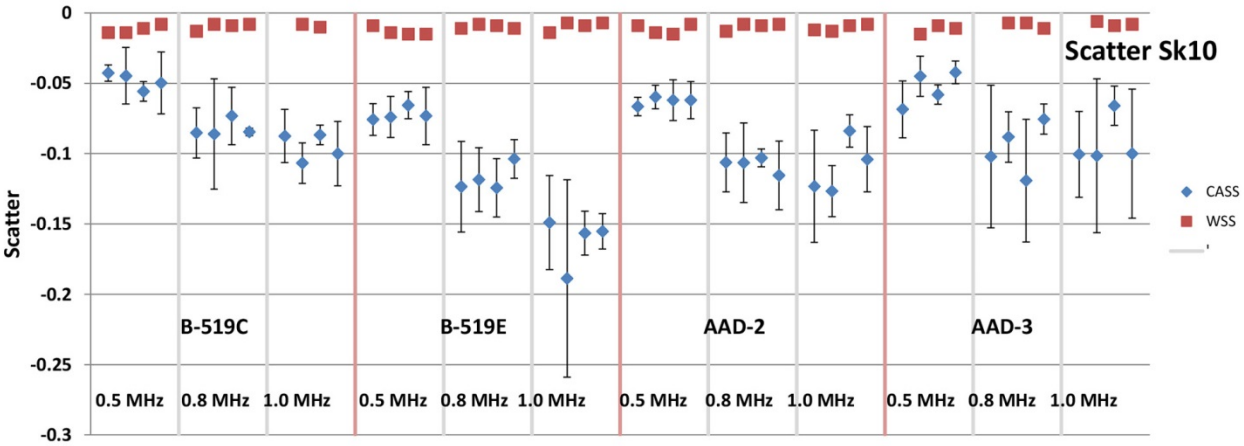

Figure 6.16. Scatter Measurements for a Beam Skew of 10 degrees on Four CASS Specimens and an Equivalent WSS Specimen with Three Probe Frequencies and Four Refracted Angles

A linear regression fit to the data as a function of frequency was made with results in Figure 6.17 for the skew 0 data (Sk0). The regression lines suggest that the scatter of the equiaxed data as a function of frequency is approximately two and a half times greater than that measured in the columnar data.

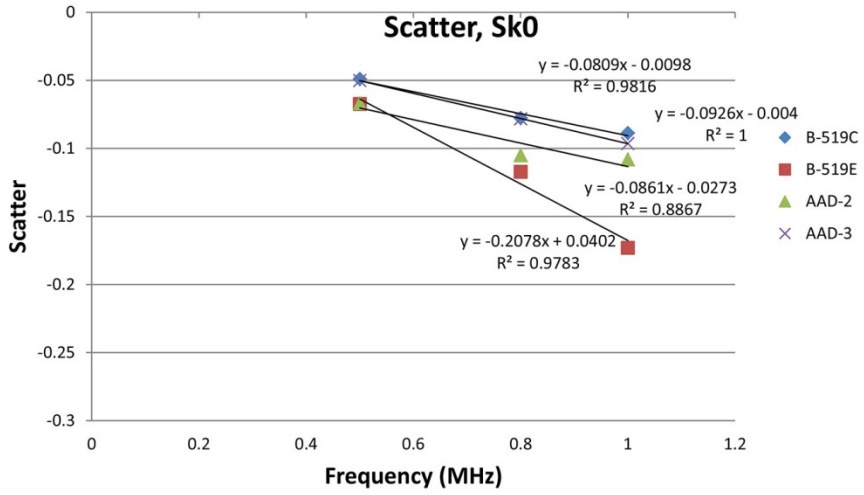

Figure 6.17. Average Scatter as a Function of Frequency at a Beam Skew Angle of 0 degrees for the Four Specimens

6.4 Partitioning and Scatter Comparison

Fisher's linear discriminant analyses were performed on the partitioning and scatter data to further show the significance of the experimental parameters. The experimental parameters include refracted and beam skew angles and probe frequency. Scatter plots were drawn with inputs selected from the previously shown GUI in Figure 6.9. The feature used for data classification was also selected via the GUI. As an example, the probe frequency has been shown to affect beam scatter and partitioning. A plot of the 0.5- and 1.0-MHz data from the four CASS specimens at skew 0 degrees, the four refracted angles, and four slices is displayed in Figure 6.18. The calculated curve, one that minimized the classification cost or error, that separates the data into the two classes, based on frequency, is shown. Partitioning (horizontal axis) is on a log scale, resulting in a semi-log boundary rather than linear. The 0.5-MHz data are correctly classified 90% of the time and the 1.0-MHz data 78% of the time. Sound field coherency or scatter measurements are represented in the vertical axis and appear to be the dominant feature in class separation. This implies that scatter is highly affected by probe frequency and partitioning to a lesser extent.

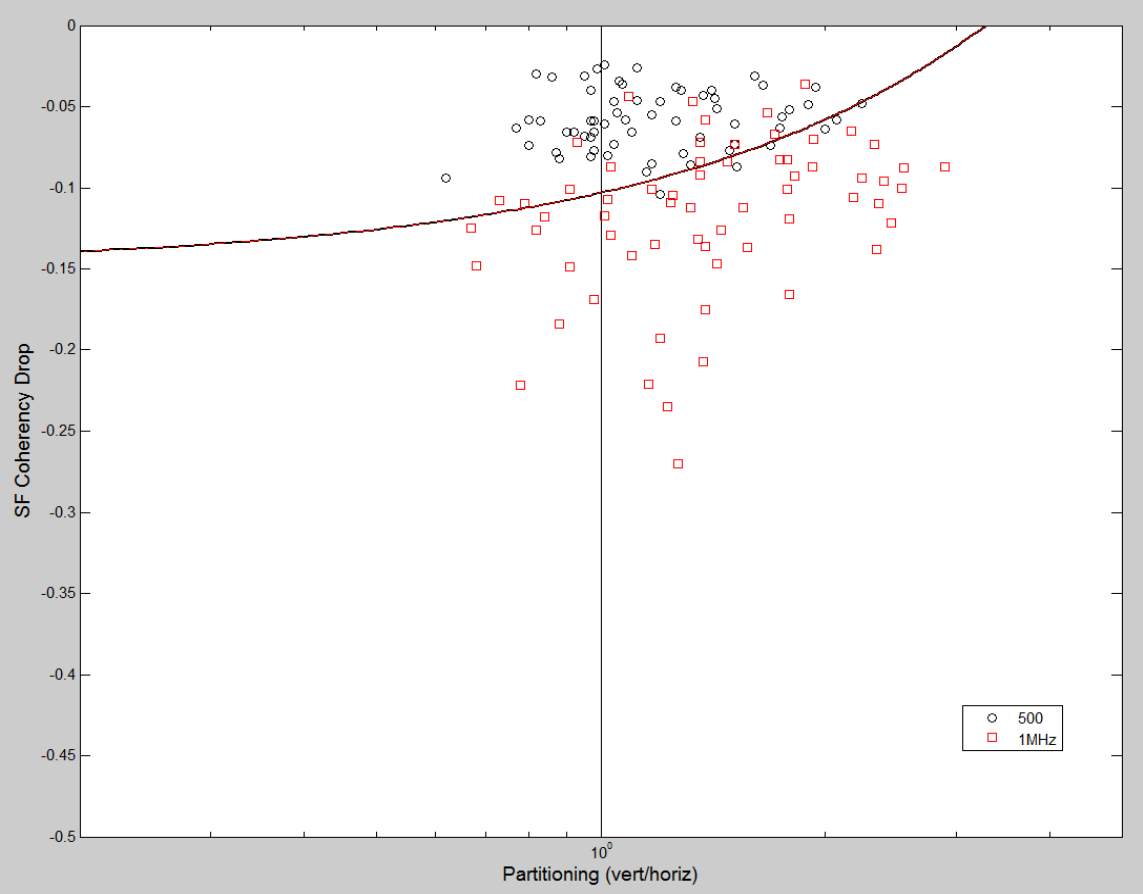

Figure 6.18. Sorting by Probe Frequency for the Four Specimens at a Beam Skew of 0 degrees, Four Refracted Angles, and Four Slices

Classification results for all three probe frequencies on a per-specimen basis are displayed in Figures 6.19 through 6.22. These figures allow one to view the effects of specimen microstructure when sorting measurements of sound field coherency and partitioning by frequency. The lines in the figures represent the boundaries between the classifications based on frequency. Specifically, one line represents the boundary between the 0.5- and 0.8-MHz data, another line the boundary between the 0.5- and 1.0-MHz data, and the third line the boundary between the 0.8- and 1.0-MHz data. A summary of the correct classifications are listed in Table 6.2. As expected, the greatest percentage of correctly classified data occurs when comparing the 0.5- and 1.0-MHz data, showing they are more distinct. When the 0.8-MHz data is included, there is increased data overlap and the correct classification percentages drop. The B-519E data is, however, still well classified when comparing the 0.5- and 0.8-MHz data. This again is explained by the greater effects of scatter with increasing frequency that were observed in the equiaxed specimen.

Figures 6.19 through 6.22 show the effects of probe frequency on combined scatter and partition values. For instance, the B-519C data in Figure 6.19 show the 0.5-MHz data with the lowest scatter and nominally a lower grouping of partitioning than the 0.8- and 1.0-MHz data. The B-519E data in Figure 6.20 show partition values approximately equal across the three frequencies but scatter increases with increasing frequency. Specimen AAD-2 (Figure 6.21) demonstrates less scatter at 0.5 MHz but

partitioning approximately equal to the higher two frequencies. Lastly, specimen AAD-3 (Figure 6.22) shows average scatter and partition at 0.5 MHz is less than the 0.8- and 1.0-MHz data.

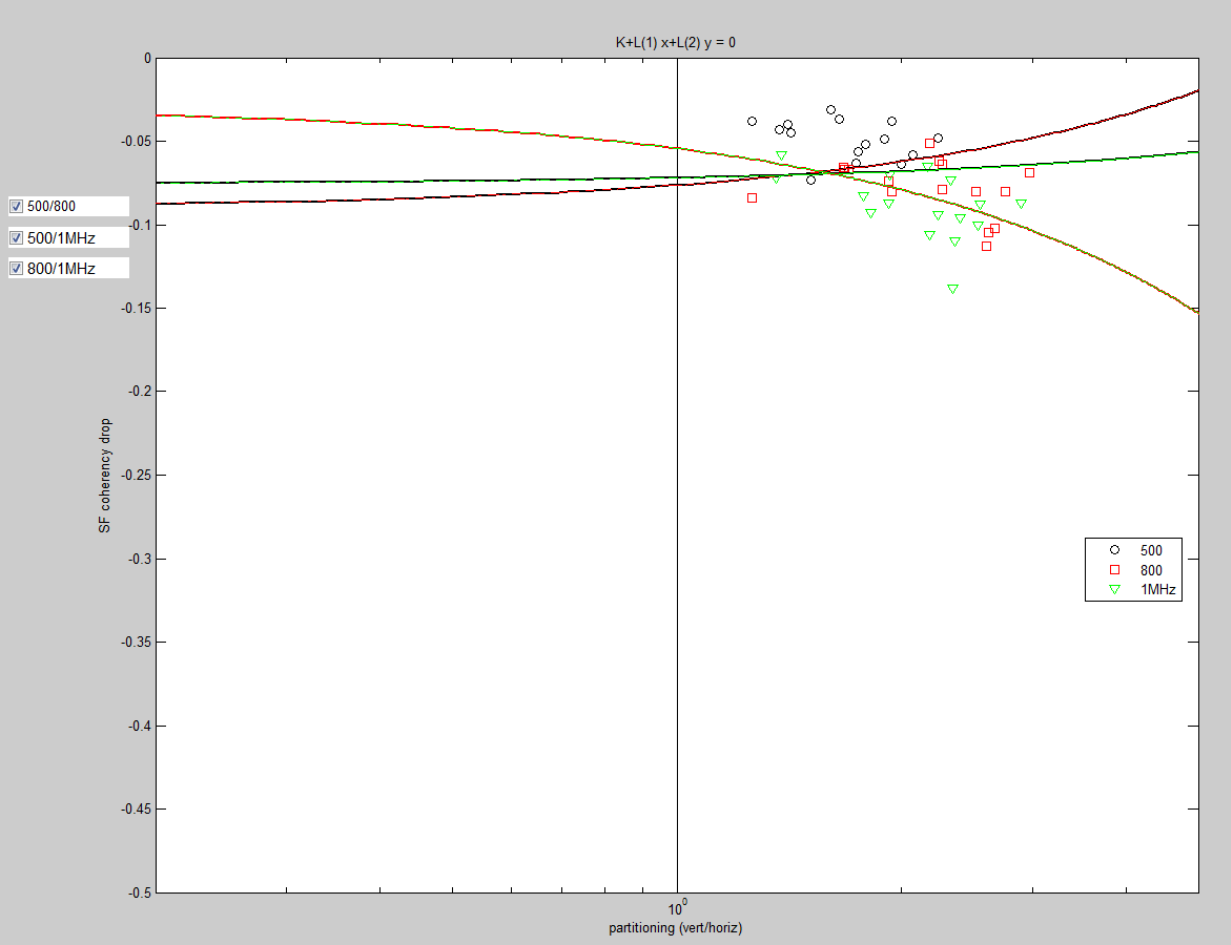

Figure 6.19. Sorting by Frequency with Specimen B-519C, Skew 0 degrees, Refracted Angles 35, 45, 55, and 70 degrees

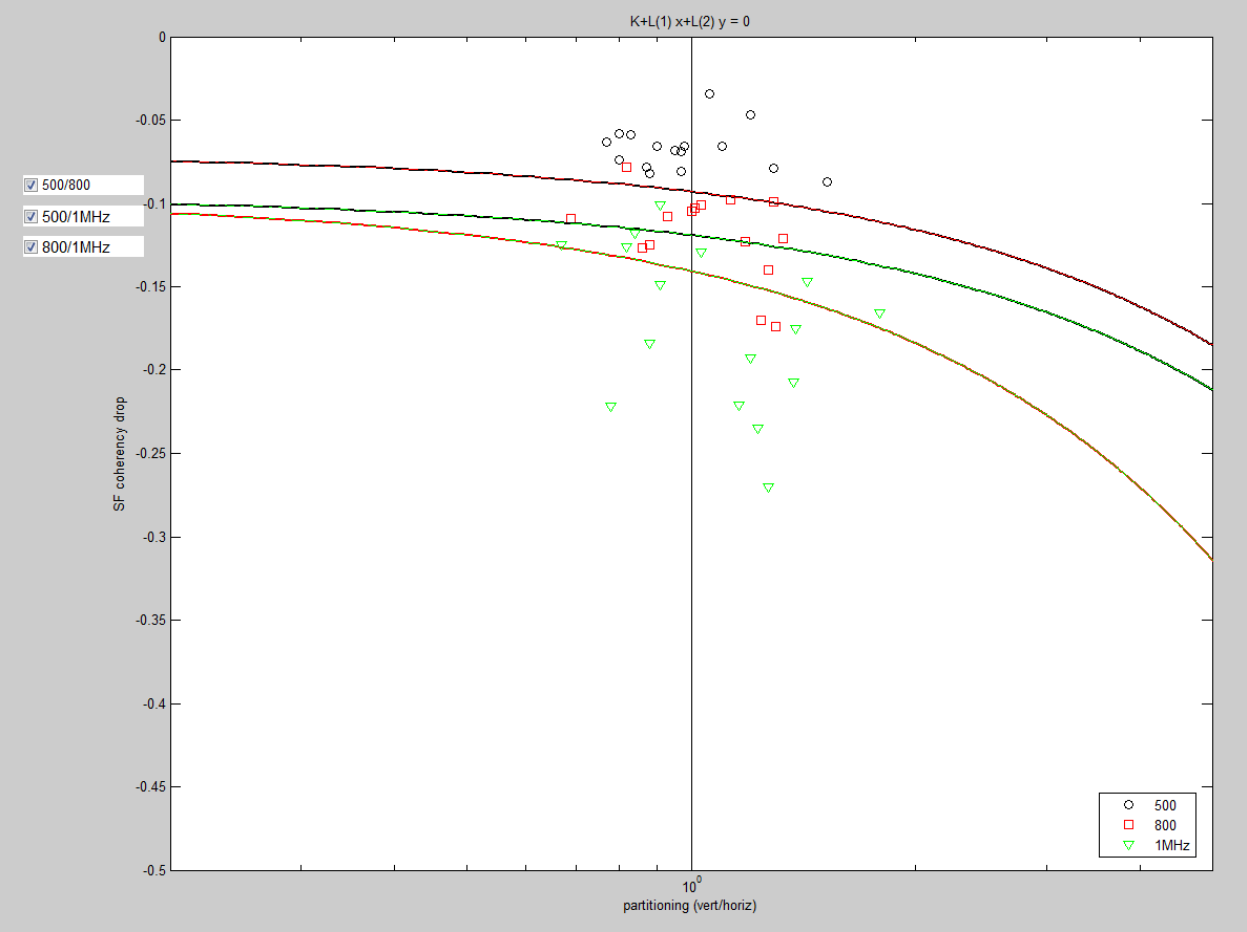

Figure 6.20. Sorting by Frequency with Specimen B-519E, Skew 0 degrees, Refracted Angles 35, 45, 55, and 70 degrees

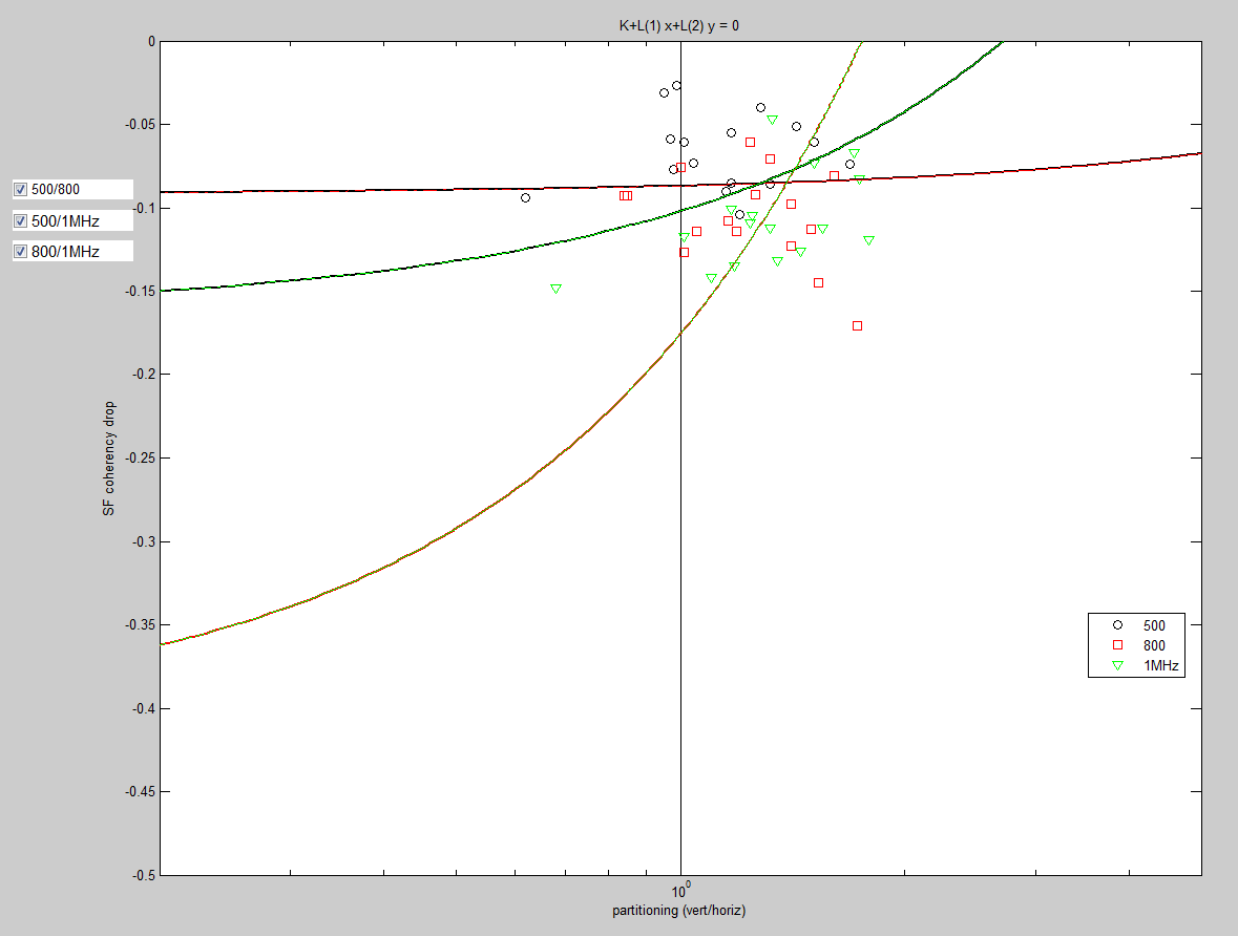

Figure 6.21. Sorting by Frequency with Specimen AAD-2, Skew 0 degrees, Refracted Angles 35, 45, 55, and 70 degrees

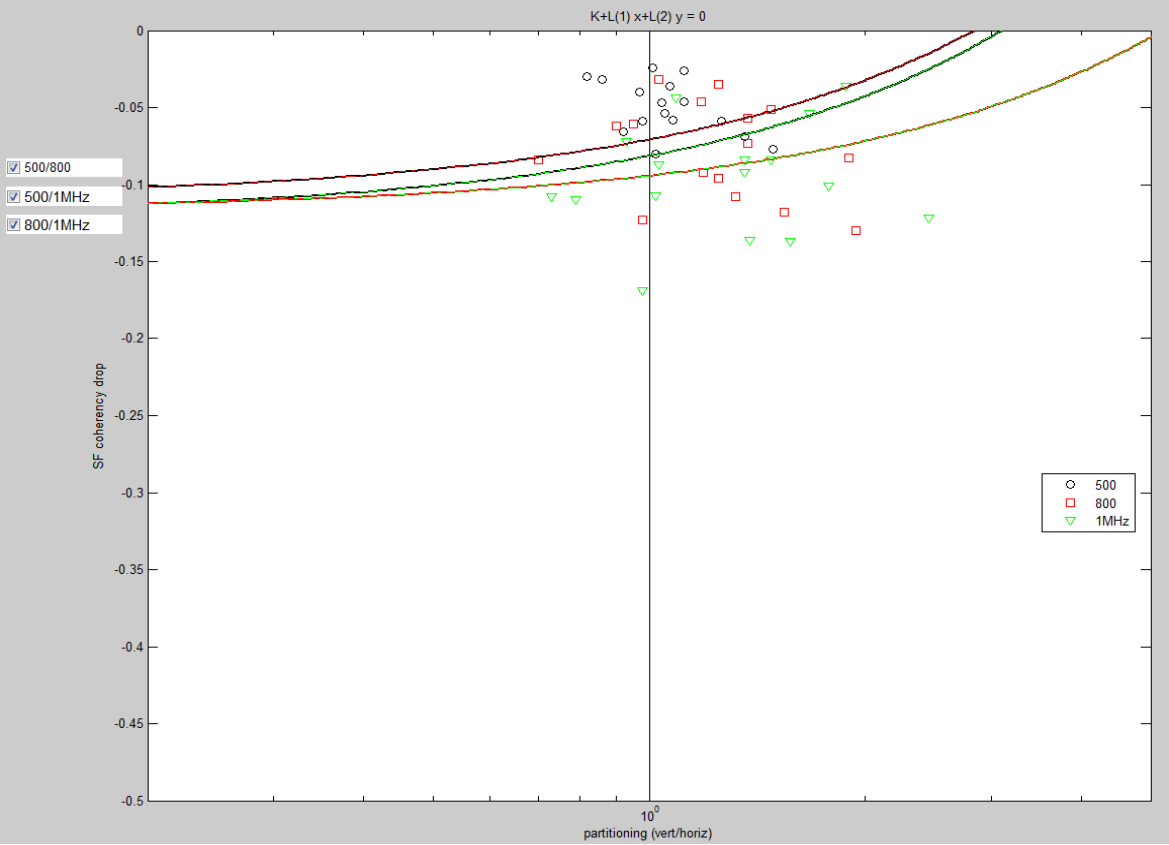

Figure 6.22. Sorting by Frequency with Specimen AAD-3, Skew 0 degrees, Refracted Angles 35, 45, 55, and 70 degrees

Table 6.2. Classification Results from Sorting by Frequency for Skew 0, all Four Refracted Angles, and Four Slices

Specimen	Compare Frequency, F1, MHz	Compare Frequency, F2, MHz	F1 Correct Classification, %	F2 Correct Classification, %
B-519C, B-519E, AAD-2, AAD-3	0.5	0.8	83	73
	0.5	1	90	78
	0.8	1	63	56
B-519C	0.5	0.8	87	88
	0.5	1	93	88
	0.8	1	69	63
B-519E	0.5	0.8	100	87
	0.5	1	100	94
	0.8	1	87	56
AAD-2	0.5	0.8	75	75
	0.5	1	81	94
	0.8	1	63	56
AAD-3	0.5	0.8	81	63
	0.5	1	88	75
	0.8	1	56	63

The effects of probe skew angle were demonstrated by sorting the data in terms of skew 0 and 10 degrees as these angles are typically used in ultrasonic inspections (unlike the SkT). The results are plotted in Figure 6.23 for specimen B-519C and Figure 6.24 for specimen B-519E at 0.5 MHz, four refracted angles, and four slices. The data show that there is not a strong effect on scatter and partitioning as a result of the beam skew angle. Appendix D contains the 1.0-MHz results for these two specimens and show similar results. The AAD-2, 0.5-MHz data exhibited lower partitioning with a 10-degree skew angle as compared to a 0-degree skew angle. Otherwise the AAD-2 and AAD-3 data at 0.5 and 1.0 MHz did not show a correlation of beam skew with scatter and partitioning. These data plots are in Appendix D.

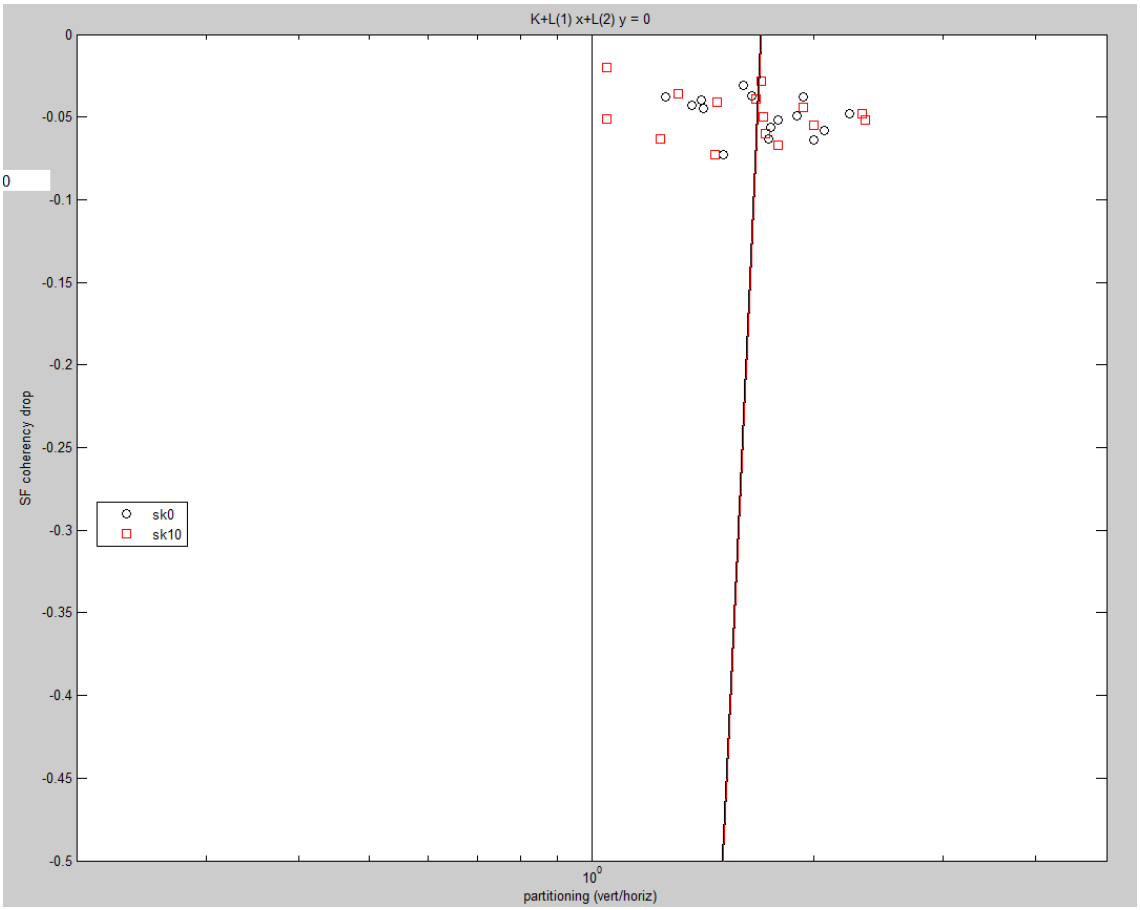

Figure 6.23. Sort by Probe Skew for Specimen B-519C at 0.5 MHz, Four Refracted Angles, and Four Positions

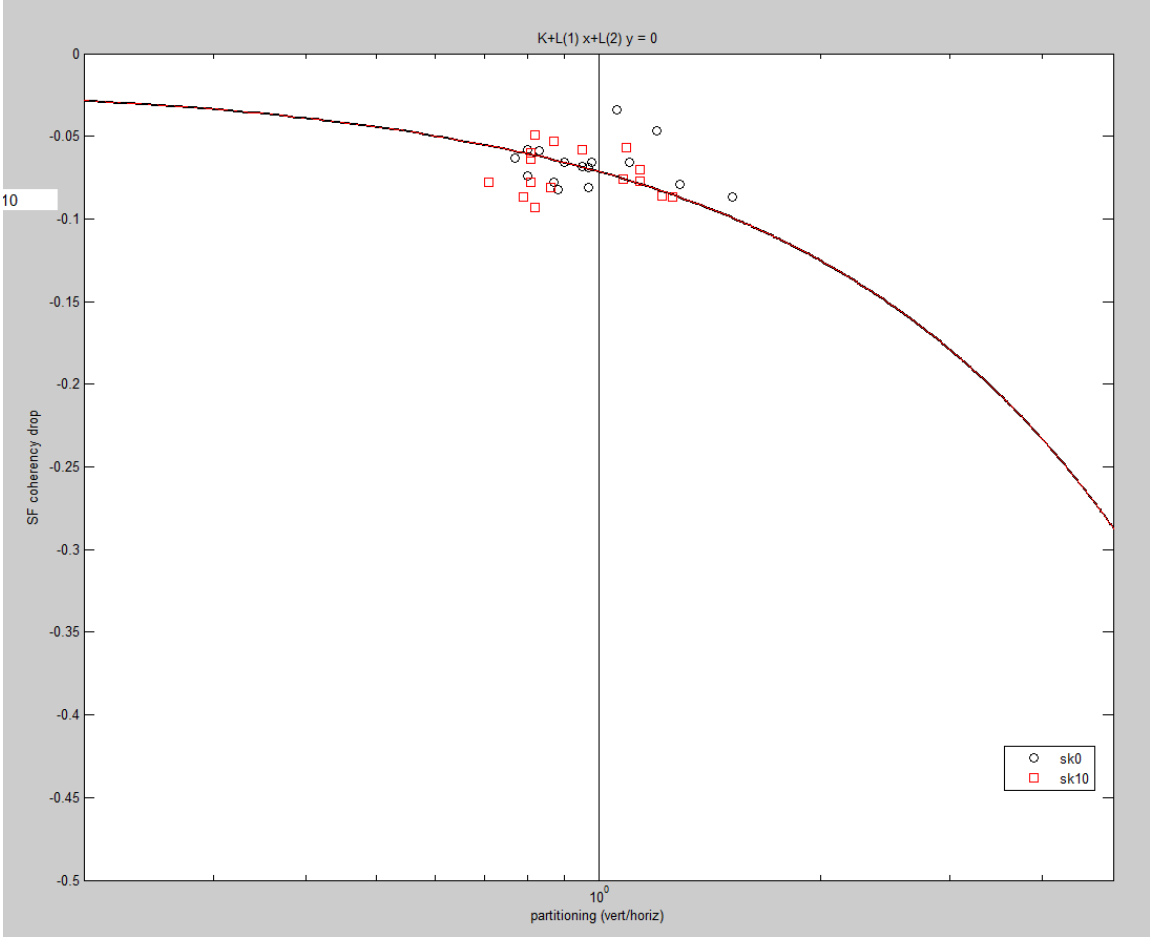

Figure 6.24. Sort by Probe Skew for Specimen B-519E at 0.5 MHz, Four Refracted Angles, and Four Positions

The sort-by-refracted angle plots show limited or no separation of the data in terms of beam partitioning and scatter for the equiaxed, columnar, and mixed banded data. This indicates that partition and scatter are not strongly related to refracted angle. Again, there is limited data with at most only four points per refracted angle (from the four cut faces). A minor effect was seen in specimen B-519E showing some correlation with refracted angle and partitioning. The results are shown in Figures 6.25 and 6.26 for the 0.5- and 1.0-MHz data at a skew angle of zero degrees. Greater partitioning was observed in the 0.5-MHz data at a refracted angle of 45 degrees and in the 1.0-MHz data at 55 degrees. Appendix D shows the results for the B-519C, AAD-2, and AAD-3 data which were inconclusive.

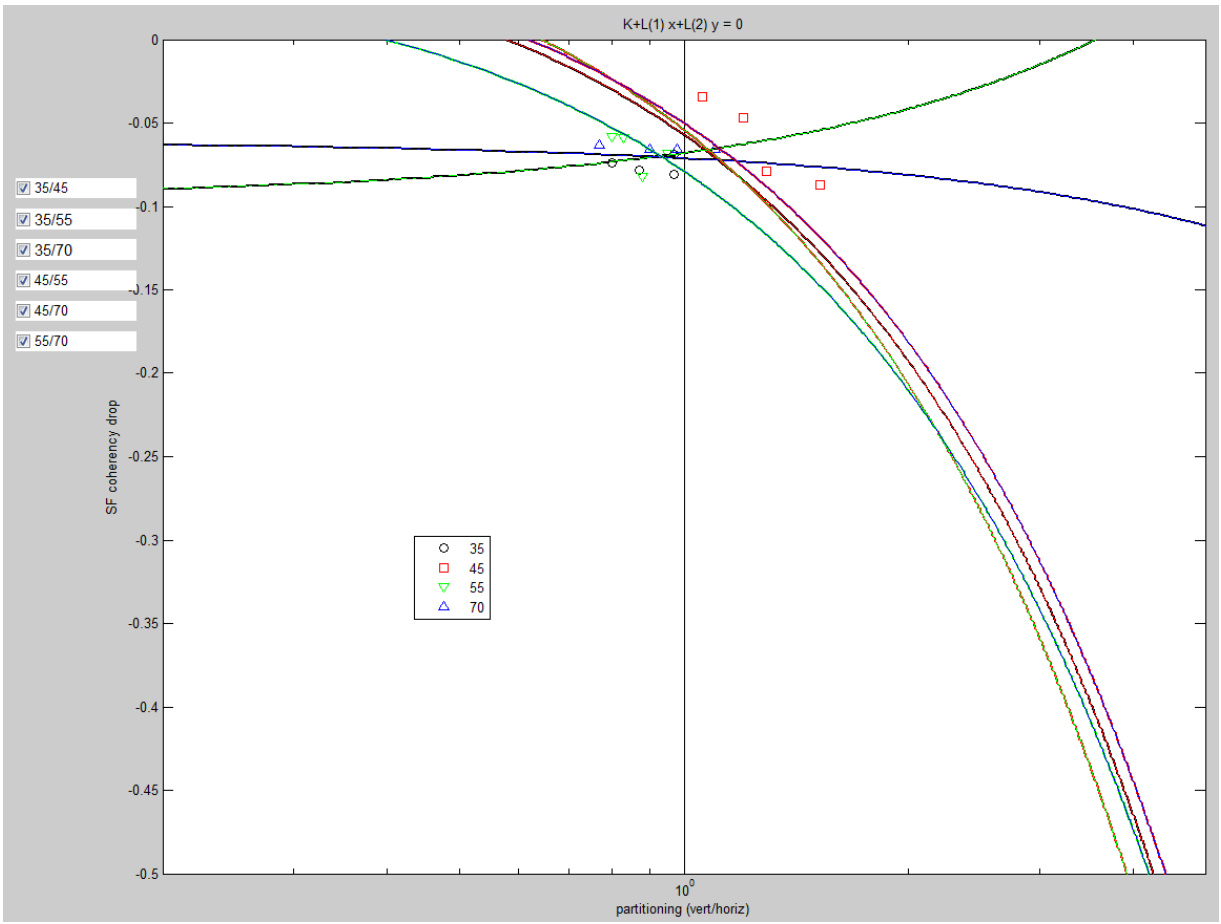

Figure 6.25. Sort by Refracted Angle for Specimen B-519E at 0.5 MHz, Skew 0 degrees, and Four Positions

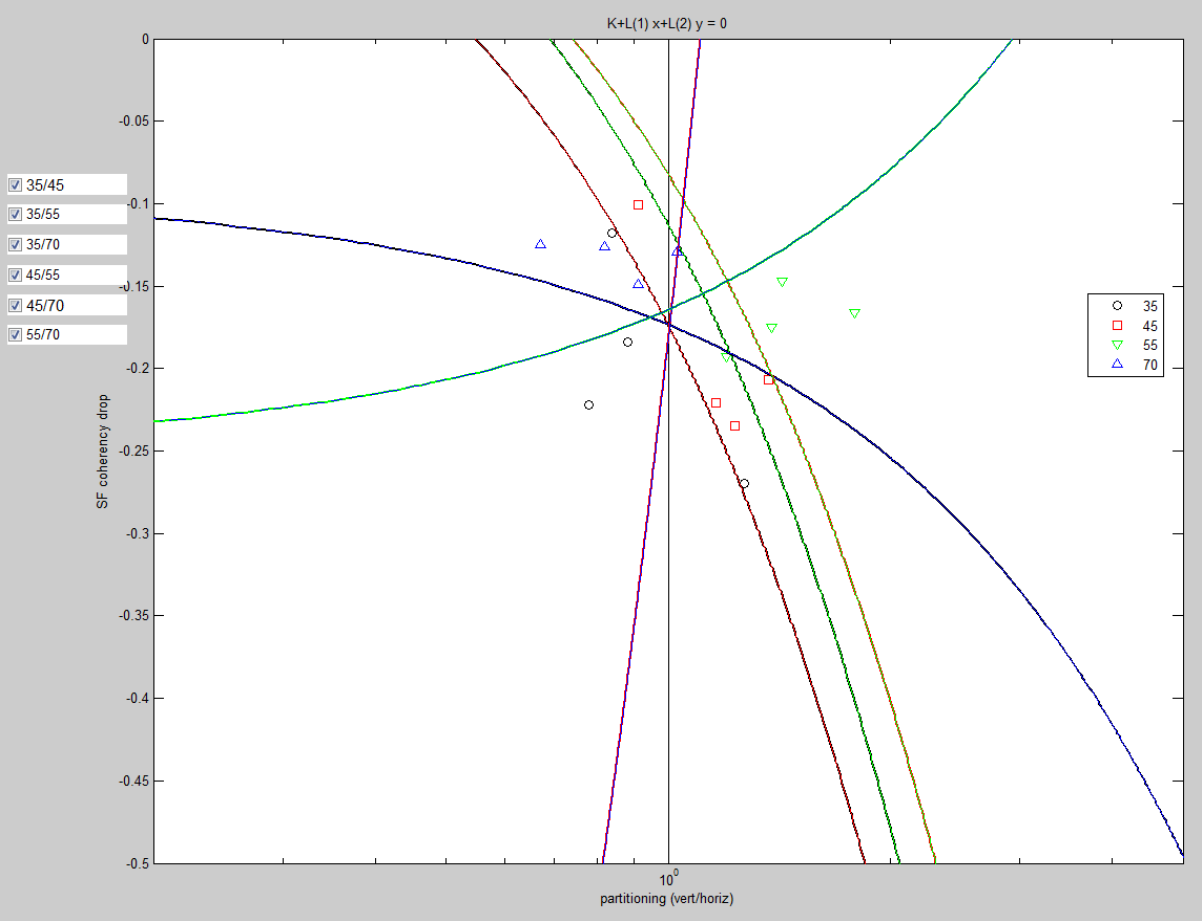

Figure 6.26. Sort by Refracted Angle for Specimen B-519E at 1.0 MHz, Skew 0 degrees, and Four Positions

6.5 Peak Amplitude

The peak amplitude of each recorded sound field was also measured and normalized to 1.0 across the several different gain settings used during data acquisition. The results are displayed in Figures 6.27 through 6.29 for skew T, 0, and 10 and give a comparative indication of attenuation in these CASS materials. As previously noted, the specimen data are delineated with red lines and probe frequency with gray lines. Within each specimen and probe frequency group, the four points represent refracted angles of 35, 45, 55, and 70 degrees. Error bars on the CASS data (blue diamonds) represent one standard deviation. The WSS data are represented as red squares.. The WSS peak responses were expected to be greater at all three probe frequencies but the data do not show this to be true. CASS and WSS peak responses are similar at 0.5 MHz while CASS responses are 10 to 15 dB lower than the WSS values at 0.8 and 1.0 MHz. While this phenomenon in not clearly understood, it does indicate a degraded response in CASS materials at the two higher probe frequencies as compared to the 0.5-MHz probe.

Perhaps the peak amplitude response is simply explained in terms of the probe frequency. At the lower frequency, enough of the beam is propagating through the material to register a response with peak amplitude that is similar to the peak amplitude in the well-formed beam in the WSS material. Then at the higher two probe frequencies, beam scatter plays a more significant role and the peak amplitude response is lowered. If scatter exhibits an approximately frequency squared relationship, then the difference between a 0.5 and a 1.0 MHz response is 12 dB. Clearly all of the CASS sound fields show signs of degradation in terms of beam coherence when compared to the WSS sound fields so a peak amplitude analysis alone can be misleading. This suggests that further studies may need to be pursued to fully understand the observed phenomena. Similarly, a thorough frequency response analysis was not performed and could be an area for further study.

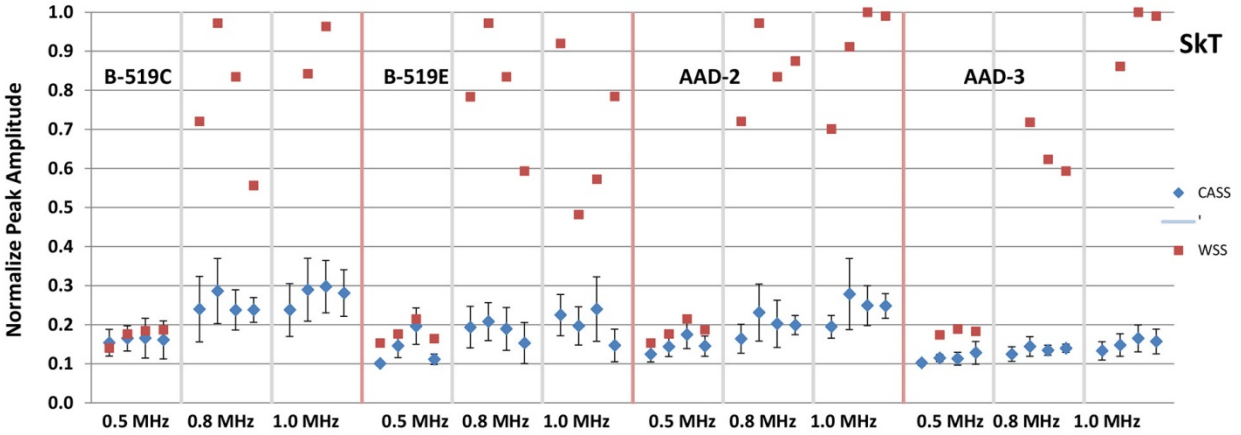

Figure 6.27. Amplitude Measurements for a Beam Skew of SkT on Four CASS Specimens and an Equivalent WSS Specimen with Three Probe Frequencies and Four Refracted Angles

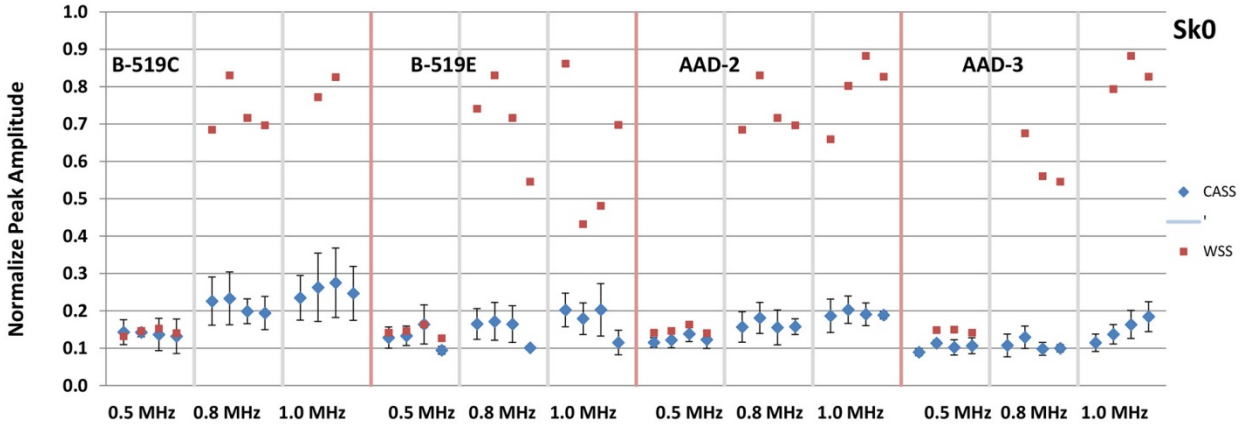

Figure 6.28. Amplitude Measurements for a Beam Skew of Sk0 on Four CASS Specimens and an Equivalent WSS Specimen with Three Probe Frequencies and Four Refracted Angles

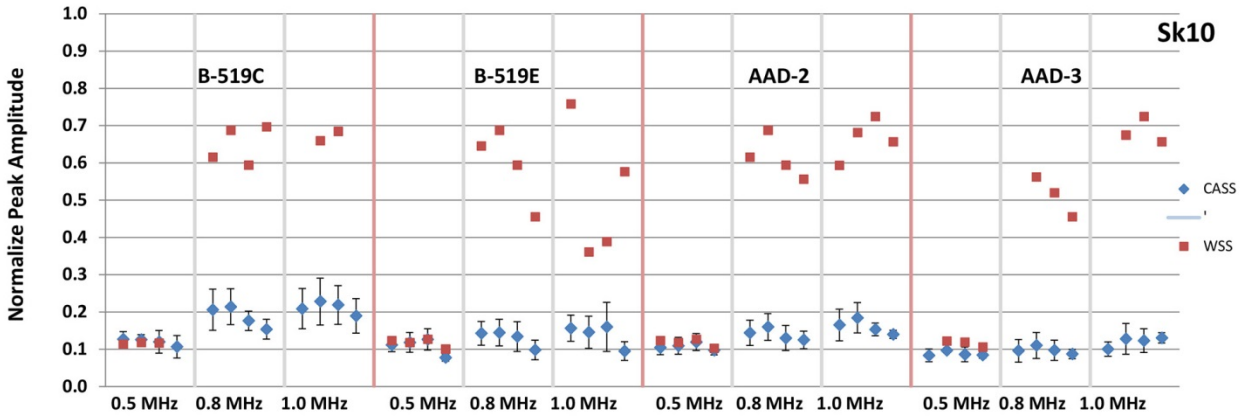

Figure 6.29. Amplitude Measurements for a Beam Skew of Sk10 on Four CASS Specimens and an Equivalent WSS Specimen with Three Probe Frequencies and Four Refracted Angles

6.6 Beam Redirection

In addition to characterizing the beam coherency in terms of partitioning and scatter, it was important to determine if the beam effectively insonified the intended target. The approach taken for this determination was to calculate the theoretical beam center position and then measure the center of the data image and compare the two. Positional coordinates were referenced to the fiducial at the ID of the specimen; specifically, the fiducial had a location of −5.0 mm (−0.20 in.) in the radial direction and 0 in the circumferential direction (Figure 6.30). A data image was defined by its horizontal (x) or circumferential extent and its vertical (y) or through-wall (radial) extent at the −6 dB points. The coordinates of the center of each data image were determined for the given CASS data sets (0.5-. 0.8-, and 1.0-MHz probes; four specimens; four cut surfaces; 35-, 45-, 55-, and 70-degree refracted angles; and four skew angles, T, −10, 0 and 10). Similar measurements were made on the WSS data sets except no −10-degree skew data were acquired. Note that the WSS data included the same probe frequencies and refracted angles but had only one surface measurement (i.e., no cut faces). An example of the data acquired is listed in Table 6.2 for the 0.5-MHz probe on specimen B-519C with skew angles of 0 and 10 degrees. The horizontal values correspond to a line in the circumferential direction (X in Figure 6.30) and the vertical values represent the through-wall or radial direction (Y in Figure 6.30). Plots were generated to show the theoretical positions along with the empirical data. The results for specimen B-519C at 0.5 MHz are shown in Figure 6.31 for the CASS data and in Figure 6.32 for the corresponding WSS data. Refracted angles are represented by shape and theoretical data points are black colored. Excluding black, colors indicate the skew angle and from left to right are SkT – magenta, Sk-10° – red, Sk0° – blue, and Sk10° – green. For example, the 70-degree Sk10° data are represented as diamonds with the four green diamonds corresponding to the four relative cut positions in the CASS material in Figure 6.31. In these data, the four empirical positions fall below and to the left of the theoretical position (black diamond). The corresponding WSS data are presented in Figure 6.32. For a skew Sk10 and 70-degree refracted angle, the single data point plots only slightly to the left and below the theoretical position. It appears that the columnar microstructure has caused the beam to shift in both the circumferential and through-wall extent. Appendix E contains the complete beam location data sets for all the specimens.

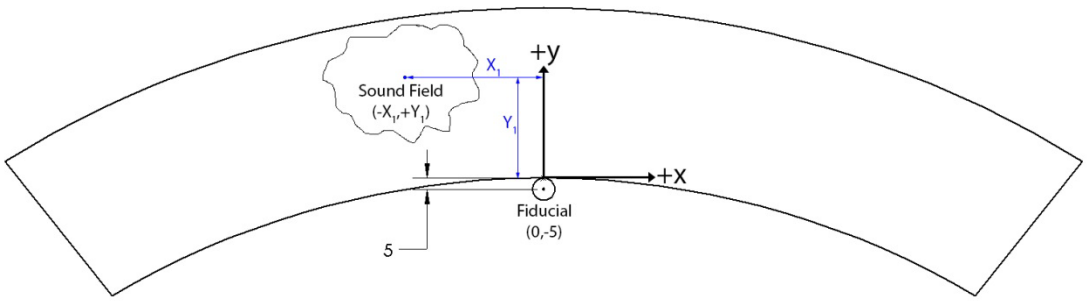

Figure 6.30. Coordinate System for Beam Redirection

Table 6.3. Sound Field Center Positions from Theoretical, WSS and CASS Data for Specimen B-519C at 0.5 MHz

B−519C 0.5 MHz		Theoretical		WSS			CASS	
		Center, mm (in.)		Center, mm (in.)			Center, mm (in.)	
Skew	Angle	Horizontal	Vertical	Horizontal	Vertical	Slice	Horizontal	Vertical
0	35	0.13 (0.01)	18.14 (0.71)	−1.65 (−0.06)	15.95 (0.63)	0	−4.45 (−0.18)	27.22 (1.07)
						1	−4.7 (−0.19)	23.23 (0.91)
						2	−3.7 (−0.15)	22.96 (0.90)
						3	−5.95 (−0.23)	23.21 (0.91)
0	45	0.37 (0.01)	27.3 (1.07)	−0.16 (−0.01)	26.19 (1.03)	0	−1.7 (−0.07)	28.72 (1.13)
						1	−2.45 (−0.10)	27.72 (1.09)
						2	−3.95 (−0.16)	28.7 (1.13)
0	55	−0.85 (−0.03)	27.52 (1.08)	−0.23 (−0.01)	27.43 (1.08)	0	−2.45 (−0.10)	25.97 (1.02)
						1	−2.2 (−0.09)	24.98 (0.98)
						2	−3.45 (−0.14)	24.7 (0.97)
						3	−3.45 (−0.14)	25.95 (1.02)
0	70	0.9 (0.04)	42.77 (1.68)	−0.2 (−0.01)	43.91 (1.73)	0	−1.95 (−0.08)	39.96 (1.57)
						1	−0.45 (−0.02)	39.46 (1.55)
						2	0.05 (0.00)	37.68 (1.48)
						3	−1.95 (−0.08)	38.68 (1.52)
10	35	6.38 (0.25)	17.14 (0.67)	4.25 (0.17)	15.70 (0.62)	0	1.75 (0.07)	28.47 (1.12)
						1	−1.45 (−0.06)	23.98 (0.94)
						2	0.8 (0.03)	21.71 (0.85)
						3	−0.95 (−0.04)	24.21 (0.95)
10	45	7.12 (0.28)	26.55 (1.05)	5.74 (0.23)	24.69 (0.97)	0	5.2 (0.20)	27.47 (1.08)
						1	3.7 (0.15)	26.97 (1.06)
						2	2 (0.08)	27.95 (1.10)
10	55	9.65 (0.38)	27.27 (1.07)	8.77 (0.35)	25.94 (1.02)	0	7.2 (0.28)	25.23 (0.99)
						1	6.2 (0.24)	24.97 (0.98)
						2	8.95 (0.35)	23.7 (0.93)
						3	5.95 (0.23)	24.7 (0.97)
10	70	8.9 (0.35)	43.27 (1.70)	8.52 (0.34)	41.66 (1.64)	0	7.7 (0.30)	37.72 (1.48)
						1	5.7 (0.22)	36.71 (1.45)
						2	8.45 (0.33)	35.93 (1.41)
						3	6.7 (0.26)	35.44 (1.40)

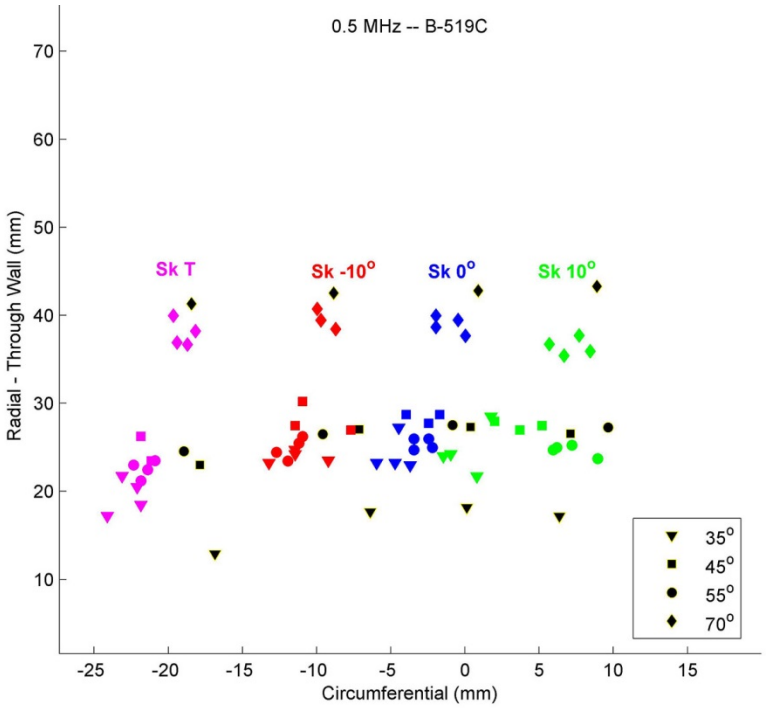

Figure 6.31. Sound Field Centers for Specimen B-519C at 0.5 MHz

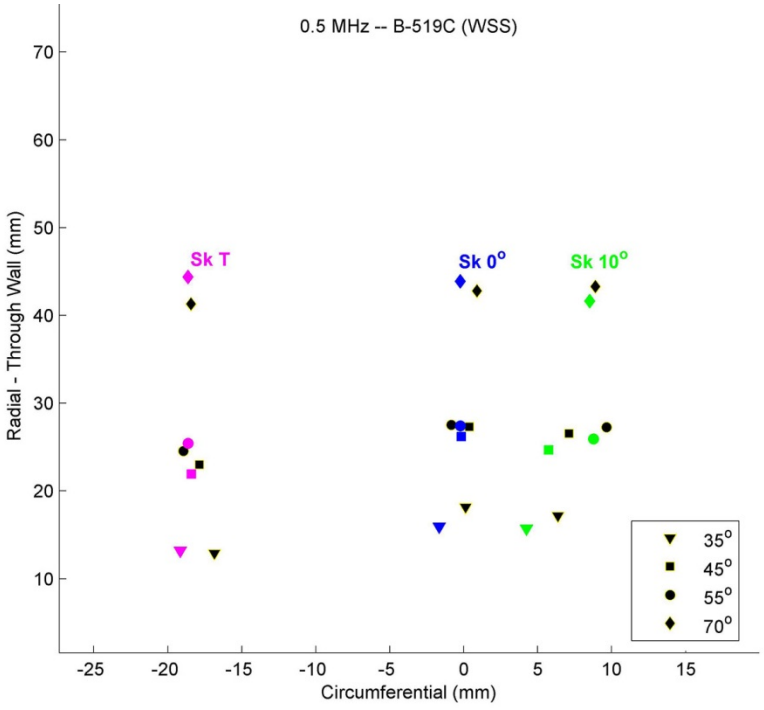

Figure 6.32. WSS Specimen Sound Field Centers at 0.5 MHz to Match Specimen B-519C

The error in an empirical data point position as compared to the theoretical position was calculated as a magnitude (= sqrt $[(\Delta x)^2 + (\Delta y)^2]$). The calculation quantifies the error which is then sorted by specimen, probe frequency, refracted and skew angles. The results are displayed in Figures 6.33 through 6.35 for the skew T, 0, and 10 degrees, respectively. In each figure, the specimen groups are delineated by the red vertical lines and the probe frequency for a specific specimen by gray vertical lines. The data points within a specimen and frequency group represent the four refracted angles, 35, 45, 55, and 70 degrees. Each point represents an average of the four faces (slices 0–3) from a specimen with plus and minus one standard deviation error bars. Because the skew 0 and 10-degree data represent actual inspection scenarios, only these results are discussed.

The WSS positional error was greatest (up to 6 mm or 0.24 in.) at 0.8 MHz and a refracted angle of 35 degrees. The radial component made up nearly all of this error. In general, the error decreased with increasing refracted angle in the 0.5- and 0.8-MHz data. This trend was not evident in the 1.0-MHz data.

In the CASS specimens, the positional error in equiaxed specimen B-519E nominally decreased with increasing refracted angle and the contributions from the circumferential and radial components were similar, within 3 mm (0.08 in.) of each other. The greatest error was seen in the 35-degree refracted data at 0.8 MHz for both skew 0 and 10 degrees. Error in the radial direction was approximately 6 mm (0.24 in.) and 3 mm (0.13 in.) in the circumferential direction. The columnar specimen exhibited more positional error at 35- and 70-degree refracted angles than in the 45- and 55-degree data. This occurred for both 0- and 10-degree skew angles. The 1.0-MHz B-519C data had the most error at a 35-degree refracted angle. Error in the radial direction was approximately 10 mm (0.39 in.) and only 1–3 mm (0.04–0.12 in.) in the circumferential direction with the greater error in the skew 10-degree data. Finally, the AAD specimens produced a mixed result with error not correlating to refracted angle. The AAD-2 specimen showed greater error with the larger skew angle and also less error with increasing frequency. The specimen covered a range of 4–9 mm (0.16–0.35 in.) in average error. The AAD-3 specimen had nominally similar positional error regardless of frequency and skew. Its approximate error was 4 mm (0.16 in.).

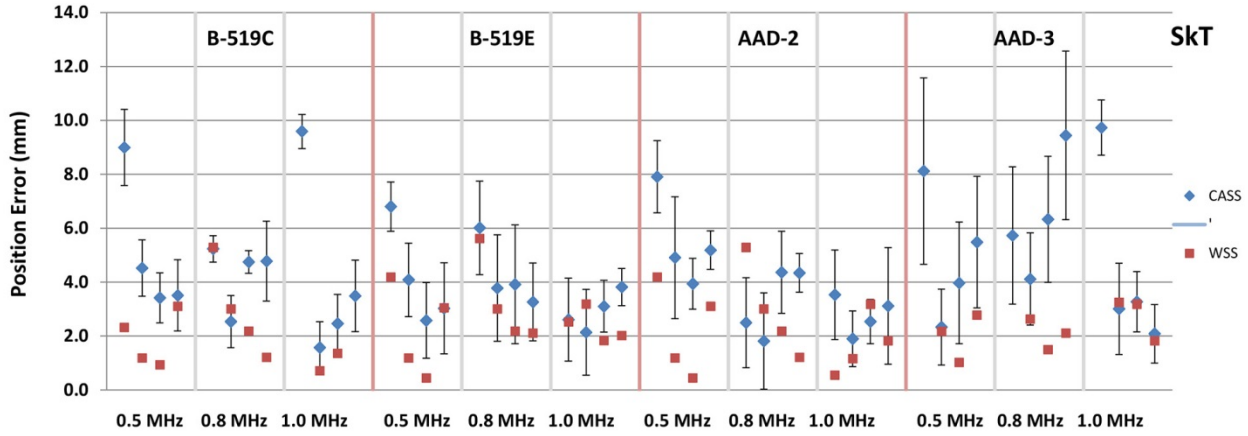

Figure 6.33. Positional Error for a Beam Skew of SkT on Four CASS Specimens and an Equivalent WSS Specimen with Three Probe Frequencies and Four Refracted Angles

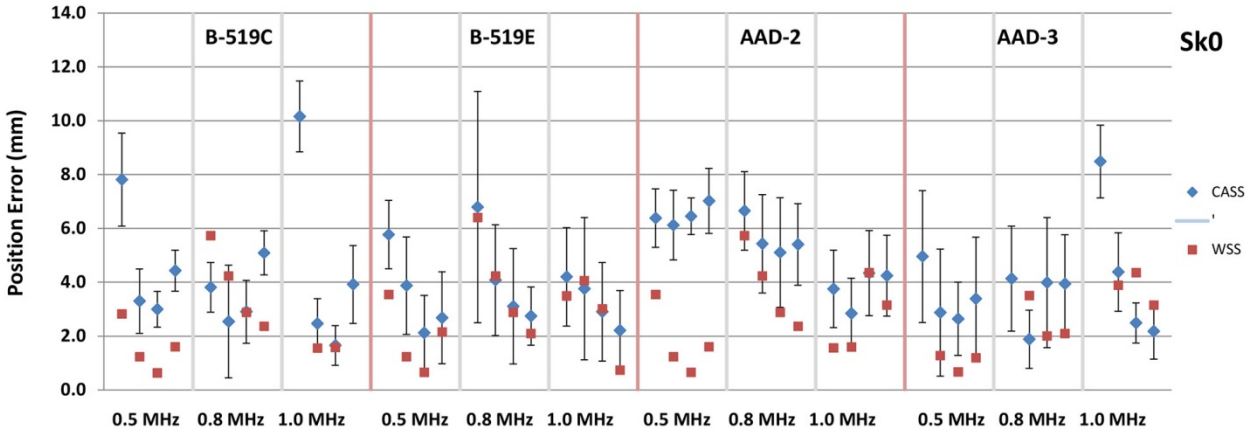

Figure 6.34. Positional Error for a Beam Skew of Sk0 on Four CASS Specimens and an Equivalent WSS Specimen with Three Probe Frequencies and Four Refracted Angles

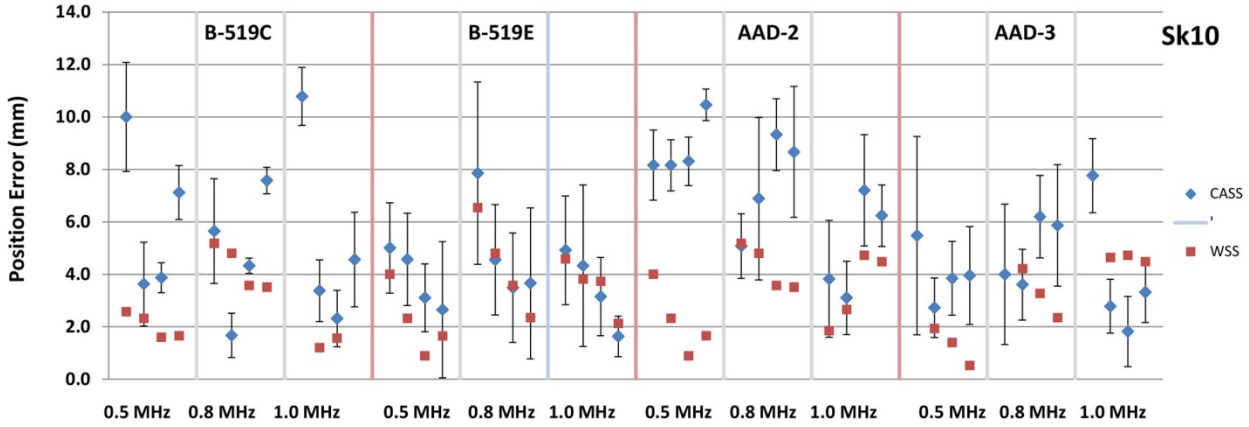

Figure 6.35. Positional Error for a Beam Skew of Sk10 on Four CASS Specimens and an Equivalent WSS Specimen with Three Probe Frequencies and Four Refracted Angles

7.0 Discussion and Conclusions

An ultrasonic phased-array beam mapping study in coarse-grained materials was conducted to better understand the effects of certain experimental input parameters on the sound beam quality and location or positional accuracy. Four examples of thick-section, coarse-grained CASS specimens were examined consisting of one columnar, one equiaxed, and two mixed-banded microstructures. Three phased-array ultrasonic probes with center frequencies of 0.5, 0.8, and 1.0 MHz were used to form the beam and theoretically focus the sound at a plane coincident with the end of the specimen. The sound field data were acquired by raster scanning the ends of the four specimens with a broadband point transducer (pinducer) in an immersion setup. Sound fields were mapped at three beam skew angles, four refracted angles, and four positions on each specimen. The positional data provided input on the grain variations and data uncertainty within a specimen. All data were benchmarked against sound field maps obtained through a fine-grained, isotropic, wrought stainless steel specimen.

The scatter and sound beam partition measurements, and combined scatter and partition plots with data classification, clearly show the effects of frequency on these variables within CASS materials. Columnar microstructures produce the greatest partitioning and equiaxed the least. Conversely, the equiaxed microstructure produced the greatest scatter while the columnar microstructure produced the least. The mixed and banded microstructures show various combinations. As a function of frequency, the columnar specimen B-519C exhibited less scatter and partitioning at 0.5 MHz than the higher two frequencies. Equiaxed specimen B-519E showed increasing scatter with increasing frequency but partitioning was similar across all three probe frequencies.

Probe skew angle (0 and 10 degree) had little effect on scatter and partition measurement in the columnar, equiaxed, and mixed AAD-3 specimens. Specimen AAD-2 at 0.5MHz showed a lower partitioning with a 10-degree skew but no difference at 1.0 MHz. Refracted angle variations showed little to no effect on scatter and partitioning. A minor effect was evident in specimen B-519E, which exhibited greater partitioning at a 45-degree refracted angle for the 0.5 MHz, skew 0-degree data and greater partitioning at a 55-degree refracted angle for the 1.0 MHz, skew 0 data. Scatter was not influenced by refracted angle in the equiaxed specimen. Refracted angle variations had insignificant effects on scatter and partition measurements in columnar specimen B-519C and the AAD specimens.

A peak amplitude analysis demonstrated that the responses for all four CASS specimens were similar to the WSS responses at the 0.5-MHz probe frequency. However, at the higher two frequencies, the CASS responses were 10–15 dB lower than responses in the fine-grained material. This diminished response with the 0.8- and 1.0-MHz probes provide further evidence that frequencies above 0.5 MHz are not expected to perform adequately when examining thick CASS materials.

Beam redirection measurements in the fine-grained WSS specimen produced positional error as large as 6 mm (0.24 in.) with the 0.8-MHz probe and a refracted angle of 35 degrees. The error was primarily in the radial direction and decreased with increasing refracted angle. Errors in the 0.5- and 1.0-MHz data were up to 4 mm (0.16 in.). The 0.5-MHz and 0.8-MHz errors inversely correlated with refracted angle, while the 1.0-MHz error showed no such correlation. These values indicate the positional error that can be expected in a specimen with thickness in the 60–80 mm (2.36–3.15 in.) range. Some of this error could be attributed to the cumulative effect of small errors between the theoretical or design focal spot position and the actual or empirical position. While the error is larger than anticipated, at this point it is

unknown as to how much of the error is attributed to probe design, modeling errors, or velocity inconsistencies.

As expected, beam redirection in the CASS material was larger than in the WSS specimen with error as large as 10 mm (0.39 in.) in the radial direction for the columnar microstructure when using 1.0 MHz, with a skew of 10 degrees and a 35-degree refracted angle. Error in the circumferential direction was only 1–3 mm (0.04–0.12 in.) in these data. The mid-range refracted angles of 45 and 55 degrees produced the least error in a columnar microstructure with probe frequency showing mixed results. Additionally, positional error decreased with increasing refracted angle, with the largest error being 6 mm (0.24 in.) radially and 3 mm (0.12 in.) circumferentially at a 0.8-MHz frequency. The mixed banded AAD-2 specimen showed greater error with a larger skew angle and also less error with increasing frequency. The specimen covered a range of 4–9 mm (0.16–0.35 in.) in average error. Mixed banded AAD-3 specimen had nominally similar positional error regardless of frequency and skew. Its approximate error was 4 mm (0.16 in.). The data suggest that an error of as much as 10 mm (0.39 in.) is not unreasonable for this material. Note that this measurement is based on the transmit path length only, so a return path could double the error received by a probe on the specimen OD.

Clearly the first priority in an ultrasonic examination is the selection of probe frequency, assuming sufficient probe aperture, element size, and number to properly form the beam. The primary objective of the examination is to effectively detect and then characterize relevant flaws in the component. Probe frequency has been shown to greatly affect scatter, and partitioning to a lesser extent. In addition to less scatter (and partly because of it), the lower frequency probe provided a peak amplitude response in the CASS material that was similar to the WSS response. Probe skew and refracted angles had minor or no effects on beam formation and should be used as needed to insonify the appropriate volume in a component. While the 0.5-MHz probe provided the least scatter and partitioning, it also provides the lowest resolution. The 0.8- or 1.0-MHz probes could be used in conjunction with the 0.5-MHz probe on the columnar or mixed-banded specimens for improvements in resolution, but the 1.0-MHz probe is not recommended for an equiaxed material evaluation. Beam redirection error could be minimized by using midrange refracted angles when possible. These results are intended to help guide inspection parameters for evaluation of CASS materials.

8.0 References

Anderson MT, SL Crawford, SE Cumblidge, KM Denslow, AA Diaz and SR Doctor. 2007. *Assessment of Crack Detection in Heavy-Walled Cast Stainless Steel Piping Welds Using Advanced Low-Frequency Ultrasonic Methods*. NUREG/CR-6933, PNNL-16292, U.S. Nuclear Regulatory Commission, Washington, D.C. ADAMS Accession No. ML071020410.

Diaz AA, SR Doctor, BP Hildebrand, FA Simonen, GJ Schuster, ES Andersen, GP McDonald and RD Hasse. 1998. *Evaluation of Ultrasonic Inspection Techniques for Coarse-Grained Materials*. NUREG/CR-6594, PNNL-11171, U.S. Nuclear Regulatory Commission, Washington, D.C.

Diaz AA, RV Harris Jr. and SR Doctor. 2008. *Field Evaluation of Low-Frequency SAFT-UT on Cast Stainless Steel and Dissimilar Metal Weld Components*. NUREG/CR-6984, PNNL-14374, U.S. Nuclear Regulatory Commission, Washington, D.C.

Doctor SR, GJ Schuster, LD Reid and TE Hall. 1996. *Real-Time 3-D SAFT-UT Evaluation and Validation*. NUREG/CR-6344, PNNL-10571, U.S. Nuclear Regulatory Commission, Washington, D.C.

Good MS and LG Van Fleet. 1987. "Ultrasonic Beam Profiles in Coarse Grained Materials." In *8th International Conference on NDE in the Nuclear Industry*, pp. 657-666. November 17-20, 1986, Kissimmee, Florida. American Society for Metals International, Metals Park, Ohio.

Good MS and LG Van Fleet. 1988. "Mapping of Ultrasonic Fields in Solids." In *Review of Progress in Quantitative Nondestructive Evaluation*, pp. 637-646. June 22-26, 1987, Williamsburg, Virginia. Plenum Press, New York.

Good MS and LG Van Fleet. 1990. "Phase Mapping of Ultrasonic Fields Passed Through Centrifugally Cast Stainless Steel." In *Review of Progress in Quantitative Nondestructive Evaluation*, pp. 1975-1982. July 15-20, 1990, La Jolla, California. Plenum Press, New York.

Hall TE, LD Reid and SR Doctor. 1988. *The SAFT-UT Real-Time Inspection System - Opeerational Principles and Implementation*. NUREG/CR-5075, PNNL-6413, U.S. Nuclear Regulatory Commission, Washington, D.C.

Kestenbach H-J and MA Meyers. 1976. "The Effect of Grain Size on the Shock-Loading Response of 304-Type Stainless Steel." *Metallurgical Transactions A, Physical Metallurgy and Material Science* 7A:1943-1950.

Ruud CO, AA Diaz and MT Anderson. 2009. *Grain Structure Identification and Casting Parameters of Austenitic Stainless Steel (CASS) Piping*. PNNL-19002, Pacific Northwest National Laboratory, Richland, Washington.

Szilard J, Ed. 1982. *Ultrasonic Testing Non-conventional Testing Techniques*. John Wiley & Sons, New York. Chapters 1 and 6.

Appendix A

Examined Faces of Specimens B519C, B591E, AAD2 and AAD3 – Polished and Etched

Appendix A

Examined Faces of Specimens B519C, B591E, AAD2 and AAD3 – Polished and Etched

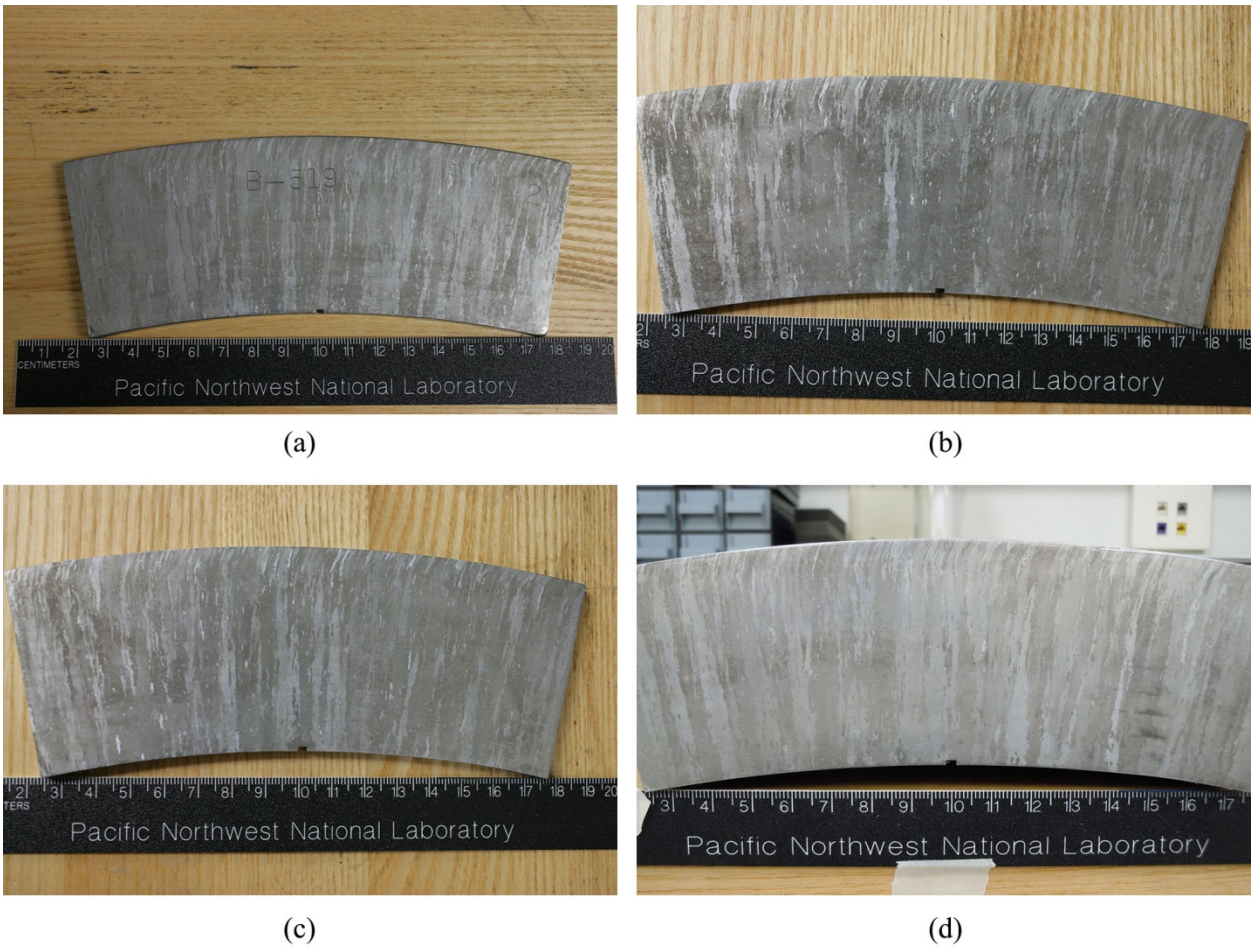

(a) (b)

(c) (d)

Figure A.1. Four Cut Faces of Specimen B519C with: (a) Original Face, (b) After First Cut, (c) After Second Cut, and (d) After Third and Final Cut

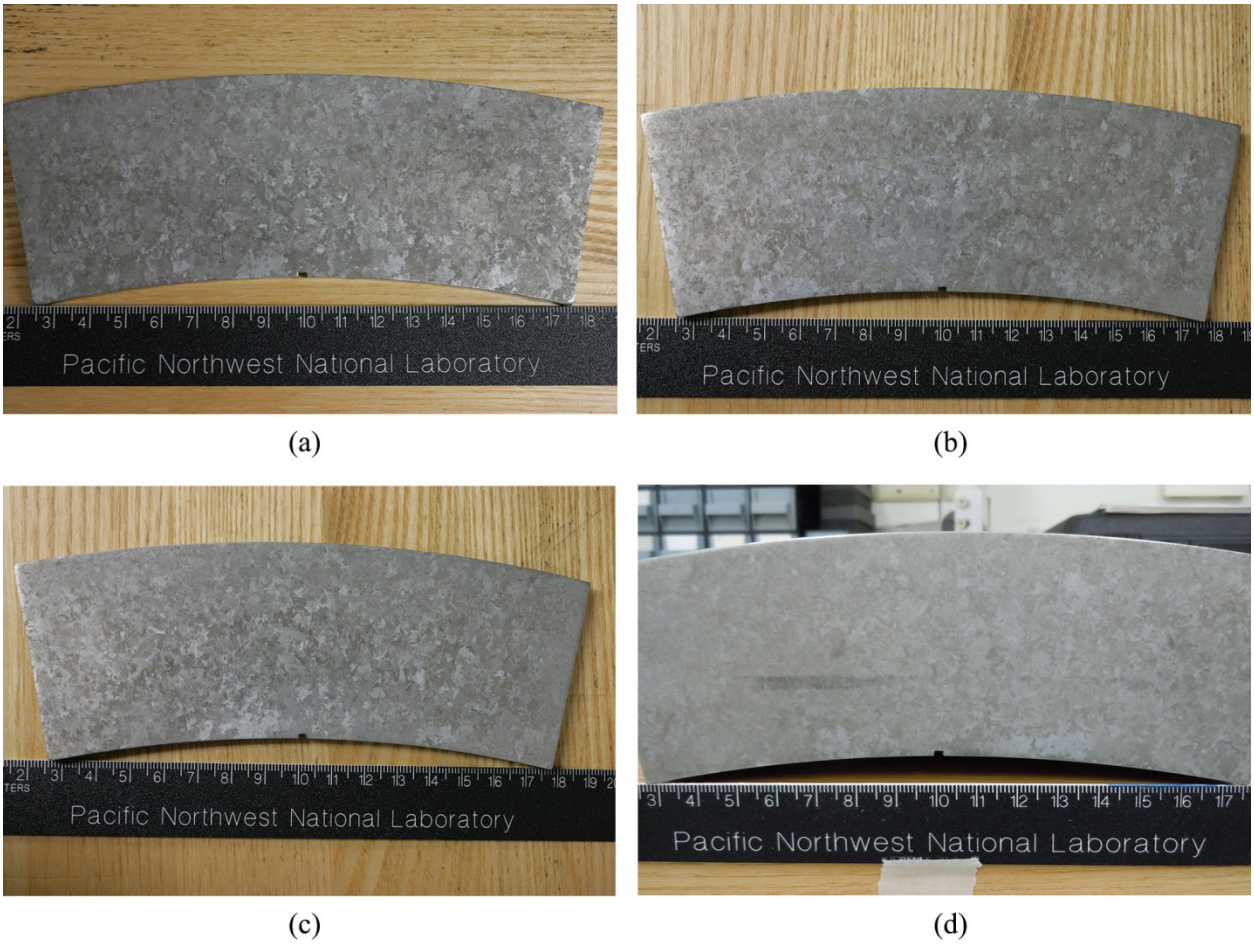

Figure A.2. Four Cut Faces of Specimen B519E with: (a) Original Face, (b) After First Cut, (c) After Second Cut, and (d) After Third and Final Cut

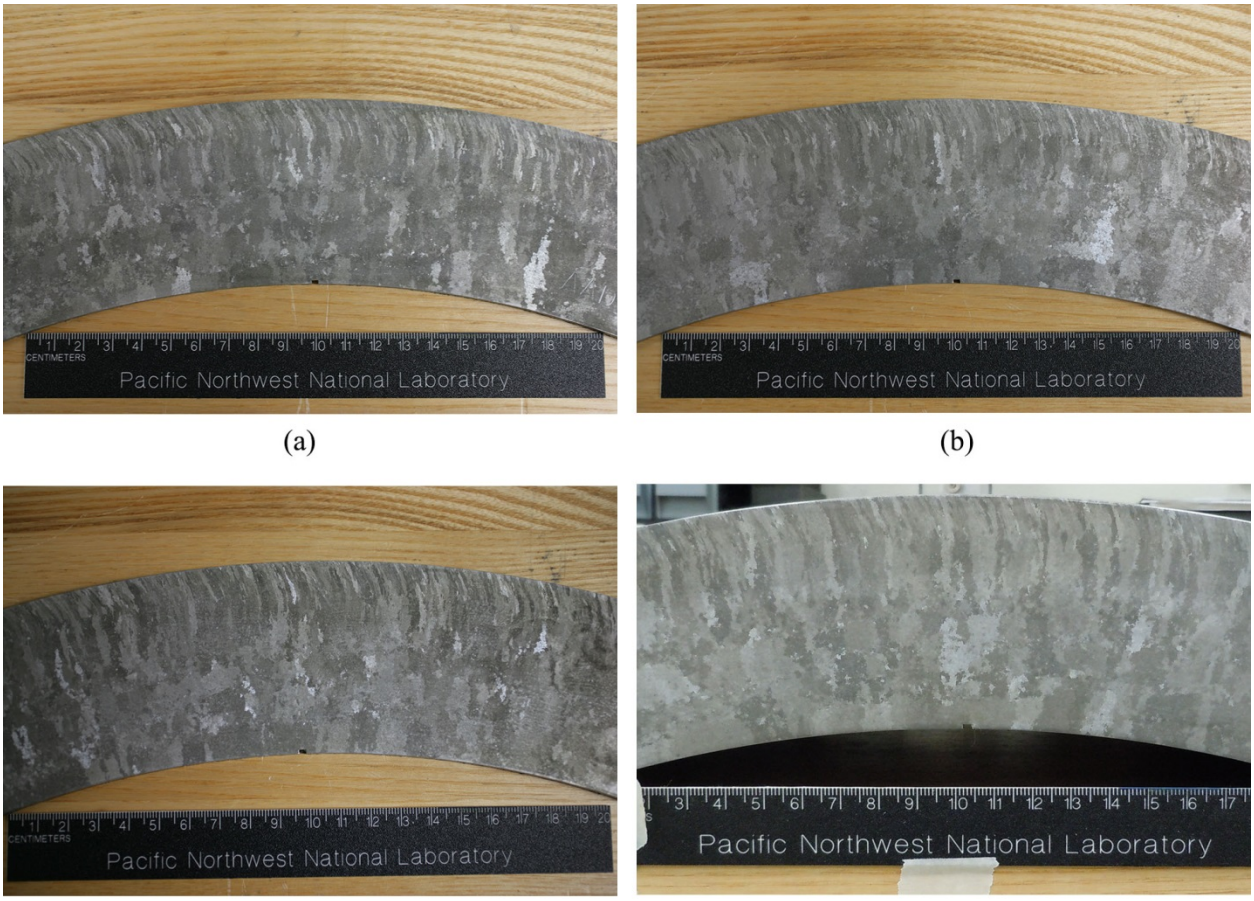

Figure A.3. Four Cut Faces of Specimen AAD2 with: (a) Original Face, (b) After First Cut, (c) After Second Cut, and (d) After Third and Final Cut

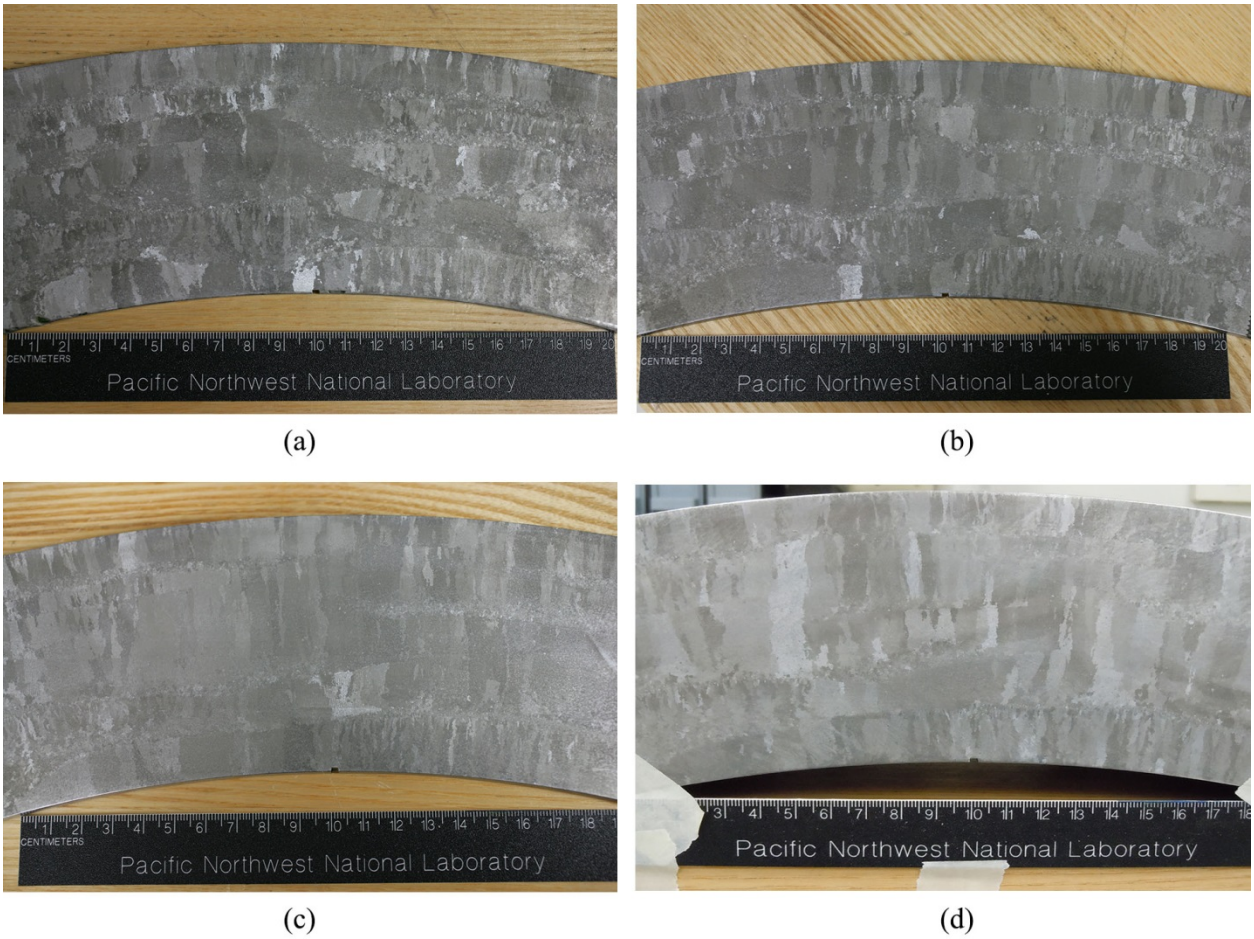

Figure A.4. Four Cut Faces of Specimen AAD3 with: (a) Original Face, (b) After First Cut, (c) After Second Cut, and (d) After Third and Final Cut

Appendix B

Sound Field Images in CASS

Appendix B

Sound Field Images in CASS

B.1 Frequency 0.5 MHz (B.1-16)

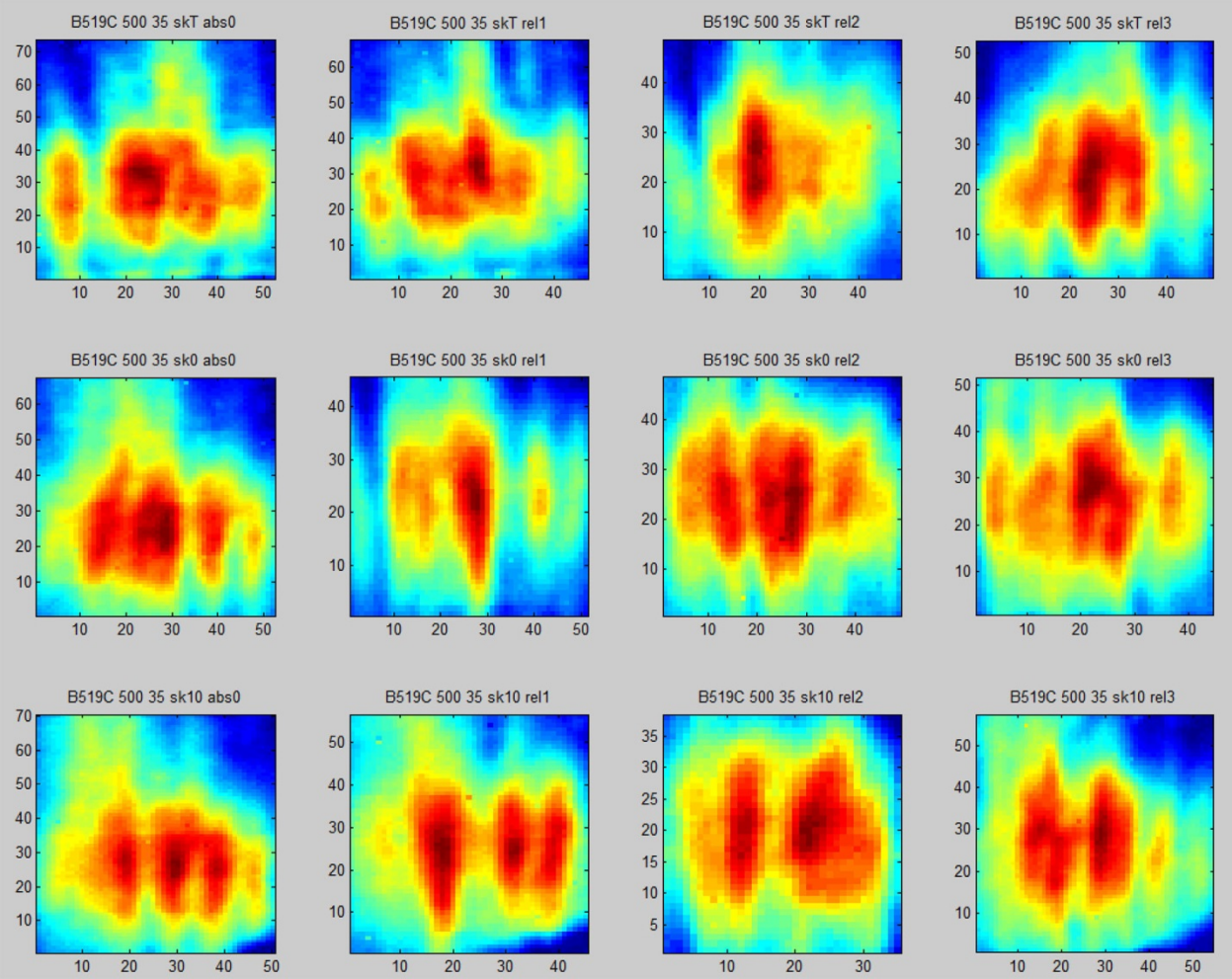

Figure B.1. Frequency 0.5 MHz, Specimen B519C, Refracted Angle 35 degrees, Cuts 0-3 Left to Right and SkT, Sk0, and Sk10 Top to Bottom

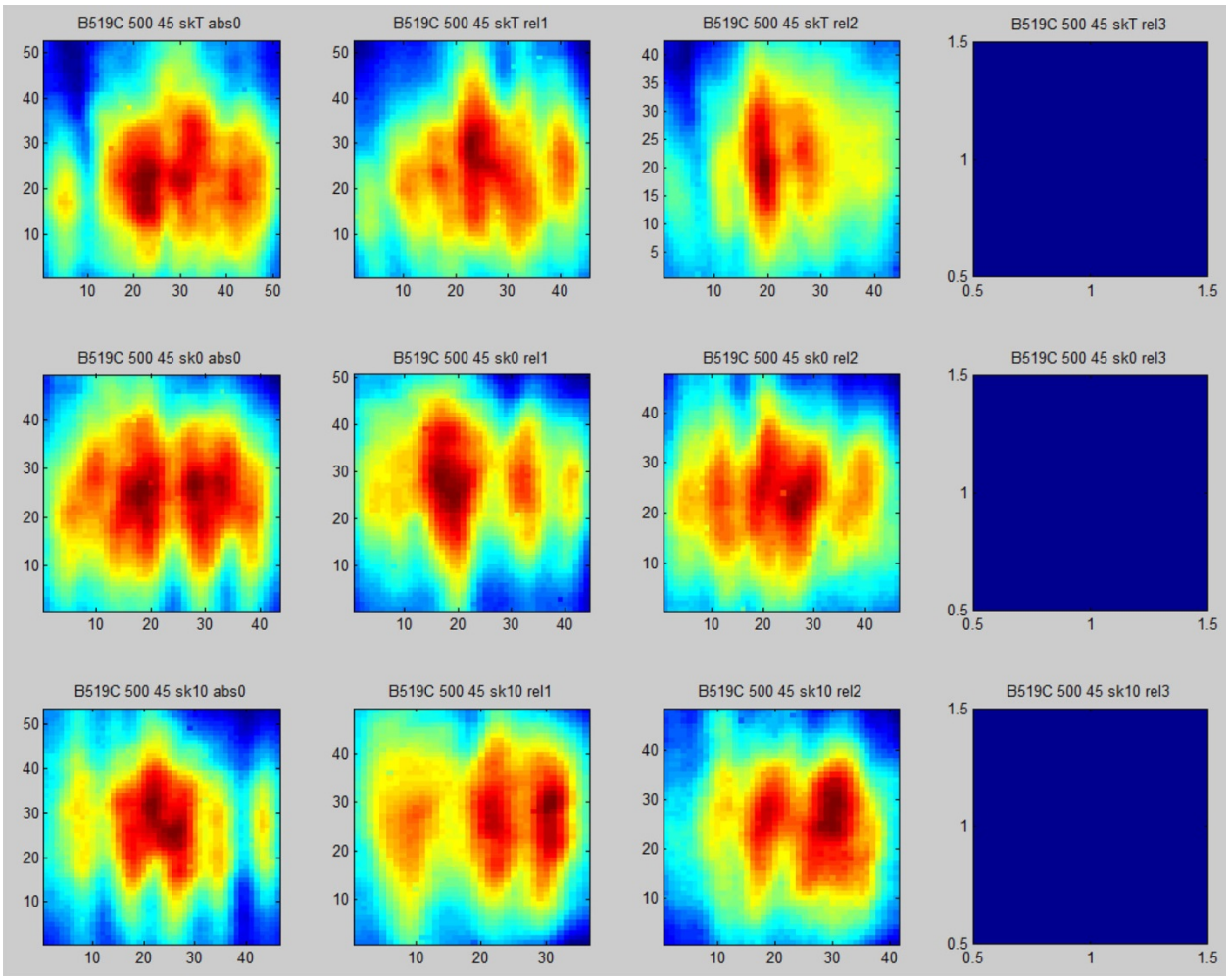

Figure B.2. Frequency 0.5 MHz, Specimen B519C, Refracted Angle 45 degrees, Cuts 0-3 Left to Right and SkT, Sk0, and Sk10 Top to Bottom

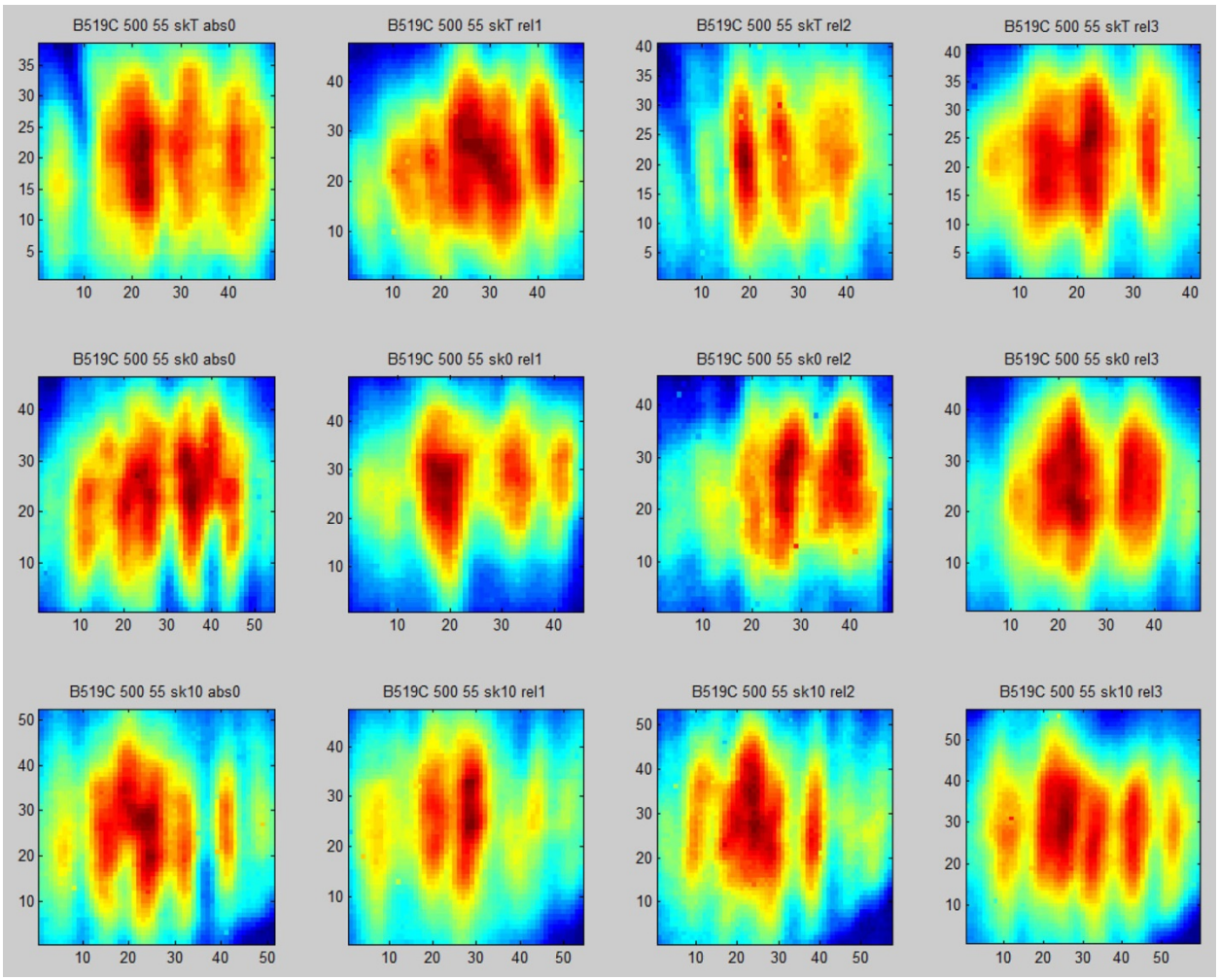

Figure B.3. Frequency 0.5 MHz, Specimen B519C, Refracted Angle 55 degrees, Cuts 0-3 Left to Right and SkT, Sk0, and Sk10 Top to Bottom

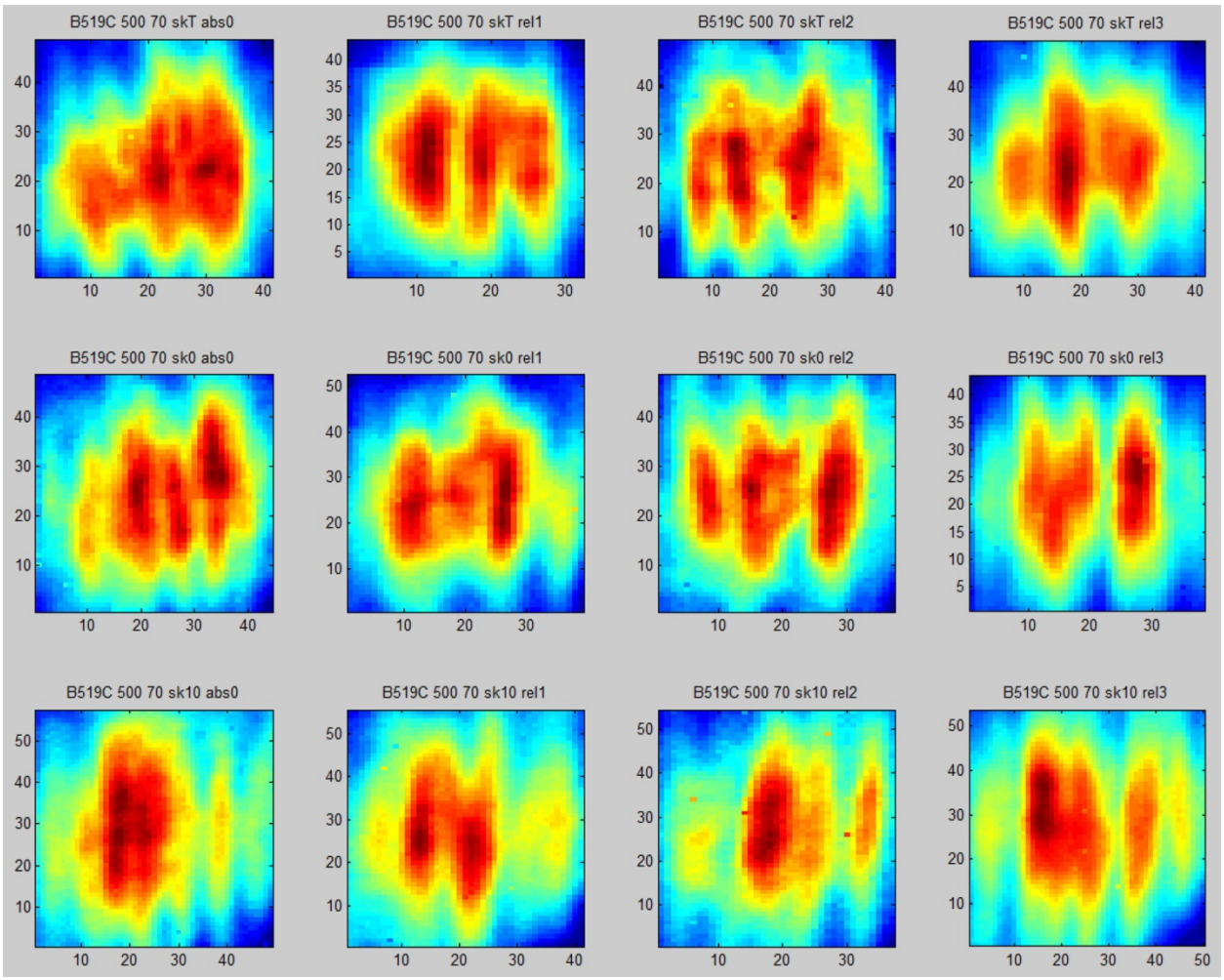

Figure B.4. Frequency 0.5 MHz, Specimen B519C, Refracted Angle 70 degrees, Cuts 0-3 Left to Right and SkT, Sk0, and Sk10 Top to Bottom

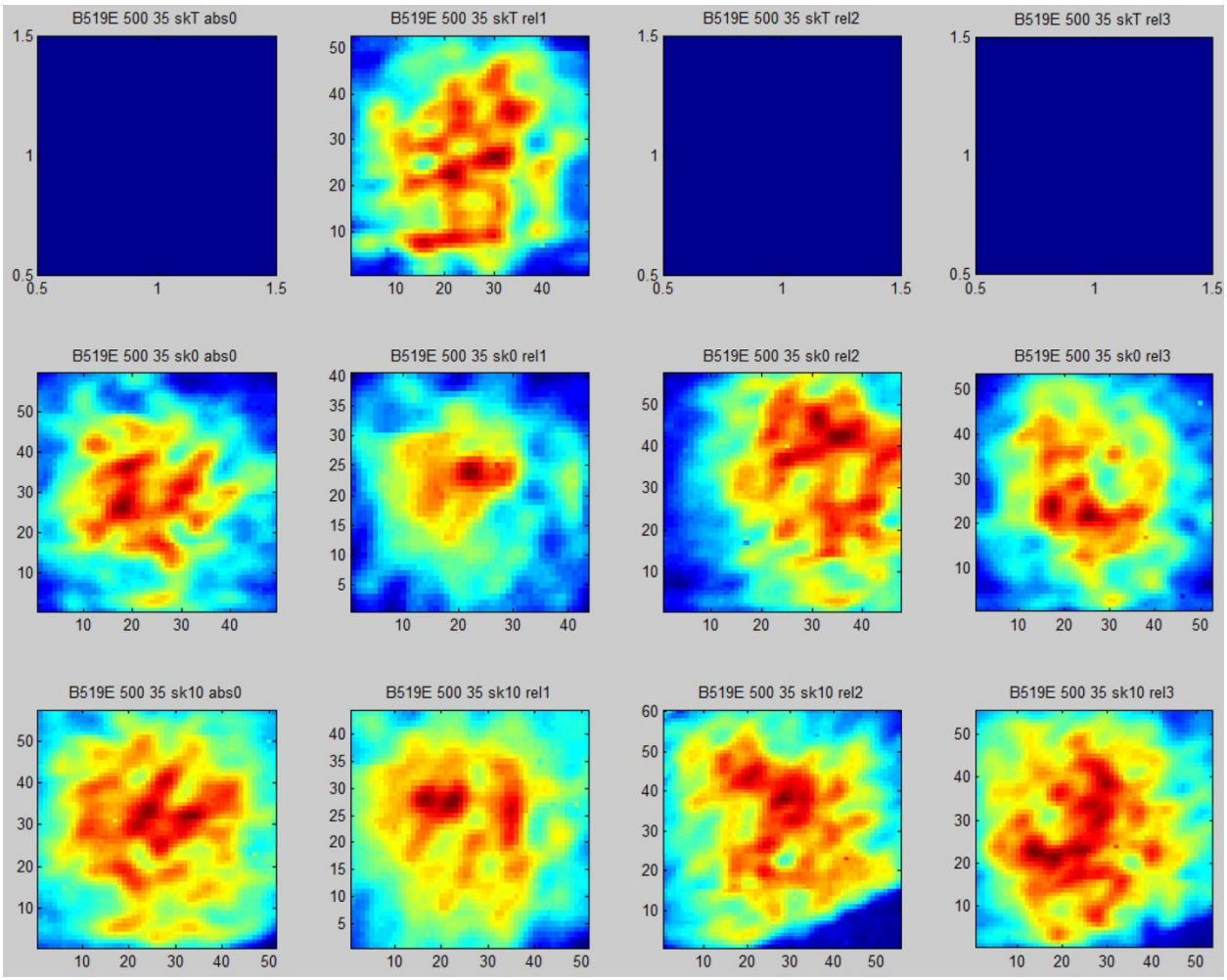

Figure B.5. Frequency 0.5 MHz, Specimen B519E, Refracted Angle 35 degrees, Cuts 0-3 Left to Right and SkT, Sk0, and Sk10 Top to Bottom

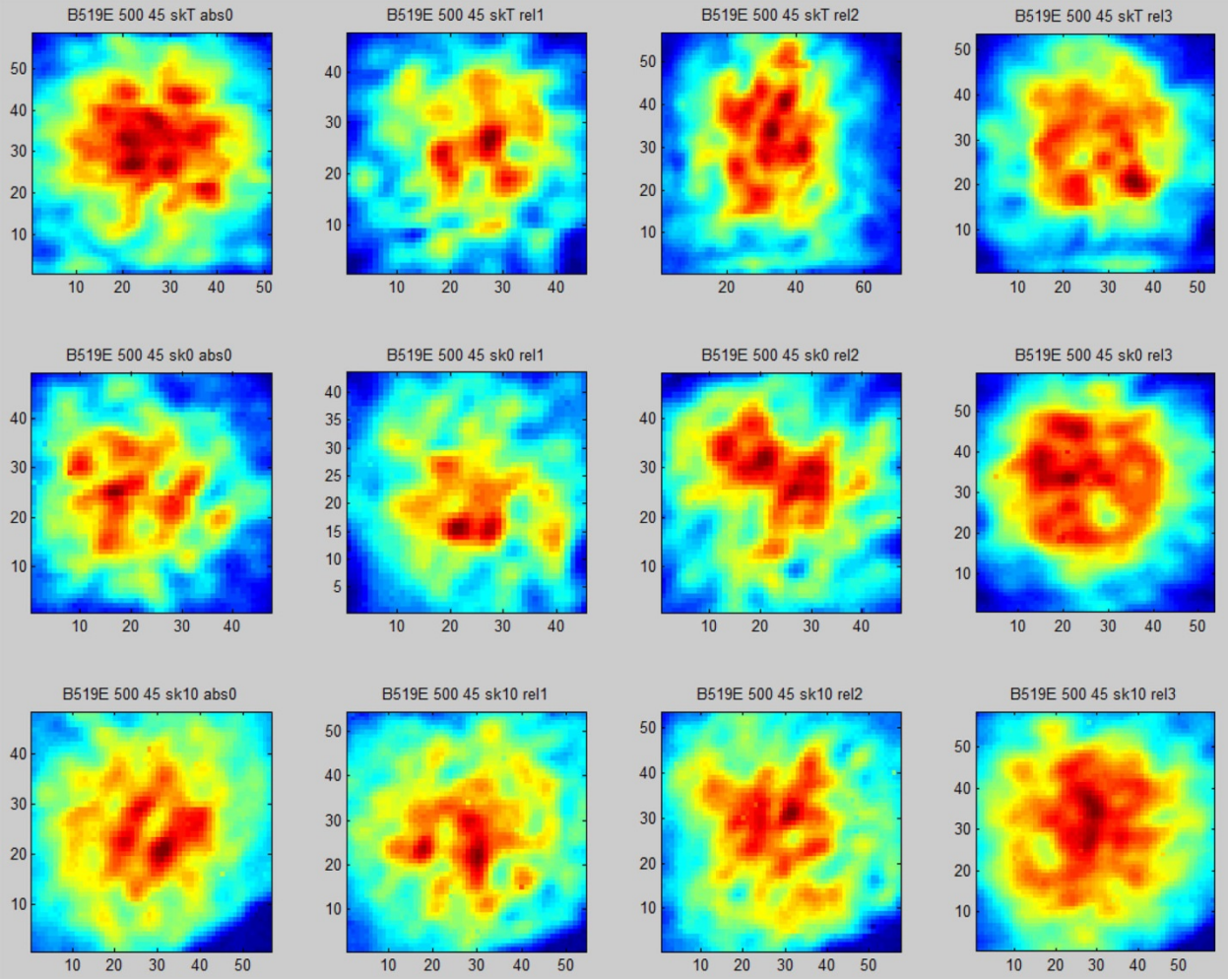

Figure B.6. Frequency 0.5 MHz, Specimen B519E, Refracted Angle 45 degrees, Cuts 0-3 Left to Right and SkT, Sk0, and Sk10 Top to Bottom

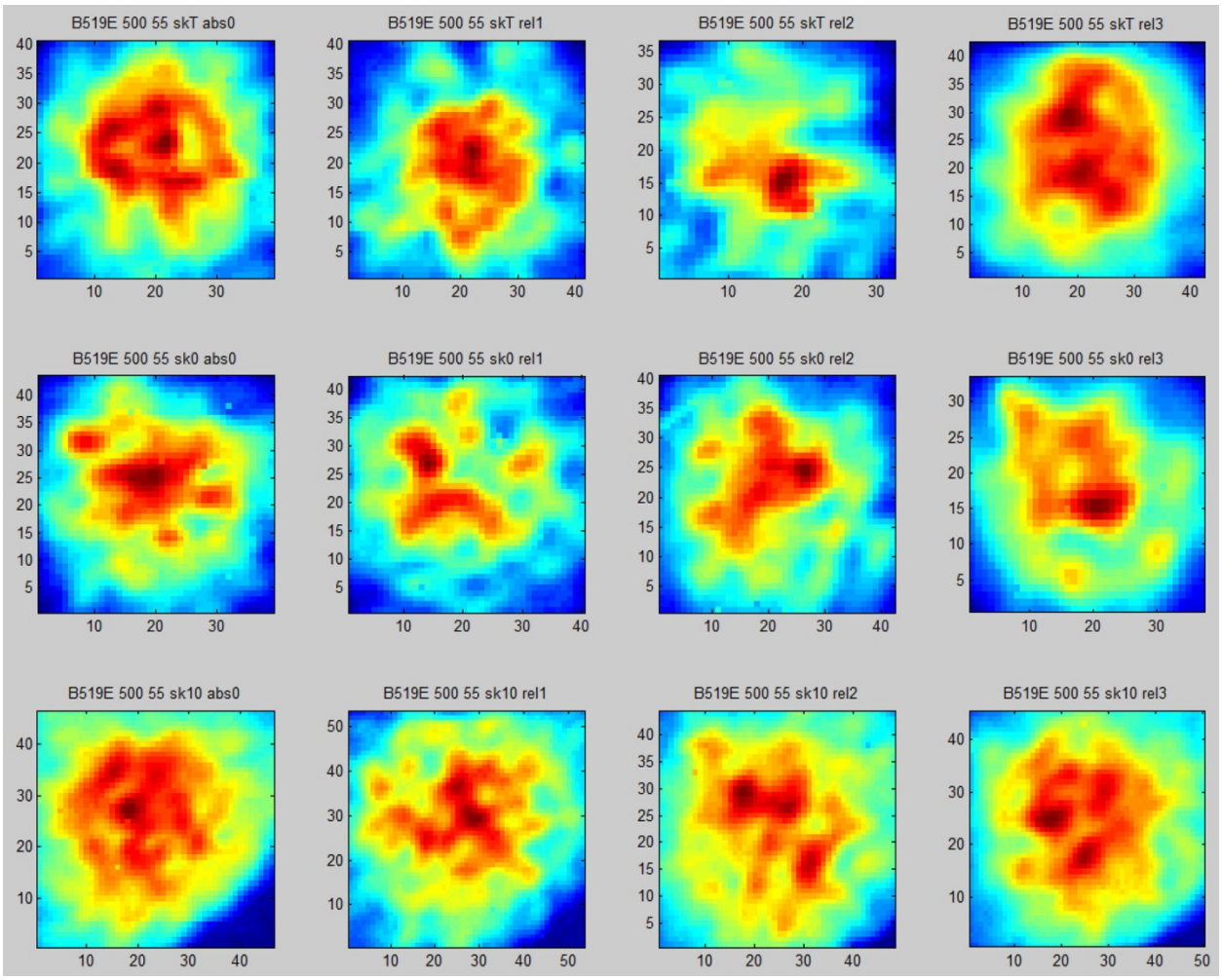

Figure B.7. Frequency 0.5 MHz, Specimen B519E, Refracted Angle 55 degrees, Cuts 0-3 Left to Right and SkT, Sk0, and Sk10 Top to Bottom

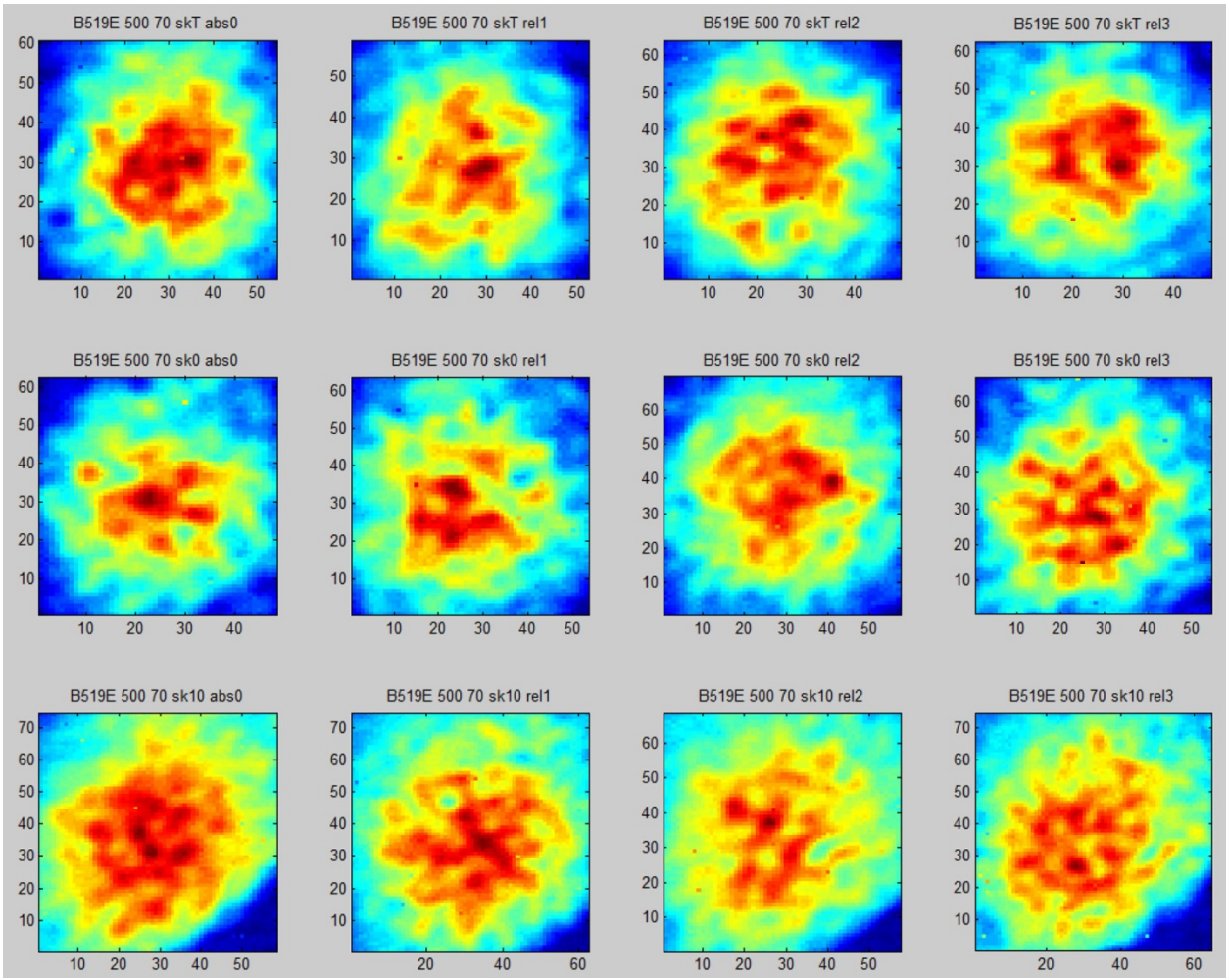

Figure B.8. Frequency 0.5 MHz, Specimen B519E, Refracted Angle 70 degrees, Cuts 0-3 Left to Right and SkT, Sk0, and Sk10 Top to Bottom

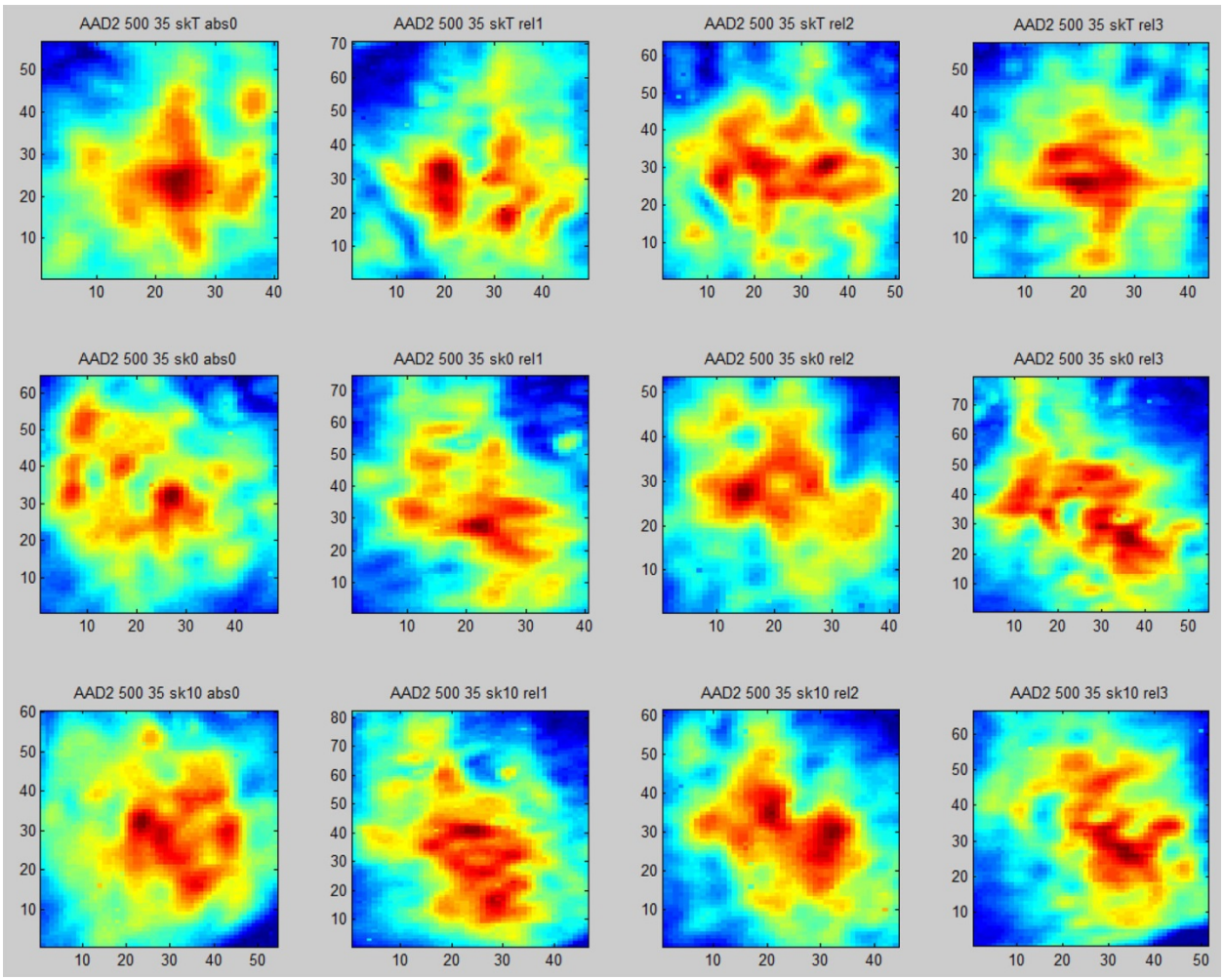

Figure B.9. Frequency 0.5 MHz, Specimen AAD2, Refracted Angle 35 degrees, Cuts 0-3 Left to Right and SkT, Sk0, and Sk10 Top to Bottom

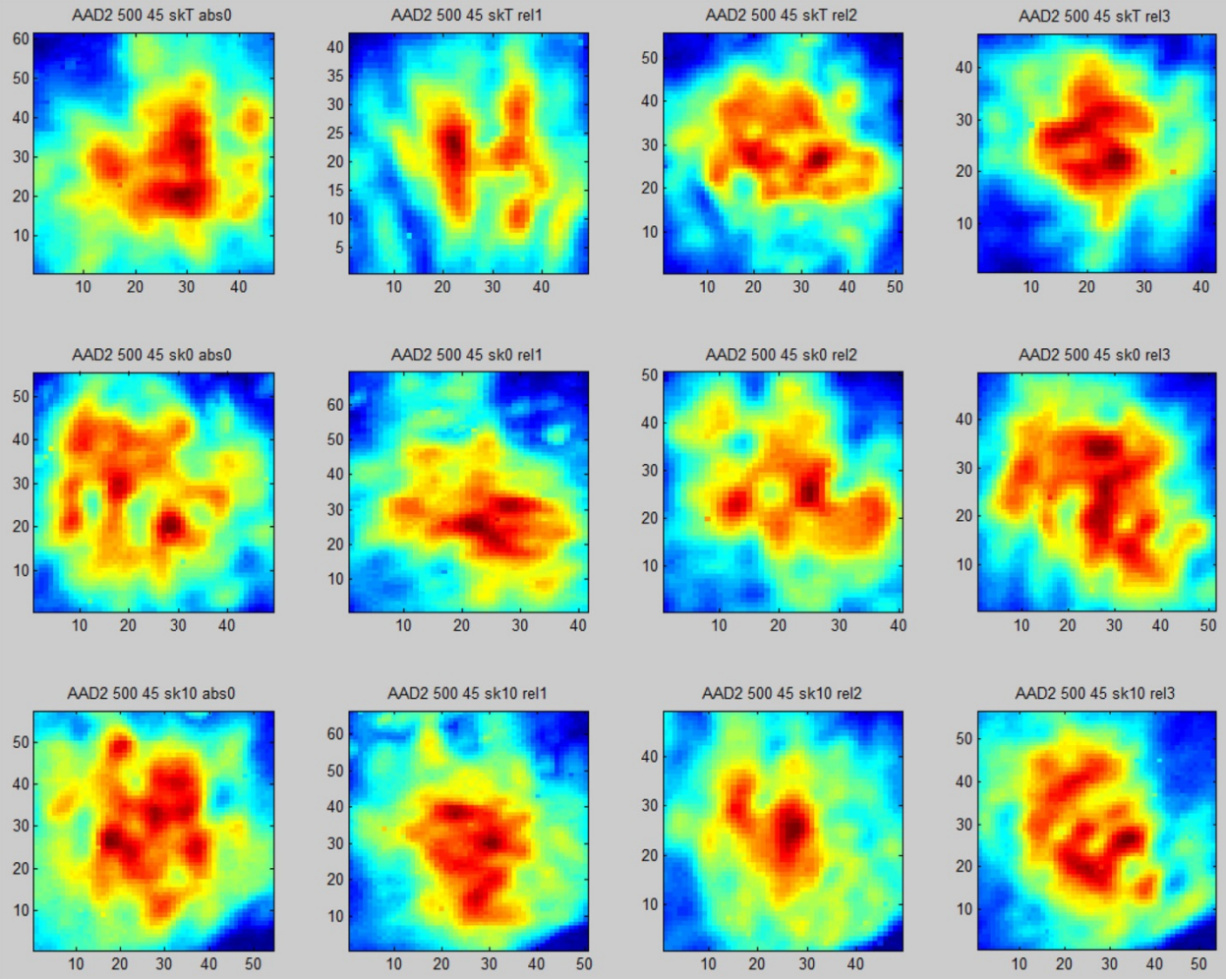

Figure B.10. Frequency 0.5 MHz, Specimen AAD2, Refracted Angle 45 degrees, Cuts 0-3 Left to Right and SkT, Sk0, and Sk10 Top to Bottom

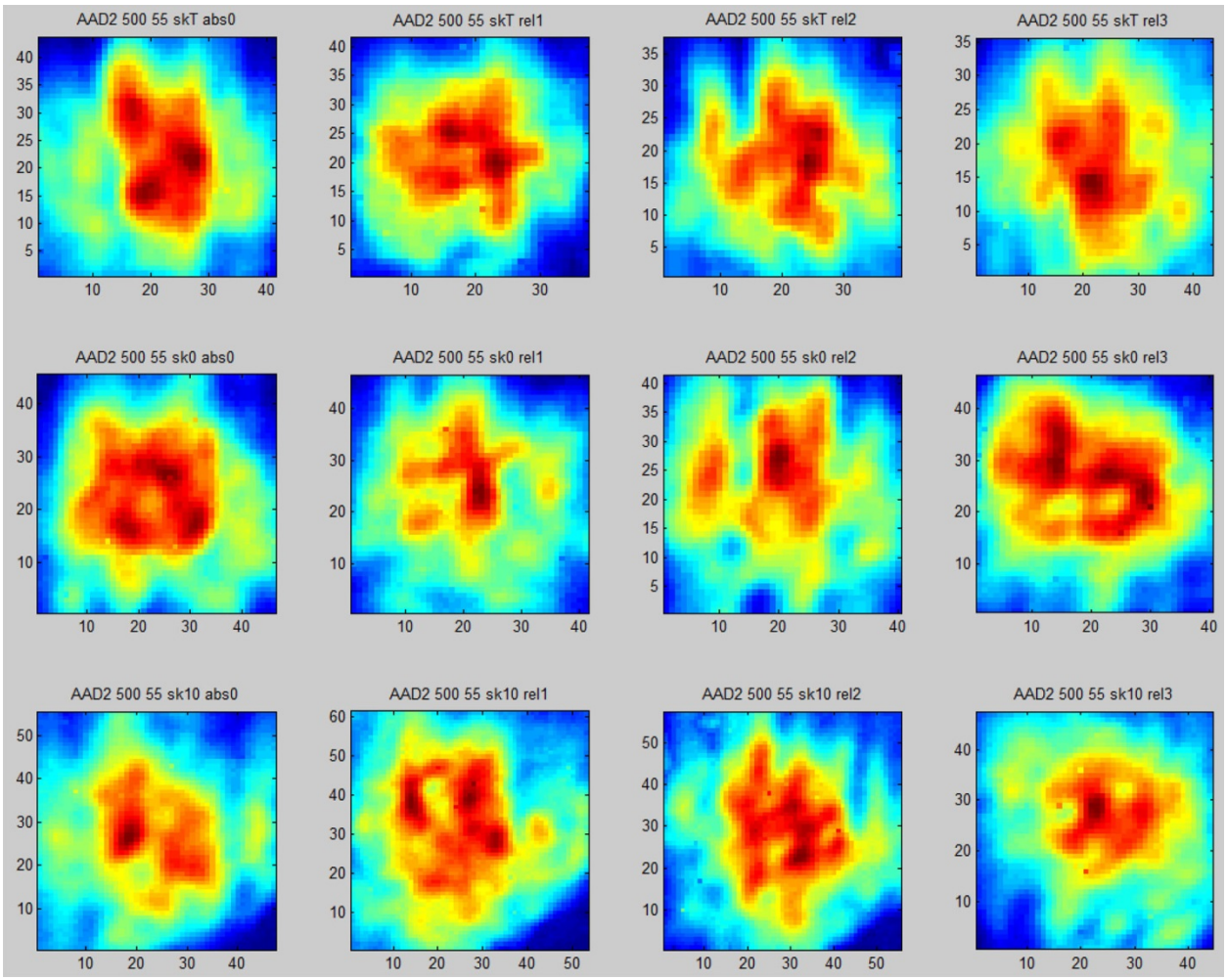

Figure B.11. Frequency 0.5 MHz, Specimen AAD2, Refracted Angle 55 degrees, Cuts 0-3 Left to Right and SkT, Sk0, and Sk10 Top to Bottom

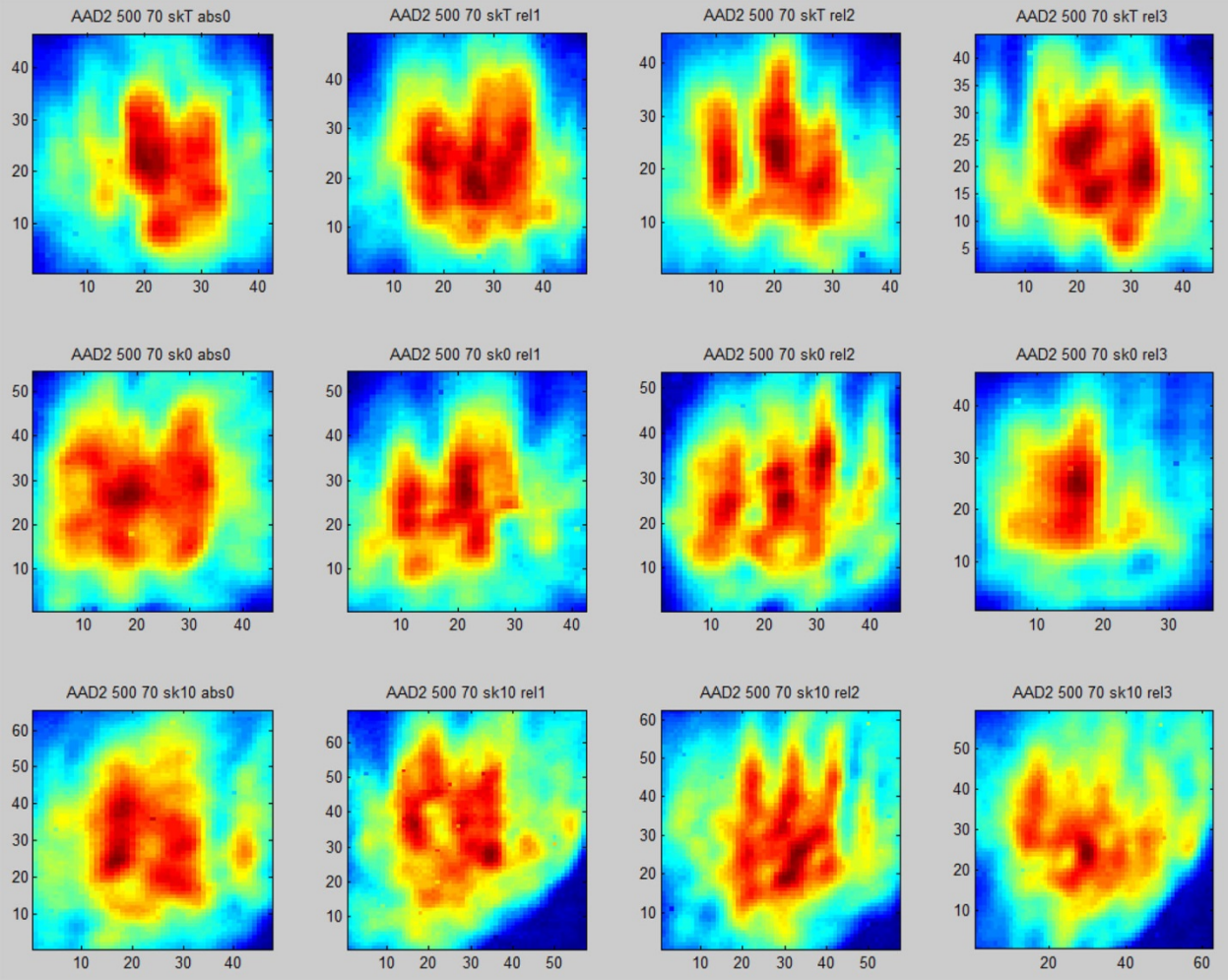

Figure B.12. Frequency 0.5 MHz, Specimen AAD2, Refracted Angle 70 degrees, Cuts 0-3 Left to Right and SkT, Sk0, and Sk10 Top to Bottom

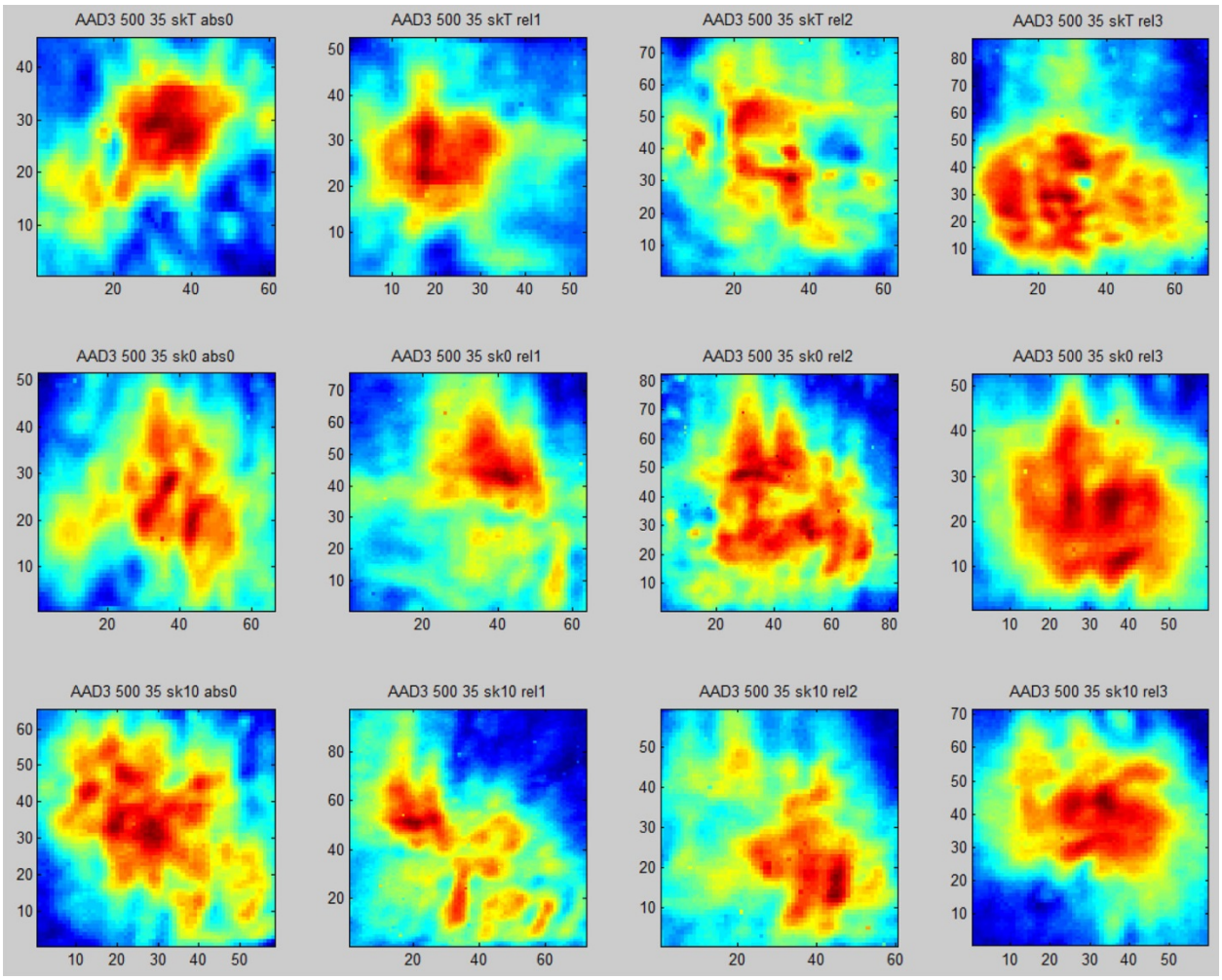

Figure B.13. Frequency 0.5 MHz, Specimen AAD3, Refracted Angle 35 degrees, Cuts 0-3 Left to Right and SkT, Sk0, and Sk10 Top to Bottom

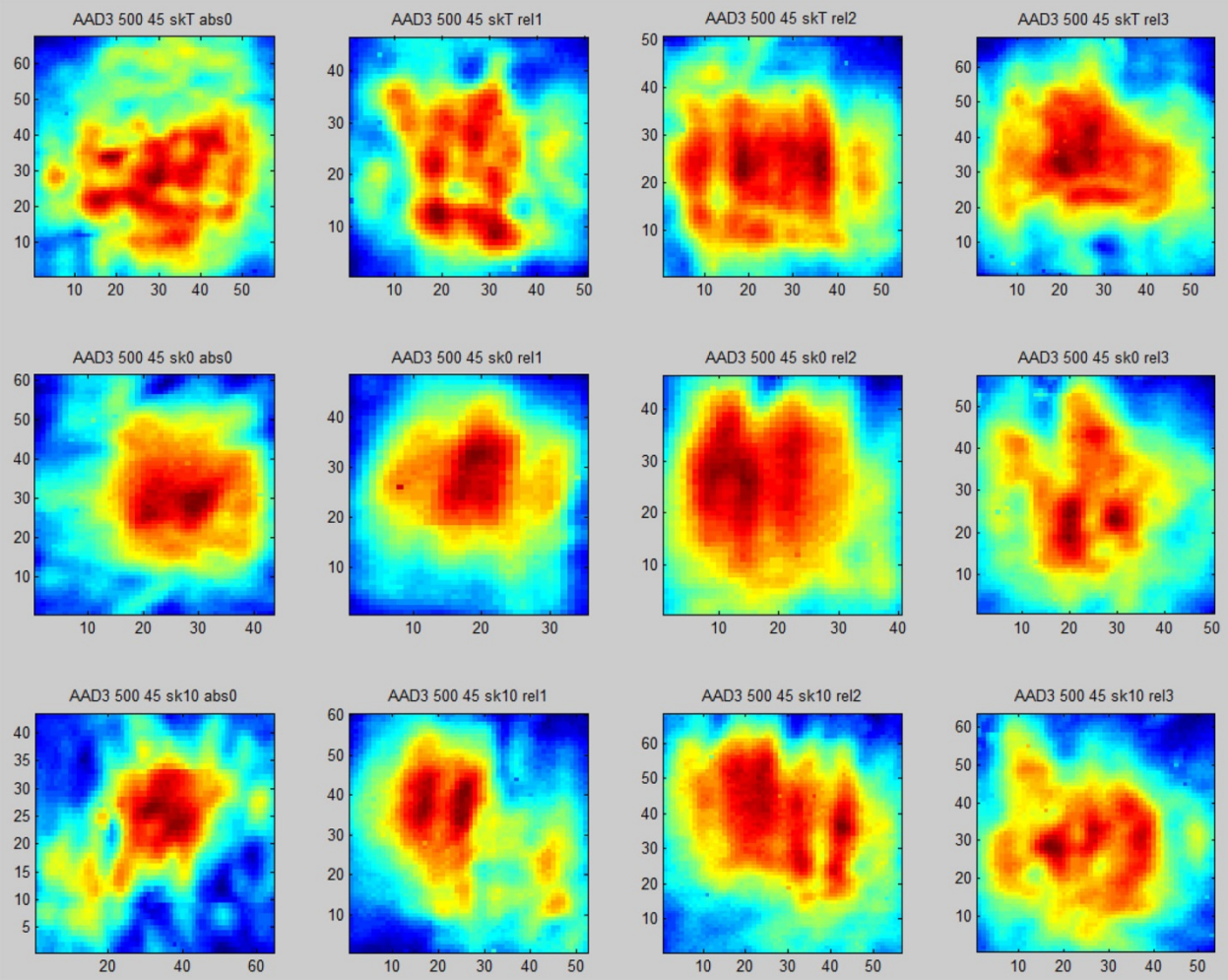

Figure B.14. Frequency 0.5 MHz, Specimen AAD3, Refracted Angle 45 degrees, Cuts 0-3 Left to Right and SkT, Sk0, and Sk10 Top to Bottom

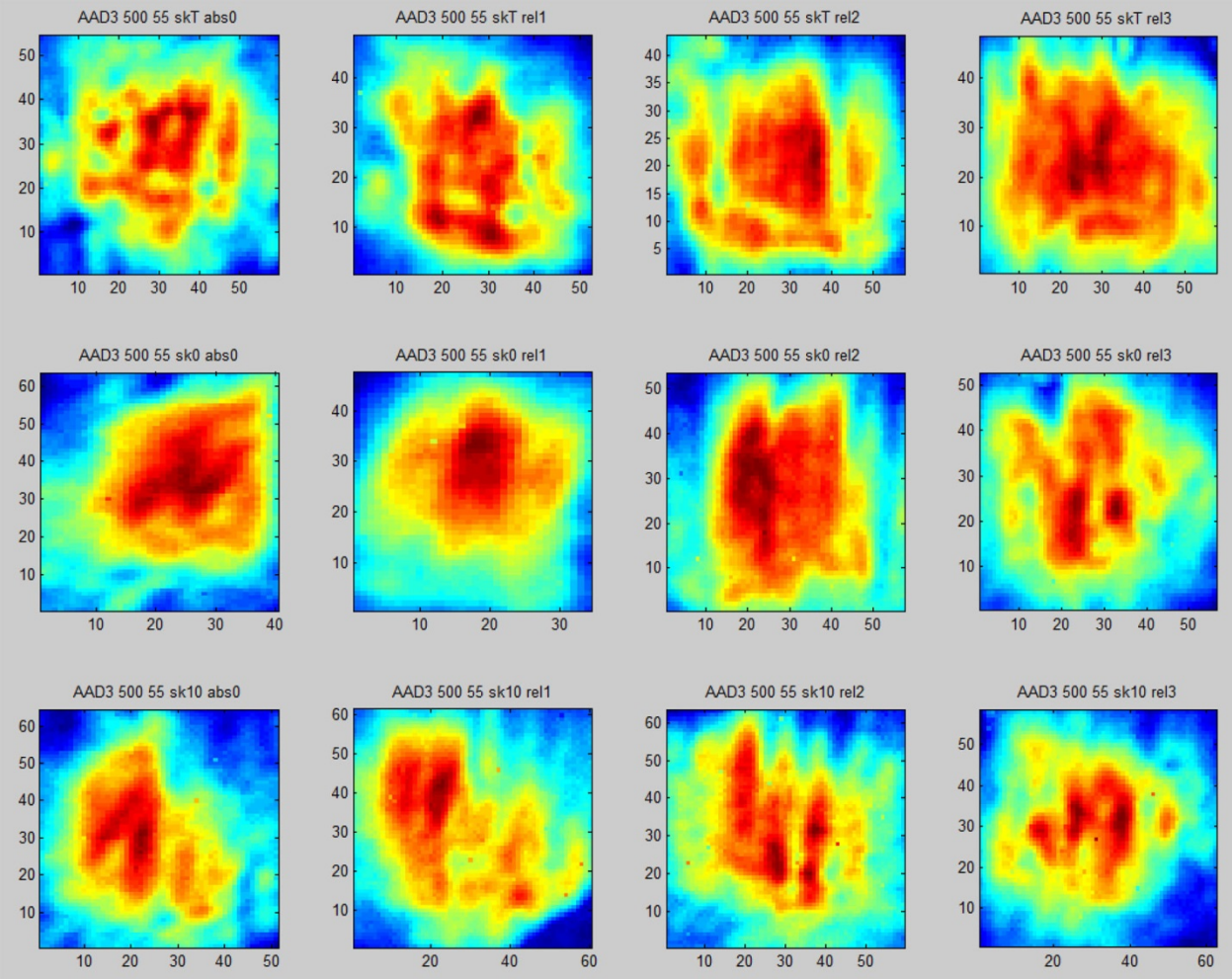

Figure B.15. Frequency 0.5 MHz, Specimen AAD3, Refracted Angle 55 degrees, Cuts 0-3 Left to Right and SkT, Sk0, and Sk10 Top to Bottom

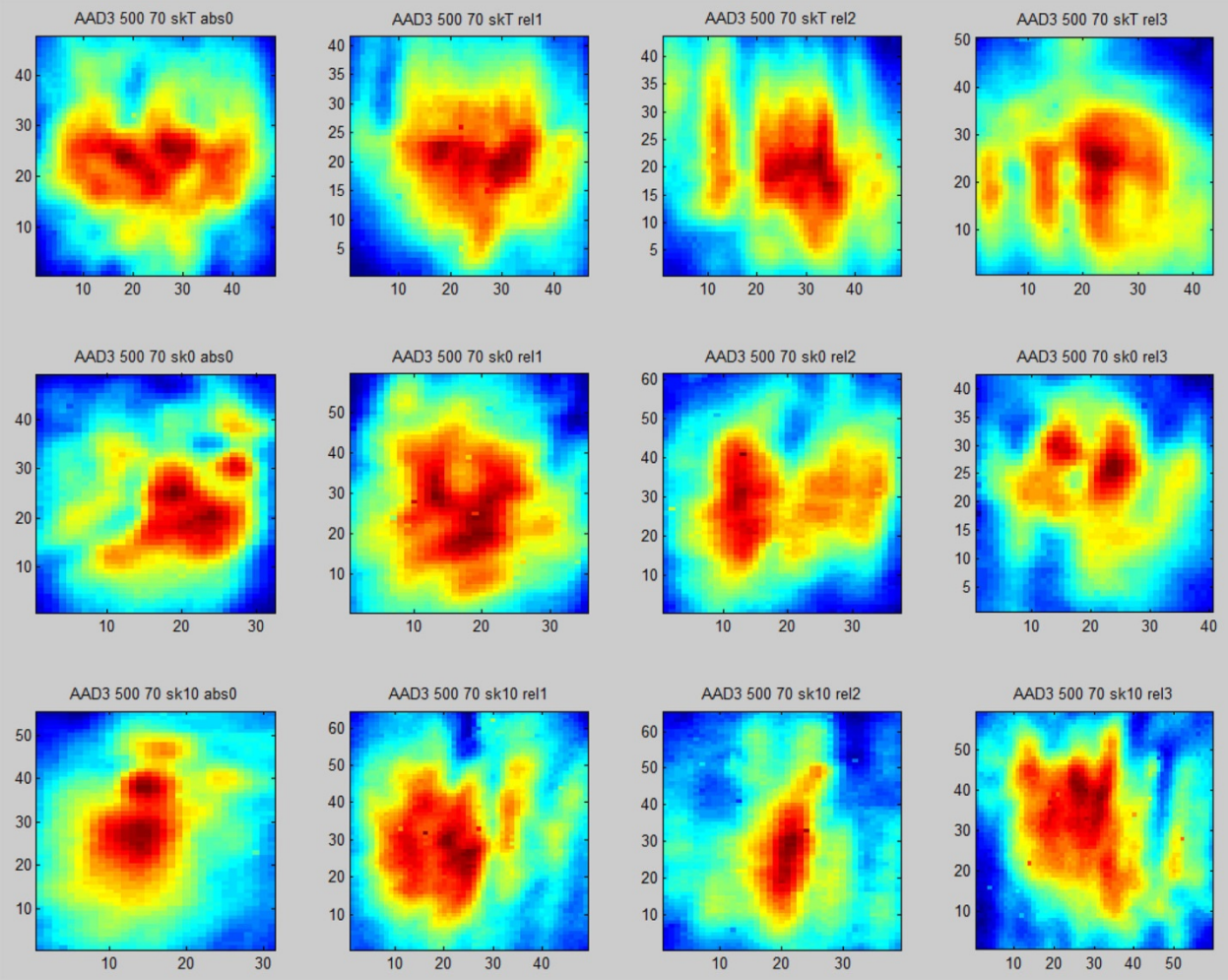

Figure B.16. Frequency 0.5 MHz, Specimen AAD3, Refracted Angle 70 degrees, Cuts 0-3 Left to Right and SkT, Sk0, and Sk10 Top to Bottom

B.2 Frequency 0.8 MHz (B.17-32)

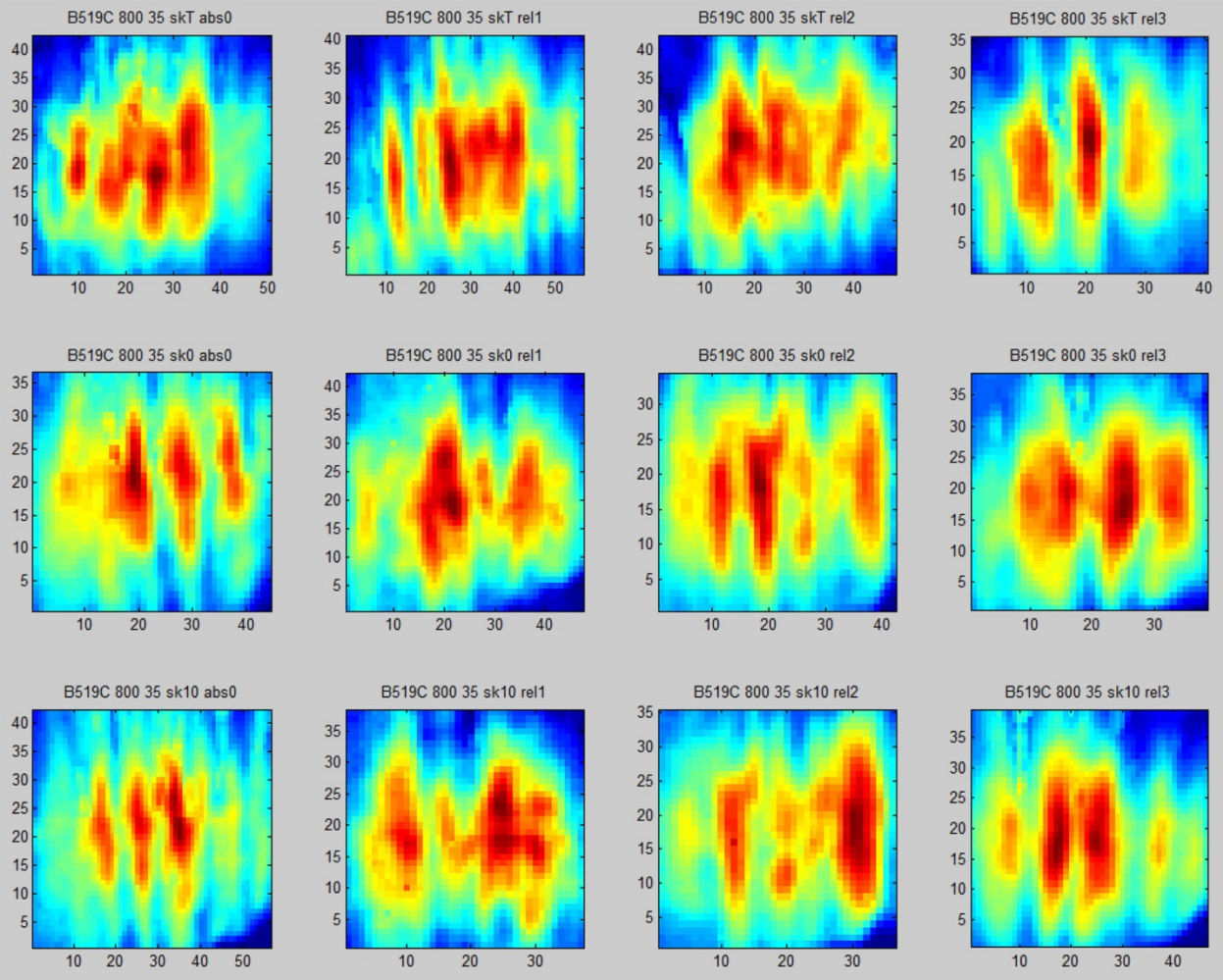

Figure B.17. Frequency 0.8 MHz, Specimen B519C, Refracted Angle 35 degrees, Cuts 0-3 Left to Right and SkT, Sk0, and Sk10 Top to Bottom

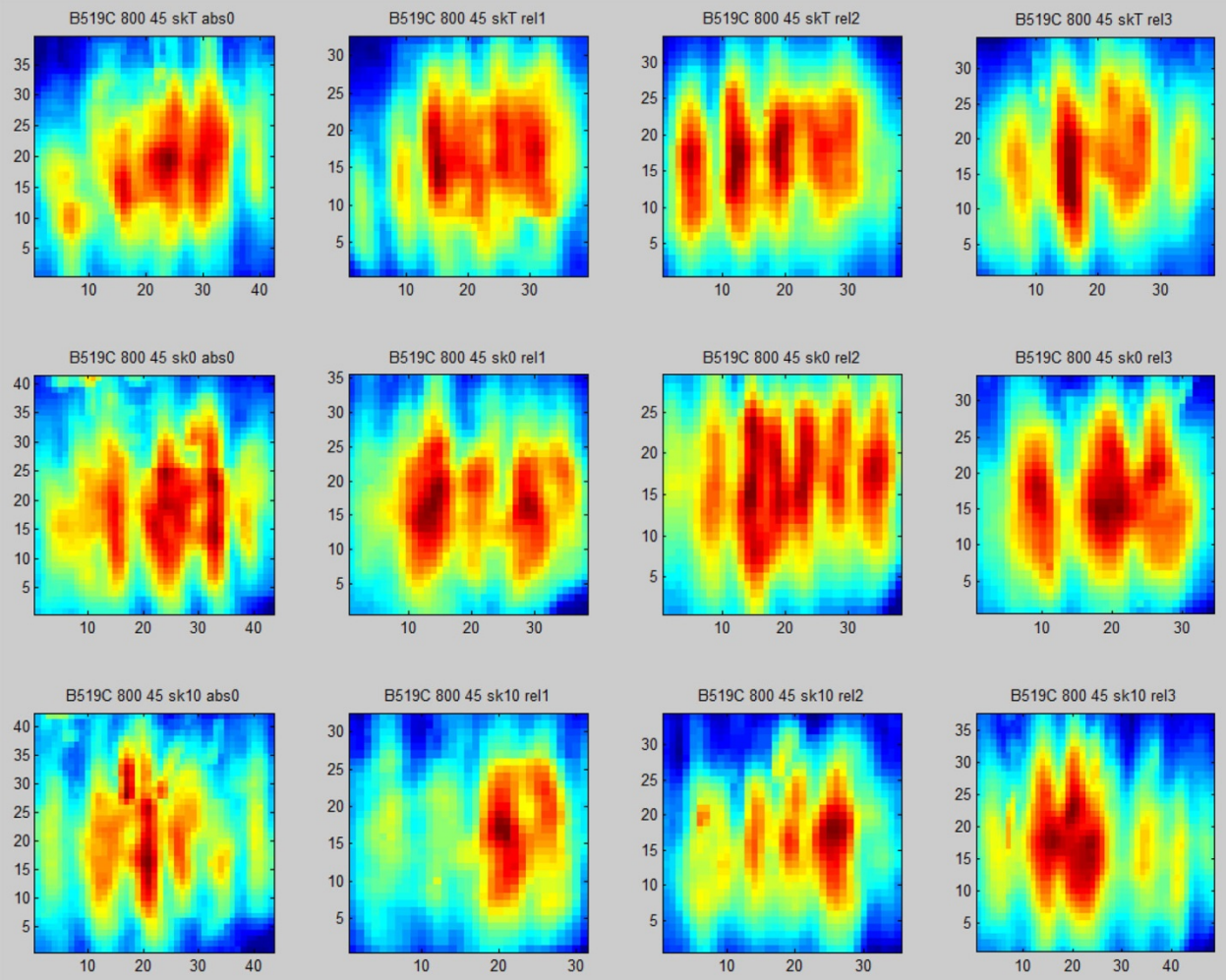

Figure B.18. Frequency 0.8 MHz, Specimen B519C, Refracted Angle 45 degrees, Cuts 0-3 Left to Right and SkT, Sk0, and Sk10 Top to Bottom

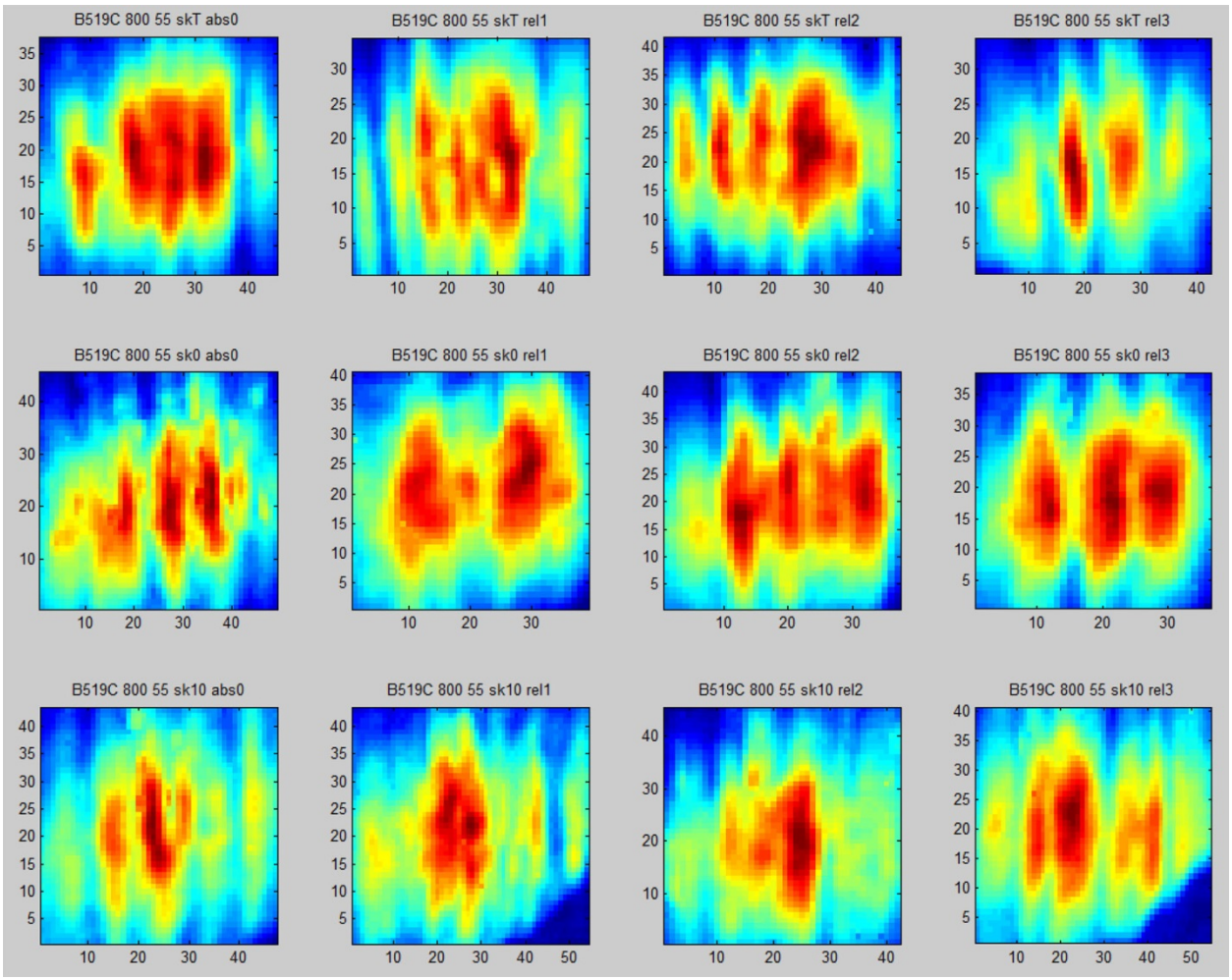

Figure B.19. Frequency 0.8 MHz, Specimen B519C, Refracted Angle 55 degrees, Cuts 0-3 Left to Right and SkT, Sk0, and Sk10 Top to Bottom

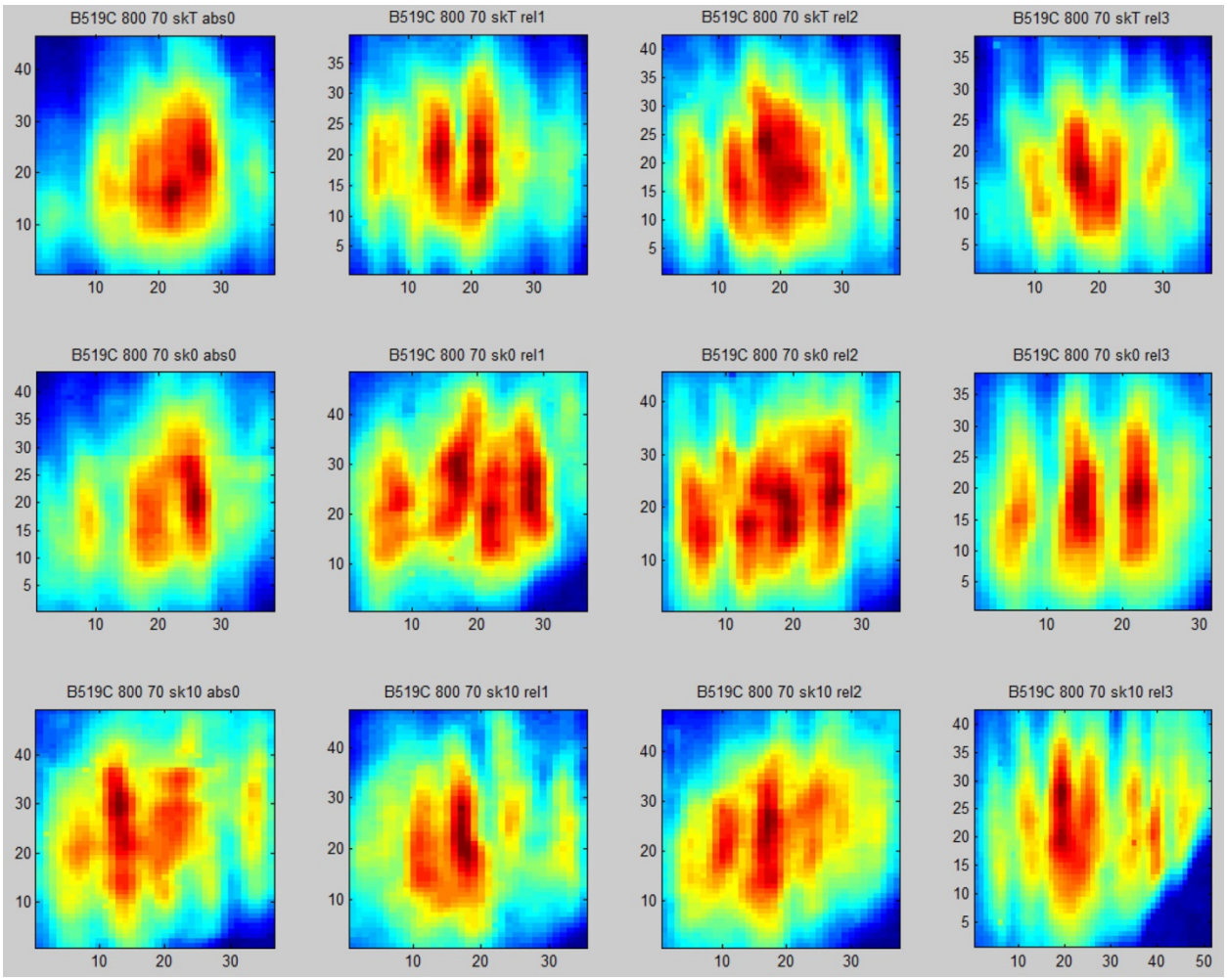

Figure B.20. Frequency 0.8 MHz, Specimen B519C, Refracted Angle 70 degrees, Cuts 0-3 Left to Right and SkT, Sk0, and Sk10 Top to Bottom

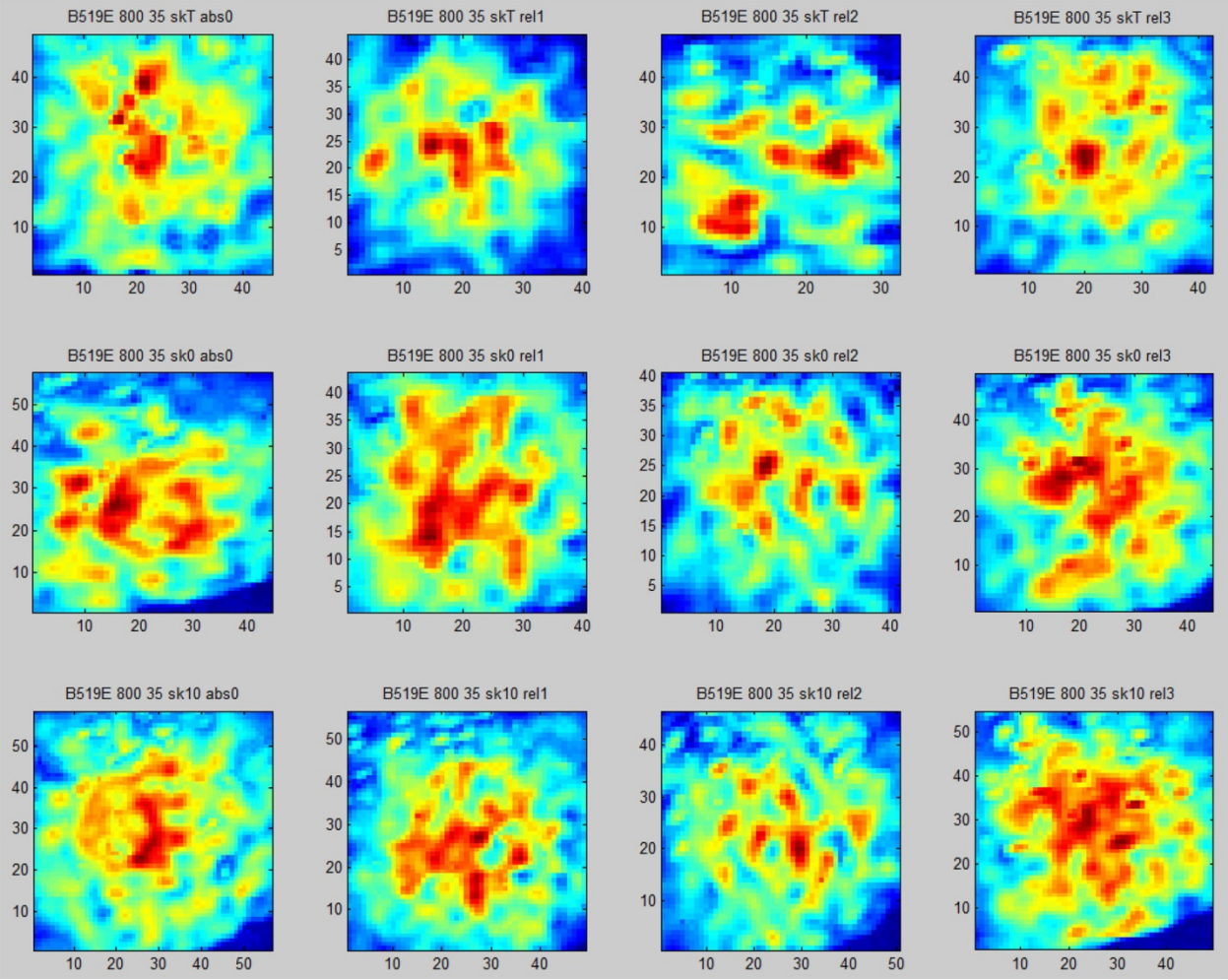

Figure B.21. Frequency 0.8 MHz, Specimen B519E, Refracted Angle 35 degrees, Cuts 0-3 Left to Right and SkT, Sk0, and Sk10 Top to Bottom

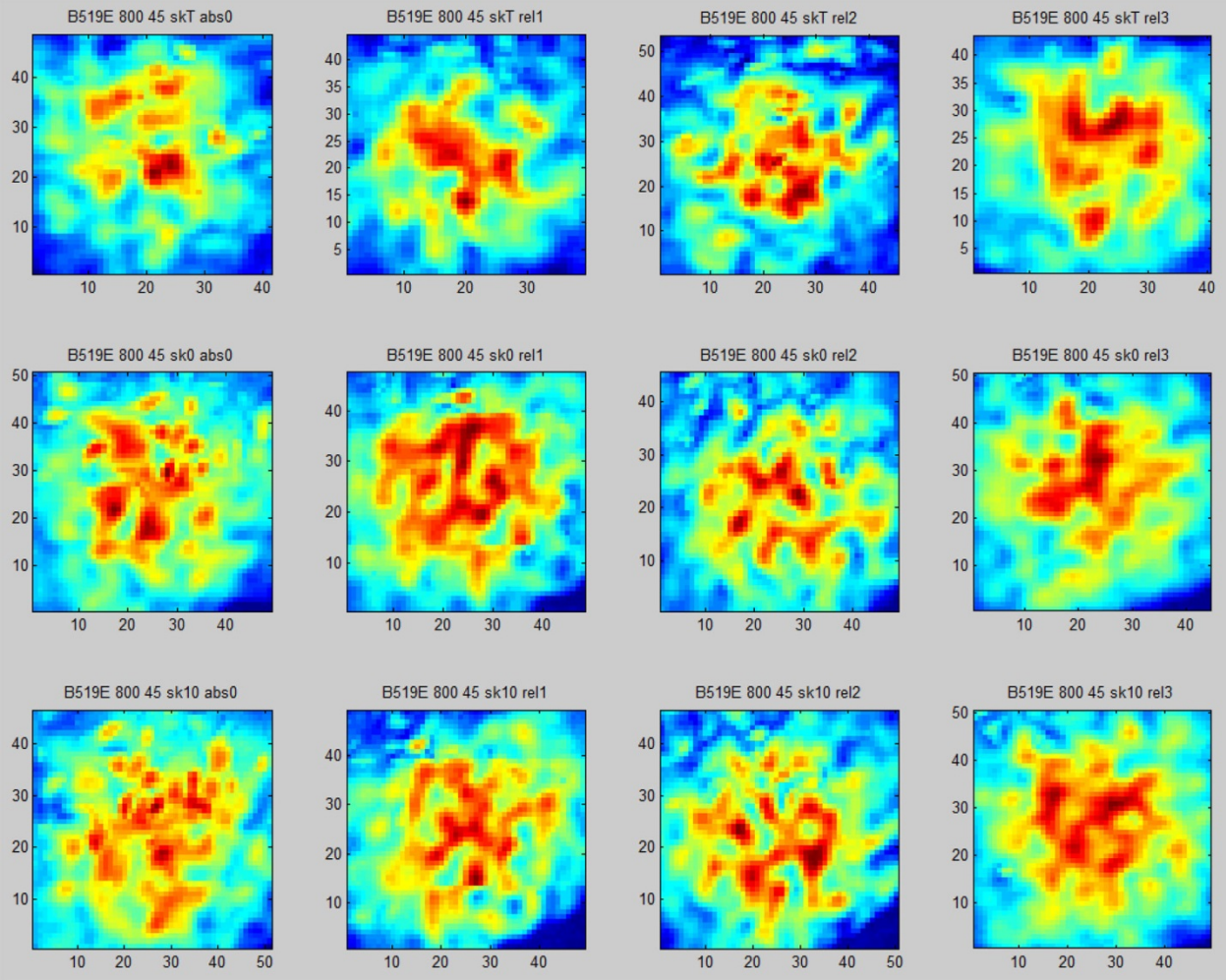

Figure B.22. Frequency 0.8 MHz, Specimen B519E, Refracted Angle 45 degrees, Cuts 0-3 Left to Right and SkT, Sk0, and Sk10 Top to Bottom

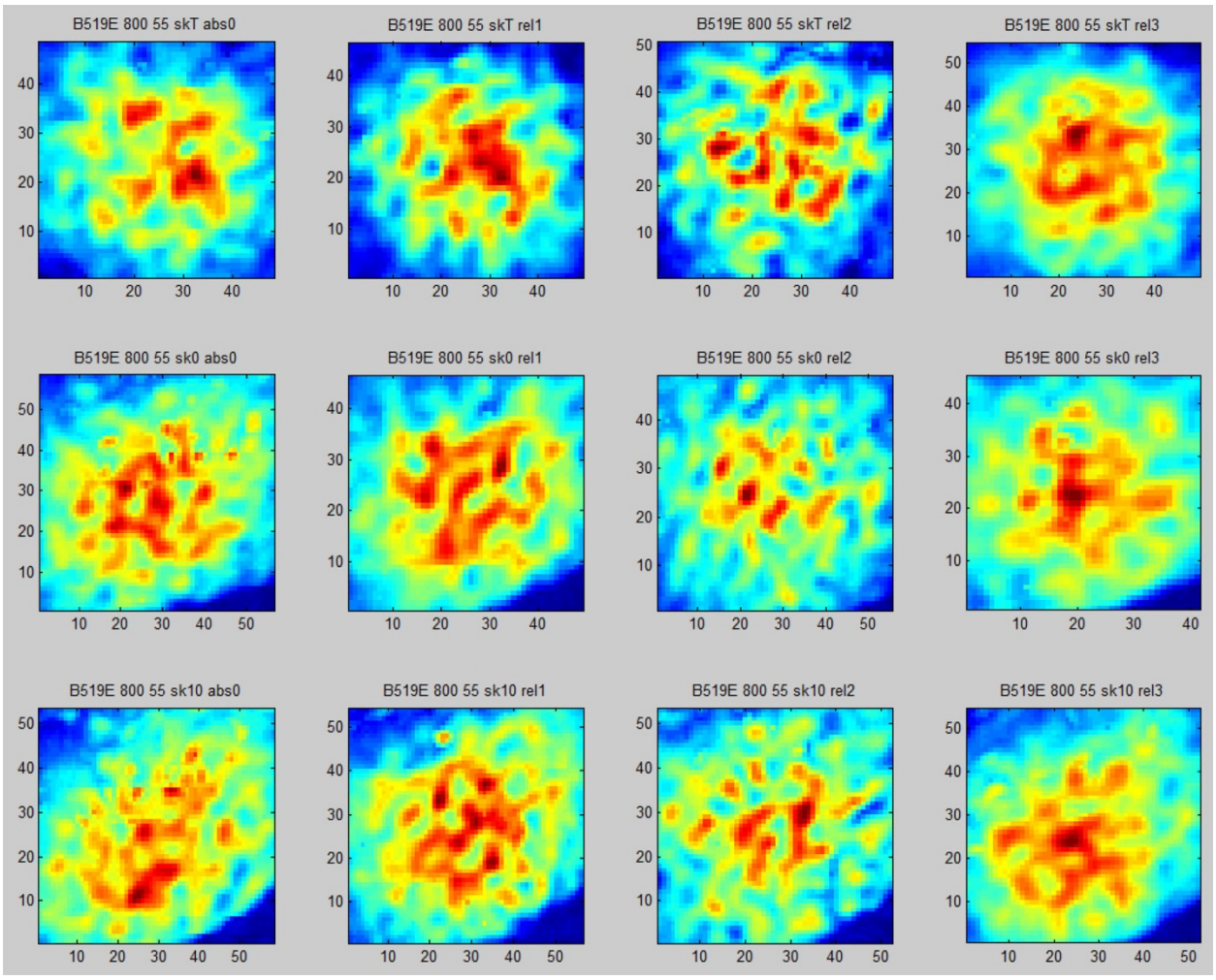

Figure B.23. Frequency 0.8 MHz, Specimen B519E, Refracted Angle 55 degrees, Cuts 0-3 Left to Right and SkT, Sk0, and Sk10 Top to Bottom

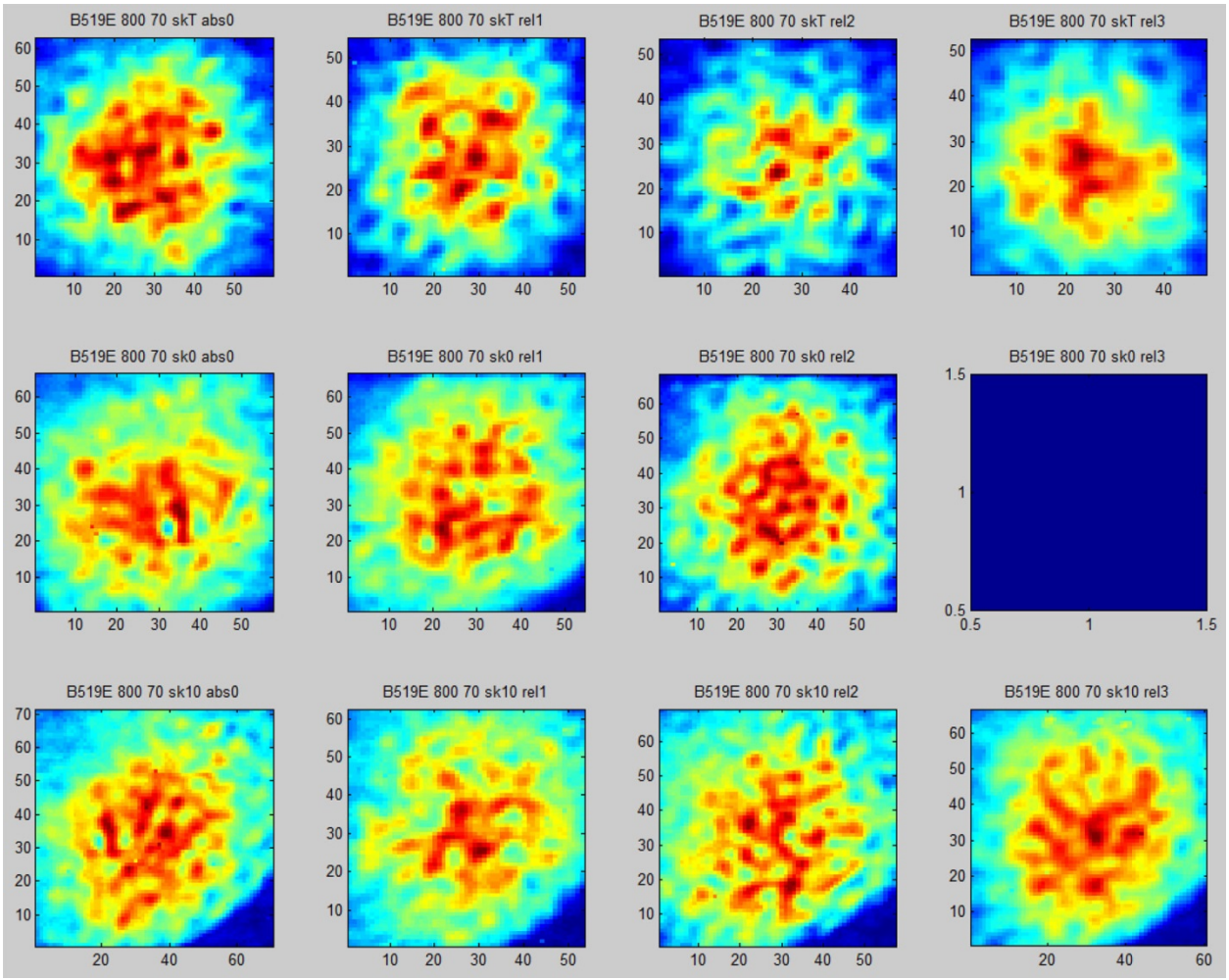

Figure B.24. Frequency 0.8 MHz, Specimen B519E, Refracted Angle 70 degrees, Cuts 0-3 Left to Right and SkT, Sk0, and Sk10 Top to Bottom

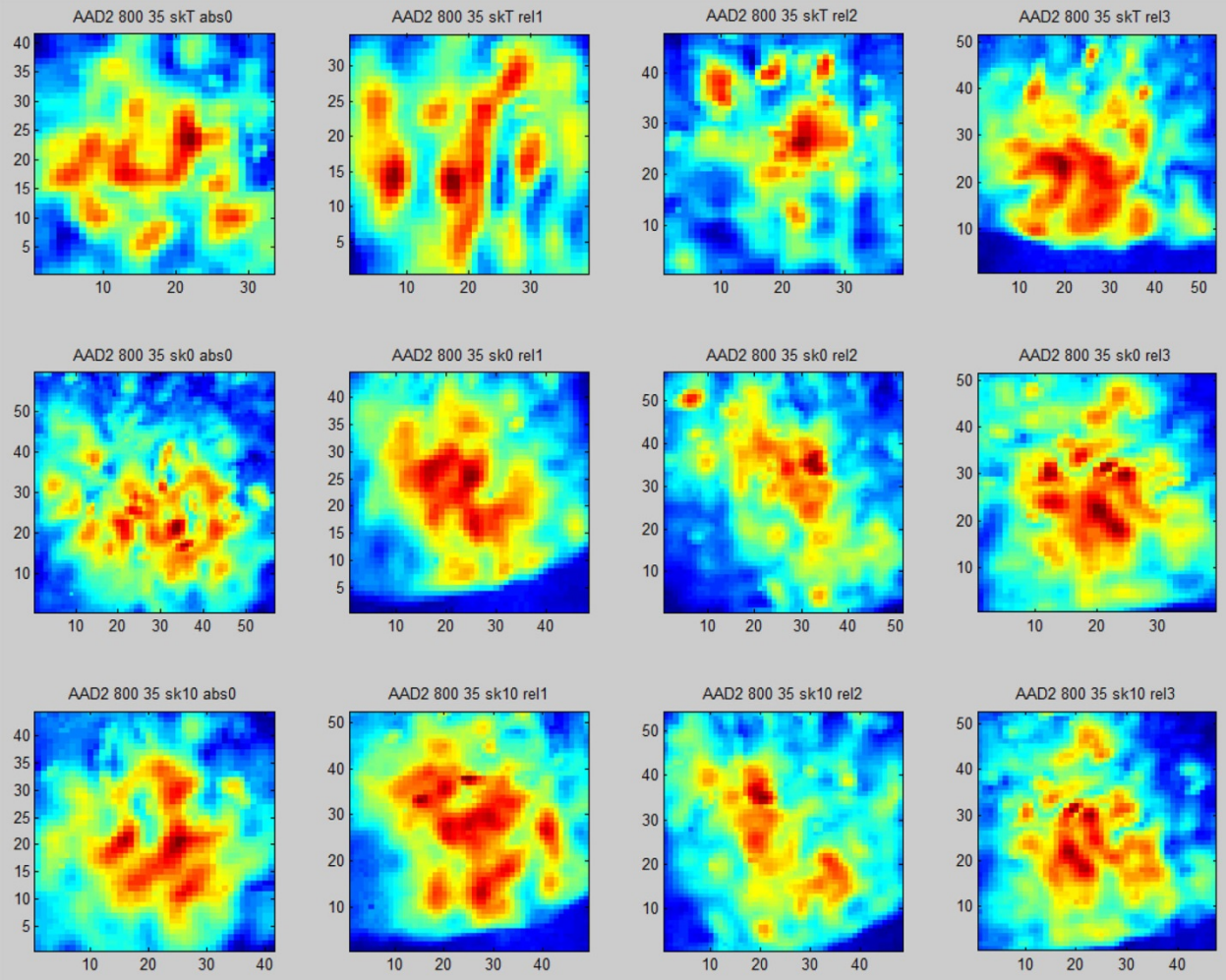

Figure B.25. Frequency 0.8 MHz, Specimen AAD2, Refracted Angle 35 degrees, Cuts 0-3 Left to Right and SkT, Sk0, and Sk10 Top to Bottom

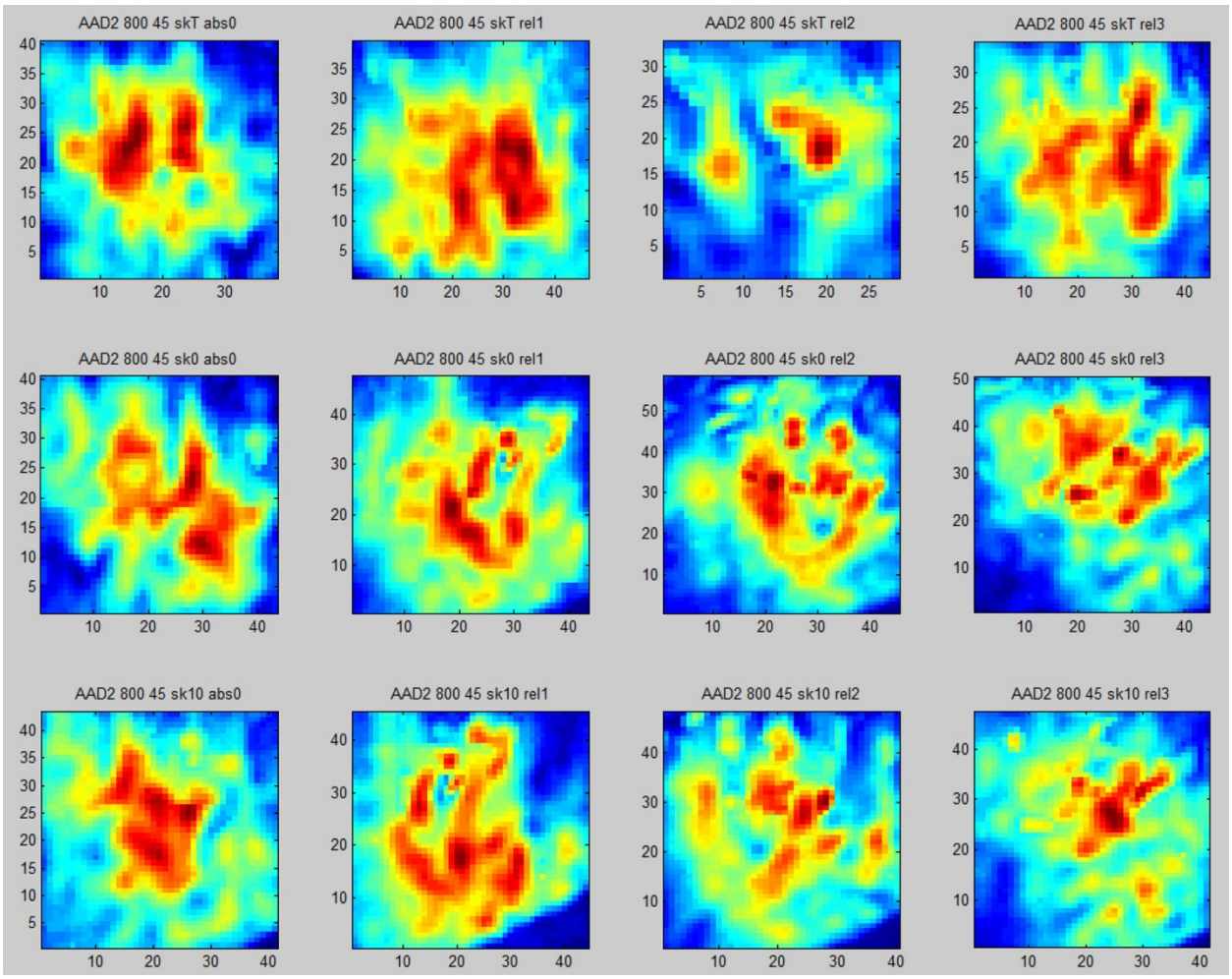

Figure B.26. Frequency 0.8 MHz, Specimen AAD2, Refracted Angle 45 degrees, Cuts 0-3 Left to Right and SkT, Sk0, and Sk10 Top to Bottom

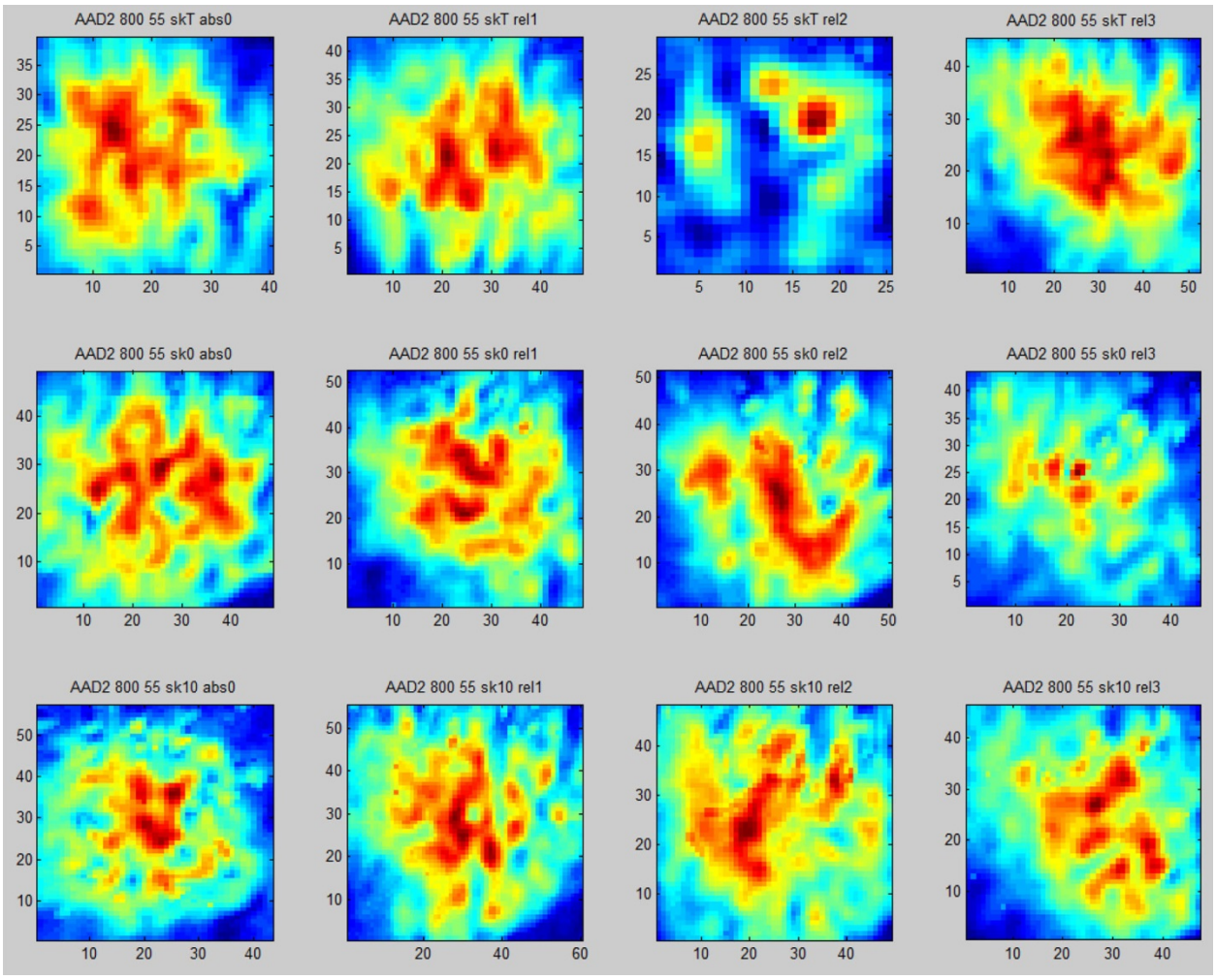

Figure B.27. Frequency 0.8 MHz, Specimen AAD2, Refracted Angle 55 degrees, Cuts 0-3 Left to Right and SkT, Sk0, and Sk10 Top to Bottom

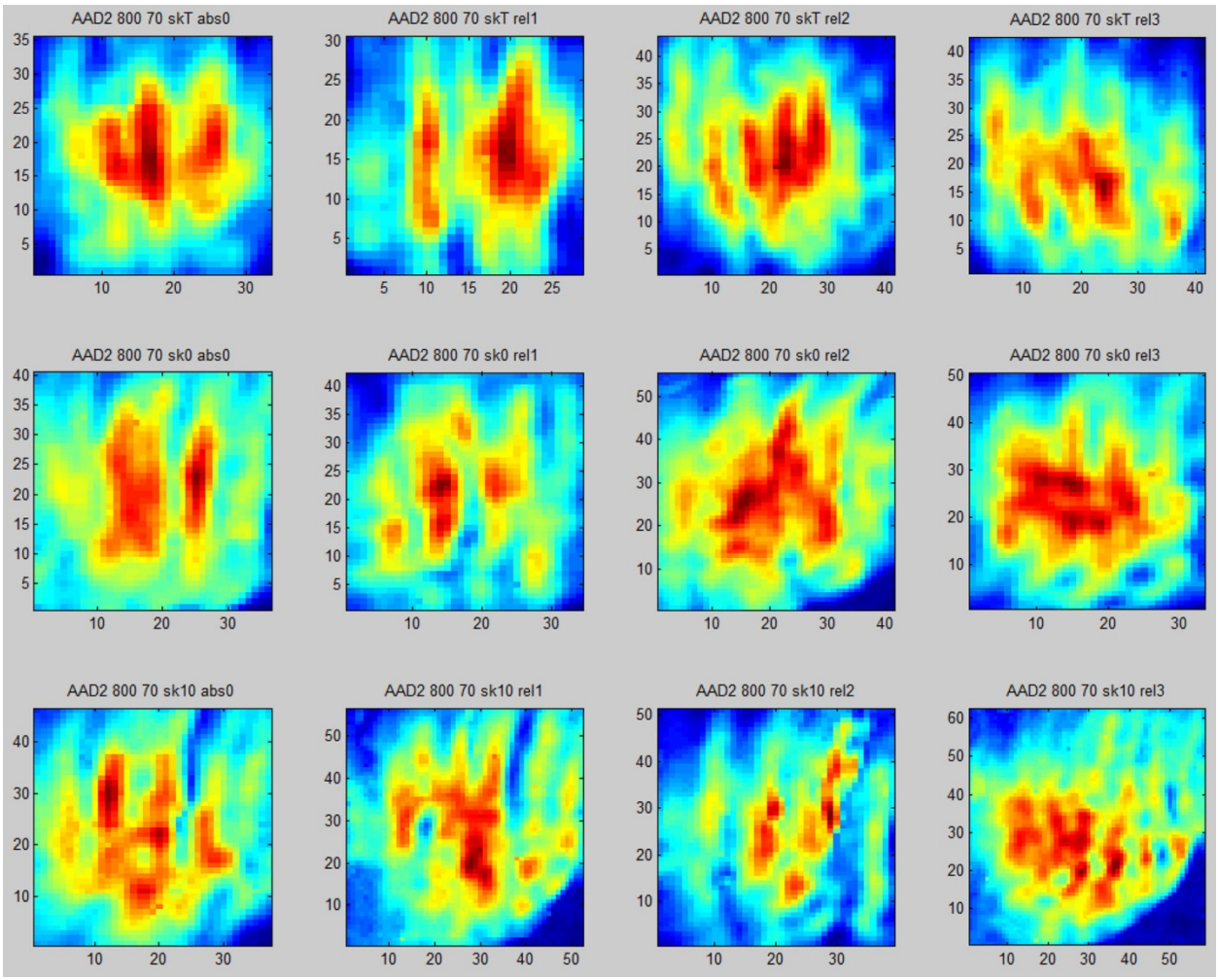

Figure B.28. Frequency 0.8 MHz, Specimen AAD2, Refracted Angle 70 degrees, Cuts 0-3 Left to Right and SkT, Sk0, and Sk10 Top to Bottom

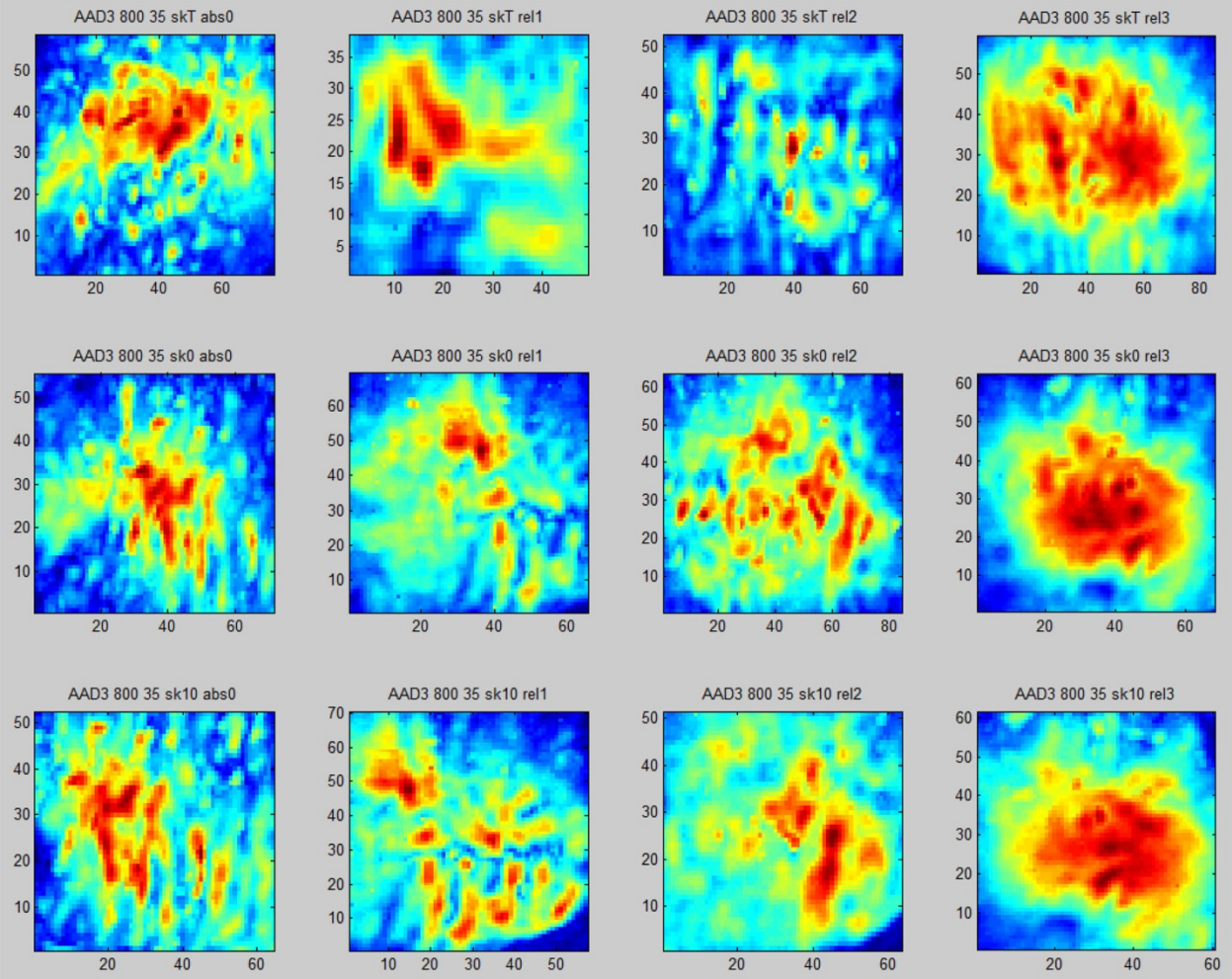

Figure B.29. Frequency 0.8 MHz, Specimen AAD3, Refracted Angle 35 degrees, Cuts 0-3 Left to Right and SkT, Sk0, and Sk10 Top to Bottom

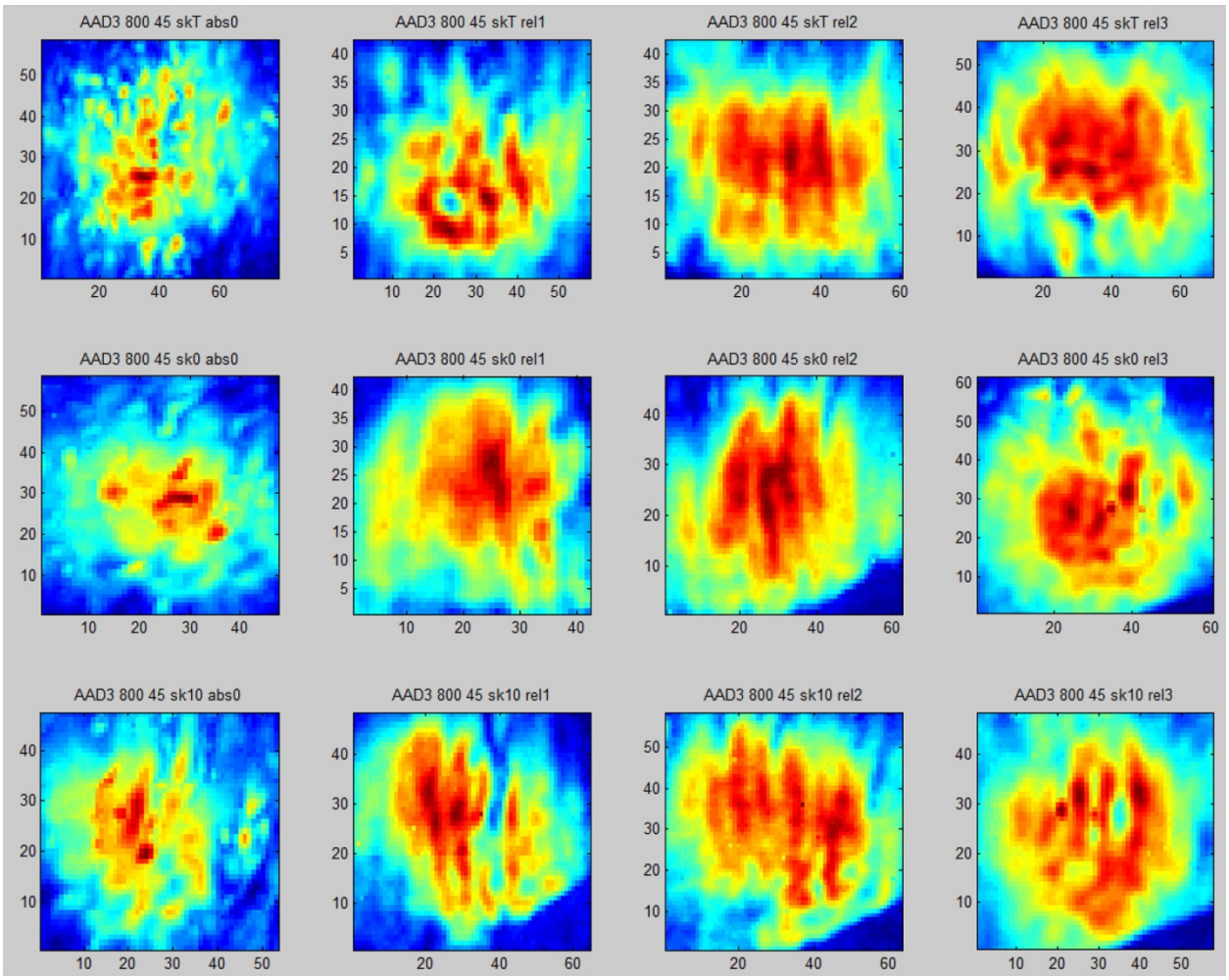

Figure B.30. Frequency 0.8 MHz, Specimen AAD3, Refracted Angle 45 degrees, Cuts 0-3 Left to Right and SkT, Sk0, and Sk10 Top to Bottom

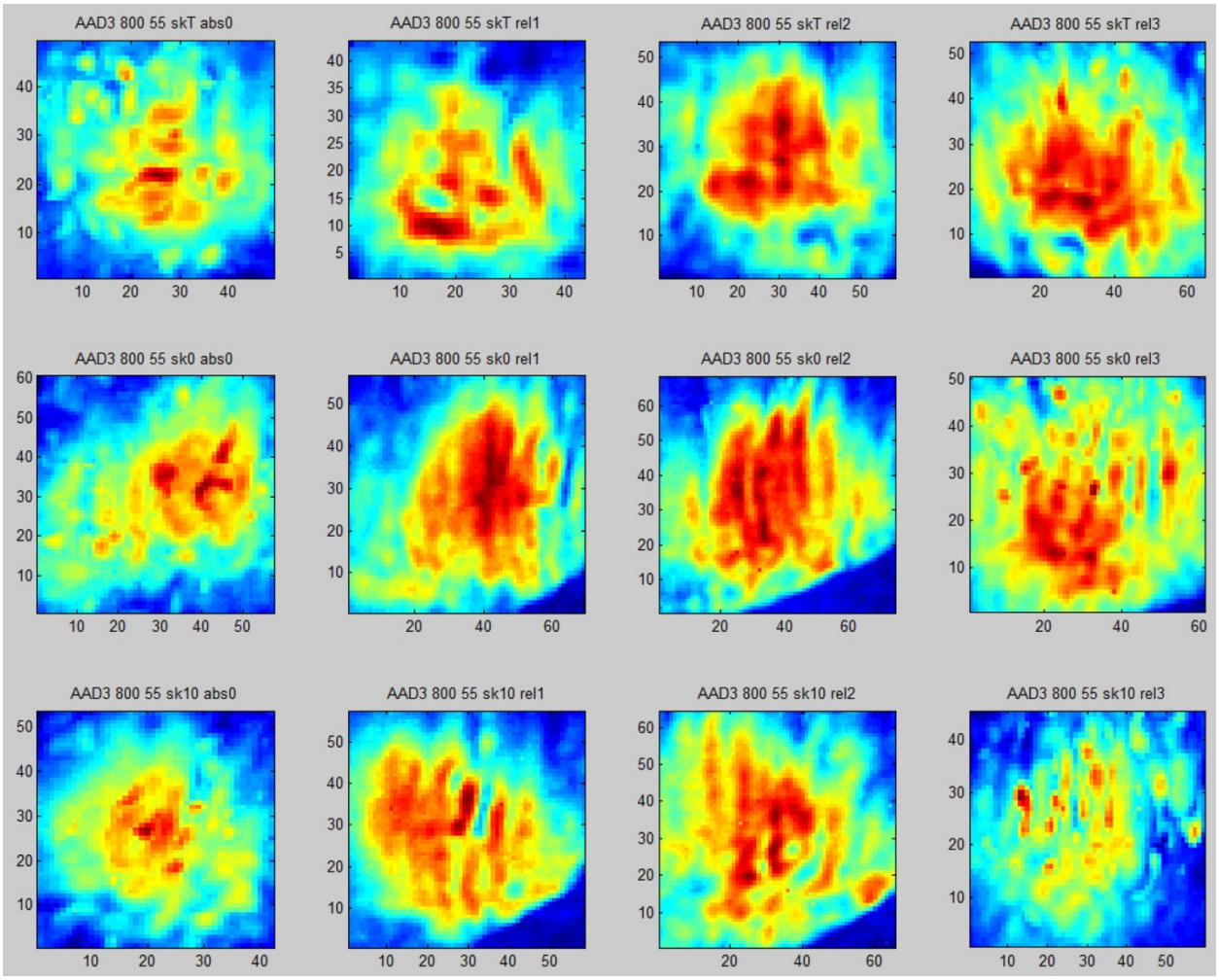

Figure B.31. Frequency 0.8 MHz, Specimen AAD3, Refracted Angle 55 degrees, Cuts 0-3 Left to Right and SkT, Sk0, and Sk10 Top to Bottom

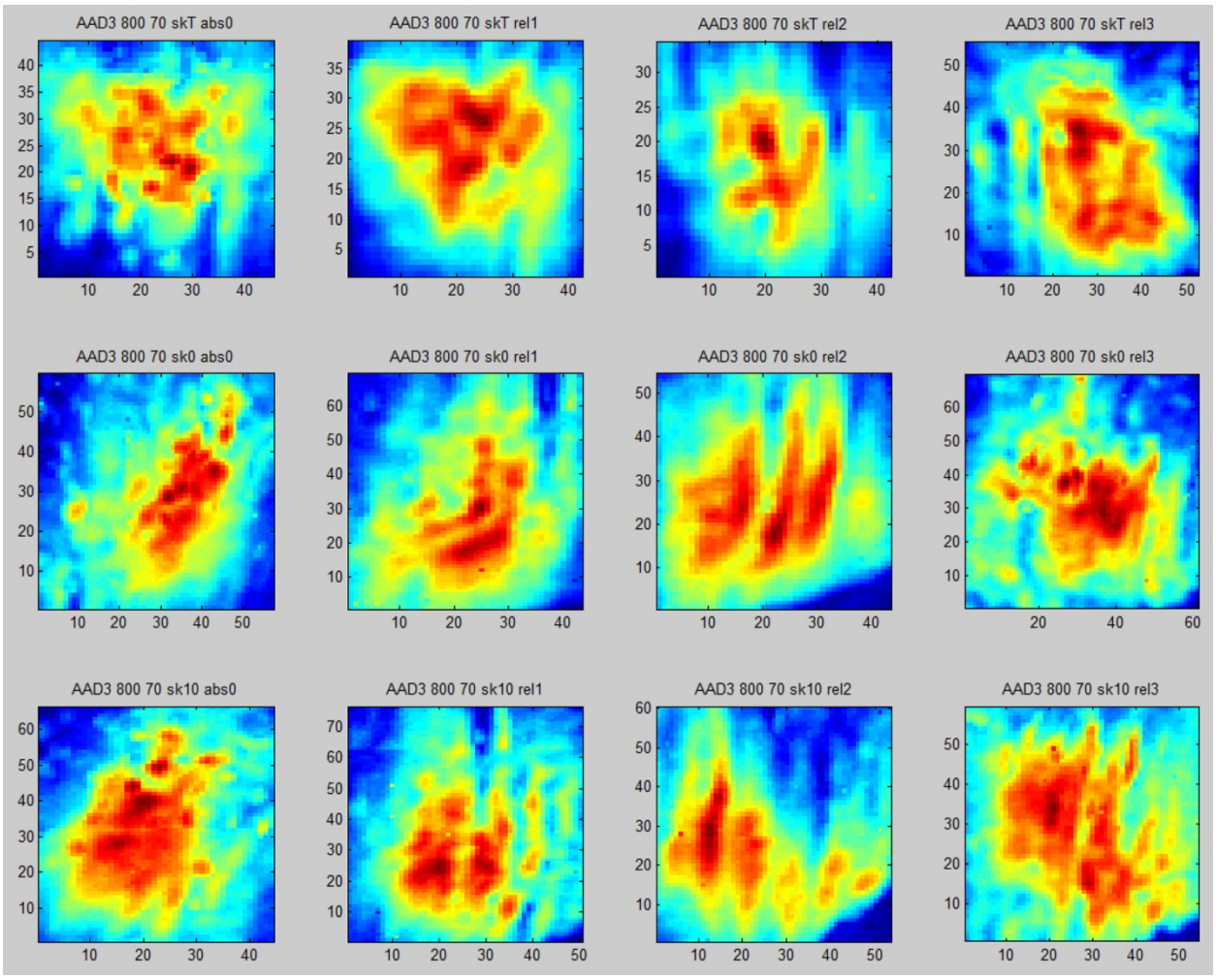

Figure B.32. Frequency 0.8 MHz, Specimen AAD3, Refracted Angle 70 degrees, Cuts 0-3 Left to Right and SkT, Sk0, and Sk10 Top to Bottom

B.3 Frequency 1.0 MHz (B.33-48)

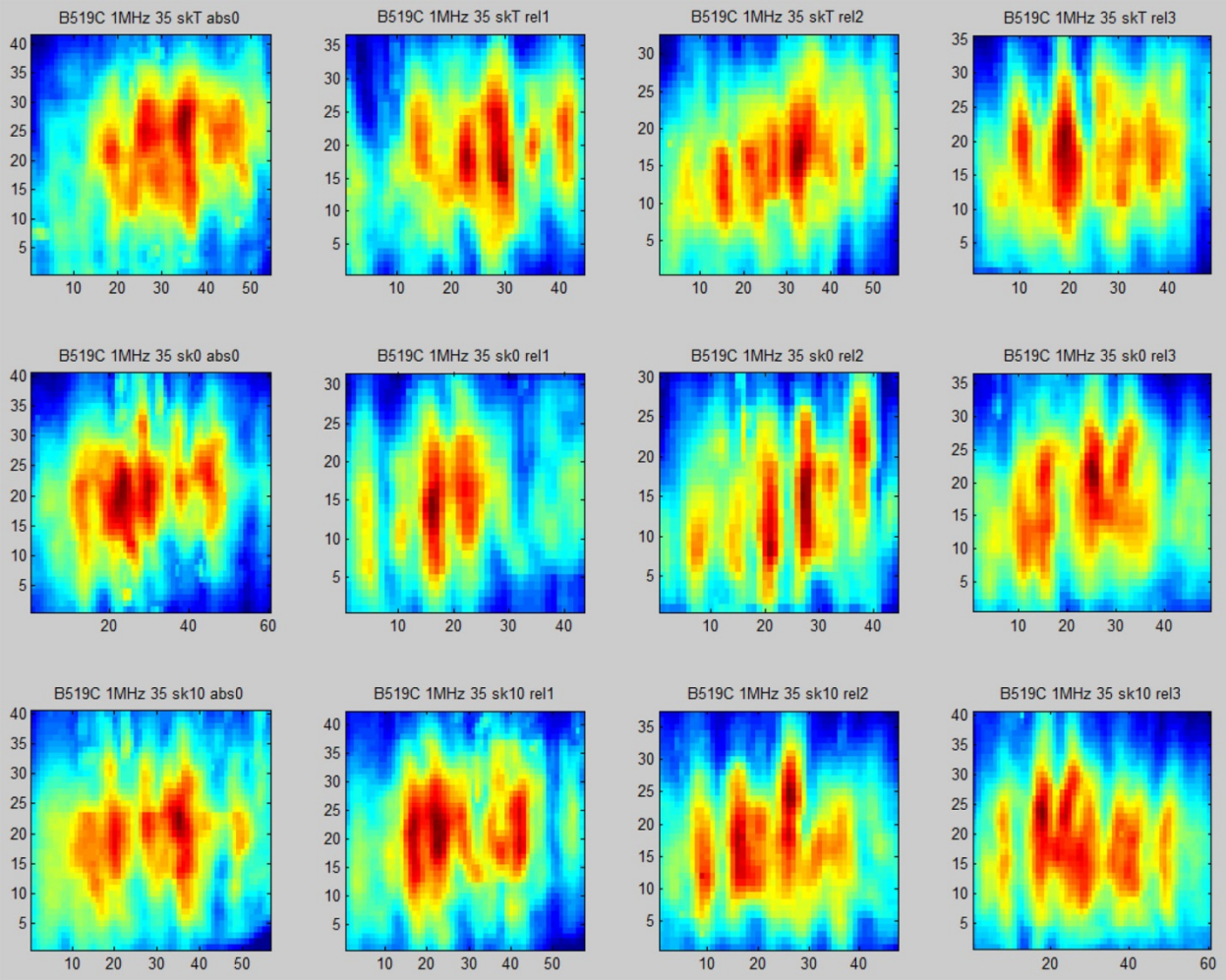

Figure B.33. Frequency 1.0 MHz, Specimen B519C, Refracted Angle 35 degrees, Cuts 0-3 Left to Right and SkT, Sk0, and Sk10 Top to Bottom

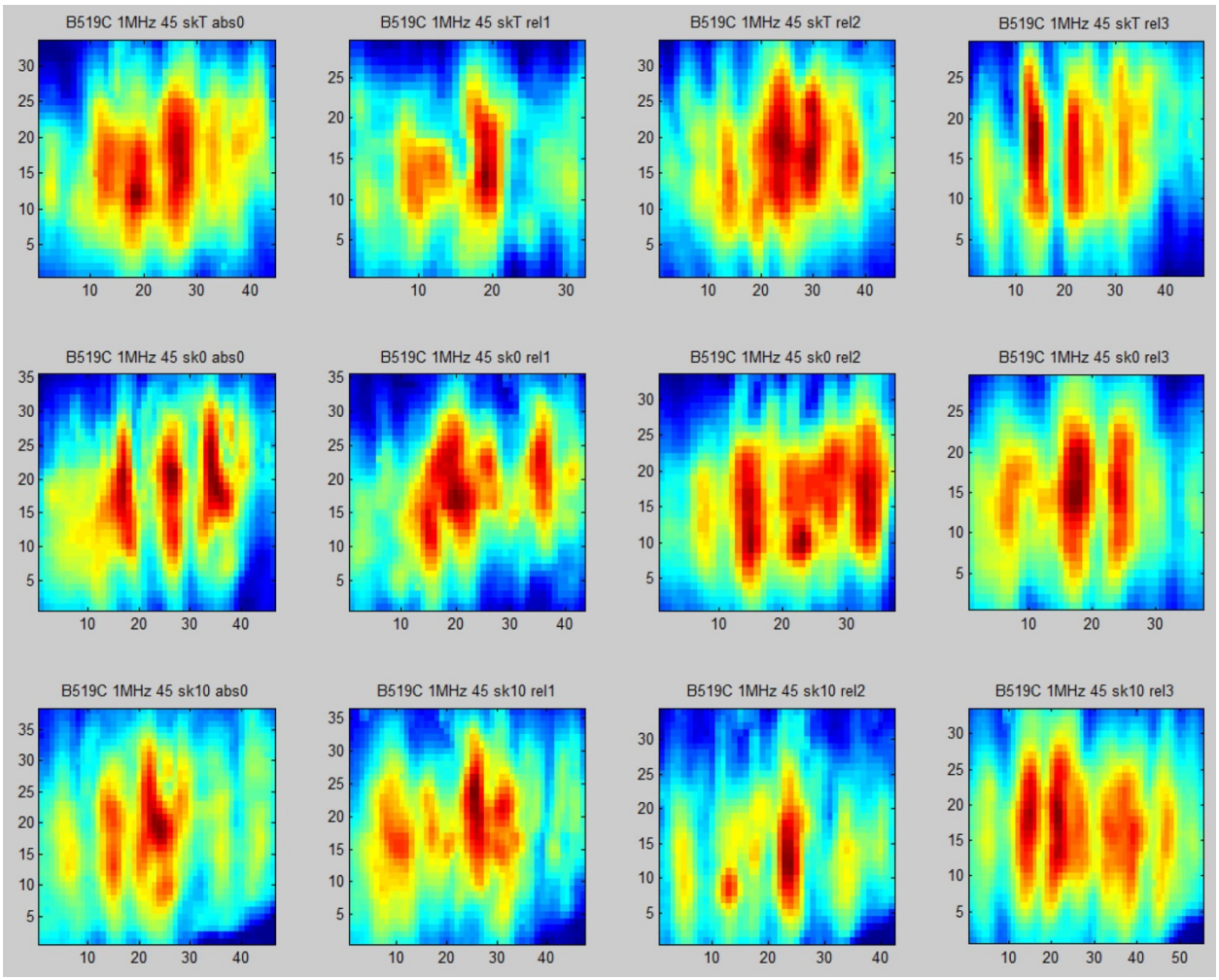

Figure B.34. Frequency 1.0 MHz, Specimen B519C, Refracted Angle 45 degrees, Cuts 0-3 Left to Right and SkT, Sk0, and Sk10 Top to Bottom

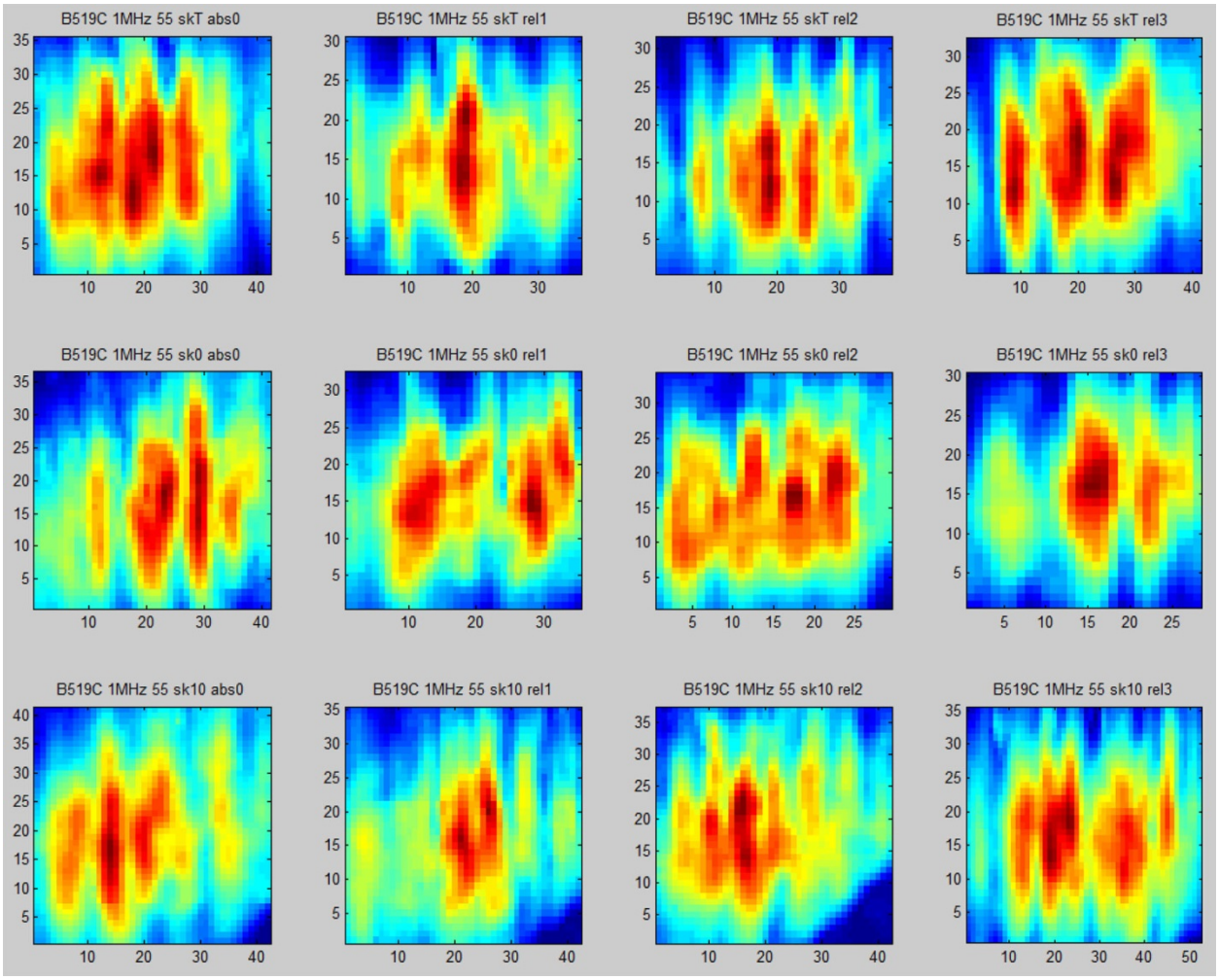

Figure B.35. Frequency 1.0 MHz, Specimen B519C, Refracted Angle 55 degrees, Cuts 0-3 Left to Right and SkT, Sk0, and Sk10 Top to Bottom

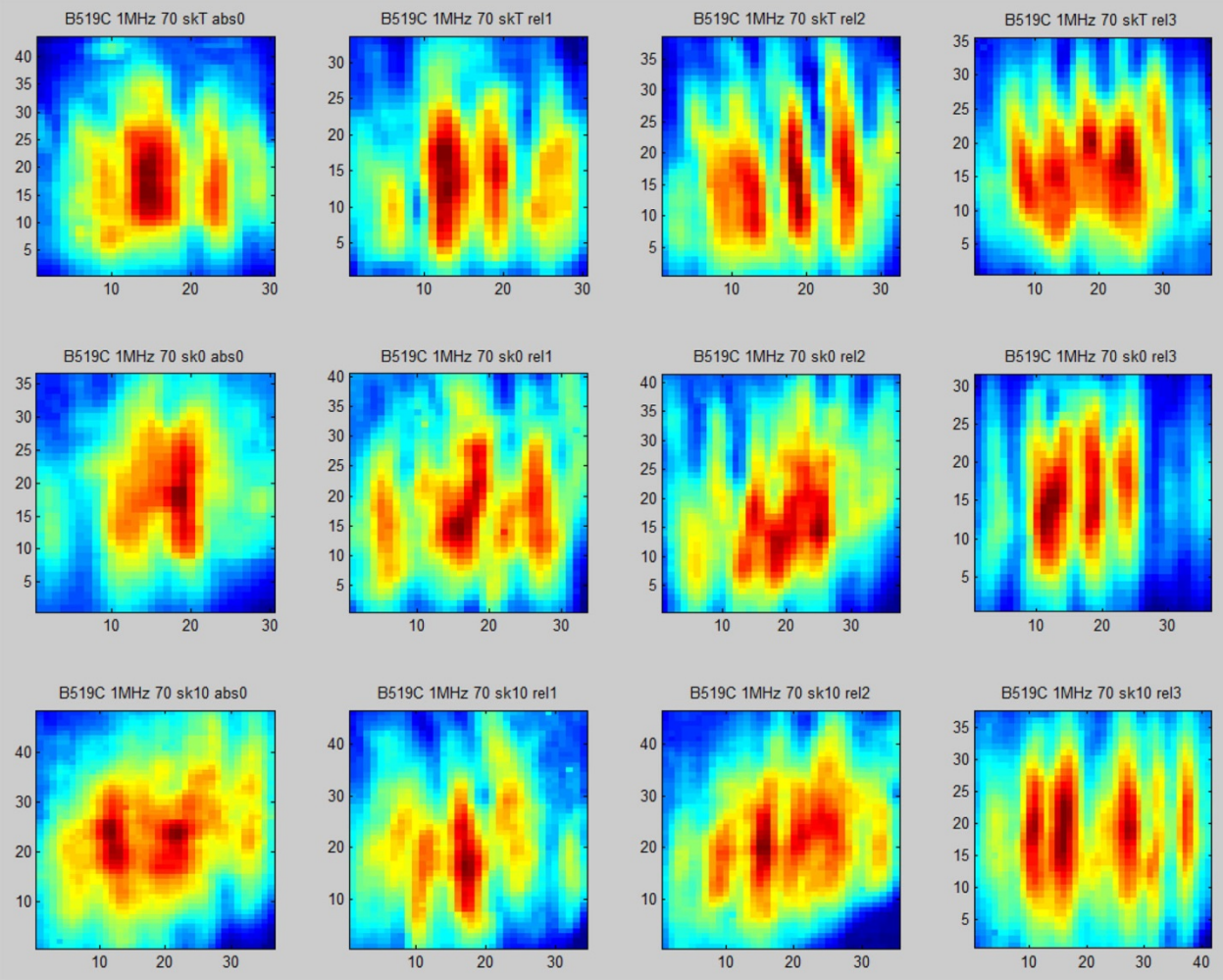

Figure B.36. Frequency 1.0 MHz, Specimen B519C, Refracted Angle 70 degrees, Cuts 0-3 Left to Right and SkT, Sk0, and Sk10 Top to Bottom

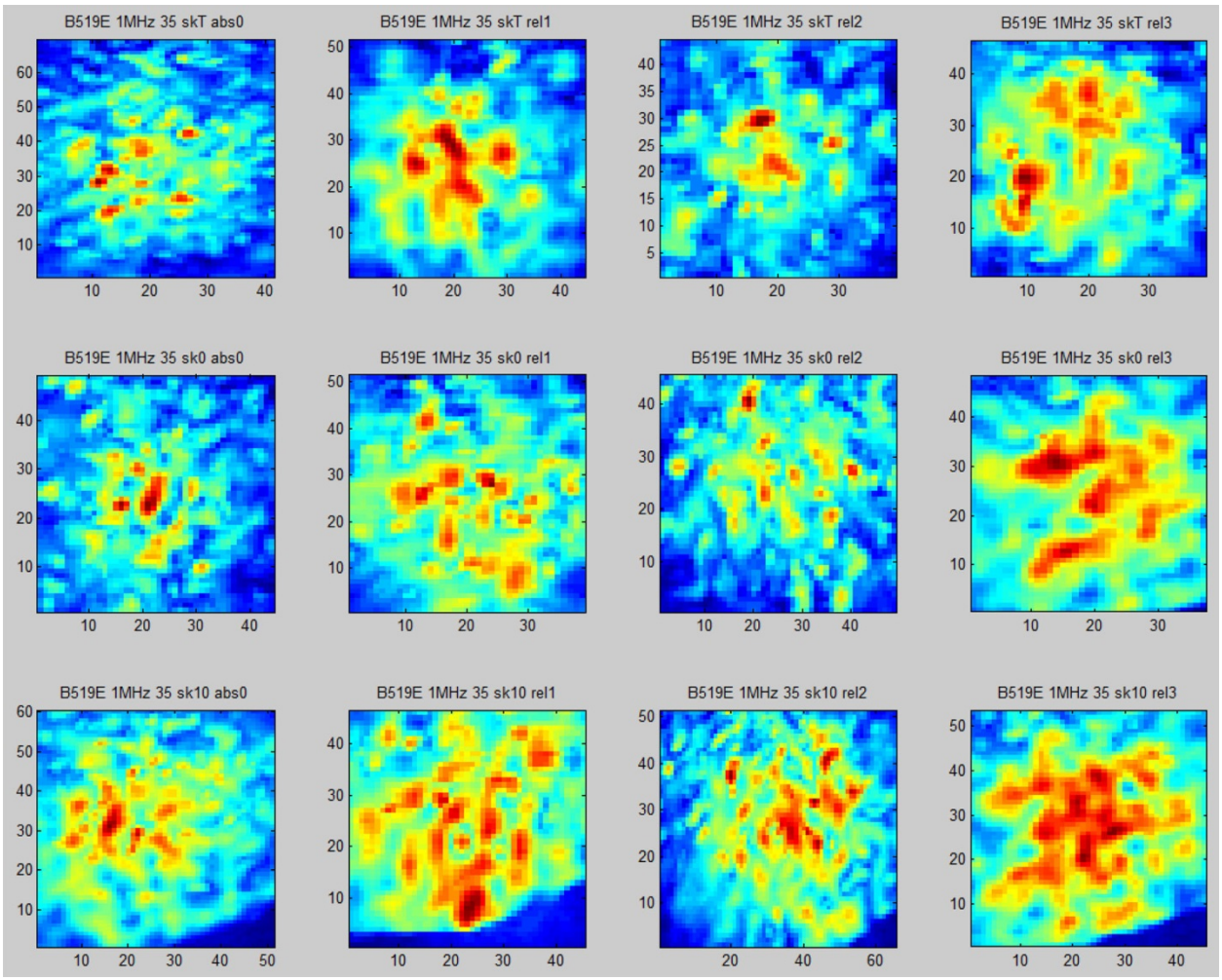

Figure B.37. Frequency 1.0 MHz, Specimen B519E, Refracted Angle 35 degrees, Cuts 0-3 Left to Right and SkT, Sk0, and Sk10 Top to Bottom

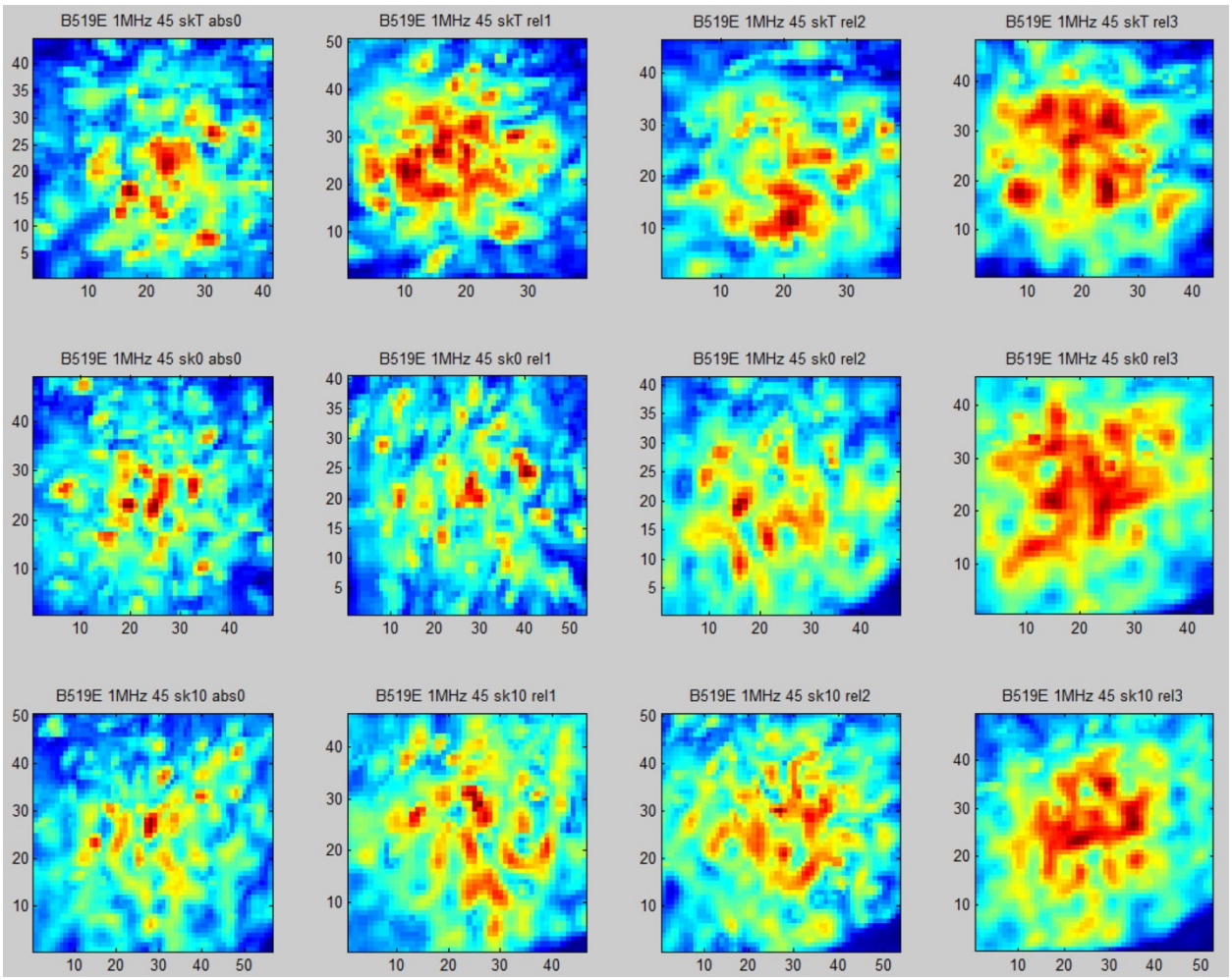

Figure B.38. Frequency 1.0 MHz, Specimen B519E, Refracted Angle 45 degrees, Cuts 0-3 Left to Right and SkT, Sk0, and Sk10 Top to Bottom

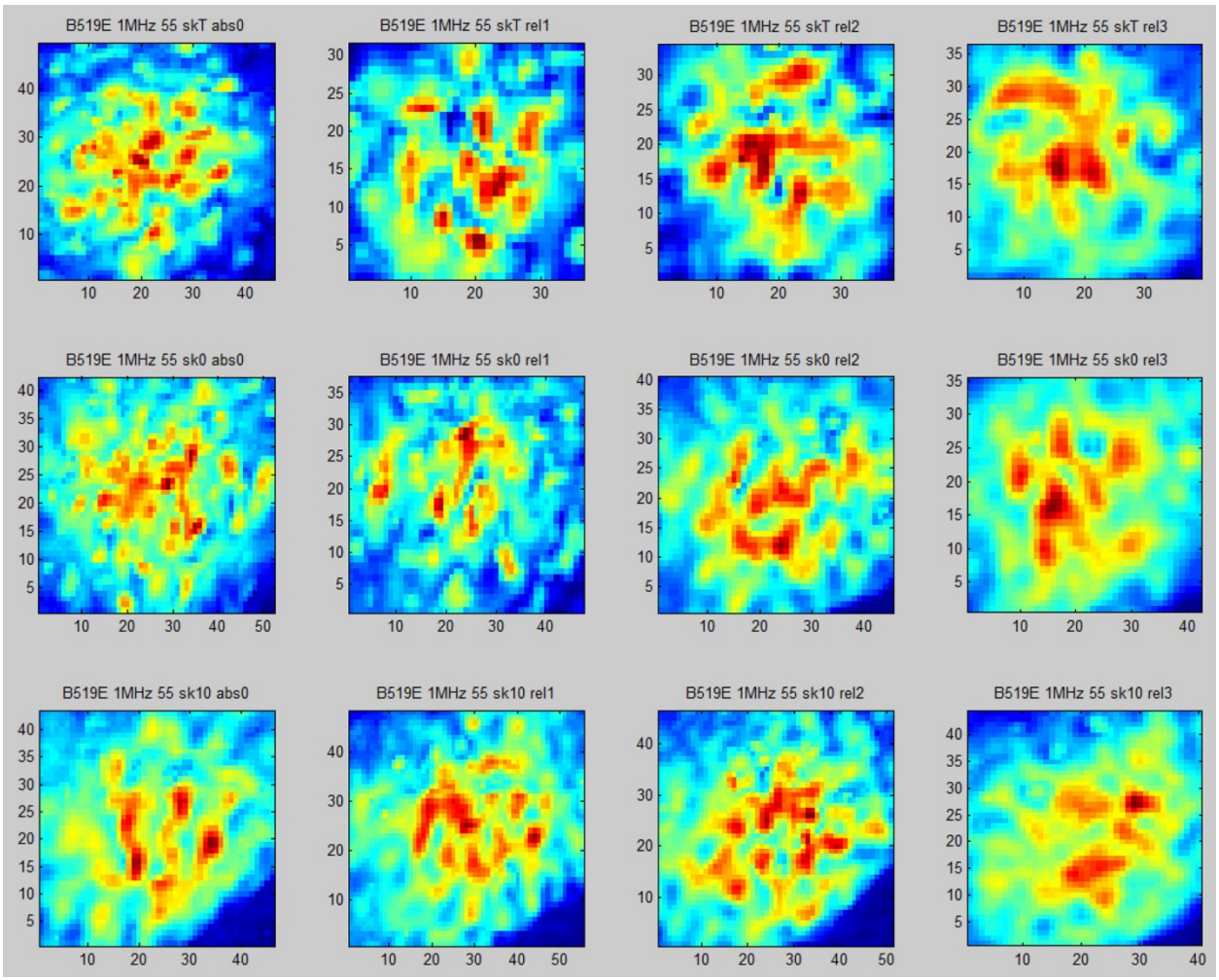

Figure B.39. Frequency 1.0 MHz, Specimen B519E, Refracted Angle 55 degrees, Cuts 0-3 Left to Right and SkT, Sk0, and Sk10 Top to Bottom

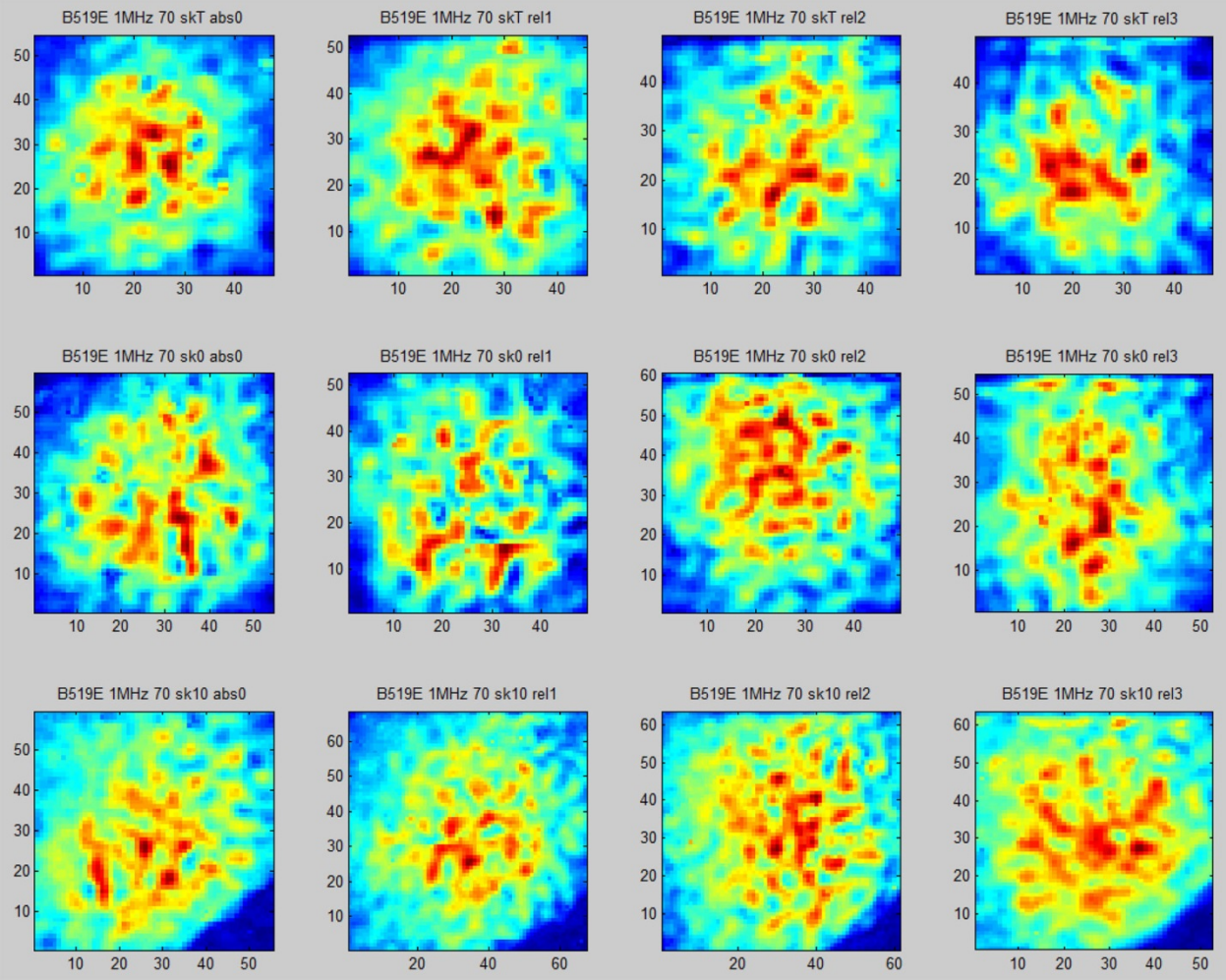

Figure B.40. Frequency 1.0 MHz, Specimen B519E, Refracted Angle 70 degrees, Cuts 0-3 Left to Right and SkT, Sk0, and Sk10 Top to Bottom

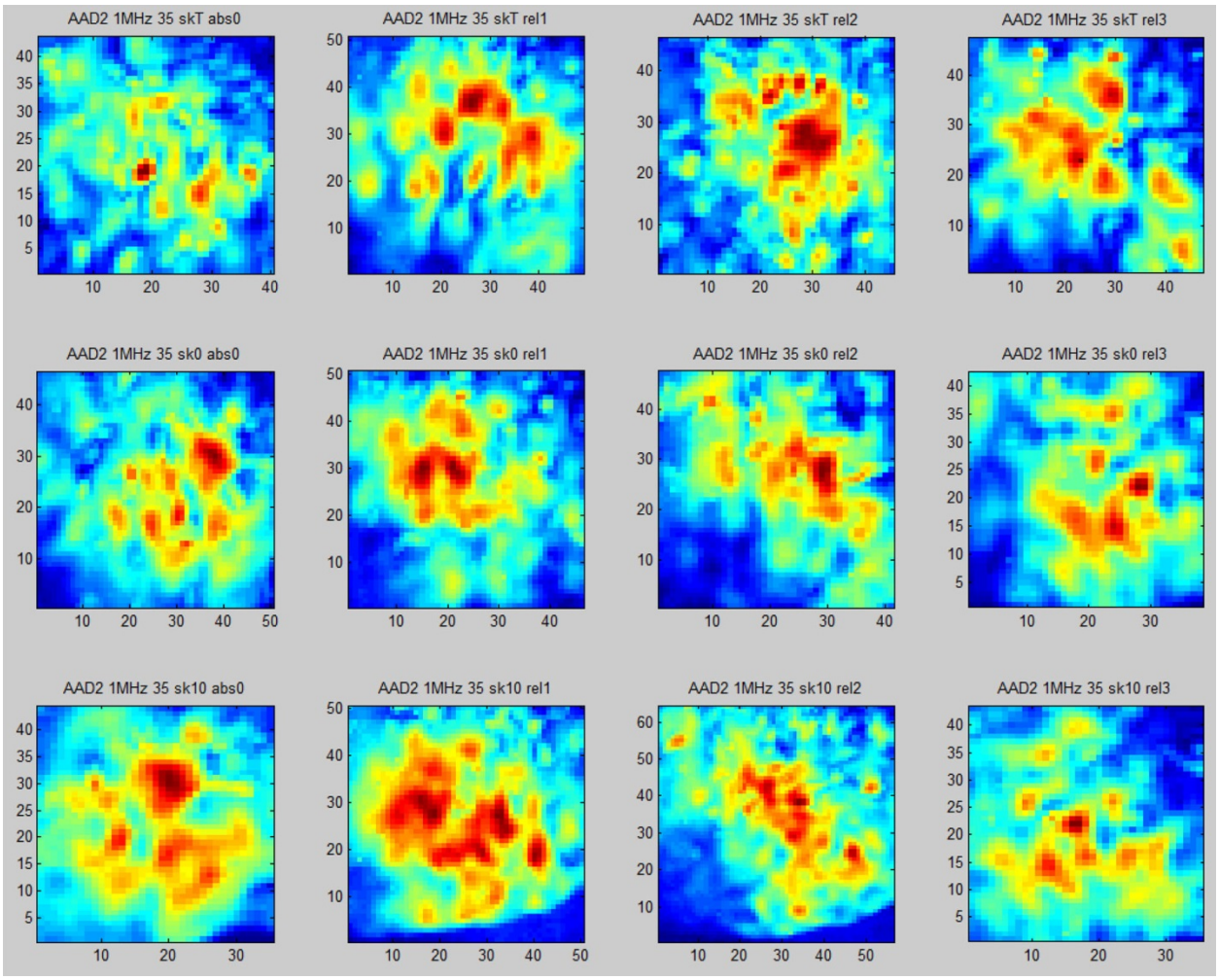

Figure B.41. Frequency 1.0 MHz, Specimen AAD2, Refracted Angle 35 degrees, Cuts 0-3 Left to Right and SkT, Sk0, and Sk10 Top to Bottom

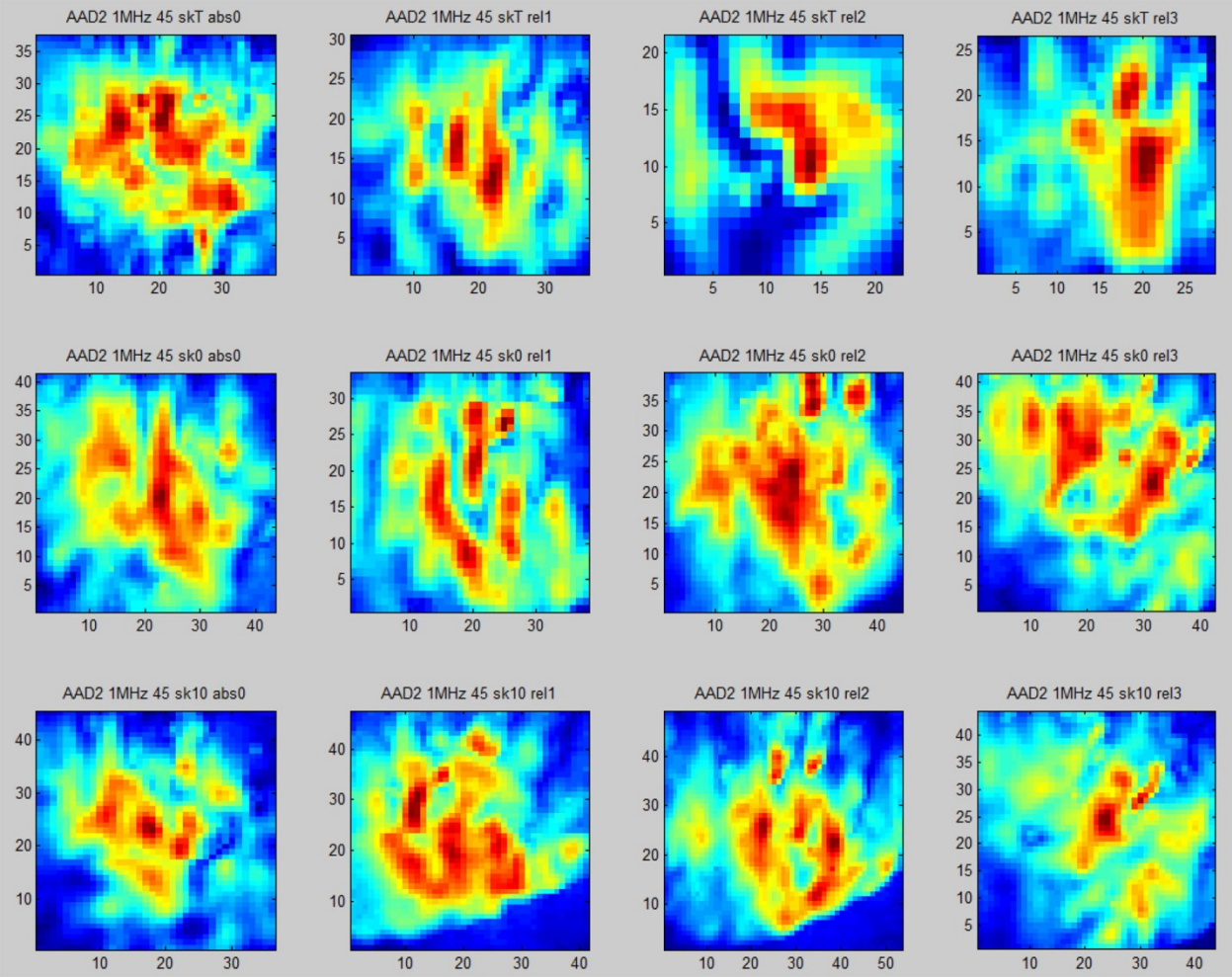

Figure B.42. Frequency 1.0 MHz, Specimen AAD2, Refracted Angle 45 degrees, Cuts 0-3 Left to Right and SkT, Sk0, and Sk10 Top to Bottom

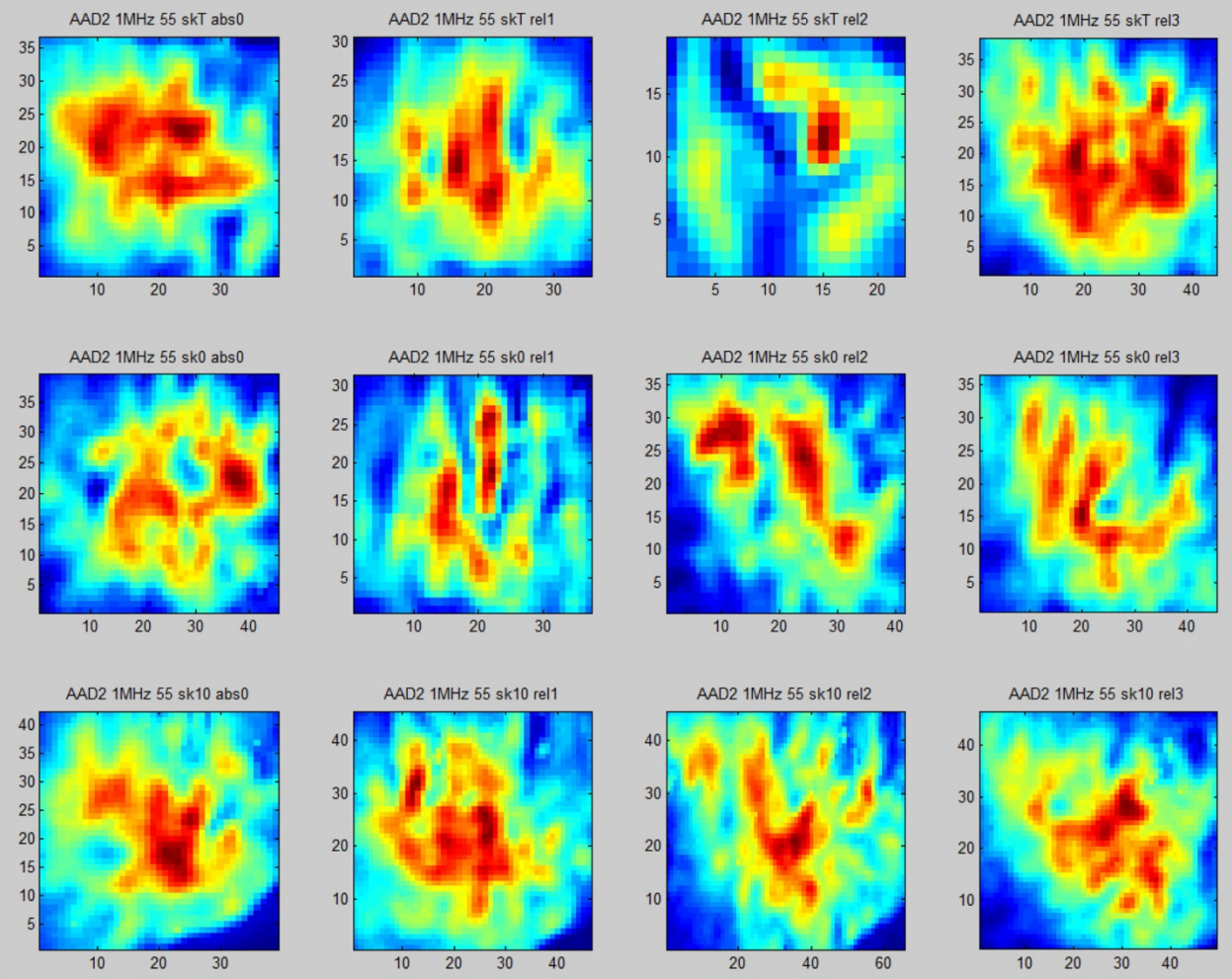

Figure B.43. Frequency 1.0 MHz, Specimen AAD2, Refracted Angle 55 degrees, Cuts 0-3 Left to Right and SkT, Sk0, and Sk10 Top to Bottom

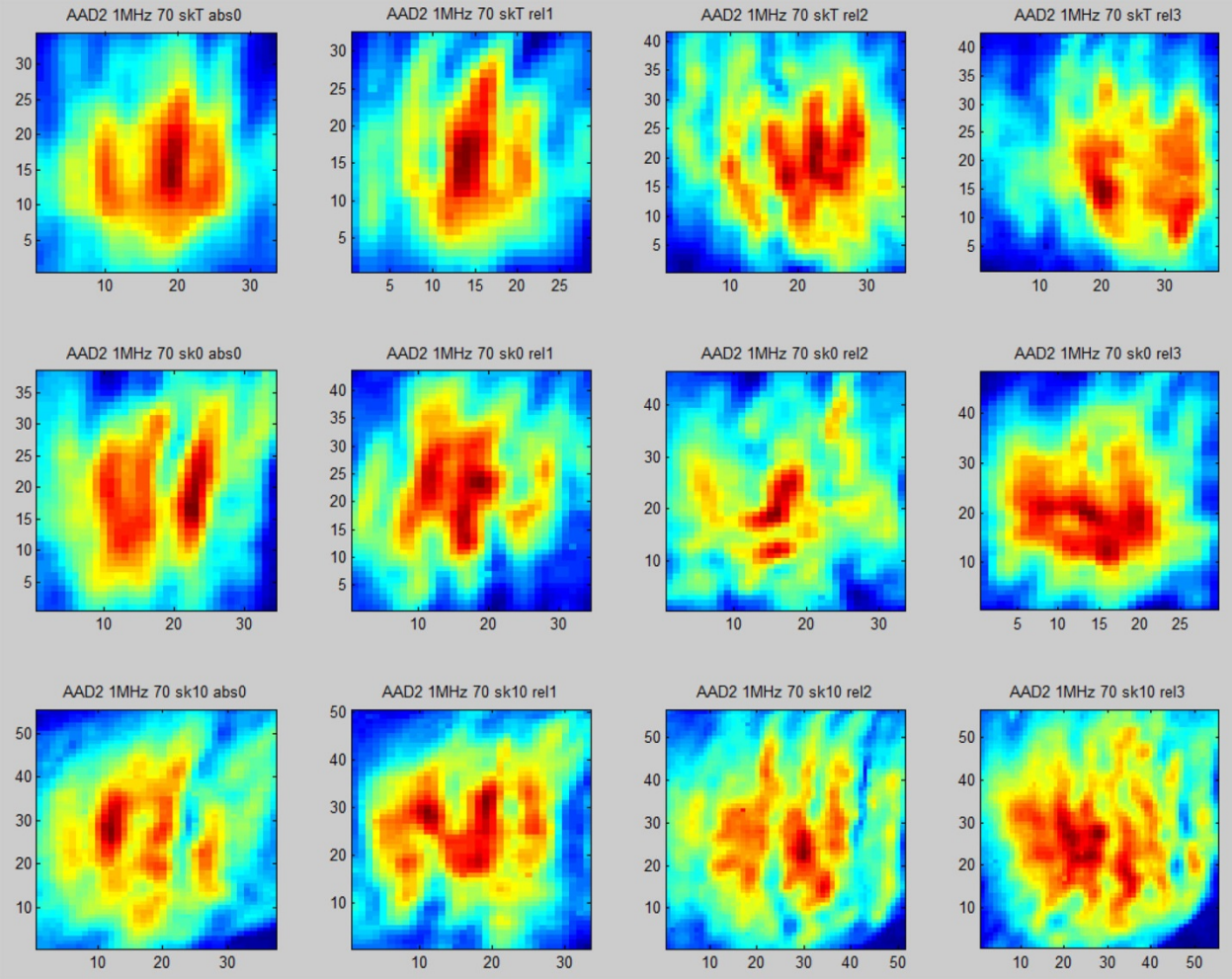

Figure B.44. Frequency 1.0 MHz, Specimen AAD2, Refracted Angle 70 degrees, Cuts 0-3 Left to Right and SkT, Sk0, and Sk10 Top to Bottom

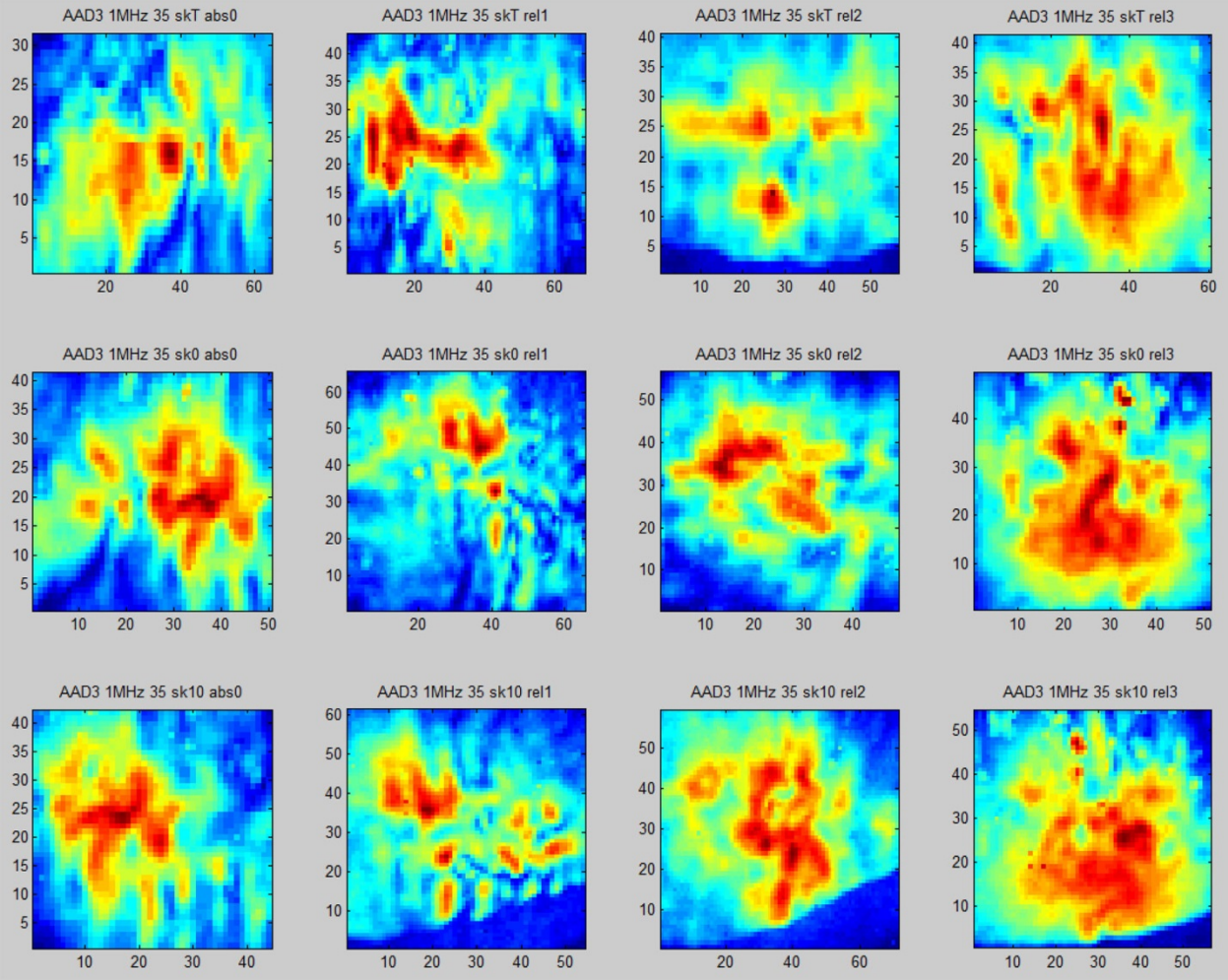

Figure B.45. Frequency 1.0 MHz, Specimen AAD3, Refracted Angle 35 degrees, Cuts 0-3 Left to Right and SkT, Sk0, and Sk10 Top to Bottom

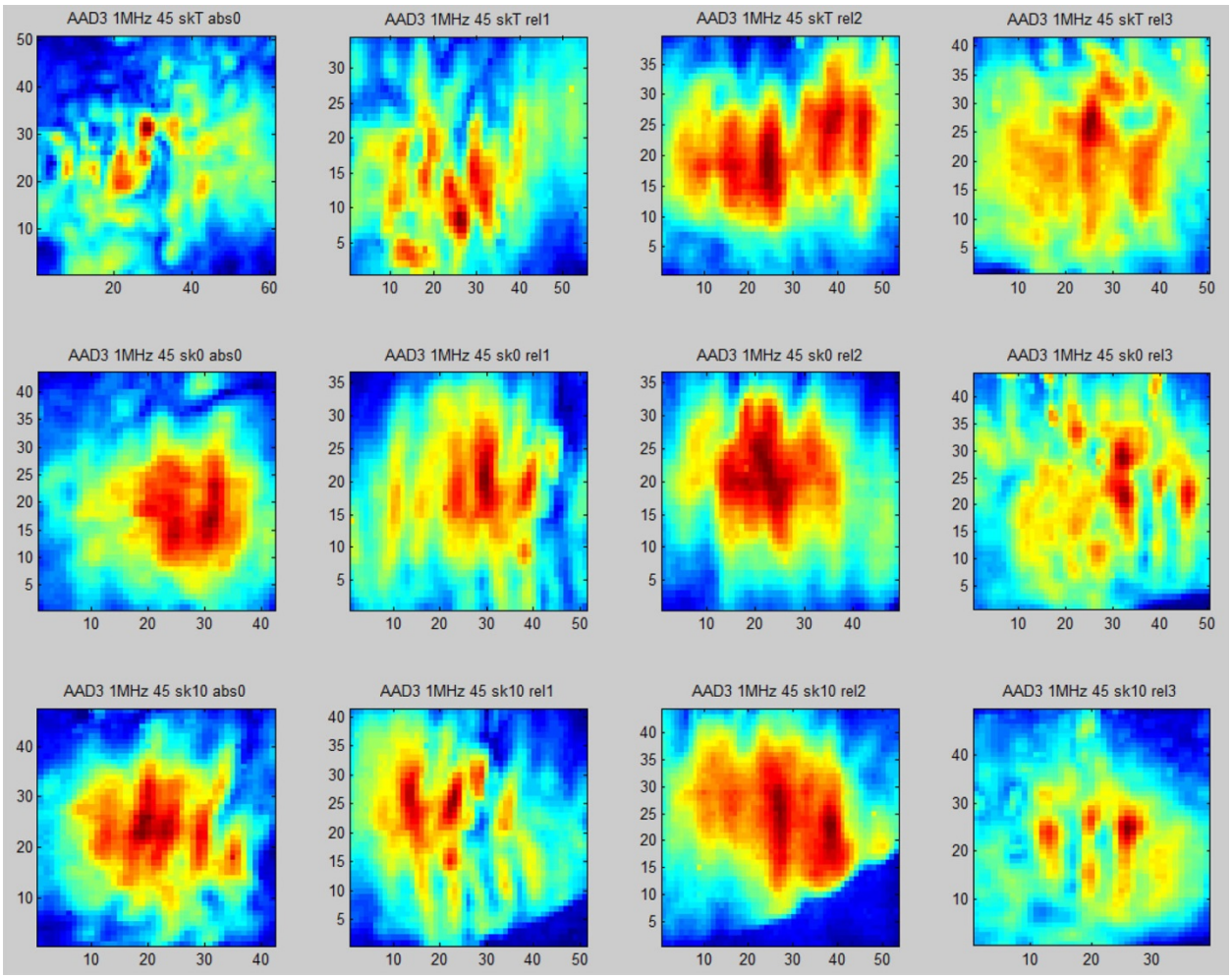

Figure B.46. Frequency 1.0 MHz, Specimen AAD3, Refracted Angle 45 degrees, Cuts 0-3 Left to Right and SkT, Sk0, and Sk10 Top to Bottom

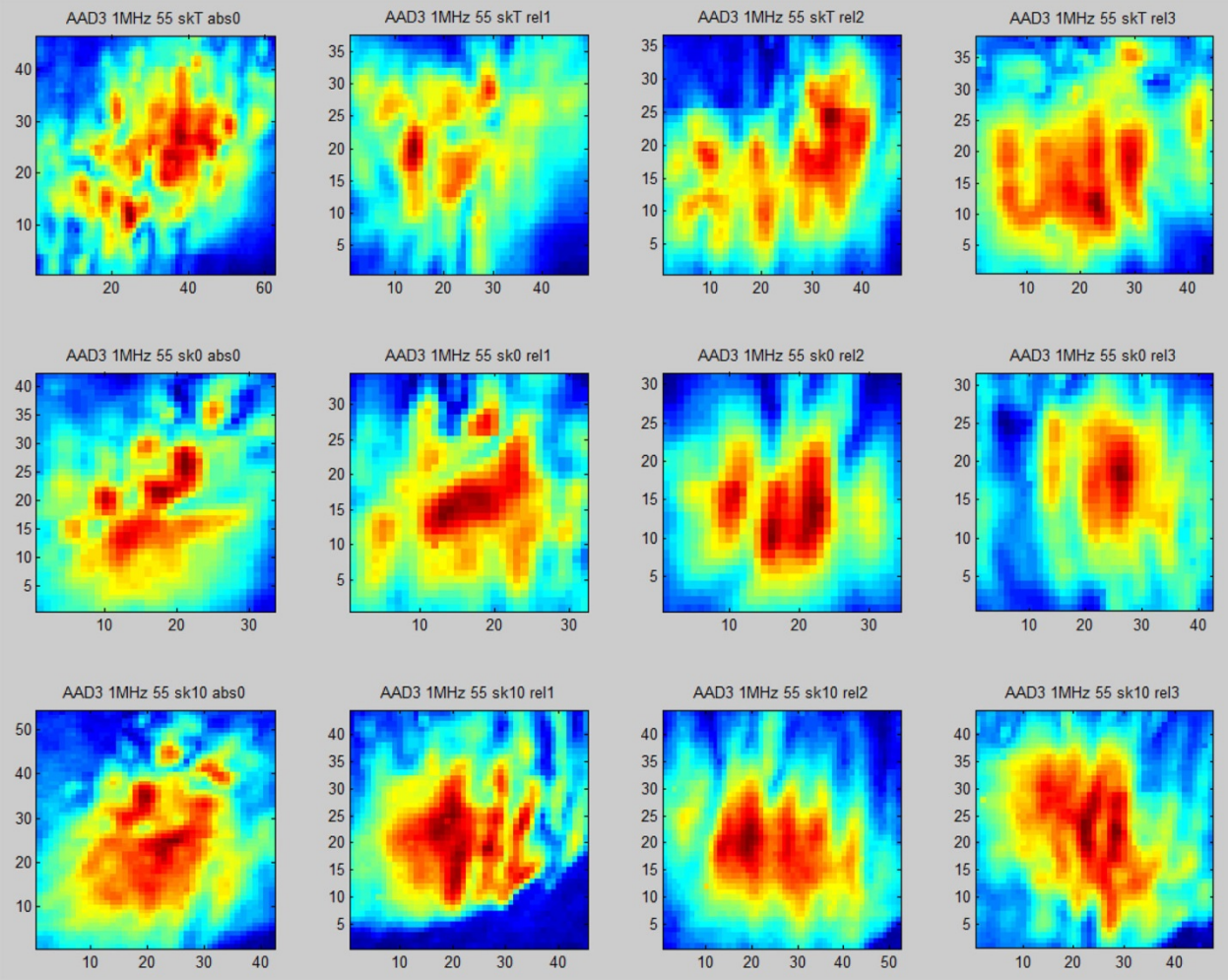

Figure B.47. Frequency 1.0 MHz, Specimen AAD3, Refracted Angle 55 degrees, Cuts 0-3 Left to Right and SkT, Sk0, and Sk10 Top to Bottom

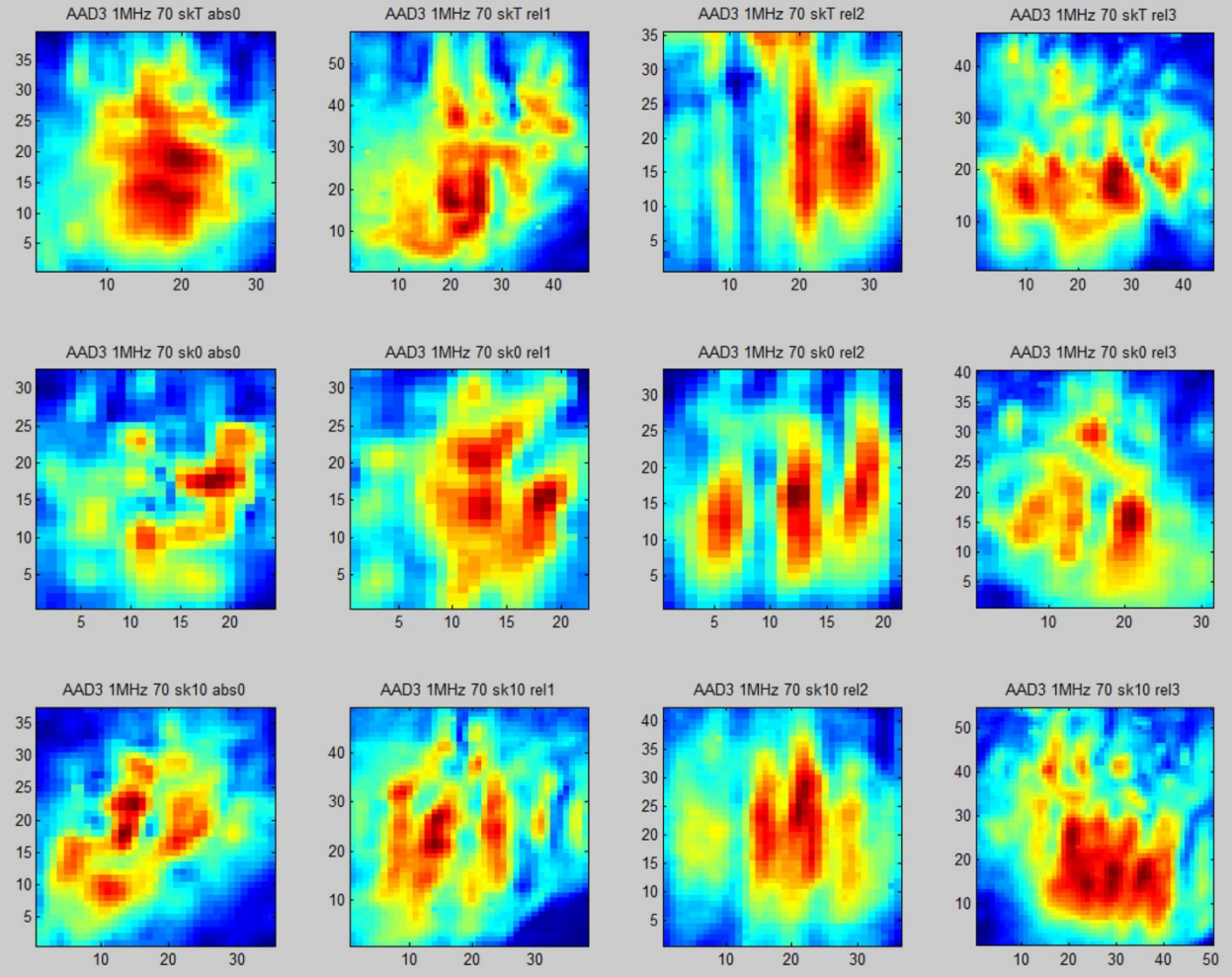

Figure B.48. Frequency 1.0 MHz, Specimen AAD3, Refracted Angle 70 degrees, Cuts 0-3 Left to Right and SkT, Sk0, and Sk10 Top to Bottom

Appendix C

Sound Field Images in WSS

Appendix C

Sound Field Images in WSS

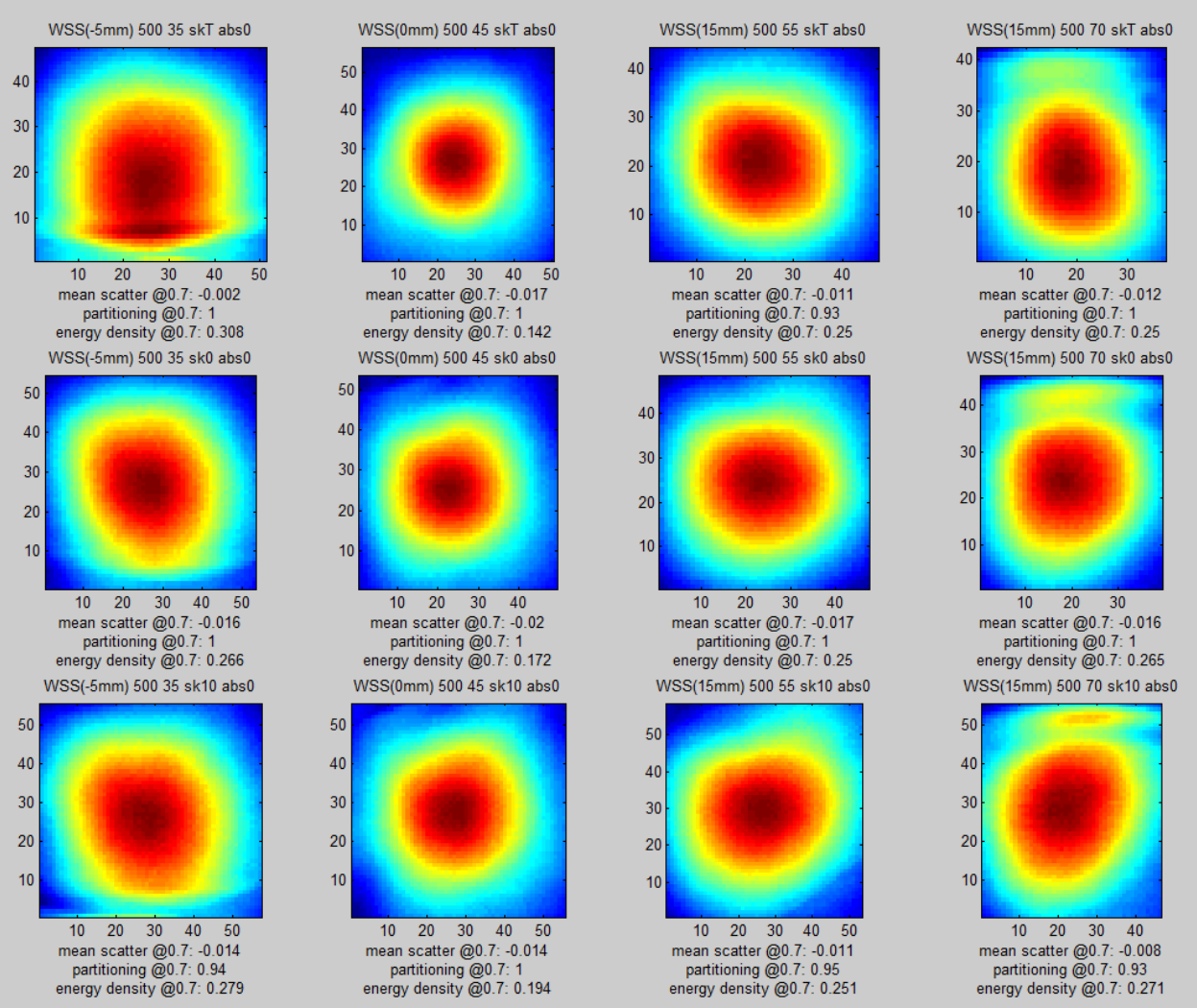

Appendix C.1. Frequency 0.5 MHz, WSS Sound Fields for Refracted Angles 35, 45, 55, and 70 Degrees (columns left to right) and Beam Skew Angles SkT, Sk0, and Sk10 (rows top to bottom)

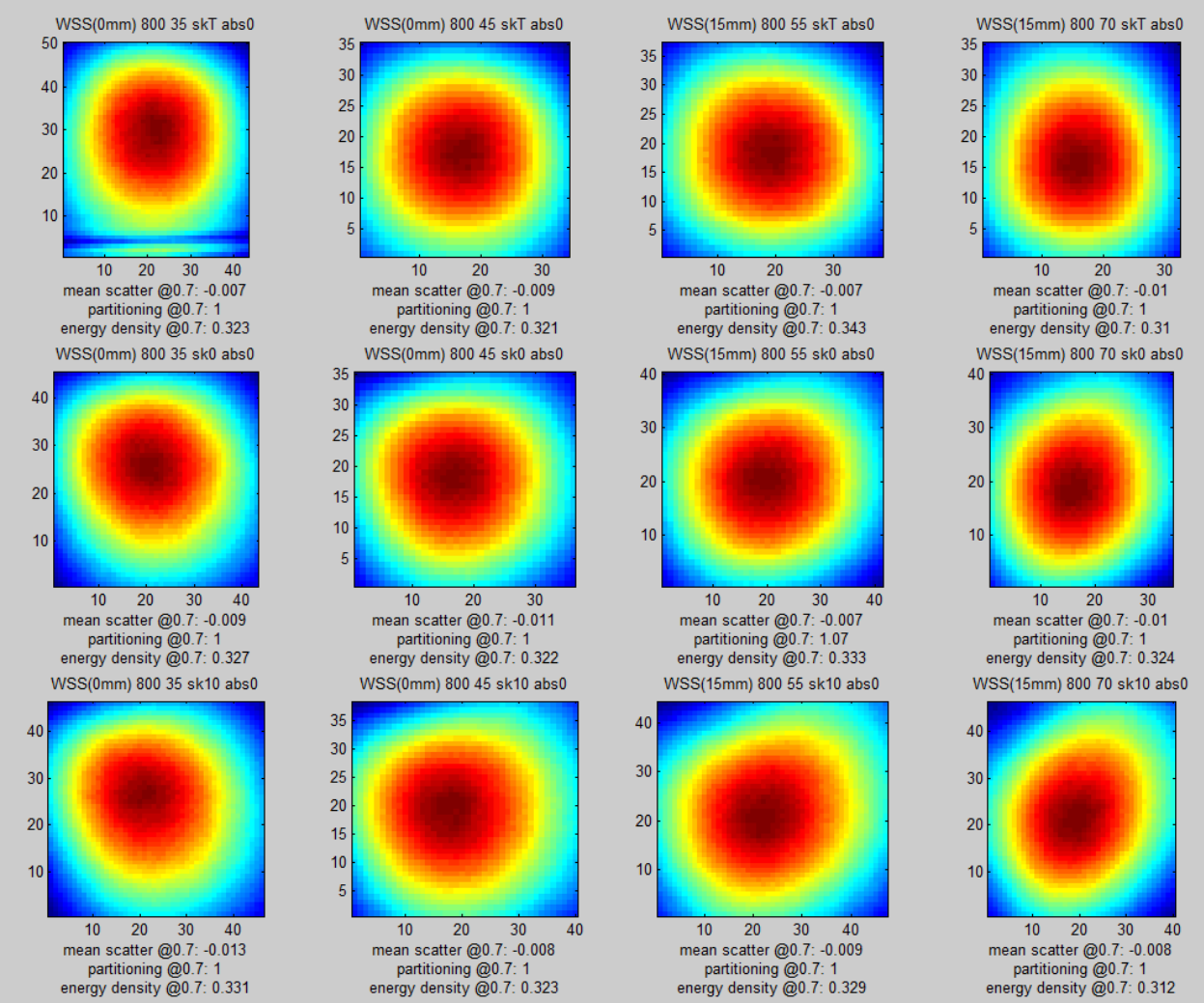

Appendix C.2. Frequency 0.8 MHz, WSS Sound Fields for Refracted Angles 35, 45, 55, and 70 Degrees (columns left to right) and Beam Skew Angles SkT, Sk0, and Sk10 (rows top to bottom)

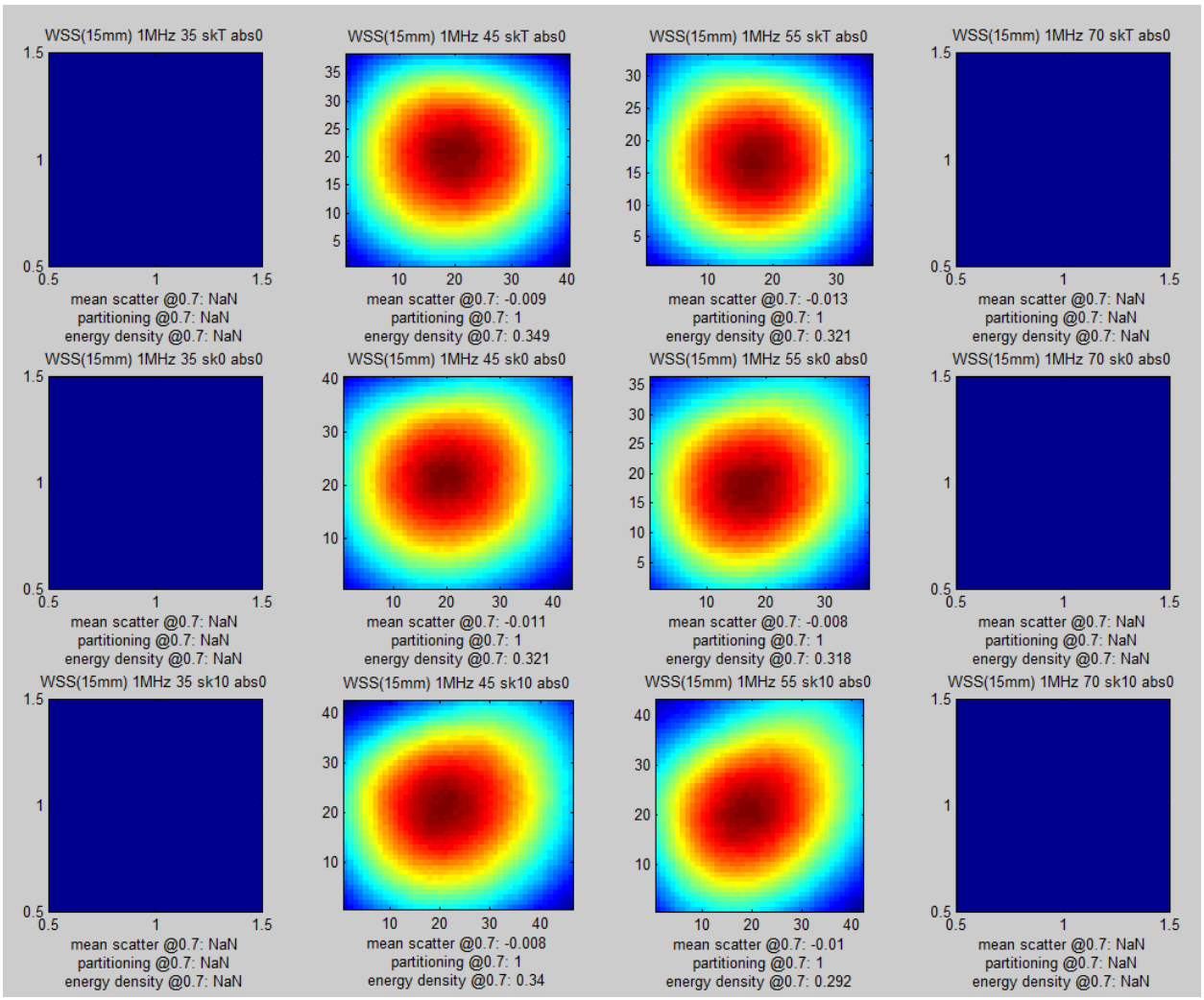

Appendix C.3. Frequency 1.0 MHz, WSS Sound Fields for Refracted Angles 35, 45, 55, and 70 Degrees (columns left to right) and Beam Skew Angles SkT, Sk0, and Sk10 (rows top to bottom)

Appendix D

Sorting of Scatter and Partition Data

Appendix D

Sorting of Scatter and Partition Data

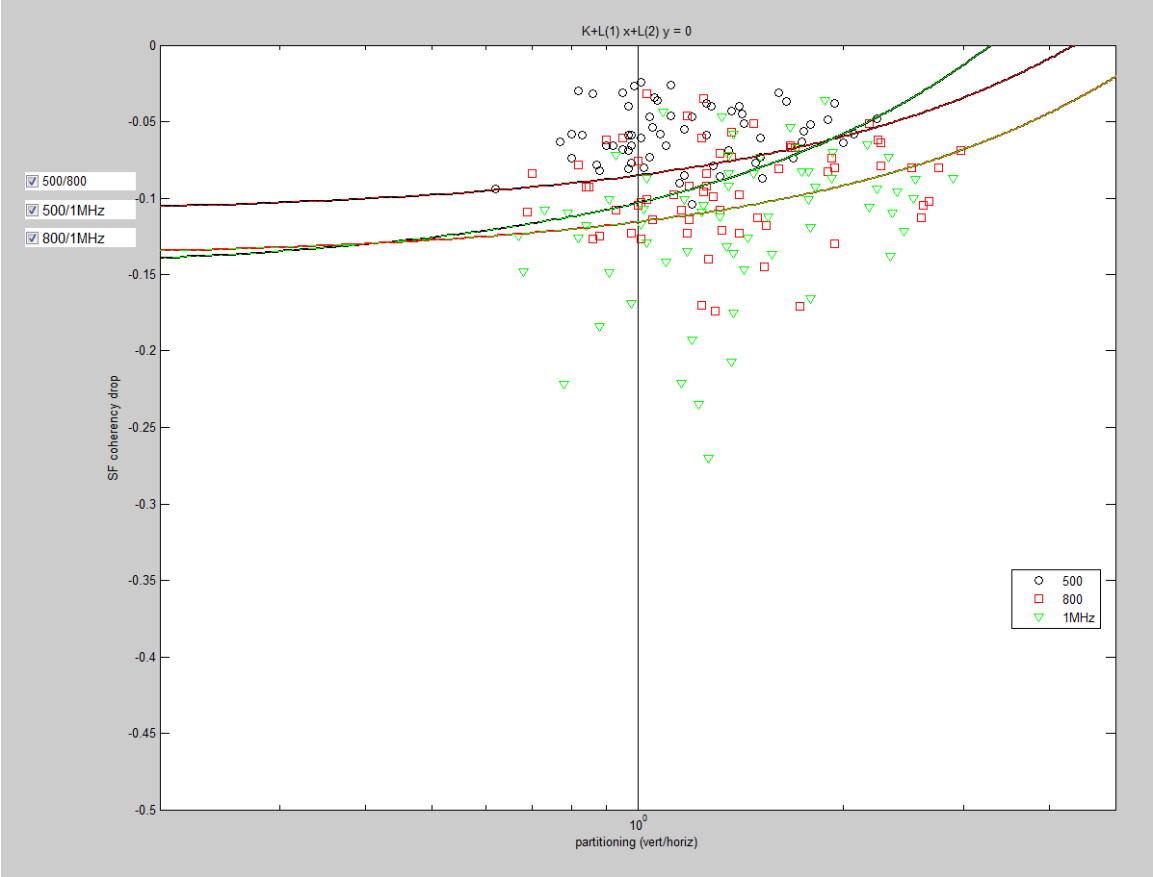

Figure D.1. Sorting by Frequency with Four Specimens, Skew 0, Four Refracted Angles, Four Positions

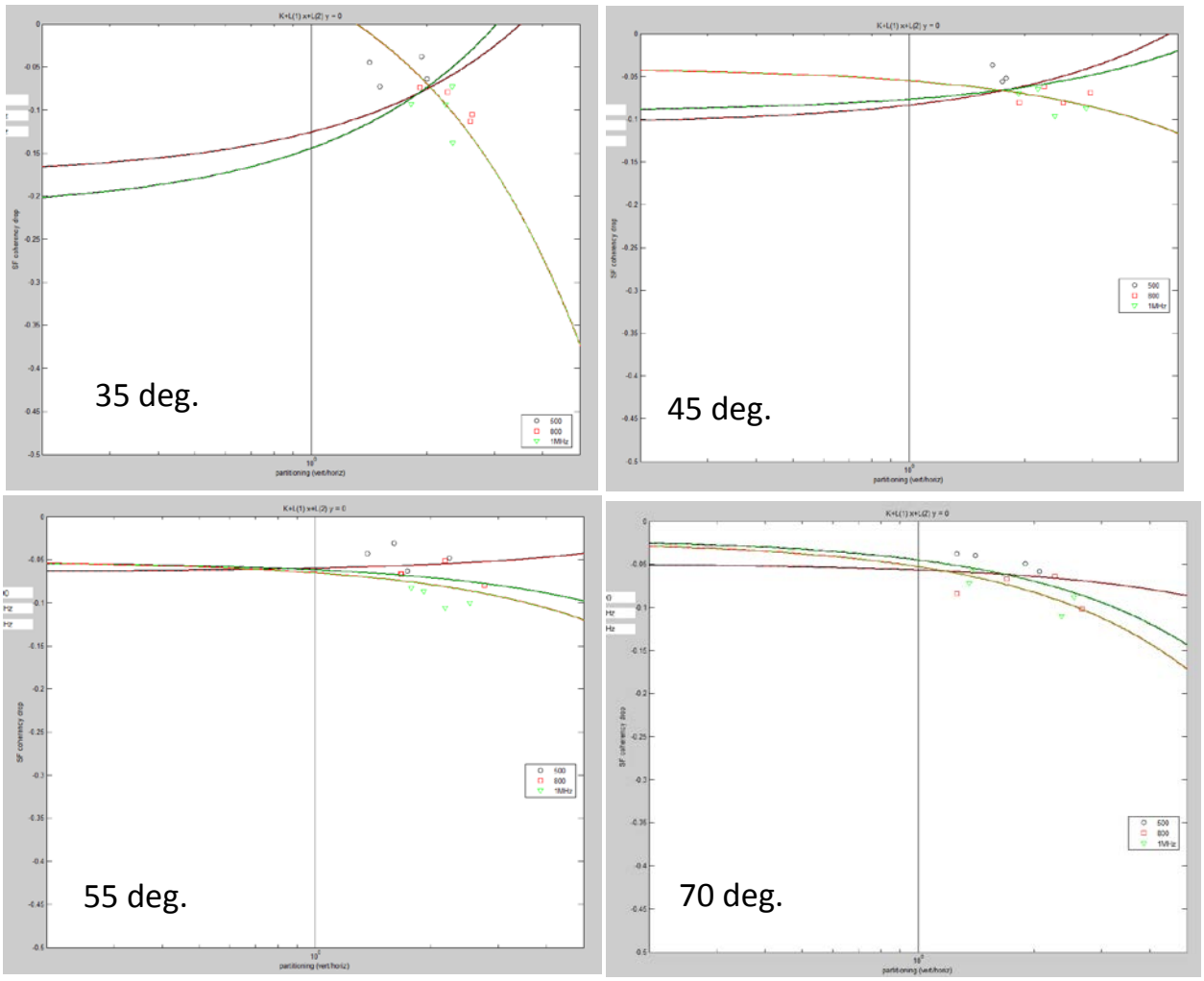

Figure D.2. Sorting by Frequency with Specimen B-519C, Skew 0 Degree, Four Positions and Refracted Angles of 35, 45, 55, and 70 Degree

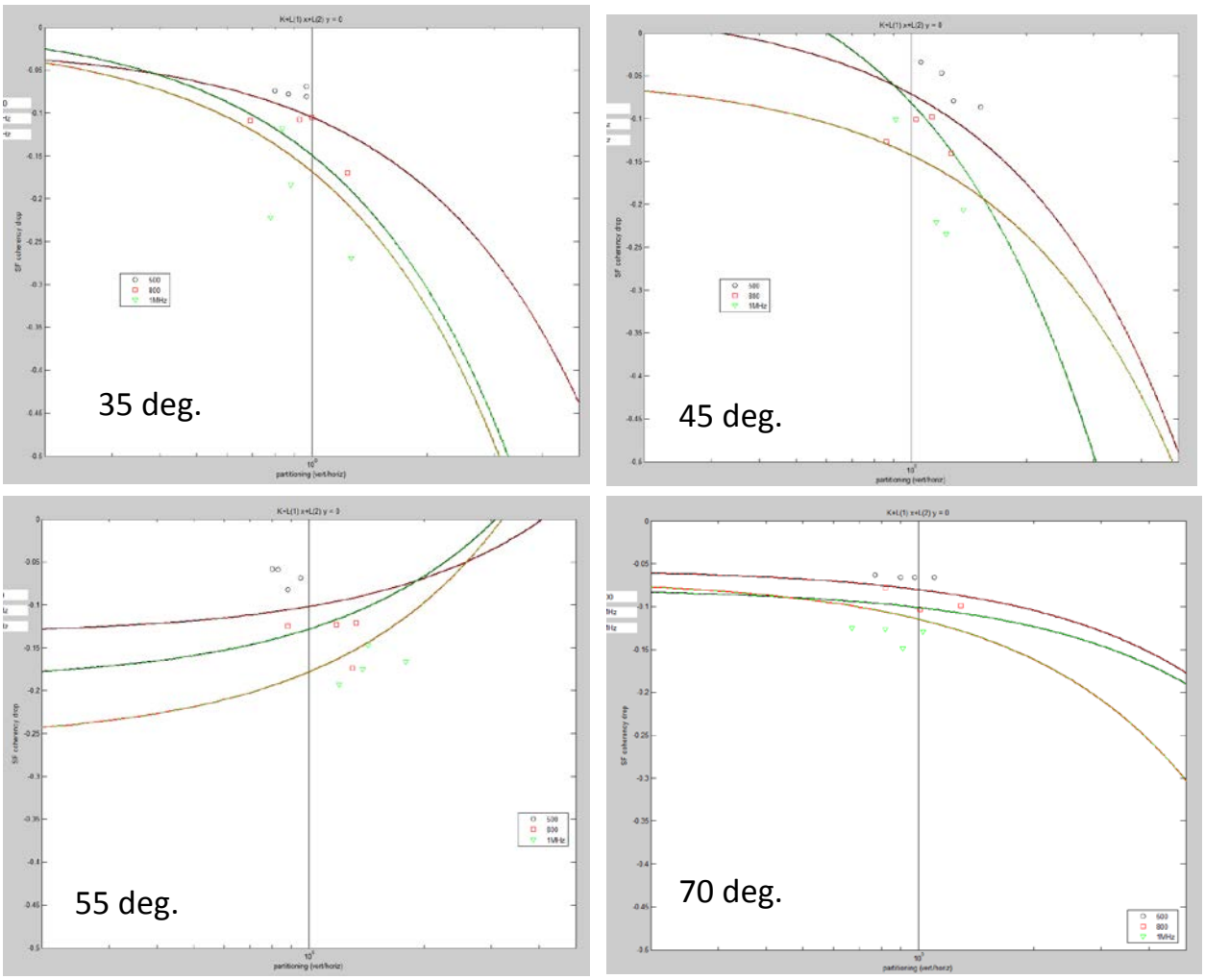

Figure D.3. Sorting by Frequency with Specimen B-519E, Skew 0 Degree, Four Positions and Refracted Angles of 35, 45, 55, and 70 Degree

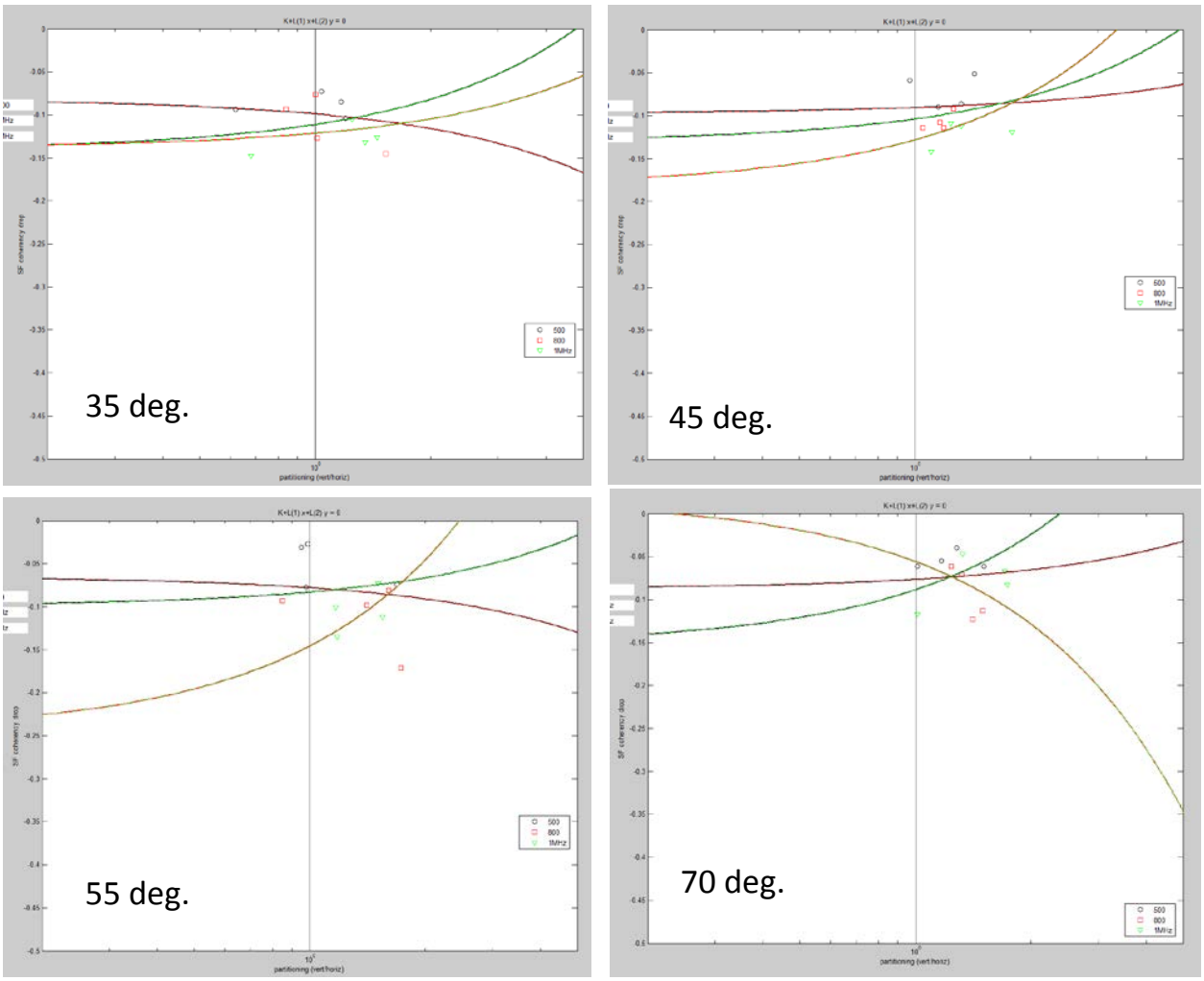

Figure D.4. Sorting by Frequency with Specimen AAD-2, Skew 0 Degree, Four Positions and Refracted Angles of 35, 45, 55, and 70 Degree

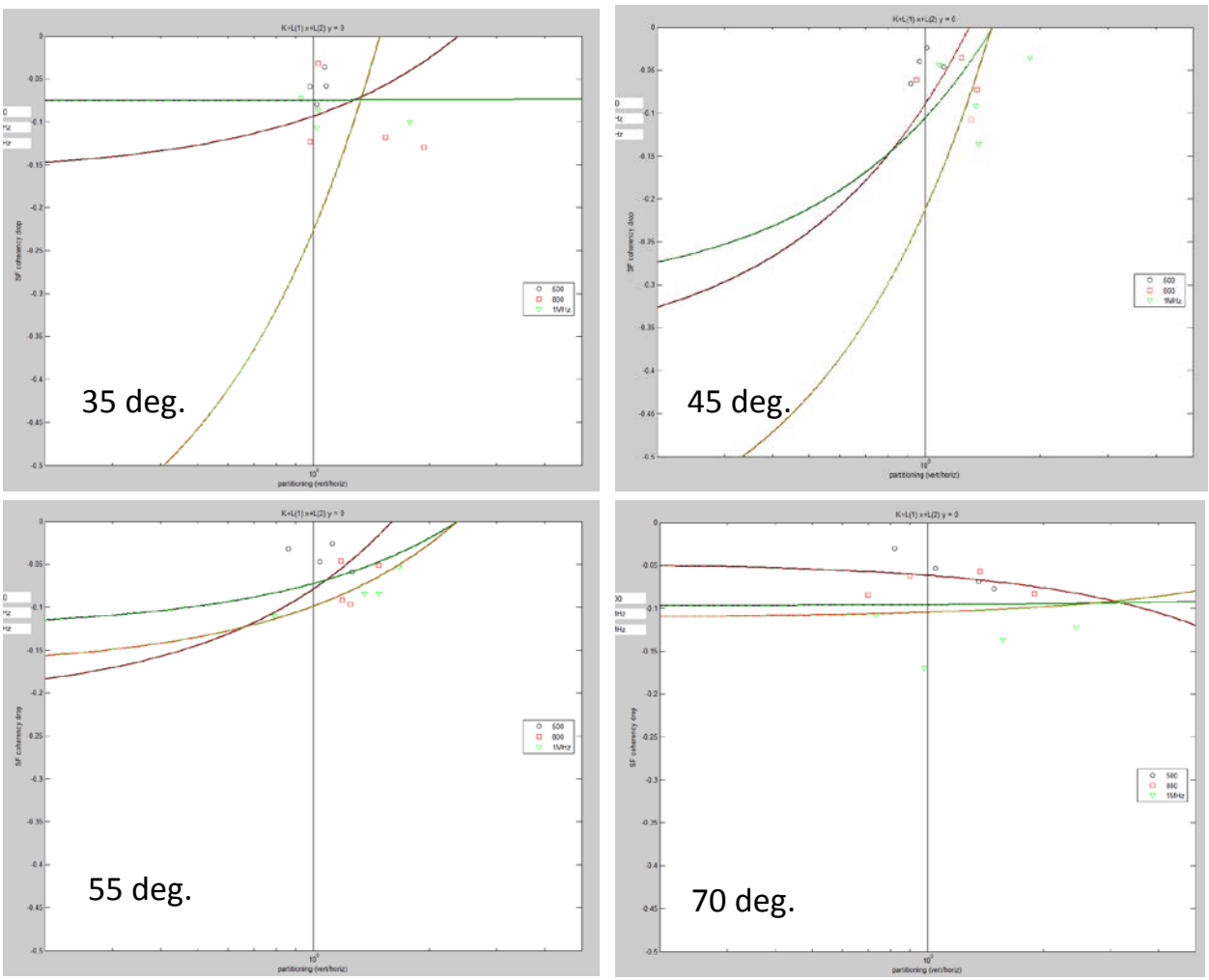

Figure D.5. Sorting by Frequency with Specimen AAD-3, Skew 0 Degree, Four Positions and Refracted Angles of 35, 45, 55, and 70 Degree

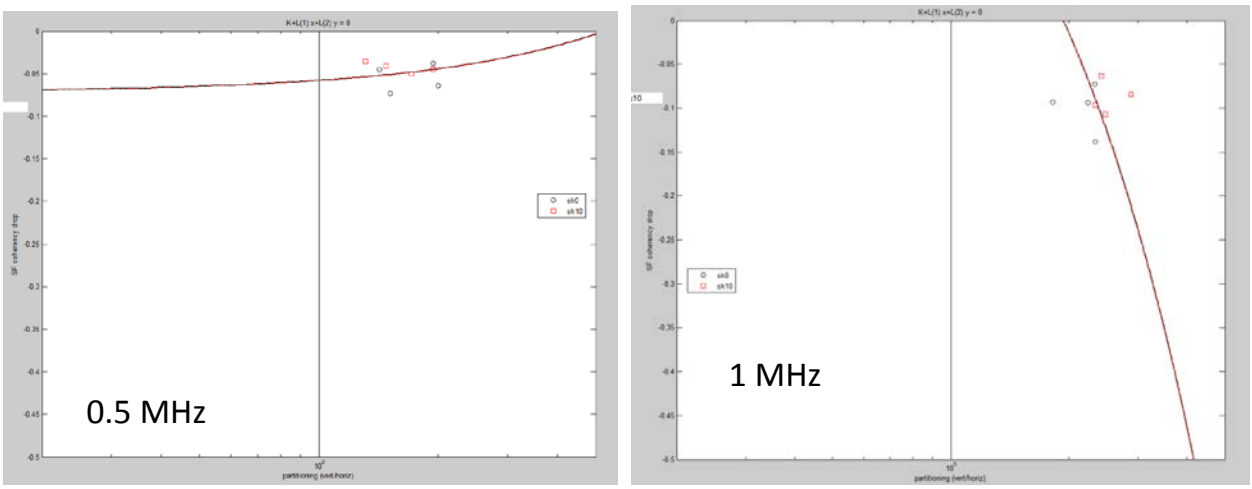

Figure D.6. Sorting by Skew Angle with Specimen B-519C, 0.5 and 1 MHz, 35-Degree Refracted Angle, Four Positions

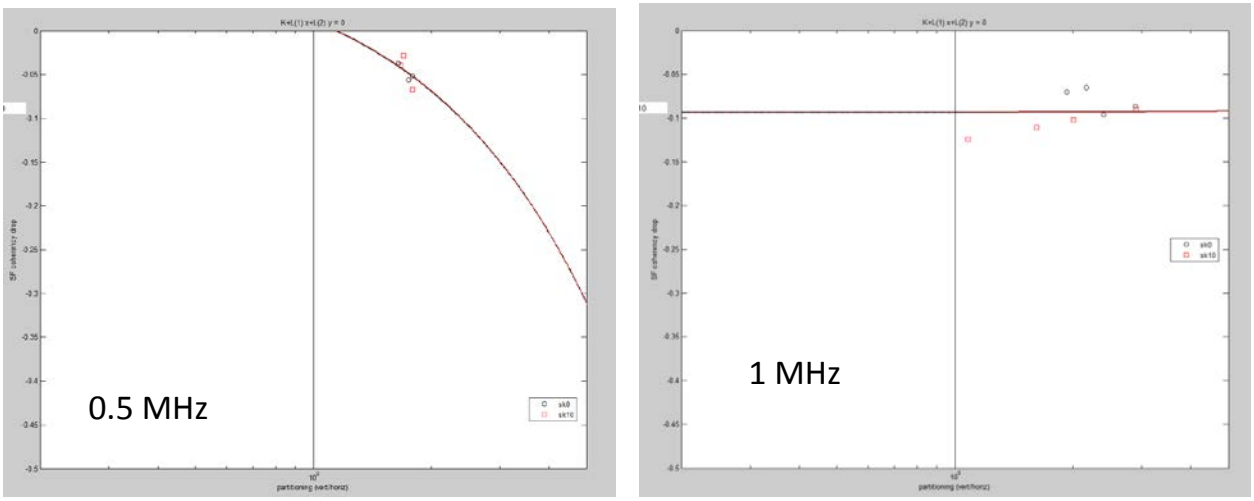

Figure D.7. Sorting by Skew Angle with Specimen B-519C, 0.5 and 1 MHz, 45-Degree Refracted Angle, Four Positions

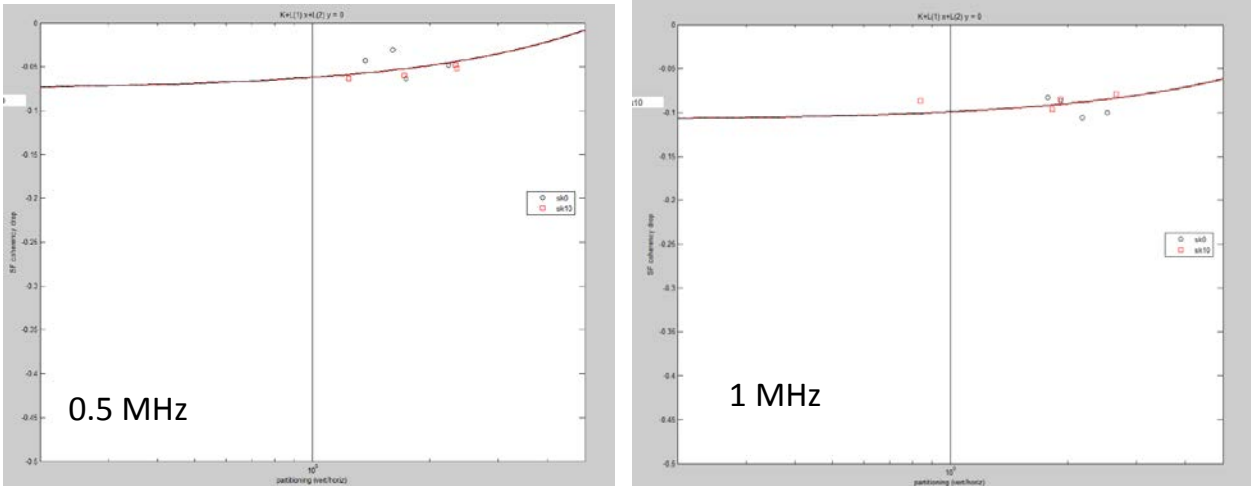

Figure D.8. Sorting by Skew Angle with Specimen B-519C, 0.5 and 1 MHz, 55-Degree Refracted Angle, Four Positions

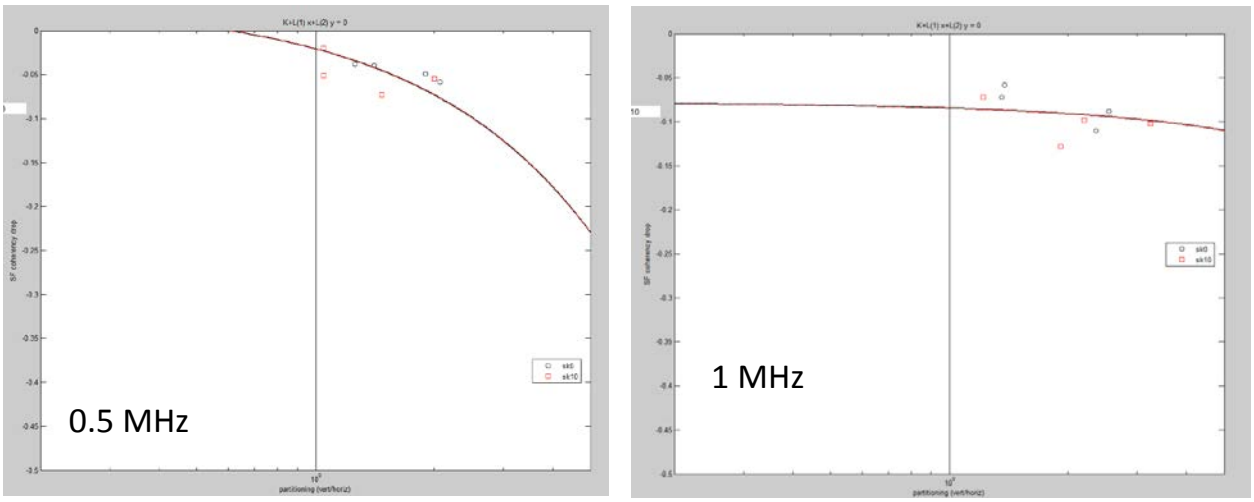

Figure D.9. Sorting by Skew Angle with Specimen B-519C, 0.5 and 1 MHz, 70-Degree Refracted Angle, Four Positions

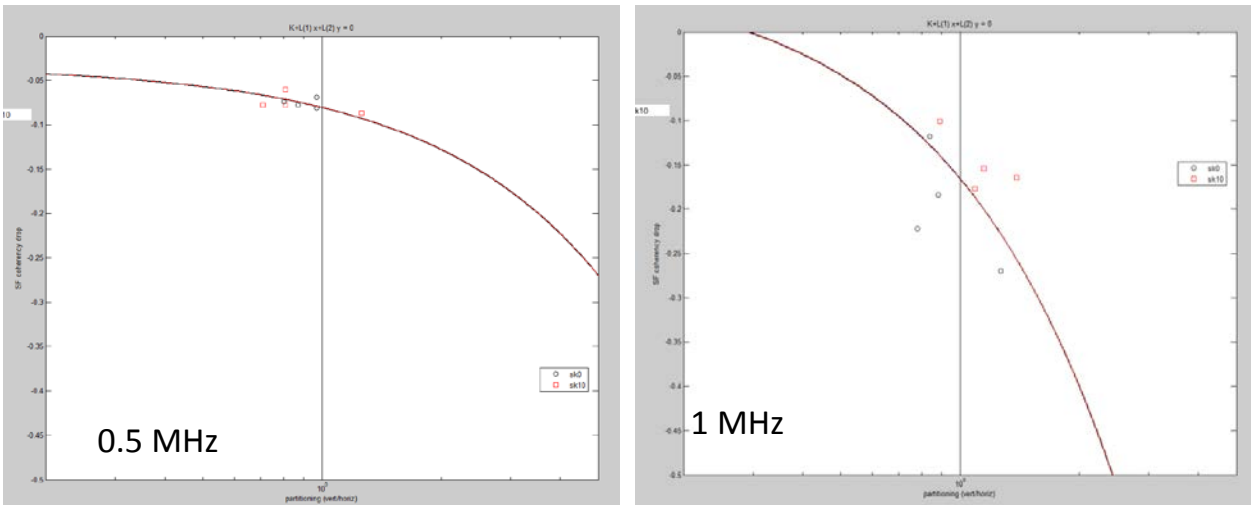

Figure D.10. Sorting by Skew Angle with Specimen B-519E, 0.5 and 1 MHz, 35-Degree Refracted Angle, Four Positions

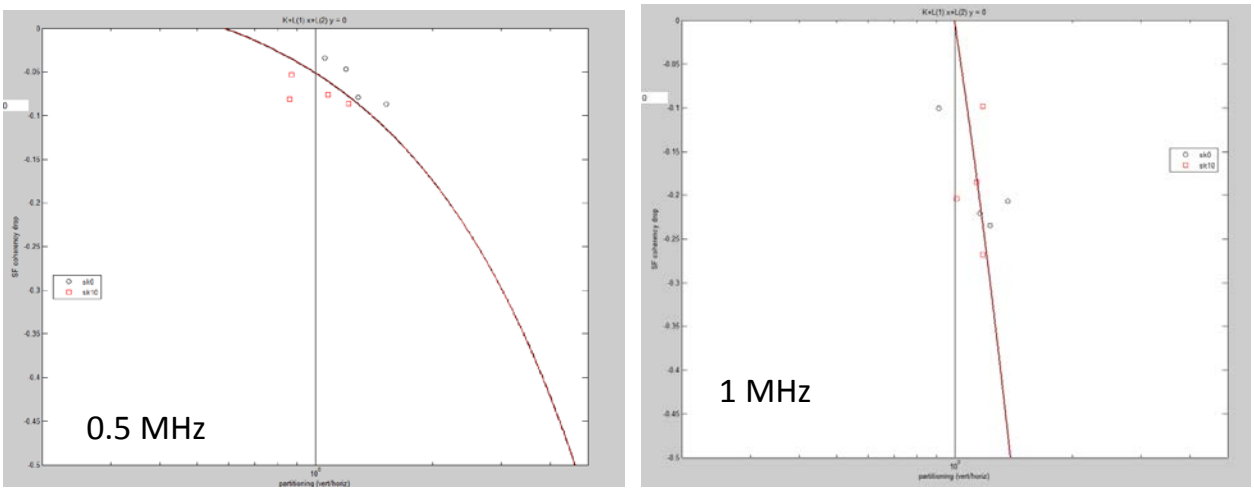

Figure D.11. Sorting by Skew Angle with Specimen B-519E, 0.5 and 1 MHz, 45-Degree Refracted Angle, Four Positions

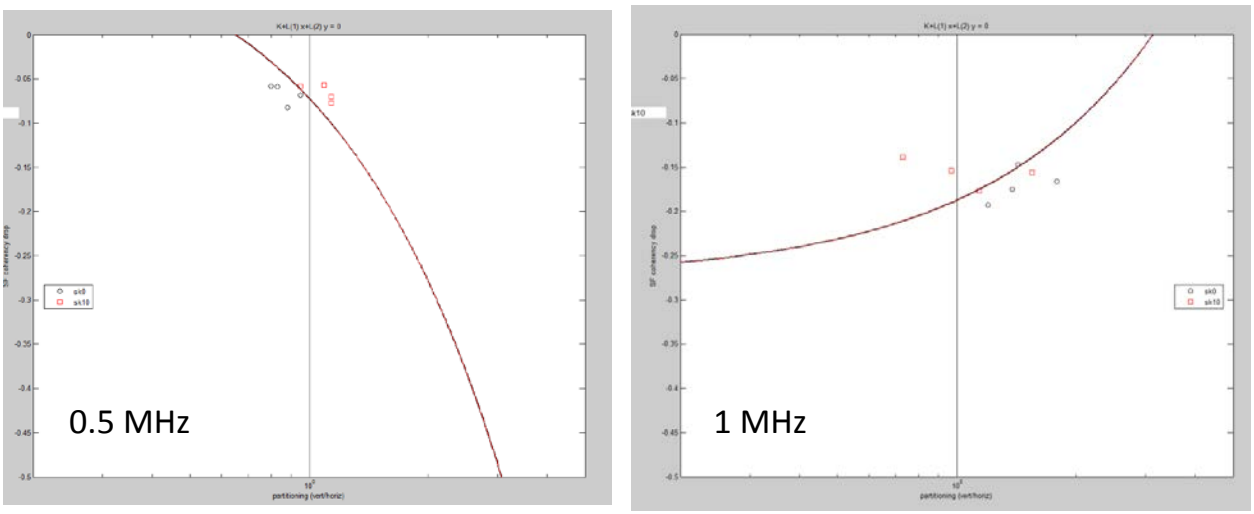

Figure D.12. Sorting by Skew Angle with Specimen B-519E, 0.5 and 1 MHz, 55-Degree Refracted Angle, Four Positions

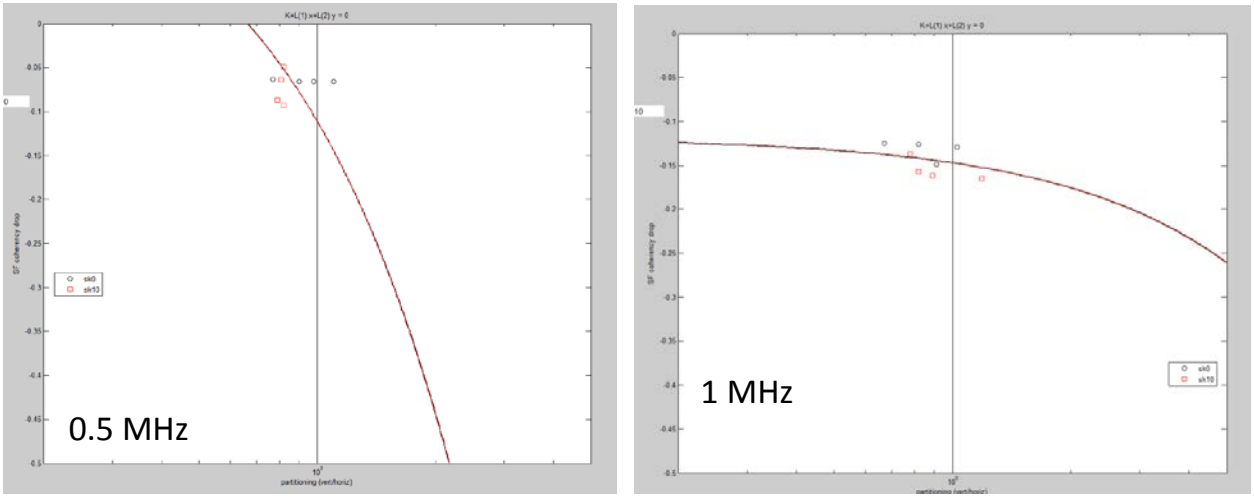

Figure D.13. Sorting by Skew Angle with Specimen B-519E, 0.5 and 1 MHz, 70-Degree Refracted Angle, Four Positions

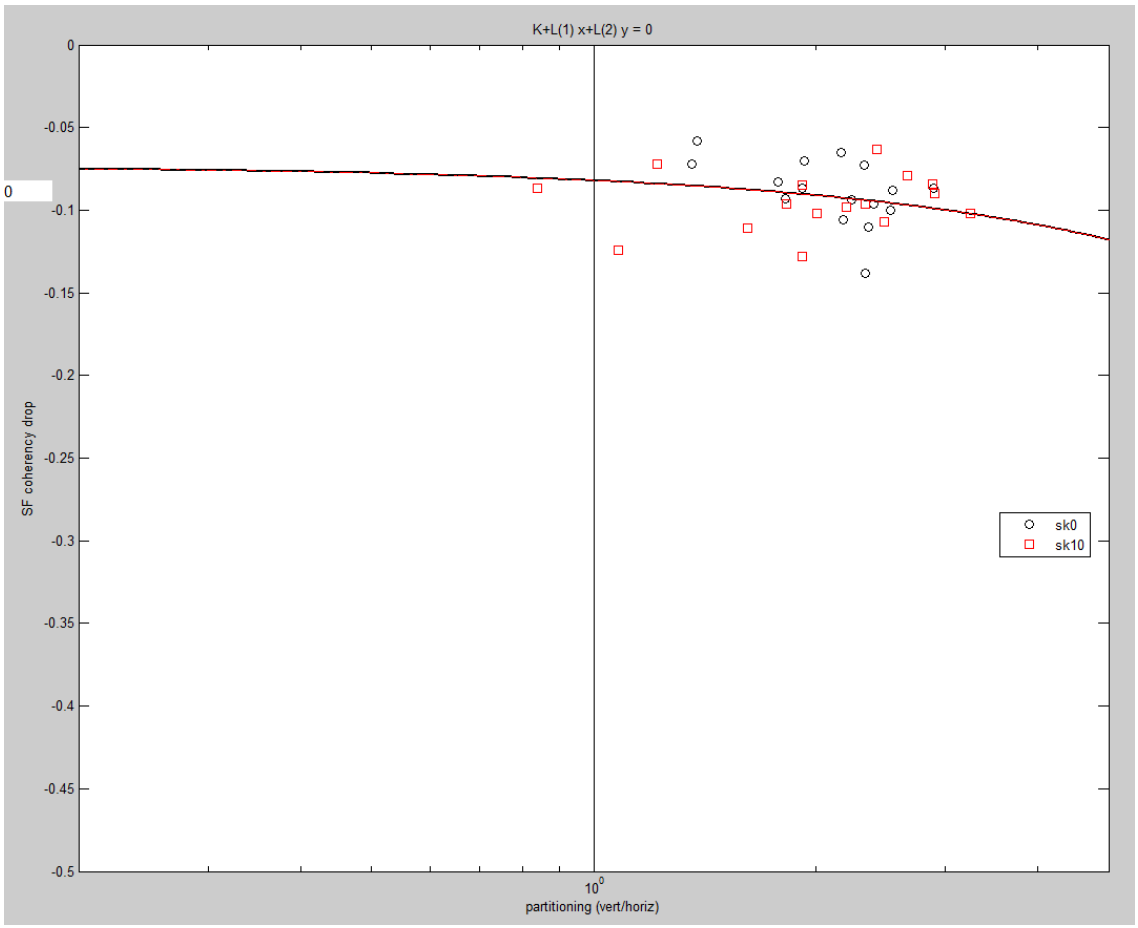

Figure D.14. Sorting by Skew Angle for Specimen B-519C at 1.0 MHz with Four Refracted Angles and Four Positions

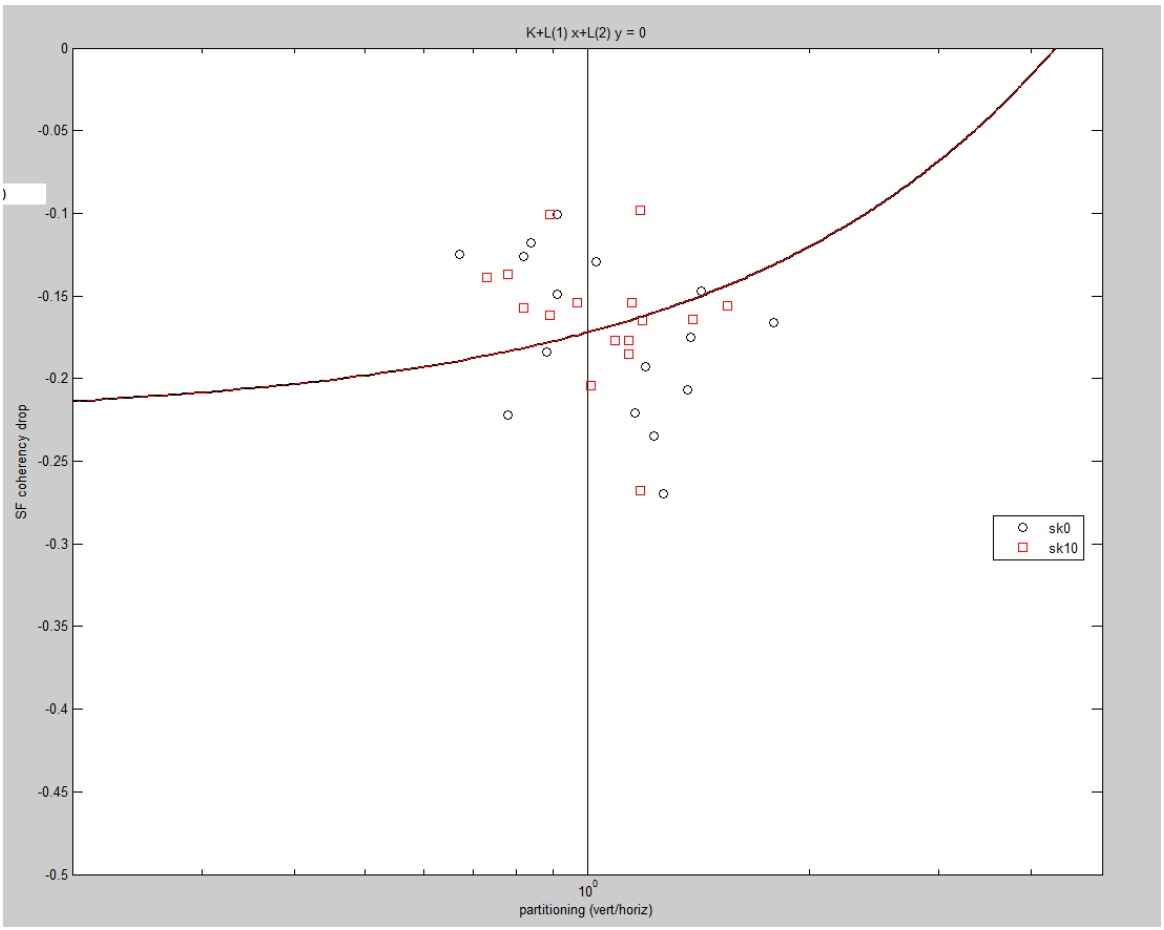

Figure D.15. Sorting by Skew Angle for Specimen B-519E at 1.0 MHz with Four Refracted Angles and Four Positions

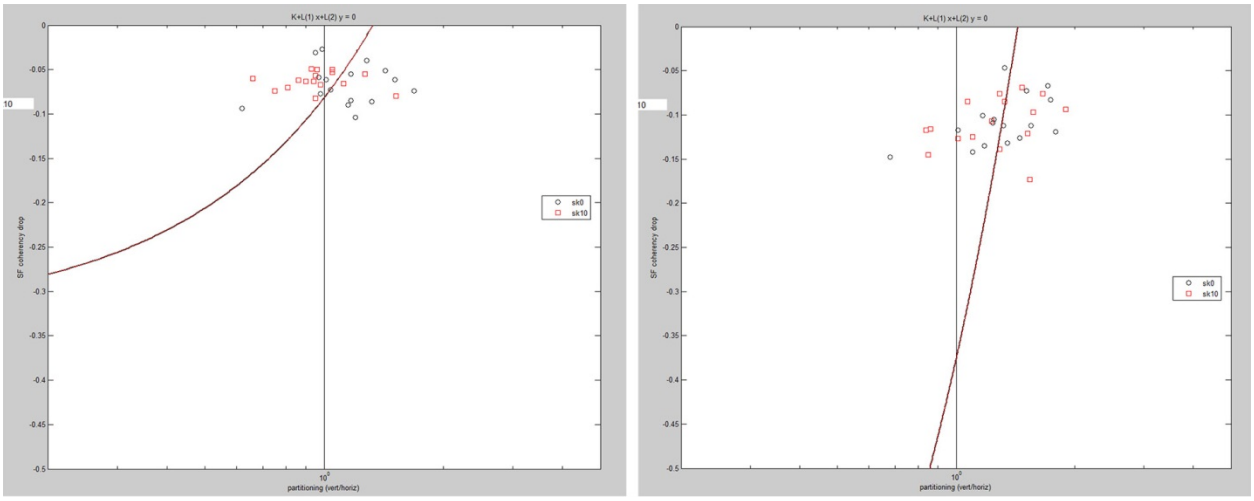

Figure D.16. Sorting by Skew Angle for Specimen AAD-2 at 0.5 (left) and 1.0 MHz (right) with Four Refracted Angles and Four Positions

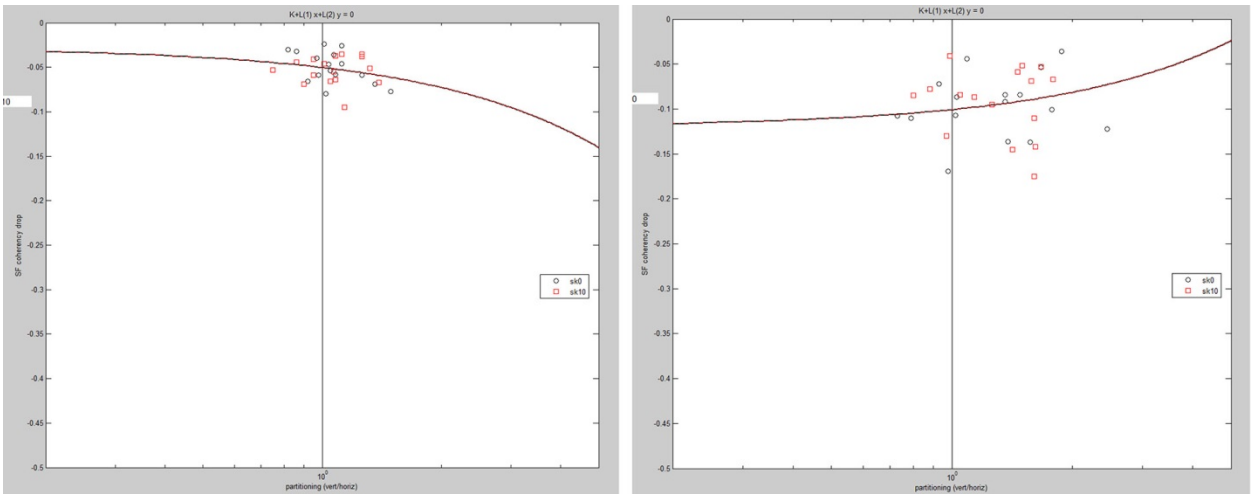

Figure D.17. Sorting by Skew Angle for Specimen AAD-3 at 0.5 (left) and 1.0 MHz (right) with Four Refracted Angles and Four Positions

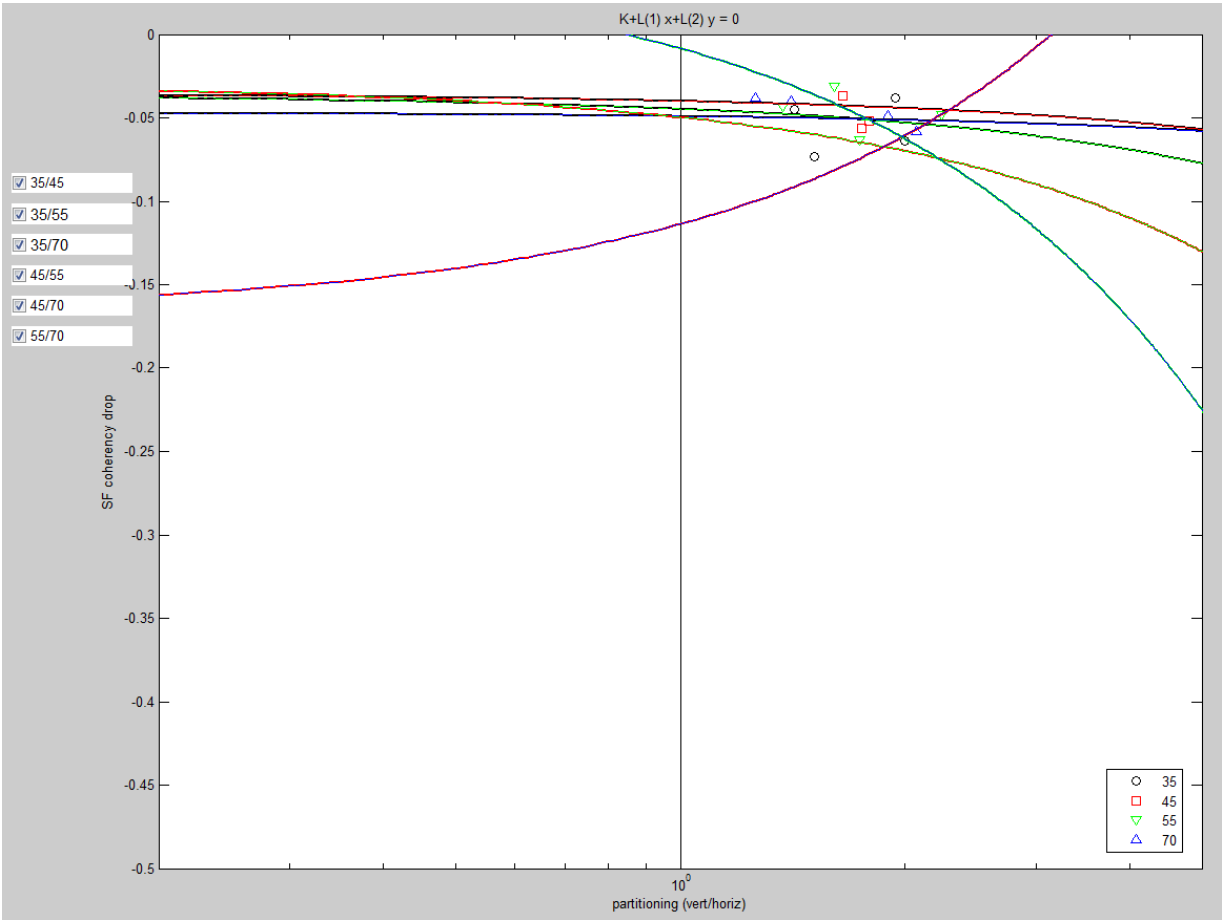

Figure D.18. Sorting by Refracted Angle for Specimen B-519C at 0.5 MHz, Skew 0 Degrees and Four Positions

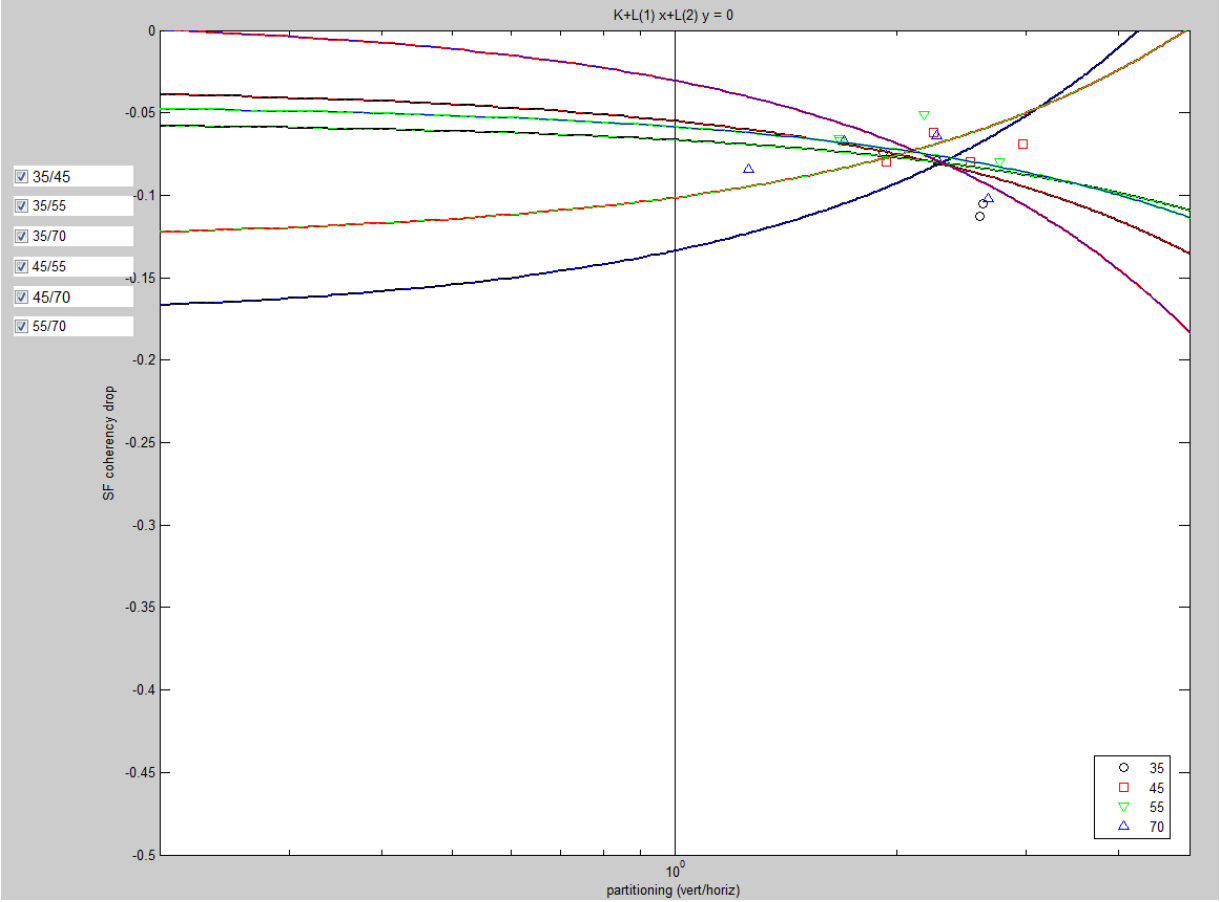

Figure D.19. Sorting by Refracted Angle for Specimen B-519C at 0.8 MHz, Skew 0 Degrees and Four Positions

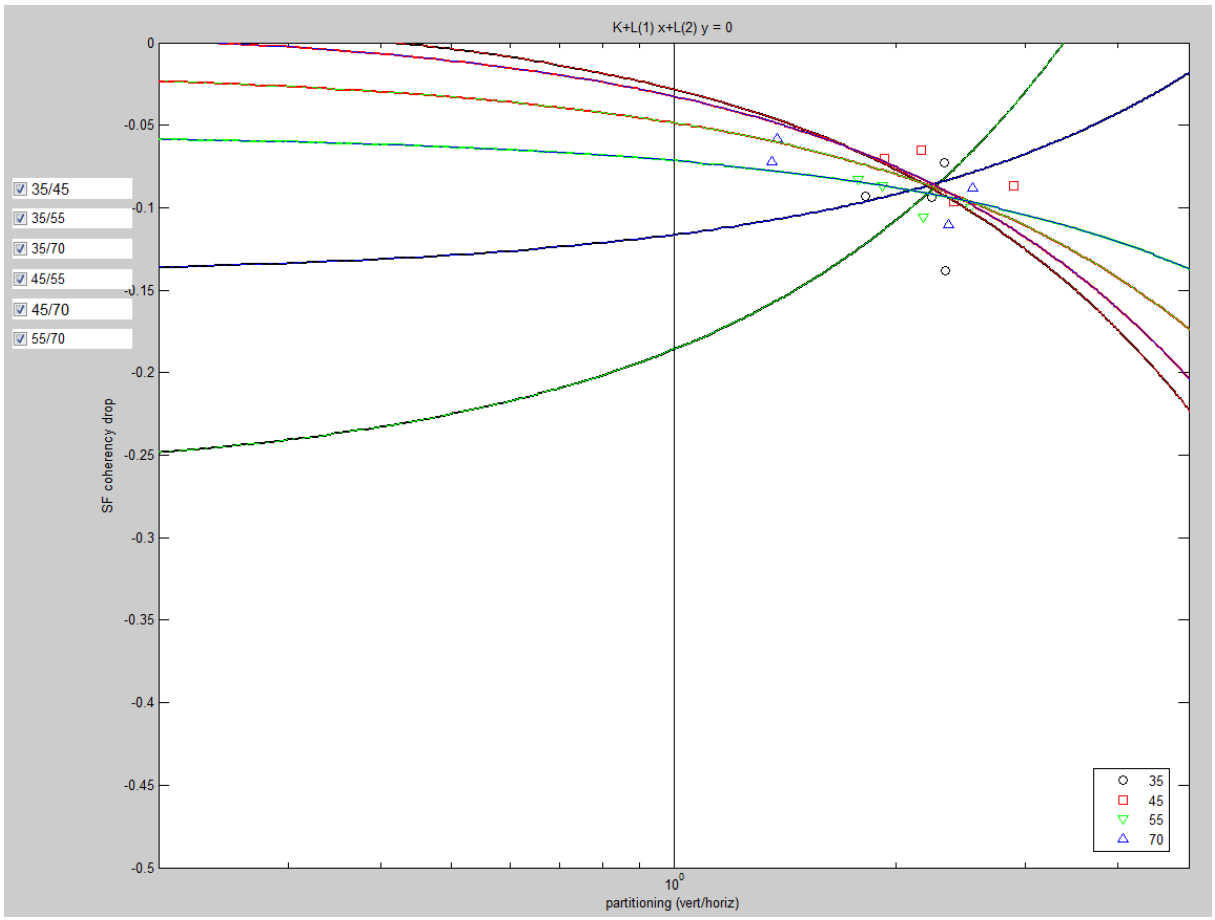

Figure D.20. Sorting by Refracted Angle for Specimen B-519C at 1.0 MHz, Skew 0 Degrees and Four Positions

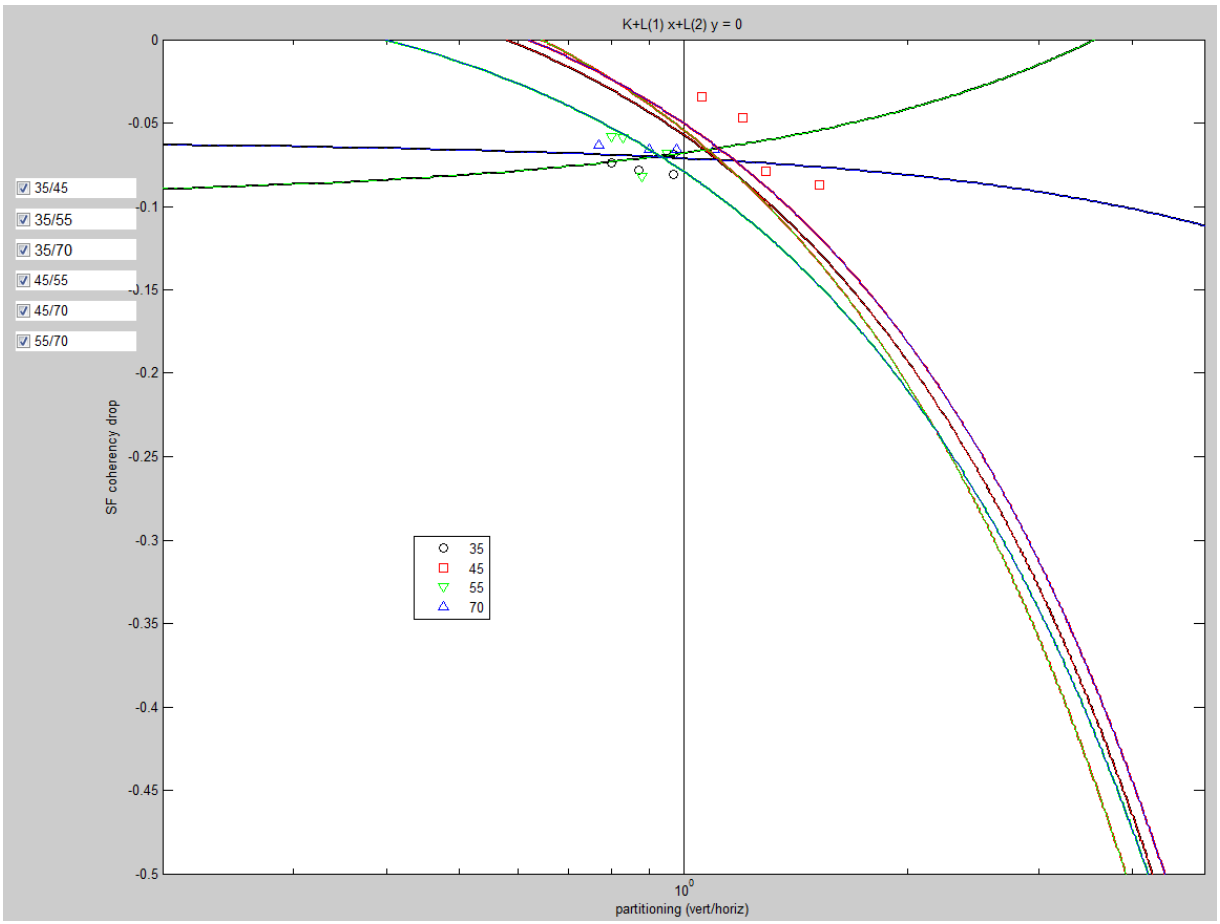

Figure D.21. Sorting by Refracted Angle for Specimen B-519E at 0.5 MHz, Skew 0 Degrees and Four Positions

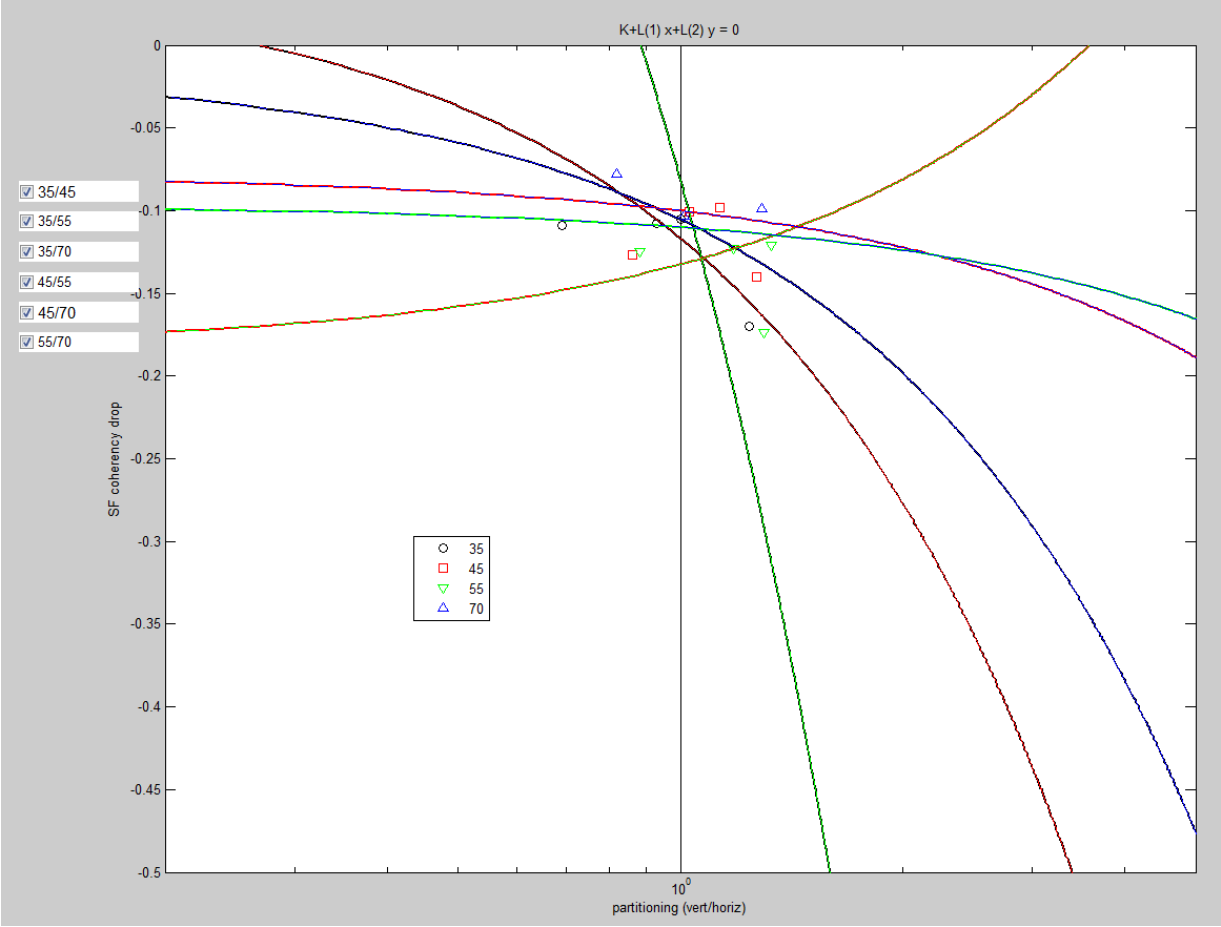

Figure D.22. Sorting by Refracted Angle for Specimen B-519E at 0.8 MHz, Skew 0 Degrees and Four Positions

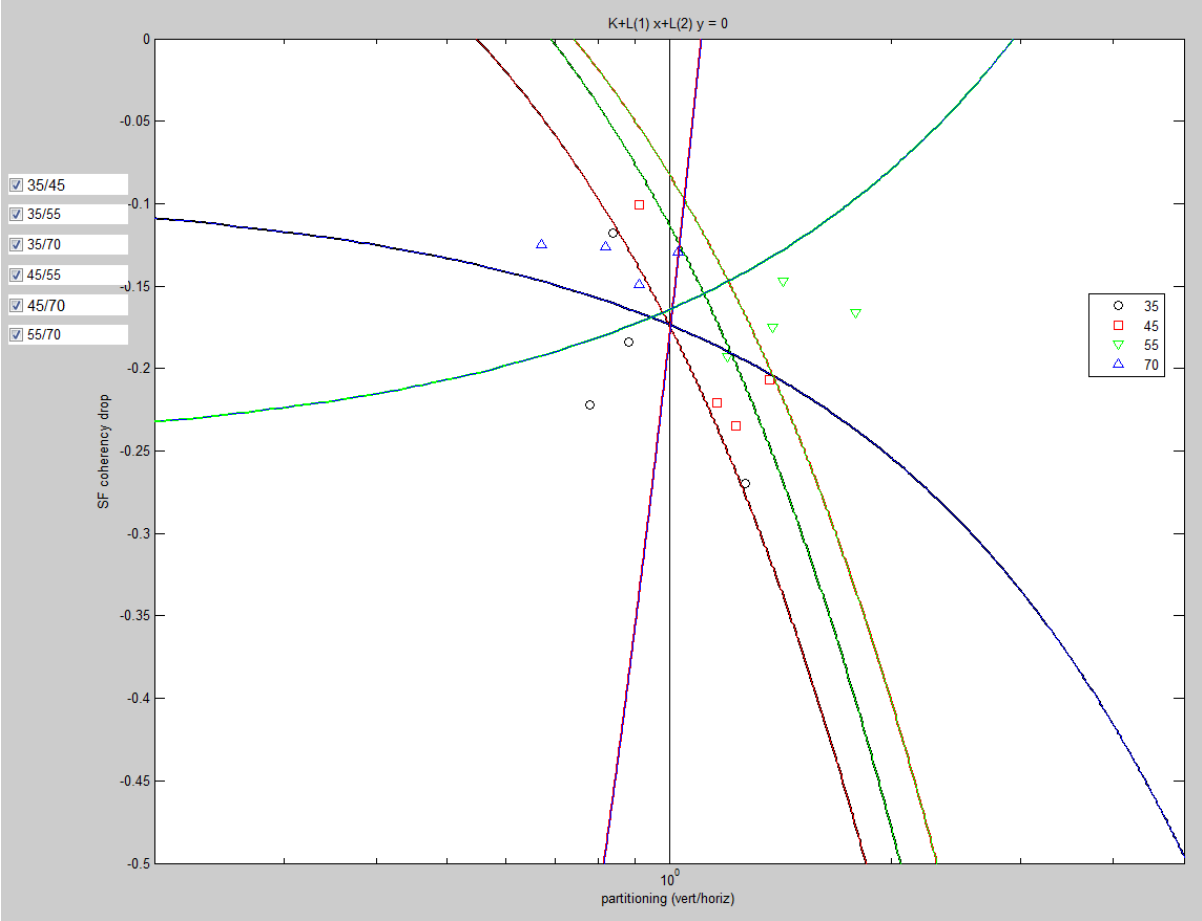

Figure D.23. Sorting by Refracted Angle for Specimen B-519E at 1.0 MHz, Skew 0 Degrees and Four Positions

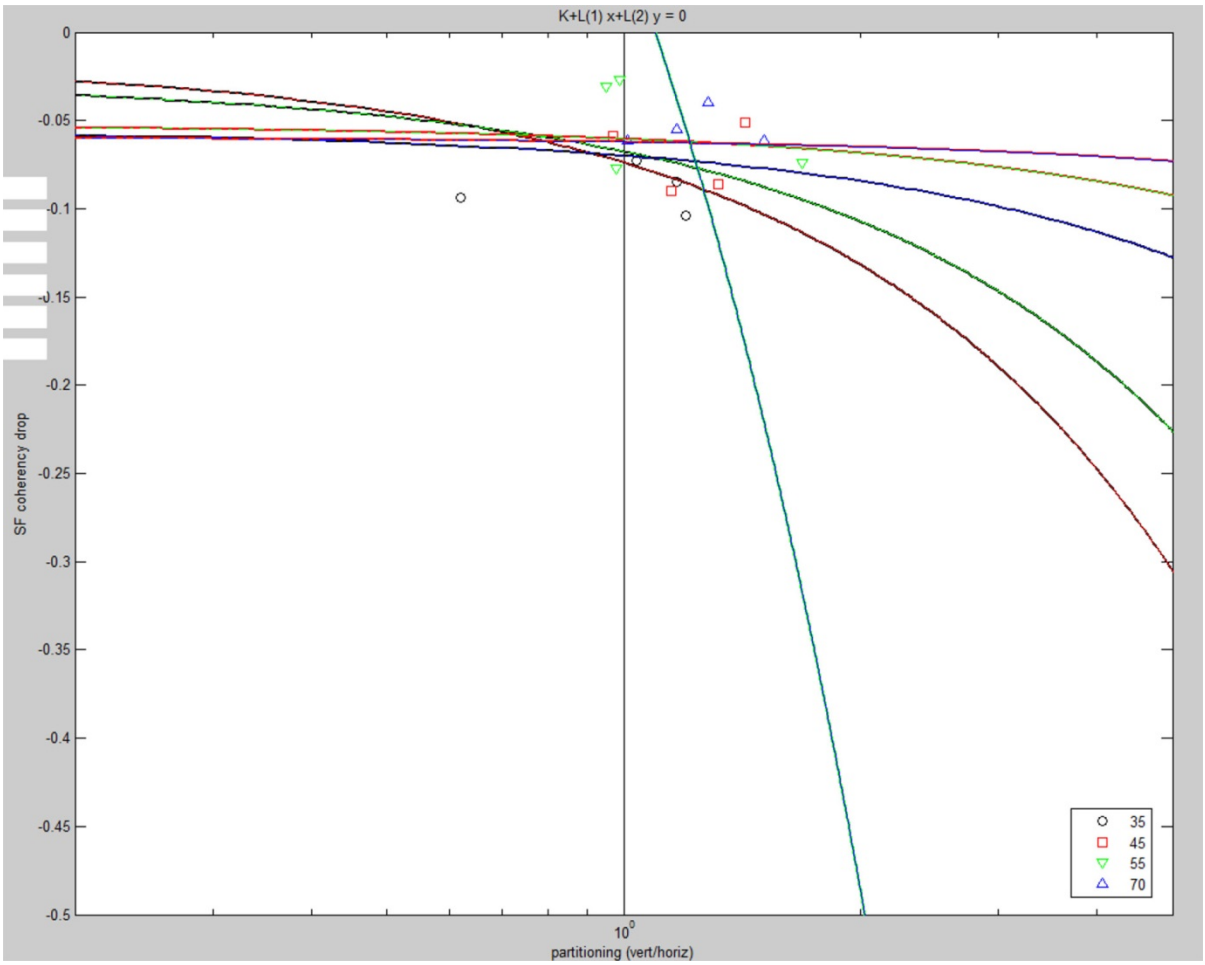

Figure D.24. Sorting by Refracted Angle for Specimen AAD-2 at 0.5 MHz, Skew 0 Degrees and Four Positions

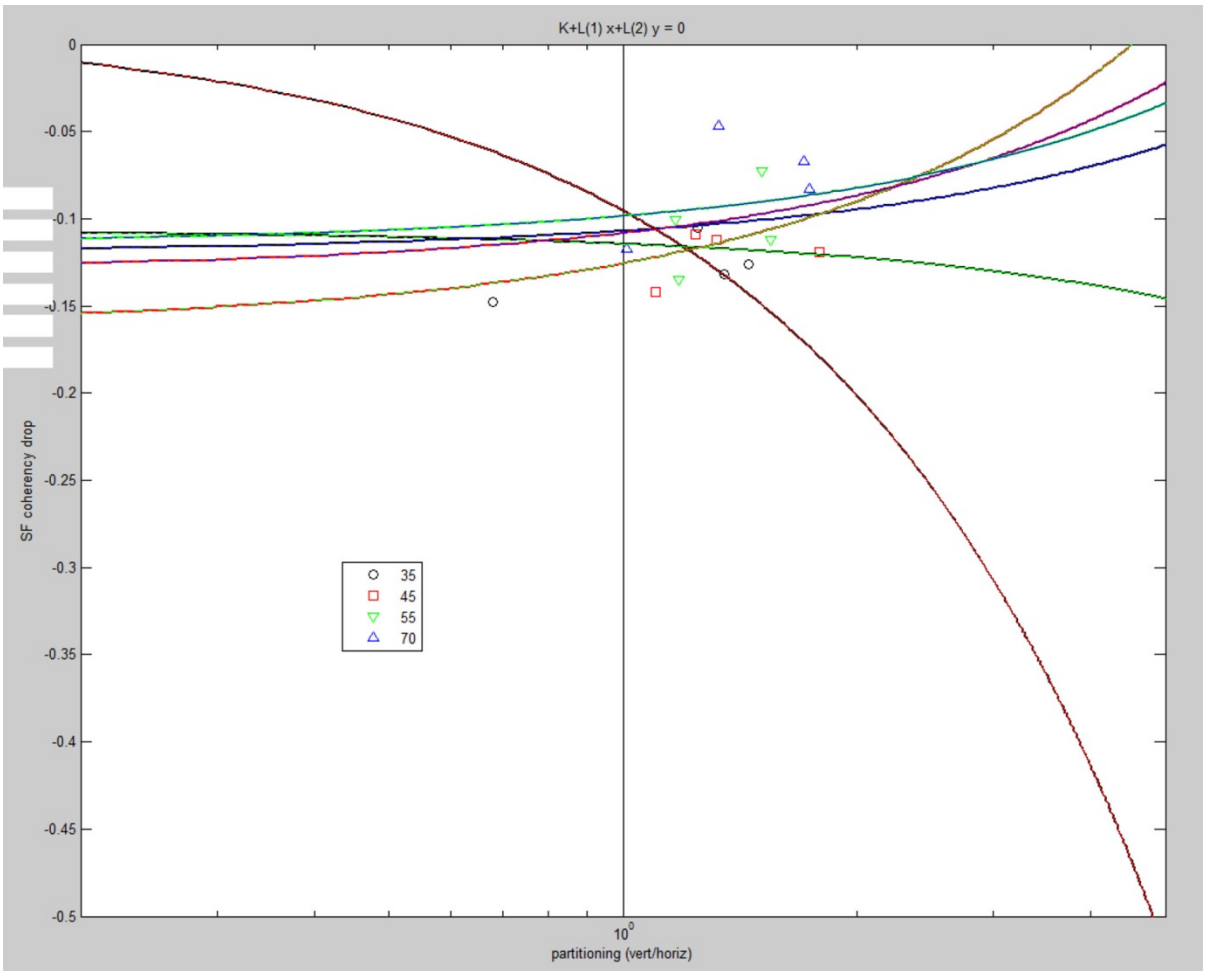

Figure D.25. Sorting by Refracted Angle for Specimen AAD-2 at 1.0 MHz, Skew 0 Degrees and Four Positions

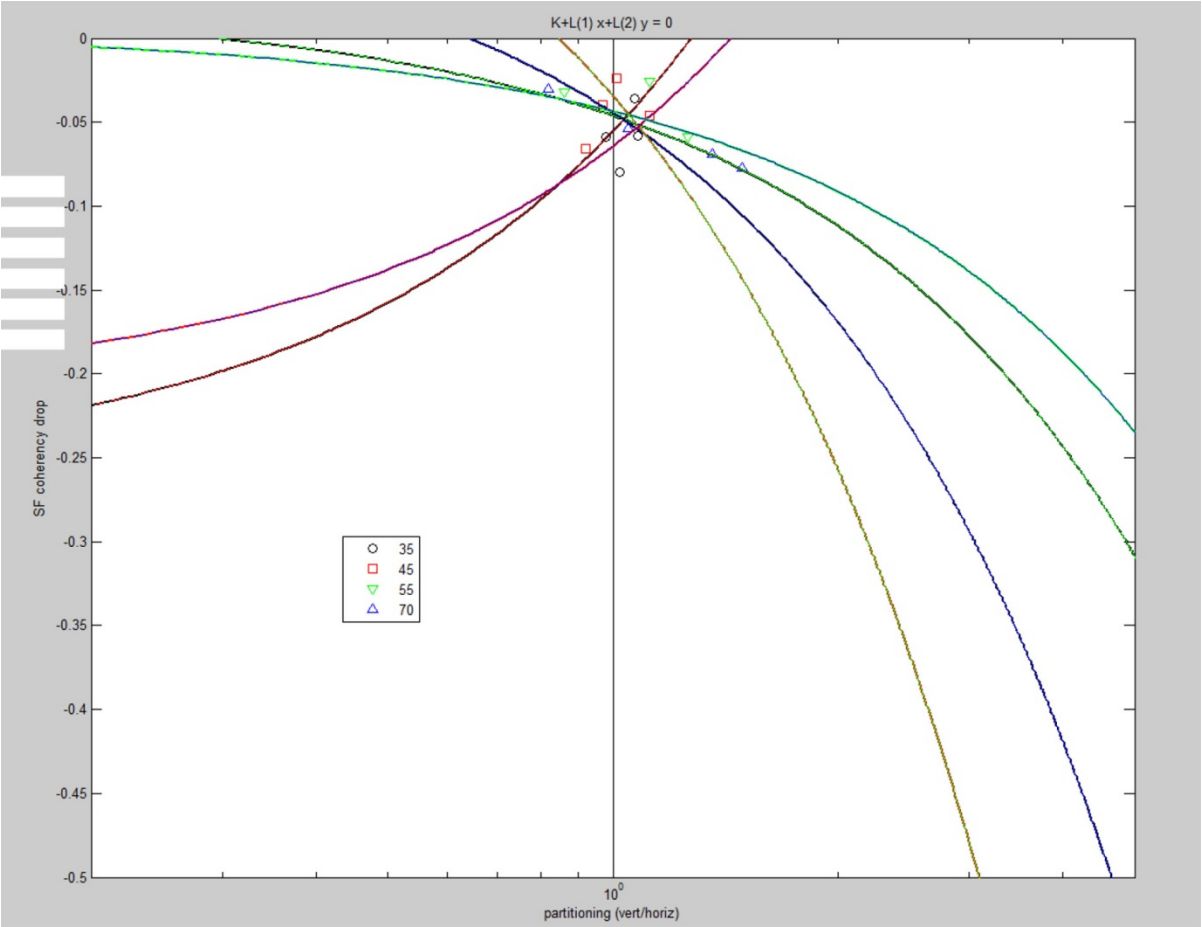

Figure D.26. Sorting by Refracted Angle for Specimen AAD-3 at 0.5 MHz, Skew 0 Degrees and Four Positions

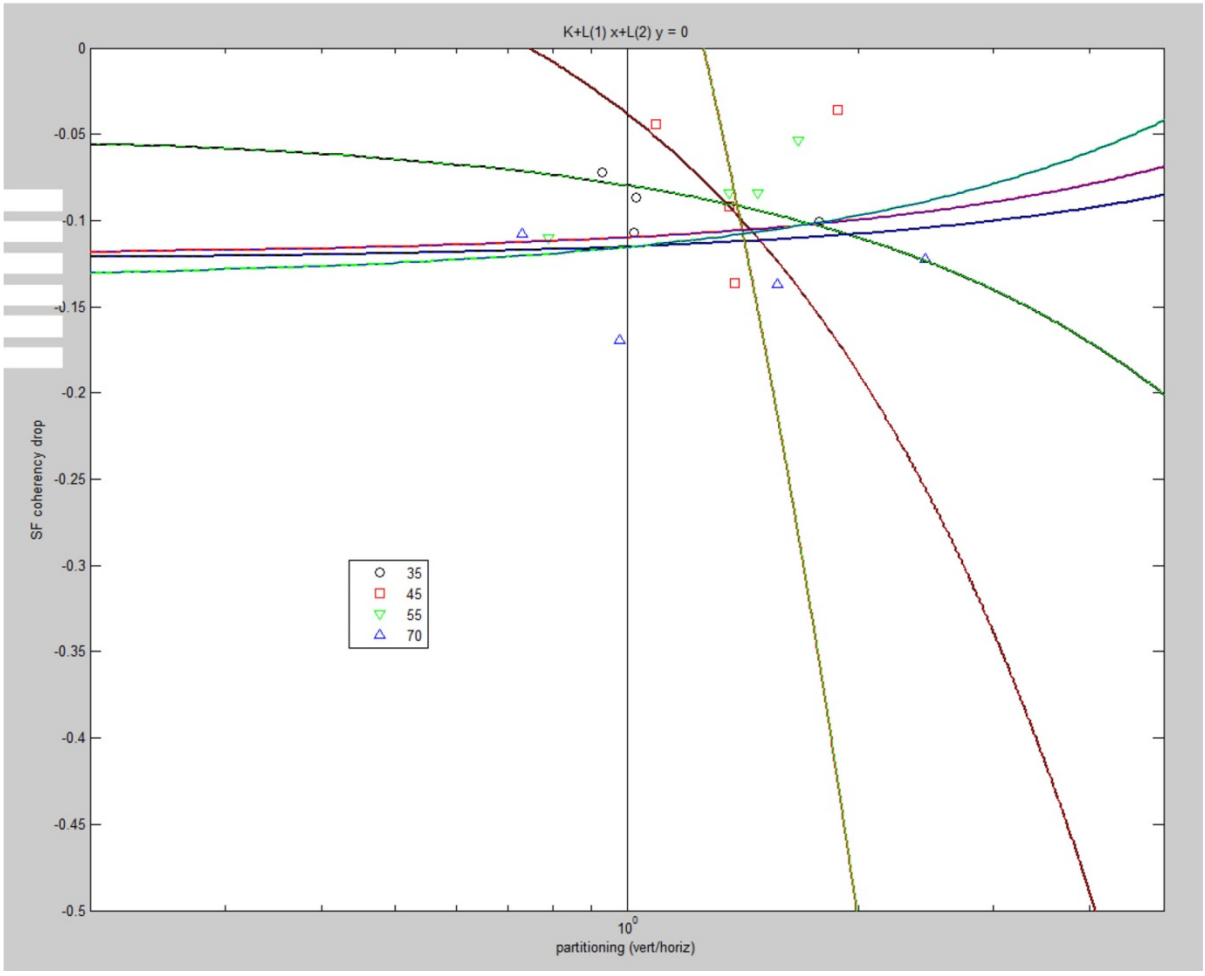

Figure D.27. Sorting by Refracted Angle for Specimen AAD-3 at 1.0 MHz, Skew 0 Degrees and Four Positions

Appendix E

Sound Field Positions

Appendix E

Sound Field Positions

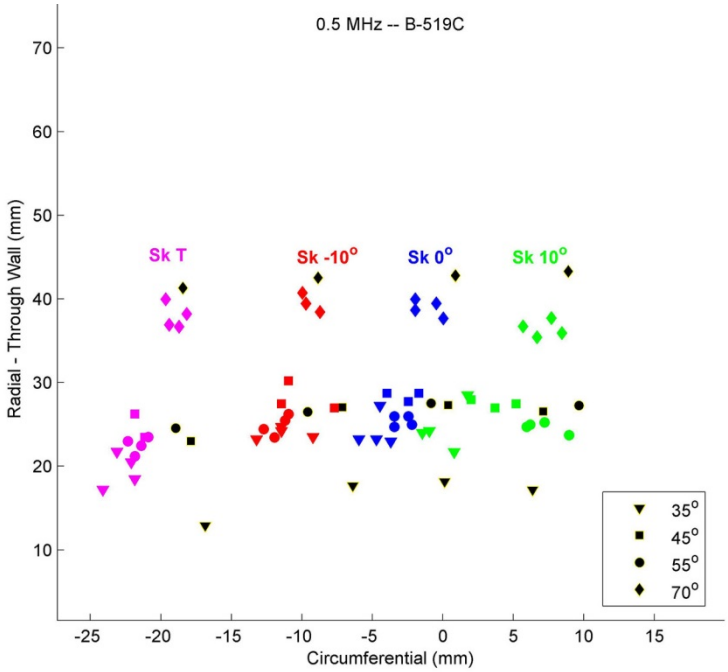

Figure E.1. Sound Field Positions in Specimen B519C with the 0.5-MHz Probe

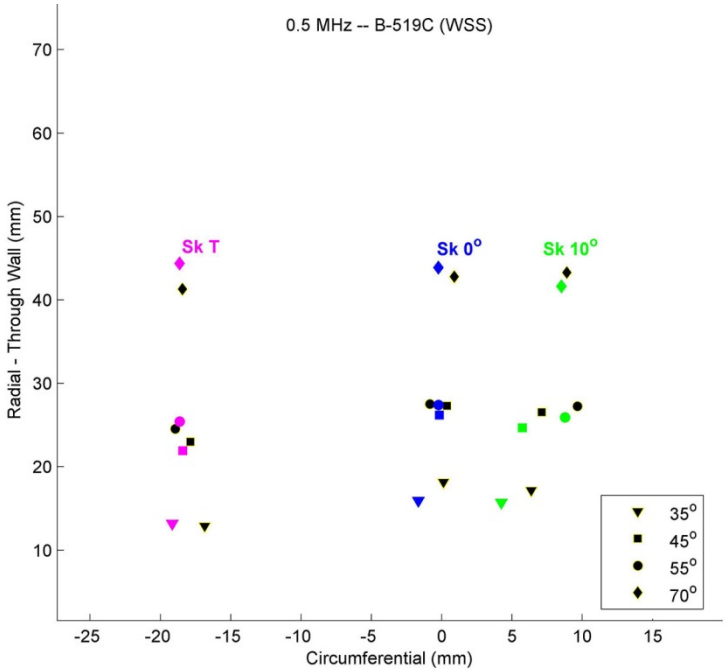

Figure E.2. Sound Field Positions in the Standard WSS Specimen with the 0.5-MHz Probe and Acquisition Prameters Corresponding to Specimen B519C

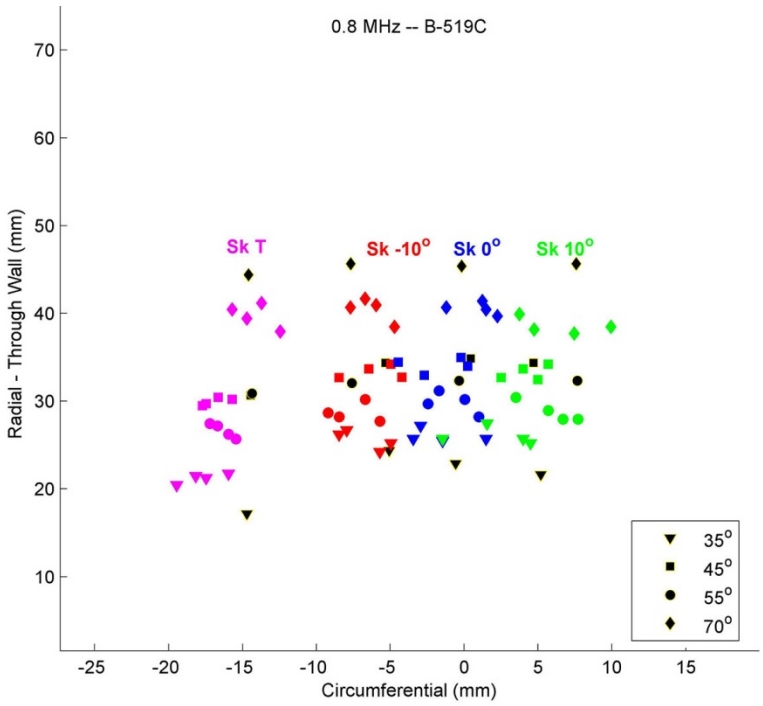

Figure E.3. Sound Field Positions in Specimen B519C with the 0.8-MHz Probe

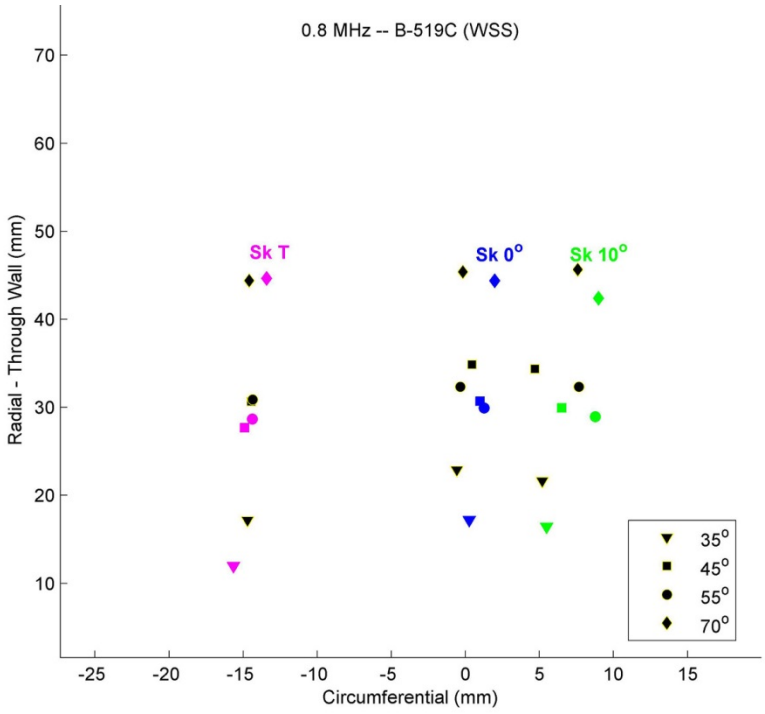

Figure E.4. Sound Field Positions in the Standard WSS Specimen with the 0.8-MHz Probe and Acquisition Prameters Corresponding to Specimen B519C

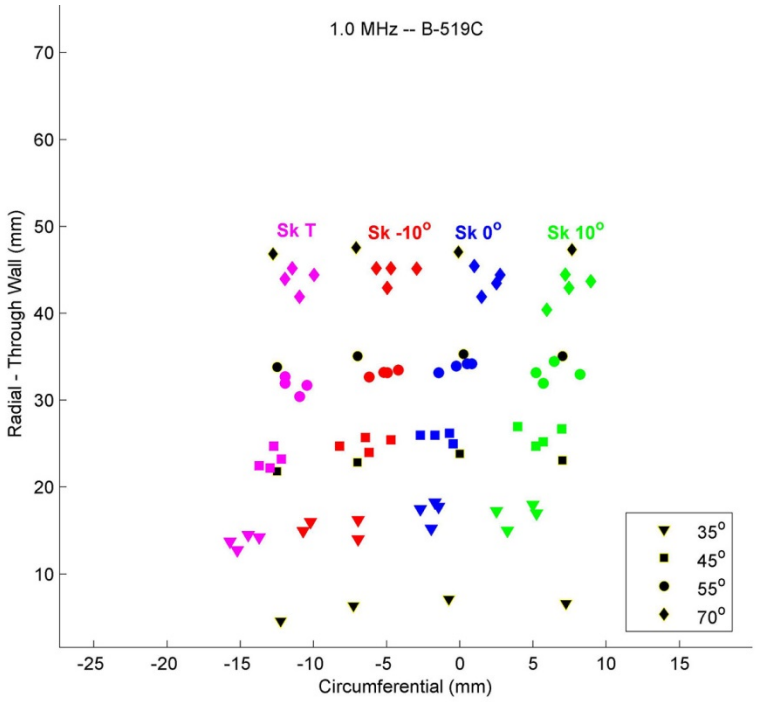

Figure E.5. Sound Field Positions in Specimen B519C with the 1.0-MHz Probe

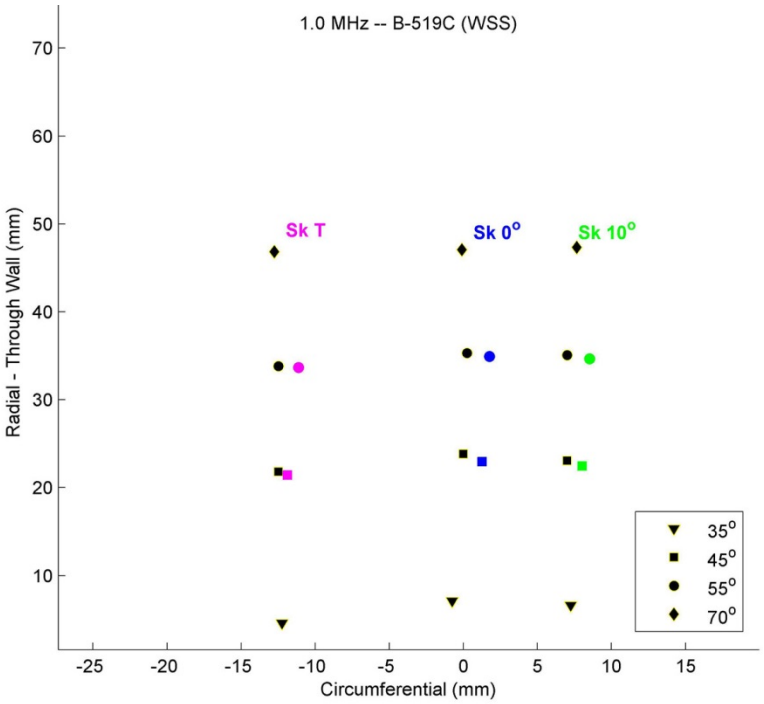

Figure E.6. Sound Field Positions in the Standard WSS Specimen with the 1.0-MHz Probe and Acquisition Prameters Corresponding to Specimen B519C

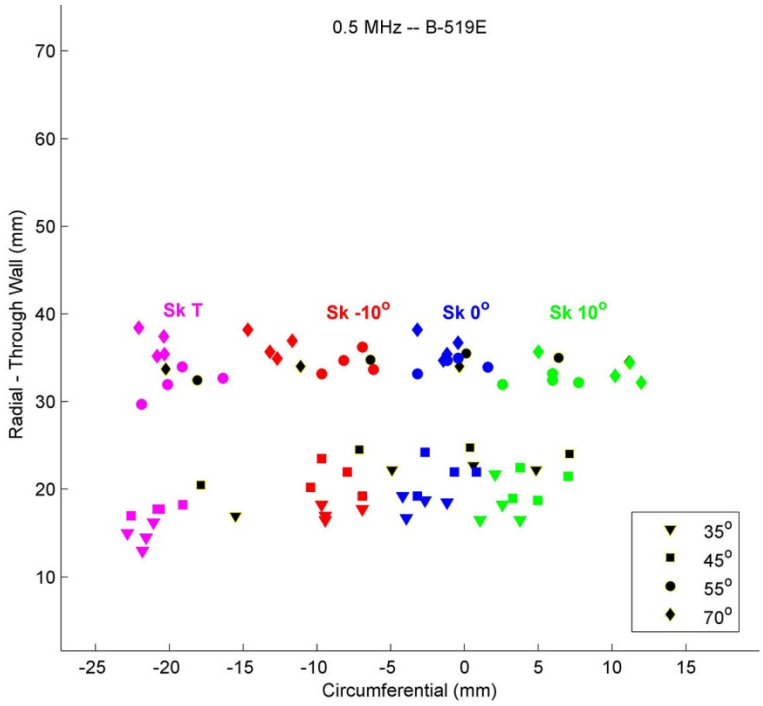

Figure E.7. Sound Field Positions in Specimen B519E with the 0.5-MHz Probe

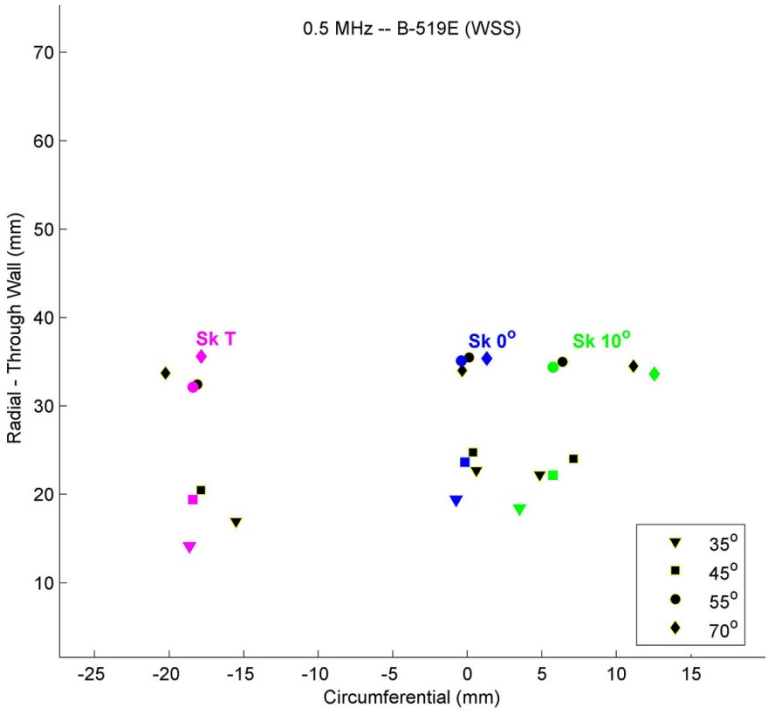

Figure E.8. Sound Field Positions in the Standard WSS Specimen with the 0.5-MHz Probe and Acquisition Prameters Corresponding to Specimen B519E

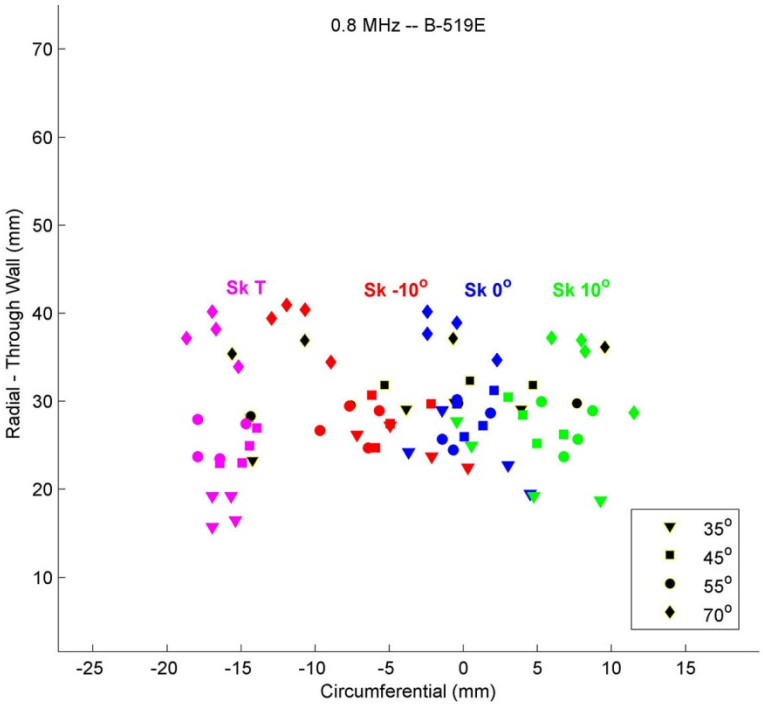

Figure E.9. Sound Field Positions in Specimen B519E with the 0.8-MHz Probe

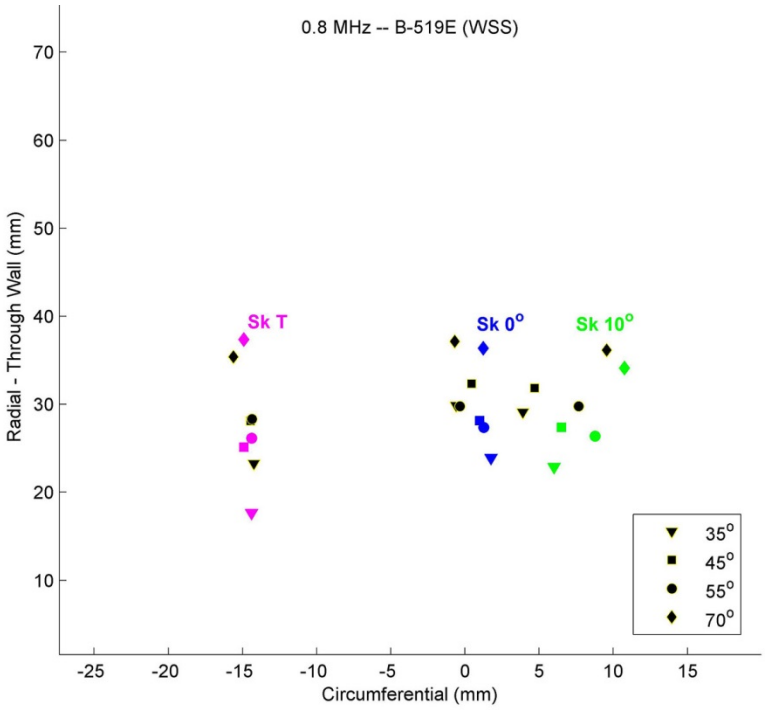

Figure E.10. Sound Field Positions in the Standard WSS Specimen with the 0.8-MHz Probe and Acquisition Prameters Corresponding to Specimen B519E

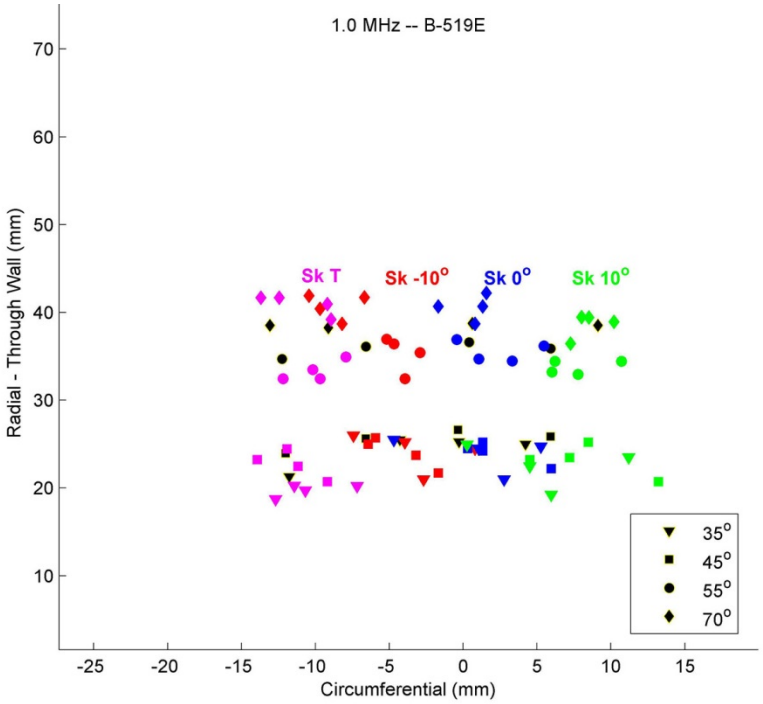

Figure E.11. Sound Field Positions in Specimen B519E with the 1.0-MHz Probe

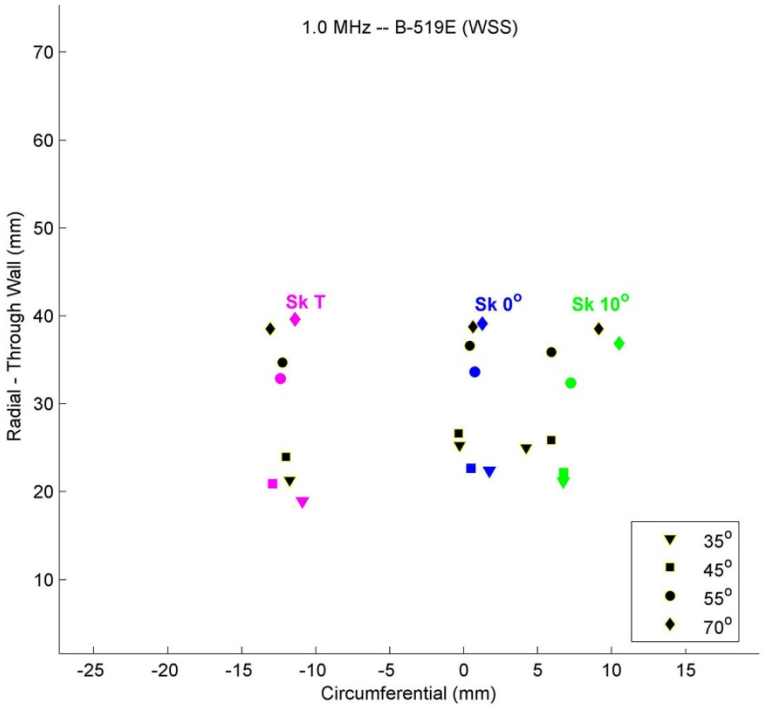

Figure E.12. Sound Field Positions in the Standard WSS Specimen with the 1.0-MHz Probe and Acquisition Prameters Corresponding to Specimen B519E

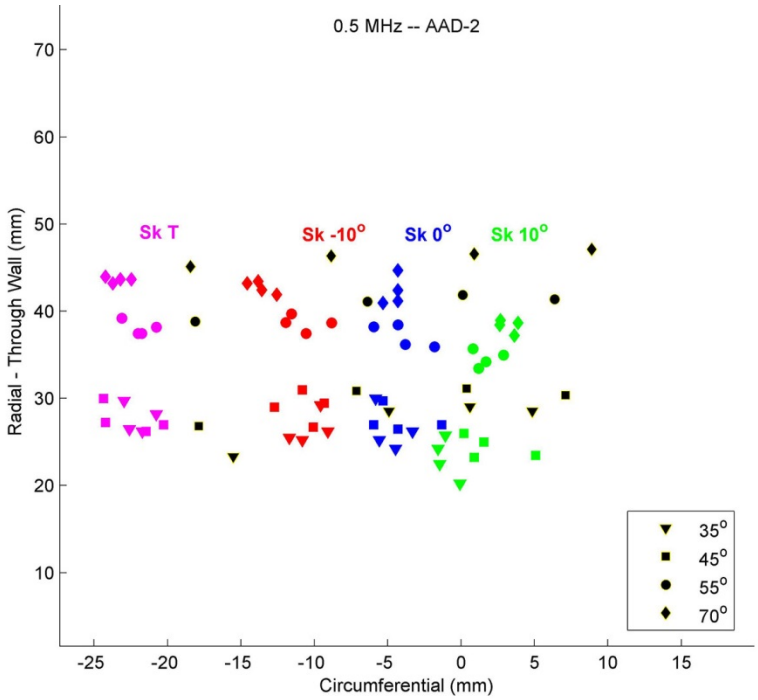

Figure E.13. Sound Field Positions in Specimen AAD2 with the 0.5-MHz Probe

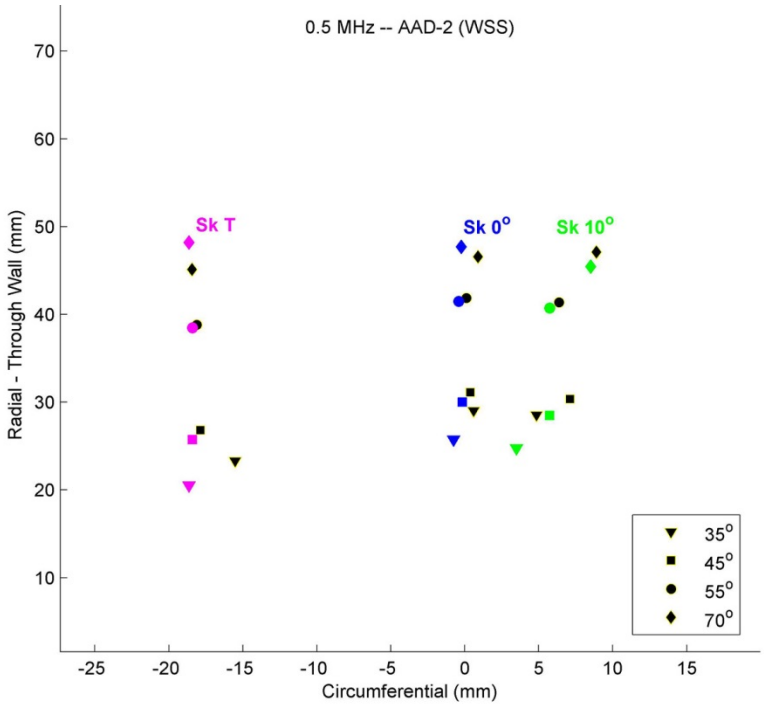

Figure E.14. Sound Field Positions in the Standard WSS Specimen with the 0.5-MHz Probe and Acquisition Prameters Corresponding to Specimen AAD2

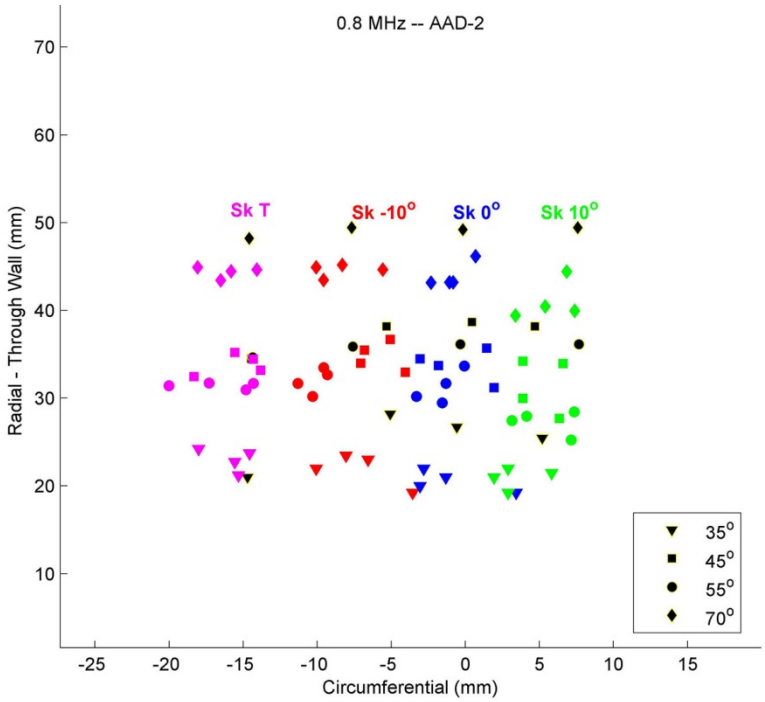

Figure E.15. Sound Field Positions in Specimen AAD2 with the 0.8-MHz Probe

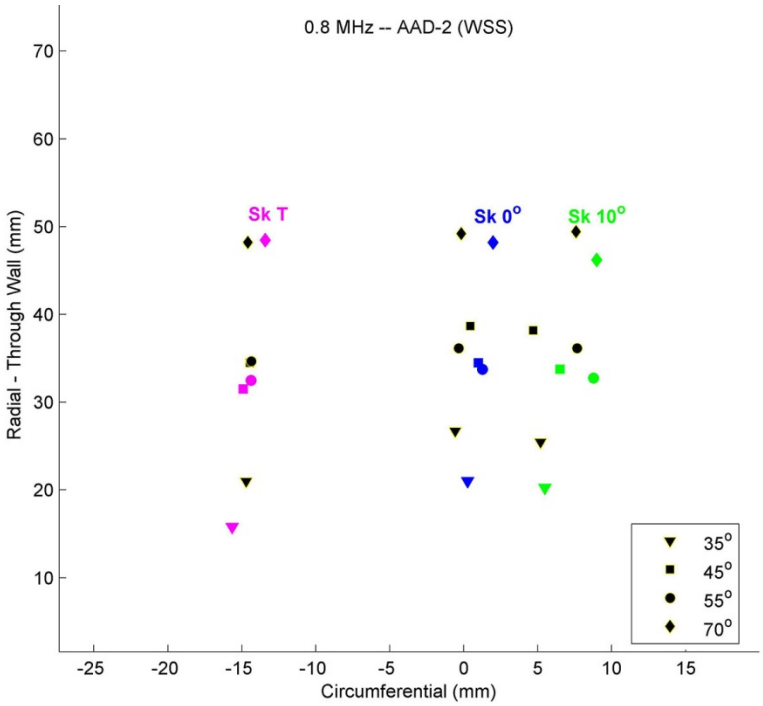

Figure E.16. Sound Field Positions in the Standard WSS Specimen with the 0.8-MHz Probe and Acquisition Prameters Corresponding to Specimen AAD2

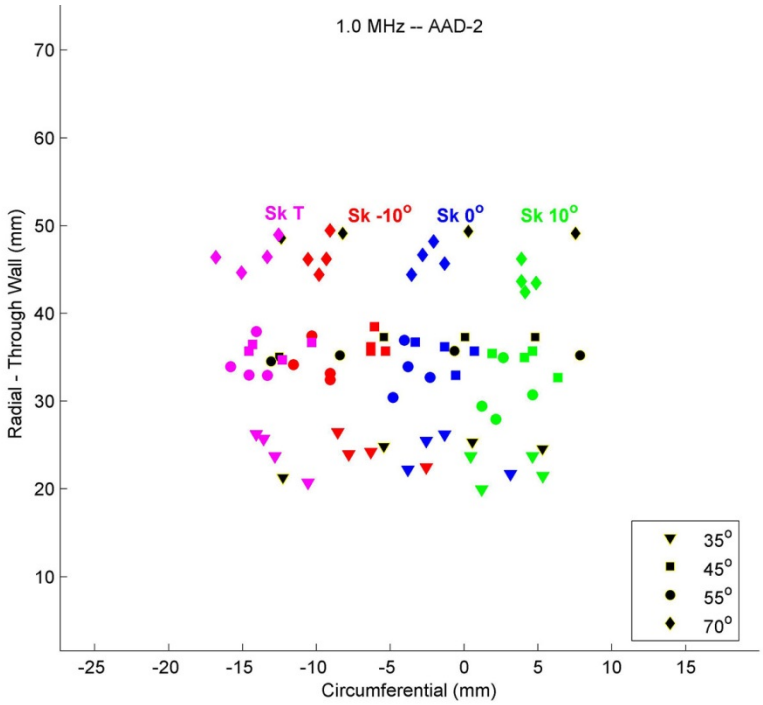

Figure E.17. Sound Field Positions in Specimen AAD2 with the 1.0-MHz Probe

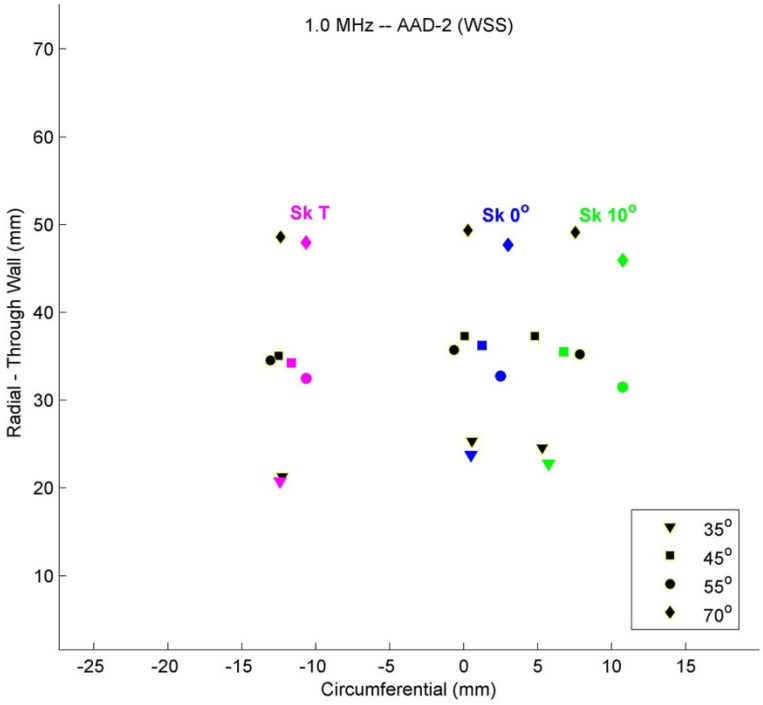

Figure E.18. Sound Field Positions in the Standard WSS Specimen with the 1.0-MHz Probe and Acquisition Prameters Corresponding to Specimen AAD2

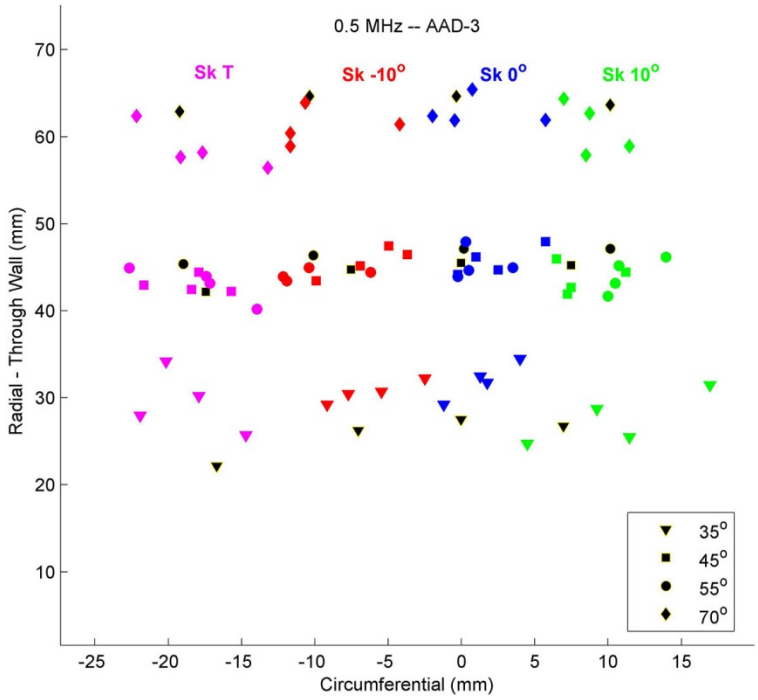

Figure E.19. Sound Field Positions in Specimen AAD3 with the 0.5-MHz Probe

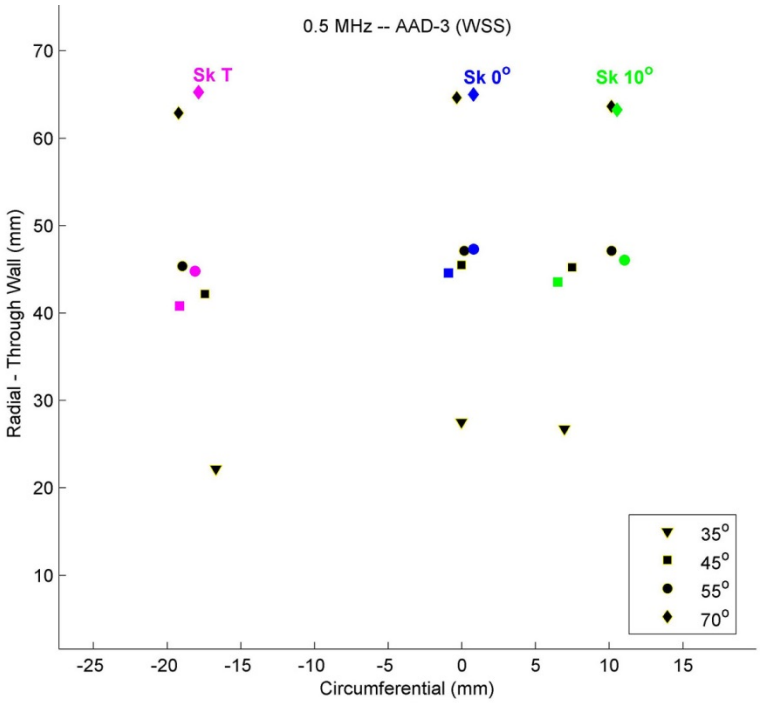

Figure E.20. Sound Field Positions in the Standard WSS Specimen with the 0.5-MHz Probe and Acquisition Prameters Corresponding to Specimen AAD3

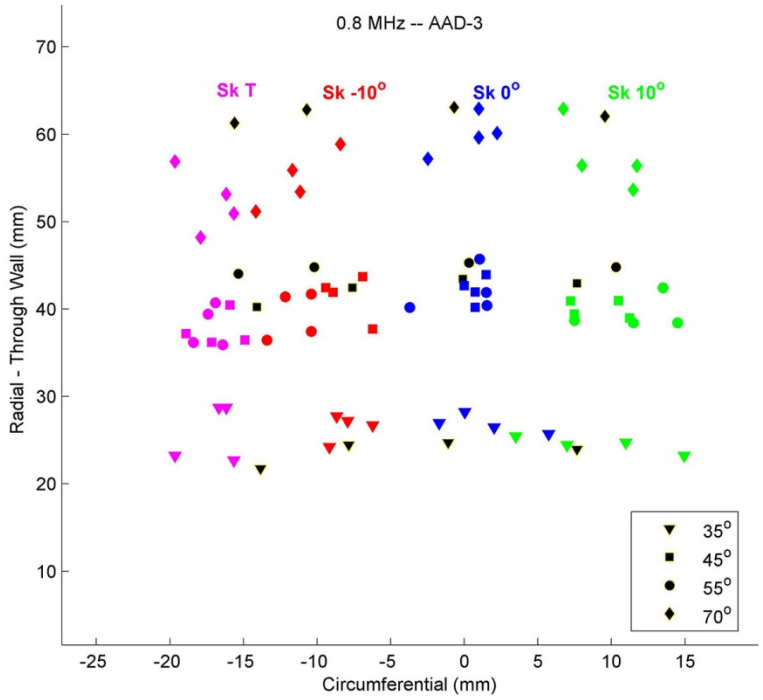

Figure E.21. Sound Field Positions in Specimen AAD3 with the 0.8-MHz Probe

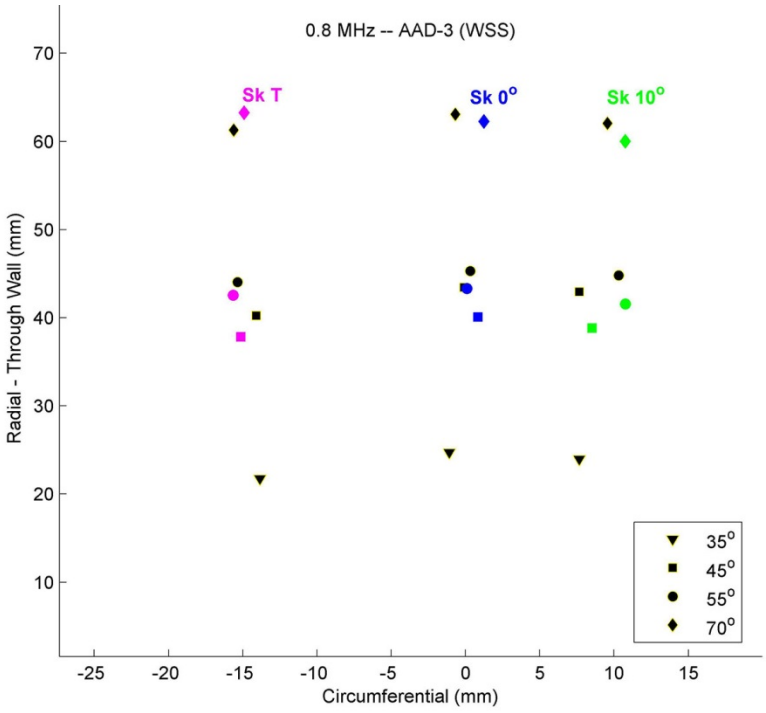

Figure E.22. Sound Field Positions in the Standard WSS Specimen with the 0.8-MHz Probe and Acquisition Prameters Corresponding to Specimen AAD3

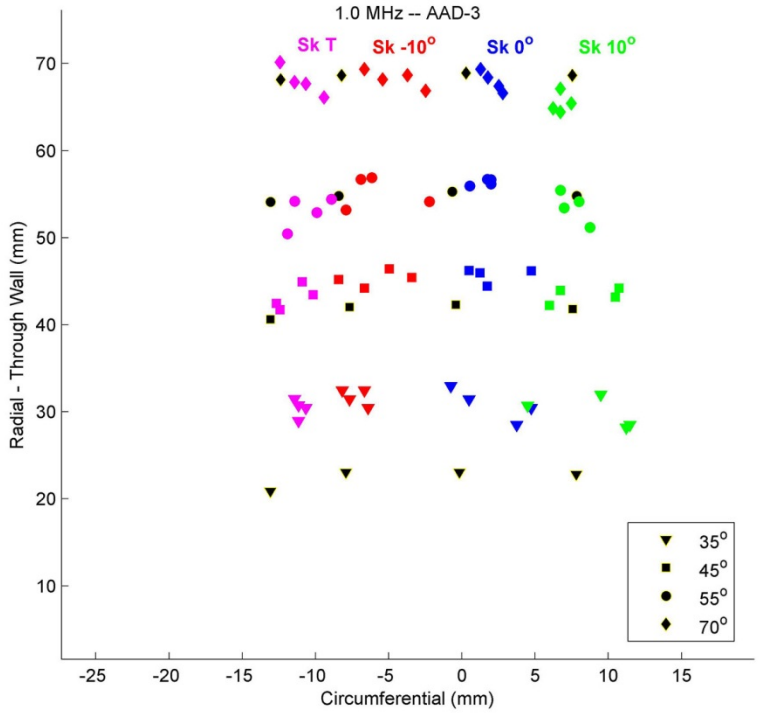

Figure E.23. Sound Field Positions in Specimen AAD3 with the 1.0-MHz Probe

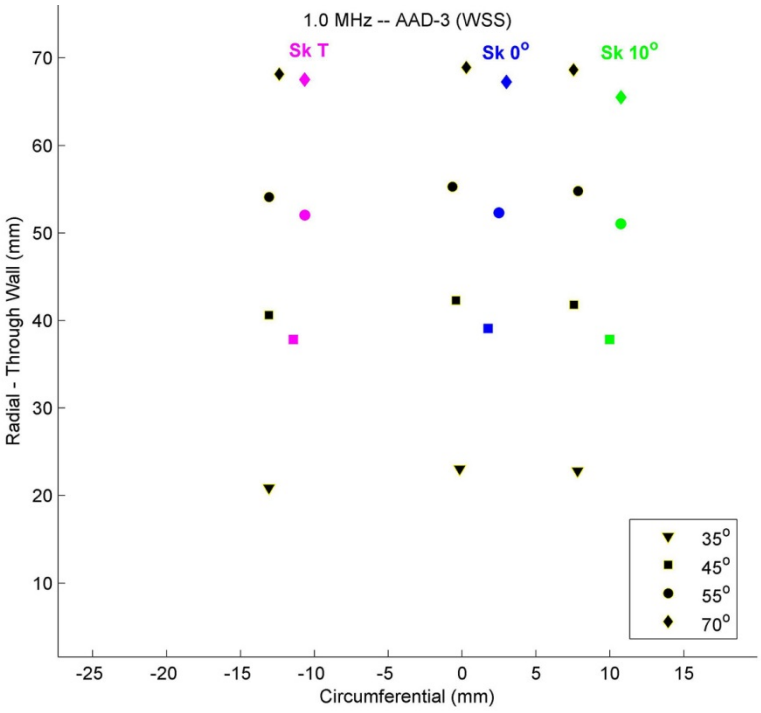

Figure E.24. Sound Field Positions in the Standard WSS Specimen with the 1.0-MHz Probe and Acquisition Prameters Corresponding to Specimen AAD3

Pacific Northwest
NATIONAL LABORATORY

U.S. DEPARTMENT OF
ENERGY

Proudly Operated by Battelle *Since 1965*

902 Battelle Boulevard
P.O. Box 999
Richland, WA 99352
1-888-375-PNNL (7665)
www.pnl.gov